
Optical Communications Research Laboratory
Stanford University

**Final Report to the
OFFICE OF NAVAL RESEARCH
for R&T Project Code 4148130-01
Grant Number: N00014-91-J-1857**

**ADVANCED OPTICAL FIBER
COMMUNICATION SYSTEMS**

For a period of three years
September 1, 1991 through August 31, 1994

Submitted by:

Prof. Leonid G. Kazovsky, Principal Investigator
Department of Electrical Engineering
Durand 202, MC-4055
Stanford University
Stanford, CA 94305-4055
Tel. No. (415) 725-3818
Fax No. (415) 723-9251
Email: leonid@sierra.stanford.edu

DECLASSIFICATION STATEMENT A

Approved for public release
Distribution Unlimited

19970716 157



DEPARTMENT OF THE NAVY
OFFICE OF NAVAL RESEARCH
SEATTLE REGIONAL OFFICE
1107 NE 45TH STREET, SUITE 350
SEATTLE WA 98105-4631

IN REPLY REFER TO:

4330
ONR 247
11 Jul 97

From: Director, Office of Naval Research, Seattle Regional Office, 1107 NE 45th St., Suite 350, Seattle, WA 98105

To: Defense Technical Center, Attn: P. Mawby, 8725 John J. Kingman Rd., Suite 0944, Ft. Belvoir, VA 22060-6218

Subj: RETURNED GRANTEE/CONTRACTOR TECHNICAL REPORTS

- 1. This confirms our conversations of 27 Feb 97 and 11 Jul 97. Enclosed are a number of technical reports which were returned to our agency for lack of clear distribution availability statement. This confirms that all reports are unclassified and are "APPROVED FOR PUBLIC RELEASE" with no restrictions.
- 2. Please contact me if you require additional information. My e-mail is *silverr@onr.navy.mil* and my phone is (206) 625-3196.


ROBERT J. SILVERMAN

DTIC QUALITY INSPECTED 2



February 15, 1995

MONTEREY

BAY

AQUARIUM

RESEARCH

INSTITUTE

Administrative Grants Officer
Mr. Linden Clausen
Office of Naval Research
Seattle Regional Office
1107 NE 45th Street, Suite 350
Seattle, WA 98105-4631

SUBJECT: FINAL TECHNICAL REPORT
ONR AWARD NO. N00014-93-1-0202

Geomorphology of Headless Submarine Canyons: Prediction of Slope Failure, Sediment Strength and Pore Pressure Gradient, and the Regular Spacing of Canyons

P.O. Box 628
7700 SANDHOLDT RD.
MOSS LANDING, CA
95039

Dear Linden:

Per ONR Research Grant Number N00014-93-1-0202 Grant Schedule Item 8 (Reports and Report Distribution) and Attachment Number 2 (Reports and Report Distribution), I am providing you one copy of the Final Technical Report for the period ending 31 October 1995. The research project entitled ***Geomorphology of Headless Submarine Canyons: Prediction of Slope Failure, Sediment Strength and Pore Pressure Gradient, and the Regular Spacing of Canyons*** is under the direction of Dr. Daniel Orange, Principal Investigator.

If you have any questions or need additional information you may contact the undersigned by (Tel.) 408-775-1776, (FAX) 408-755-1620, or (Email) chlo@mbari.org.

Sincerely,

Lonnie G. Christiansen
Grants & Accounting Specialist

Enclosure

SCIENCE, ENGINEERING
AND ADMINISTRATION

TEL (408) 775-1700

FAX (408) 775-1620

MARINE OPERATIONS
FACILITY

TEL (408) 775-1900

FAX (408) 775-1652

FEB 21 1995



Distribution List:

Scientific Officer Code 1125GG
Dr. Joseph H Kravitz
Office of Naval Research
Ballston Tower One
800 North Quincy
Arlington, VA 22217-5000

Administrative Grants Officer
Mr. Linden Clausen
Office of Naval Research
Seattle Regional Office
1107 NE 45th Street, Suite 350
Seattle, WA 98105-4631

Director, Naval Research Laboratory
Attn: Code 2627
Washington DC 20375

Defense Technical Information Center
Building 5, Cameron Station
Alexandria, VA 22304-6145

**ONR Grant N00014-93-1-0202 Final Technical Report:
Geomorphology of Headless Submarine Canyons: Prediction of Slope Failure,
Sediment Strength and Pore Pressure Gradient, and the Regular Spacing of
Submarine Canyons**

Daniel L. Orange
Monterey Bay Aquarium Research Institute, P.O. Box 628, Moss Landing, CA 95039
email: dano@mbari.org
direct/office phone: (408) 775-1761; messages: 775-1773; FAX: 775-1645

Project Summary

The Atlantis II/ALVIN program conducted in September, 1993 was successful in identifying cold seeps, determining their distribution, and measuring pore pressure gradients within and between the cold seeps. We identified four cold seeps; all cold seep sites were within canyons, and none were found along strike between canyons. Even though all fluid seeps were found in canyons, not all canyons had seeps, and the location of the seeps within the canyons differed on the landward and seaward limbs of the anticlines. This suggests both spatial and temporal variations on fluid flow. Our analysis of the geotechnical data we collected suggests that the ambient pore pressure gradients at the seeps in the canyons are above hydrostatic, but below that required to initiate slope failure. If these measurements represent steady-state, then some transient pressure pulse may be required to initiate slope failure. Our modeling suggests that seismicity or methane expulsion can produce the required transient.

Long Term Goal

The long term goal of this project is to understand the interaction between tectonic and hydrologic forcing and the resultant creation and modification of seafloor geomorphology.

Scientific or Technological Objectives

The initial objective of this project was to ground-truth the hypothesis that there is a causative relationship between geomorphology and fluid expulsion at the seafloor. Once that relationship was established, we sought to determine the hydrologic and geotechnical state of the venting and non-venting regions. The hydrologic and geotechnical data can be used together with the seafloor observations to model slope failure.

Background

The processes of accretion and tectonic compaction in active margins, and sediment loading and aquifer forcing in passive margins, lead to the expulsion of pore fluids and the generation of above-hydrostatic pore pressure gradients. These gradients affect the force balance of sediments at the seafloor via seepage force, and, if high enough, can destabilize a slope. When the material on a slope fails, the head gradient at the base of the failure will increase due to the decreased path length, and therefore the probability of failure increases within the pre-existing scar. This positive feedback will lead to the headward erosion of a canyon, resulting in the characteristic "headless" morphology of these features. Because the canyon imposes an indentation on the previously uniform constant head boundary at the seafloor, continued fluid expulsion will be attracted to canyons (and directed away from intervening regions). It is this hypothesis that we explored during the 1993 ALVIN program.

Approach

In order to study the interaction of tectonics and hydrology we used a combination of field work, modeling, and geotechnical and hydrological analysis. First, we used a USGS deep tow video and camera sled and the ALVIN submersible in the fall of 1993 to make direct observations of fluid venting in and around canyons on the Oregon margin. These fluid vents (cold seep communities) are comprised of unique faunal assemblages that can be used to infer the distribution of fluid expulsion on the margin. Once we determined the location of the cold seeps, we then used

ALVIN to deploy the deep ocean piezometers (Portable In-Situ Pore Pressure Instruments, or PISPPs) for measuring pore pressure gradients both within vent sites and between vent sites. The PISPP development and construction was supported by this project and carried out by Bobb Carson, Lehigh University. These instruments can be deployed in up to 4000m of water, are capable of measuring very small pore pressure gradients in the top 1m of the seafloor, and were deployed in deep water for the first time as part of our 1993 ALVIN field program. In addition to the hydrologic data, we also collected sediment push-cores at all of the PISPP sites (both venting and non-venting) for later geotechnical analysis. We used our observations and analyses to model the creation of headless submarine canyons. In addition, the PISPPs were deployed at seep sites in Monterey Bay and at the toe of the Costa Rica trench to augment our seafloor geotechnical database from Oregon.

Accomplishments and Results

The Atlantis II/ALVIN program conducted in September, 1993 was successful in identifying cold seeps, demonstrating that all seeps occurred within canyons, and measuring pore pressure gradients within and between the cold seeps. On the landward limb of the second landward vergent anticline a robust cold seep community occurs at the base of the steep canyon headwall. The seep is characterized by chemoautotrophic vent clams (*Calymene* and *Solemya*), Vestimentiferan tube worms, and extensive authigenic carbonate. Fluids for this seep may utilize flow paths either parallel to bedding in the hanging wall of the second thrust ridge, or may travel along the underlying thrust fault itself. Two seaward facing canyons on the third landward vergent ridge have vent clam communities (*Calymene*, scattered *Solemya*) at a different location, namely the base of the canyon near the canyon mouth (the intersection between the anticlinal ridge and the adjacent forearc basin). No seeps were found along strike at the intersection of the slope basin and anticlinal ridge. Fluids for these seeps may originate in the section beneath the second landward vergent thrust, utilize stratigraphic conduits, and may be prevented from venting in the forearc basin by a basal unconformity.

The presence of authigenic carbonate on the second ridge canyon seep, but not the third ridge, may be attributed to a difference in fluid source. Carbonate precipitates from the oxidation of methane, whereas clam and tube worm colonies require hydrogen sulfide for survival; Vestimentiferan tube worms are thought to require higher concentrations of sulfide than clams. The difference in seep fauna and carbonate suggests that the fluids supporting the robust seep at the inflection point of the headless canyon on the second landward vergent ridge may originate at deeper levels than the seep on the third landward vergent ridge.

Impact on Science, and Transitions Accomplished or Expected, If Any:

Orange has been approached separately by two oil companies (Chevron and Petrobras) to discuss the role of seepage force in triggering sediment slope failure. Both companies are exploring platform drilling in deep water on continental slopes, and are concerned over safety issues. Based upon our work in central Cascadia we have initiated a successful collaboration with Amoco for providing industry quality multi-channel seismic data and processing relevant to the ongoing STRATAFORM project in southern Cascadia.

Relationship to Other Projects, if known:

The observations and data from this project provide limits and inputs to the slope evolution models of Pratson, Coakley, Steckler and Syvitski. In addition, the hypothesis of seepage-induced spring sapping provides constraints for the slope failure/sedimentation models of Parker, Garcia, and Syvitski. The hypothesis of geomorphology-fluid linkage provided a basis for studying the STRATAFORM research area, and provides a robust data for analyzing the gully and pock mark distribution in southern Cascadia. The initial side scan and high resolution seismic data collected in 1995, and the industry MCS data mentioned above, show that gas is abundant in the subsurface, and many slope failure features identified on the surface provide evidence of fluid involvement. Finally, the techniques that we formulated for in situ hydrological and post-cruise laboratory geotechnical analysis are applicable to the STRATAFORM analysis program planned for 1996.

Statistical Information:

Daniel Lewis Orange
Monterey Bay Aquarium Research Institute
P.O. Box 628
Moss Landing, CA 95039
email: dano@mbari.org

Publications:

Orange, D.L. and Underwood, M. B. (1995) Patterns of thermal maturity as diagnostic criteria for interpretation of mélangé, *Geology*, v. 23, p. 1144-1148.

Orange, D.L., Anderson, R. S., and Breen, N. A. (1994), Regular canyon spacing in the submarine environment: the link between hydrology and geomorphology, *G.S.A. Today*, v. 4, p. 29-39.

Tobin, H.J., Moore, J.C., Mackay, M.E., Orange, D.L., and Kulm, L.D. (1993) Fluid flow along a strike-slip fault at the toe of the Oregon accretionary prism: Implications for the geometry of frontal accretion, *Geological Society of America Bulletin*, v. 105, p. 569-582.

In Press:

Barry, J.P., Robison, B. H., Greene, H.G., Baxter, C.H., Harrold, C., Kochevar, R.E., Orange, D.L., Lisin, S., Whaling, P.J., and Nybakken, J., (1996) Investigations of cold seep communities in Monterey Bay, California, using a remotely operated vehicle. Submitted, *Deep Sea Research*

McAdoo, B. G., Orange, D.L., Silver, E. A., McIntosh, K., Abbot, L., Galewsky, J., Kahn, L., and Protti, M., (1996) Seafloor structural observations, Costa Rica accretionary prism. Accepted pending minor revisions, *Geophysical Research Letters*.

Kahn, L. M., Silver, E. A., Orange, D.L., Kochevar, R., and McAdoo, B. G., (1996) Surficial evidence of fluid expulsion from the Costa Rica accretionary wedge. Accepted pending minor revisions, *Geophysical Research Letters*.

Orange, D.L., Knittle, E., Farber, D., and Williams, Q. (1996) Raman spectroscopy of hydrocarbon fluid inclusions. *Geochemical Society Special Publication "Mineral Spectroscopy: A Tribute to Roger Burns"*. Accepted.

Oral presentations at scientific meetings/conferences (Fall, 1993 AGU to Fall, 1995 AGU).

Orange, D.L., McAdoo, and Yun, J., (1995), ROV and Submersible Observations Link Fluid Flow and Canyon Formation in Monterey Bay and Cascadia. *Geological Society of America Abstracts with Programs*, v. 27, p. A129.

Underwood, M. and Orange, D.L. (1995) Patterns of thermal maturity as diagnostic tools in the interpretation of mélangé. *Geological Society of America Abstracts with Programs*, v. 27, p. A126.

Orange, D.L., Maher, N., Jacobsen, N., Greene, H.G., and Martin, J.B., (1995) Fluid venting in Monterey Bay, California: ROV studies of fluid flow along fault zones, within headless canyons,

and on mud volcanoes, The First SEPM Congress on Sedimentary Geology, Congress Program and Abstracts, v. 1, p. 95.

Martin, J.B., Lorenson, T.D., Orange, D.L., and Kvenvolden, K.A., (1995) Fluid venting in Monterey Bay, California: Compositional and isotopic evidence for possible thermogenic hydrocarbons, The First SEPM Congress on Sedimentary Geology, Congress Program and Abstracts, v. 1, p. 88-89.

Orange, D.L., Greene, H.G., Maher, N., and Connor, J., (1995) Ground-truthing multi-beam bathymetry and side-scan sonar with ROV studies, and creating geologic maps in Monterey Bay, California, in Geologic Mapping in the 21st Century, TERRA (Abstracts, European Union of Geosciences), v. 7, p. 28.

Feroli, L., Johnson, K., Orange, D., and Greene, G. (1994) In situ chemical characterization of cold seep fluid in the Monterey submarine canyon, EOS (Transactions, American Geophysical Union), v. 75, p. 734.

Greene, G., Orange, D., Mann, D., Gable, G. (1994) Fluid construction morphology on Smooth Ridge, Central California, EOS (Transactions, American Geophysical Union), v. 75, p. 598.

Orange, D.L., McAdoo, B.G., Moore, C., Tobin, H., Chezar, H., Lee, H., Reid, M., Vail, R., and Screaton, E., (1994), Headless submarine canyons and fluid flow on the toe of the Cascadia accretionary complex: All seeps are in canyons, but not all canyons have seeps, and not all seeps are alike, Geological Society of America Abstracts with Programs, v. 26, p. A458.

McAdoo, B.G., Orange, D.L., Bowering, P., Moore, C., Teas, P., Tobin, H., Chezar, H., Lee, H., Reid, M., Vail, R., Underwood, M., Linke, P., and Schluter, M. (1994), Fluid flow and submarine canyons: Observations from an ALVIN and camera-tow program of the toe of the Cascadia accretionary complex, off-shore Oregon, EOS (Transactions, American Geophysical Union), v. 75, p. 262.

Orange, D.L., Greene, H.G., Barry, J., and Kochevar, R., (1994) ROV investigations of cold seeps along fault zones and mud volcanoes in Monterey Bay, EOS (Transactions, American Geophysical Union), v. 75, p. 32.

Silver, E.A., Orange, D., Langseth, M., Gieskes, J., Abbott, L.D., Screaton, E., Kahn, L., McAdoo, B., Zulegar, E., Protti, M., You, C-F., Galewsky, J., and Feroli, L. (1994) Importance of out-of-sequence thrusts as fluid conduits in the SW Costa Rica accretionary complex, EOS (Transactions, American Geophysical Union), v. 75, p. 324.

Kahn, L.M., Silver, E.A., Orange, D.L., McAdoo, B., Feroli, L., McIntosh, K.D., Abbott, L.D., Screaton, E., Protti, M., Galewsky, J., Langseth, M., You, C-F., and Gieskes, J. (1994), Evidence of fluid venting from the Costa Rica accretionary prism, EOS (Transactions, American Geophysical Union), v. 75, p. 242.

Gieskes, J.M., You, C-F., Silver, E.A., Orange, D.L., Abbott, L.D., McAdoo, B., Galewsky, J., Kahn, L.M., Feroli, L., McIntosh, K.D., Screaton, E., Protti, M., Langseth, M. (1994) Chemistry of interstitial waters of ALVIN push cores (APC) in black, clam-hosting sediments: Costa Rica accretionary prism, EOS (Transactions, American Geophysical Union), v. 75, p. 242.

Orange, D.L., Greene, H.G., McHugh, C., Ryan, W.B.F., Reed, D., Barry, J., Kochevar, R., and Connor, J. (1993), Fluid expulsion along fault zones and mud volcanoes in Monterey Bay, EOS (Transactions, American Geophysical Union), v. 74, p. 242.

Greene, H.G., Orange, D.L., and Barry, J., (1993), Geologic diversity of cold seep communities, Monterey Bay region, Central California, U.S.A., EOS (Transactions, American Geophysical Union), v. 74, p. 578.

Orange, D.L., Anderson, R. S., and Breen, N. A. (1993), Regularly spaced submarine canyons: A proposed link between slope failure, hydrology and geomorphology, Geological Society of America Abstracts with Programs, v. 25, p. A60.

Graduate students:

2 Graduate Students (at University of California, Santa Cruz):

Brian G. McAdoo

Janet Yun

Number of female graduate students: 1

Number of minority graduate students: 2

Service on committees/panels:

DESSC (Deep Submergence Science Committee - formerly ALVIN review committee); 1993-1995

ONR STRATAFORM committee; Slope Working Group; 11/93 - present

Board of Directors, The Lyceum (a non-profit organization providing extracurricular education activities to primary and secondary school children in the Monterey-Salinas-Watsonville area); 9/94 - present

OBLISP (Ocean Borehole Laboratories, Instrumentation, and Sampling Program; December, 1994 - present)

Professional Societies:

American Geophysical Union

Geological Society of America

American Association of Petroleum Geologists

Society for Sedimentary Geology (SEPM)

TABLE OF CONTENTS

Scope of this Report	6
Contributors	7
Abstract	8

Part 1: High Dynamic Range Optical Analog Links

Chapter 1. Linewidth-Insensitive Coherent Amplitude-Modulated Links

1.1 Introduction	11
1.2 Dynamic Range of Analog Links	12
1.3 Homodyne AM-WIRNA Links	13
1.3.1 2-Port Homodyne Link Description	13
1.3.2 System Evaluation	14
1.3.3 Multi-port Homodyne Link Description	17
1.3.4 2K-port Homodyne Link Description	18
1.4 Heterodyne WIRNA Link	20
1.4.1 Link Description	20
1.4.2 System Evaluation and Optimization	21
1.4.3 Link Dynamic Range	24
1.5 Comparison Between the Techniques	24
1.6 Experimental AM-WIRNA Link	26
1.6.1 Link Description	26
1.6.2 Linewidth and the IF Bandwidth	27
1.6.3 Received Signal Power	29
1.7 Conclusions	31
Appendix 1.A Noise in Analog Optical Links	32
1.A.1 The Additive Noise	32
1.A.1.1 Thermal Noise	32
1.A.1.2 Shot Noise	32
1.A.1.3 Relative Intensity Noise	33
1.A.2 The Phase Noise	33
1.8 References	33

Chapter 2. Angle-Modulated Links	
2.1 Potential Dynamic Range Improvement Using Angle Modulation	36
2.2 Coherent PM and FM Links	37
2.2.1 Link Descriptions	37
2.2.2 Impact of Laser Linewidth, RIN, and Receiver Noise	38
2.2.3 Spurious-Free Dynamic Range	41
2.2.4 Results and Discussion	43
2.3 Reference Transport Links	48
2.4 Reference Transport in Analog Links	50
2.4.1 Why Conventional Approaches Fail	50
2.4.2 Our Novel Approach: Linewidth-Insensitive Interferometric Links	51
2.5 Optical Frequency Shifting in Heterodyne Interferometric Links	52
2.5.1 Single-Sideband Optical Frequency Shifters	52
2.5.2 A Novel Approach	53
2.6 Heterodyne Interferometric Phase-Modulated Link: Theory	54
2.6.1 Link Description	54
2.6.2 Spurious-Free Dynamic Range (SFDR)	55
2.6.3 Implementation Considerations	57
2.6.4 Results and Discussion	59
2.7 Heterodyne Interferometric Phase-Modulated Link: Experiment	60
2.8 Conclusions	64
Appendix 2.A: Derivation of PM and FM Output Currents	65
Appendix 2.B: Noise in Angle-Modulated Analog Optical Links	66
2.9 References	70

Part 2: Dynamic Wavelength Division Multiplexing Optical Networks

Chapter 3. STARNET Physical Layer: Combined ASK and PSK Modulation	
3.1 Introduction	73
3.2 STARNET Operation	75
3.3 Transceiver Description	77
3.4 Combined ASK and PSK Modulation: Theory	79
3.5 Combined ASK and PSK Modulation: Experiment	82
3.5.1 Impact of the ASK Modulation on the PSK Receiver	82
3.5.2 Impact of the PSK Modulation on the ASK Receiver	84
3.6 Optimum Amplitude Modulation Depth Experiment	86

3.7 Conclusions	86
3.8 References	87
 Chapter 4. Modeling of Combined Modulation Using Semiconductor Lasers	
4.1 Introduction	90
4.2 Combined ASK and DPSK Modulation: Theory	91
4.3 Combined ASK and DPSK Modulation: Demonstration	94
4.4 Incomplete ASK Modulation: Theory	97
4.4.1 Optically Amplified Direct Detection Versus Heterodyne ASK	97
4.4.2 Analysis of OADD Systems with Incomplete ASK Modulation	99
4.4.2.1 Rigorous Method	99
4.4.2.2 Gaussian Approximation	101
4.5 Incomplete ASK Modulation: Numerical Evaluation	103
4.5.1 Evaluation Procedure for Rigorous Method	103
4.5.2 Evaluation Procedure for Gaussian Approximation	105
4.6 Incomplete ASK Modulation: Numerical Results and Discussion	105
4.6.1 Results for Zero Linewidth	106
4.6.2 Results for Nonzero Linewidth	109
4.7 Conclusions	114
4.8 References	116
 Chapter 5. STARNET Interface	
5.1 Introduction	118
5.2 STARNET Optical Architecture	119
5.3 STARNET Electronic Interface Architecture	121
5.3.1 Moderate-Speed Subnetwork	121
5.3.2 High-Speed Subnetwork	122
5.4 High-Speed Interface Architecture	123
5.4.1 Packet Transmission and Reception	124
5.4.2 Network Bottlenecks and Bandwidth Allocation	127
5.4.3 Virtual Circuit Routing	128
5.4.4 Service Segregation	129
5.4.5 Summary and Status	130
5.5 STARNET Performance	131
5.6 Conclusions	134
5.7 References	135

Part 3: Nonlinear Effects in Fiber

Chapter 6. Impact of Fiber Nonlinearities on Optical Communication Systems

6.1 Introduction	137
6.2 Impact of Four-Wave Mixing on Optical WDM Systems	137
6.3 Statistical Distribution of FWM in ASK Optical WDM Systems	140
6.4 Impact of Four-Wave Mixing on FSK Optical WDM Systems	143
6.5 Theoretical Analysis of Cross-Phase Modulation in Dispersive Fibers	146
6.6 Stimulated Brillouin Scattering	150
6.7 Fiber-Induced Parasitic Phase Modulation	151
6.8 Conclusions	153
Conclusions	154
List of Publications During This Project	158

SCOPE OF THIS REPORT

This report covers the work performed during the three-year duration of Office of Naval Research Grant No. N00014-91-J-1857 for R&T Project Code 4148130-01. The termination date of the project is August 31, 1994. The report is organized as follows: The contributors to this work are listed. The abstract contains a brief description of the research performed. Part 1 describes our work on high dynamic range optical analog links. Within Part 1, Chapter 1 covers linewidth-insensitive coherent amplitude-modulated links and Chapter 2 covers coherent angle-modulated links and linewidth-insensitive interferometric links. Part 2 describes our work on dynamic wavelength division multiplexing (WDM) networks. Within Part 2, Chapter 3 covers the physical layer of STARNET, a coherent WDM communication network built at Stanford. Chapter 4 addresses the impact of semiconductor laser linewidth on STARNET physical layer performance. Chapter 5 covers the electronic interface architecture of STARNET. Part 3 describes our work with nonlinear effects in fiber. Within Part 3, Chapter 6 covers the impact of fiber nonlinearities such as four-wave mixing (FWM), cross-phase modulation (XPM), stimulated Brillouin scattering (SBS), and fiber-induced parasitic phase modulation on optical communication systems. This report ends with conclusions and a list of publications generated during this project.

CONTRIBUTORS

Principal Investigator: Prof. Leonid G. Kazovsky

Graduate Students: Sanjay K. Agrawal
Charles F. Barry
Ting-Kuang Chiang
Jason C. Fan
Thomas K. Fong
Michael J. Hickey
R. Theodore Hofmeister
Robert F. Kalman
Chung-Li Lu
Ciro A. Noronha
Delfin Jay M. Sabido IX
Nina L. Taranenko
Yuri N. Taranenko

Collaborators: Sergio Benedetto, Politecnico di Torino, Torino, Italy
S. Chandrasekhar, Bell Laboratories, Crawford Hill, NJ
Debasish Datta, Indian Inst. of Technology, Kharagpur, India
Anders Djupsjobacka, Ericsson Telecom, Stockholm, Sweden
Gennadi Fikshan, GTE Laboratories, Waltham, MA
Joseph Goodman, Stanford University, Stanford, CA
Richard Gross, GTE Laboratories, Waltham, MA
Gunnar Jacobsen, Tele Danmark Research, Horsholm, Denmark
Nobuyuki Kagi, Furukawa Electric Co., Hiratsuka, Japan
Uziel Koren, Bell Laboratories, Crawford Hill, NJ
B. Lagerstrom, Ericsson Telecom, Stockholm, Sweden
Hojoon Lee, Science and Eng. Foundation, Seoul, South Korea
Karen Liu, IBM Watson Research Ctr., Yorktown Hts., NY
Michel Marhic, Northwestern University, Chicago, IL
Pierluigi Poggiolini, Politecnico di Torino, Torino, Italy
Masafumi Tabara, Furukawa Electric Co., Hiratsuka, Japan
M. Okan Tanrikulu, SUNY, Buffalo, NY
Ozan Tonguz, SUNY, Buffalo, NY
F. Joachim Westphal, Heinrich Hertz Inst., Berlin, Germany

ABSTRACT

During this project, our research has focused on three major aspects of advanced optical fiber communication systems: high dynamic range optical analog links, dynamic wavelength division multiplexing (WDM) optical networks, and fiber nonlinearities.

In the area of high dynamic range optical analog links, we have theoretically investigated the dynamic range performance of homodyne and heterodyne coherent amplitude-modulated links using the WIRNA (Wideband - Rectifier - NArrowband) demodulator structure. We have experimentally demonstrated the linewidth-insensitivity of the heterodyne WIRNA link and have compared its measured spurious-free dynamic range (SFDR) performance with theoretical results. We have theoretically investigated the dynamic range performance of heterodyne coherent angle-modulated links using both phase and frequency modulation. We have theoretically investigated a novel class of analog links called interferometric links, which are linewidth-insensitive and can utilize angle modulation. We have derived the SFDR of the heterodyne interferometric phase modulated (HIPM) link and have built a proof-of-concept demonstration of this link.

In the area of dynamic wavelength division multiplexing (WDM) networks, we have investigated and designed an experimental coherent WDM optical network called STARNET with a throughput of 3 Gb/s/node. We have experimentally demonstrated simultaneous transceiver operation for high-speed 2.488 Gb/s PSK data and lower-speed 125 Mb/s ASK data using externally modulated solid-state lasers. We have theoretically investigated the optimum ASK modulation depth for this transceiver and have experimentally confirmed our results. We have theoretically investigated the impact of semiconductor laser linewidth on a transceiver using high-speed DPSK data and lower-speed ASK data and have experimentally demonstrated simultaneous transceiver operation for these modulation formats. We have derived the optimum filter bandwidths to balance phase and additive noise effects in ASK demodulation under a variety of conditions using both a rigorous series expansion method and the Gaussian approximation. We have designed a distributed fast packet switch workstation to network interface that provides electronic buffering and switching for the data channel in WDM optical networks. We have constructed and tested a high-speed interface in STARNET; the printed circuit board version of the interface has been operational without modification since January 1994. We have developed software from the driver level to the applications layer.

In the area of fiber nonlinearities, we have evaluated the performance of optical WDM systems in the presence of four-wave mixing (FWM) by both theoretical model and simulation. We have found that the probability density function of FWM interference is non-Gaussian and is well approximated by the Student's t-distribution. We have theoretically investigated the impact of modulation frequency on cross-phase modulation (XPM) in dispersive fibers. We have experimentally observed the extra noise generated by stimulated Brillouin scattering (SBS) in optical fiber. We have experimentally observed phase modulation caused by thermal acoustic vibrations in fiber. We have performed a theoretical analysis of the impact of this parasitic phase modulation on ultra-long distance DPSK communication systems.

PART 1:

HIGH DYNAMIC RANGE OPTICAL ANALOG LINKS

Chapter 1

Coherent Amplitude-Modulated Links

1.1 Introduction

Wideband, high dynamic range analog fiber-optic links have been investigated extensively for use in antenna remoting, cable television distribution, and wide-area cellular applications [1-4]. These links are well-suited for the transmission of analog signals with bandwidths above 1 GHz, due to the difficulty in digitizing such signals with sufficient resolution. Previous work has emphasized intensity modulated direct detection (IMDD) links using current injection or external electro-optic modulation [5]. Though direct modulation is simple, the chirp of conventional distributed feedback (DFB) semiconductor lasers is undesirable. The integratability of laser and modulator on the same chip makes external modulation an attractive option. This choice also eliminates the need for highly linear lasers with uniform modulation response over a wide band.

To date, analog links based on coherent detection (CD) have received relatively little attention; a notable exception is subcarrier-multiplexed systems for video distribution [6]. In a CD system, the field from a local oscillator (LO) laser is combined with the signal field prior to detection. CD systems have several potential advantages over DD systems. Coherent systems can approach shot noise-limited performance with sufficient LO laser power. In addition, CD systems are able to separate wavelength division multiplexed signals with high frequency resolution, and can detect the phase of the optical carrier. Thus, while DD systems are well-suited to amplitude modulation (AM), CD systems can use AM, phase modulation (PM), or frequency modulation (FM).

The laser phase noise associated with the wide linewidth of semiconductor lasers can cause substantial performance degradation in coherent analog links. This phenomenon represents a major obstacle to the application of coherent techniques to analog optical links. In AM coherent links, either synchronous or asynchronous detection can give linewidth-insensitive performance. Conventional synchronous receivers require phase-locking between the transmitter and the LO lasers. The phase-locking is difficult to achieve and leads to extremely stringent requirements on the laser linewidth. Asynchronous receivers using WIRNA (Wldeband-Rectifier-NArrowband filter)

processing have been shown to be effective in achieving linewidth-insensitive performance in ASK (amplitude shifted keying) homodyne and heterodyne digital systems [7, 8]. Since the phase information is discarded in the WIRNA receiver, it works effectively with amplitude modulation.

In this chapter, the analog version of the ASK homodyne and heterodyne digital systems are analyzed. In Section 1.2, the main performance measure of analog links, the dynamic range, is described. In Section 1.3, a multiport homodyne WIRNA link is studied. Section 1.4 investigates the performance of a heterodyne WIRNA link. Section 1.5 examines the practical issues in implementing these links. Section 1.6 describes the experimental heterodyne WIRNA link built in our laboratory and provides some comparison between experiment and theory. Section 1.7 presents the conclusions of this work. Section 1.8 provides references. Appendix 1.A describes the properties of different system noises.

1.2 Dynamic Range of Analog Links

An important measure of analog link performance is the dynamic range, defined as the ratio of the largest signal the system can transport to the smallest. The dynamic range is equivalent to the signal-to-noise ratio (SNR) for a particular modulation index, as shown in Fig. 1-1. The fundamental limit of the dynamic range (FLDR) is defined as the maximum attainable SNR, assuming a maximum possible modulation depth of 1. This is the case in AM links but not necessarily in angle-modulated links. The FLDR is limited by noise.

In any real optical link, nonlinearities generated by link components will also interfere with link performance by creating spurious intermodulation products that can mask or mimic real signals. Therefore, the *spurious-free* dynamic range (SFDR) is often used as a measure of system performance. The SFDR is the dynamic range where the maximum signal level is limited by the intermodulation products. By biasing a Mach-Zehnder (MZ) external amplitude modulator at its half-power transmission point, the second-order nonlinearities generated by imperfect amplitude modulation are eliminated. As a result, the optimum modulation depth corresponding to link SFDR is the modulation depth for which the noise power in the signal band is equal to the third-order nonlinearity power in the signal band.

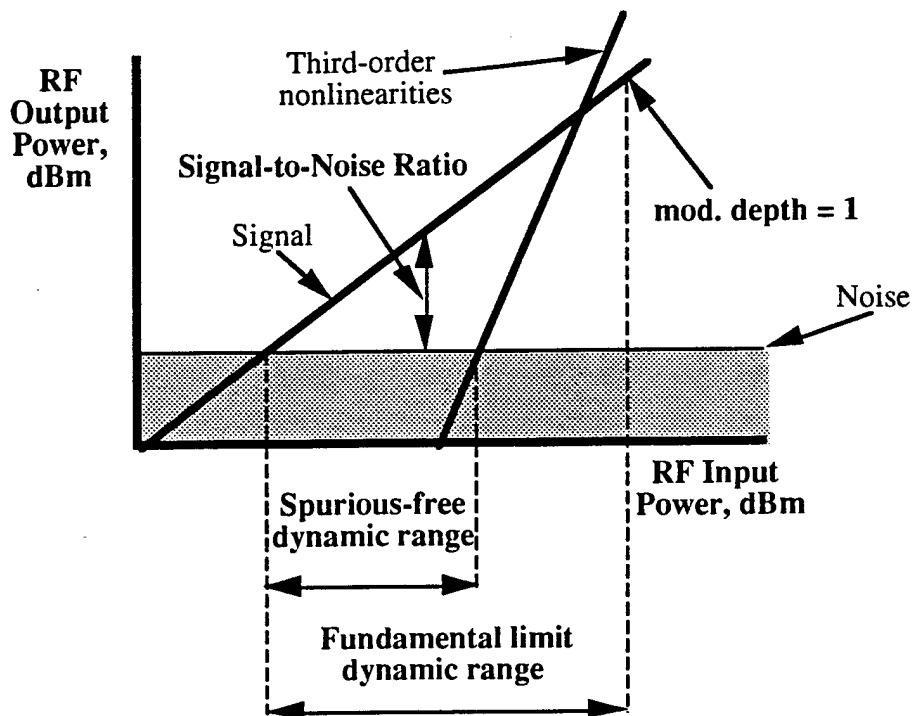


Figure 1-1. Diagram of performance measures of analog links.

1.3 Homodyne AM-WIRNA Links

In a homodyne system, the frequency of the incoming signal and the LO are the same. Since the electrical output of the photodetector is a baseband signal, large bandwidth photodetectors are not required. Also, baseband processing can avoid degradation due to overlapping of the signal spectrum with the noise peak of semiconductor lasers.

In this section, we discuss three types of homodyne WIRNA links; (a) the 2-port homodyne link, (b) the multi-port homodyne link and (c) the 2K-port homodyne link (for $K > 1$). We show that the 2-port homodyne link suffers from the degradation caused by the baseband processing, while the 2K-port link obtains the best performance, although the structure is complicated in practice.

1.3.1 2-Port Homodyne Link Description

The block diagram of an externally modulated coherent AM link using an optical 90° hybrid phase diversity WIRNA homodyne receiver is shown in Fig. 1-2. The optical signal from the transmitter laser is modulated by an electro-optic modulator. The optical frequency of the local oscillator is same as that of the optical signal. The optical signal and

the local oscillator output are combined by an optical 90° hybrid. The polarization state of the receiver optical signal is tracked using a polarization controller and a feedback control technique is used to match the polarization state of $E_{LO}(t)$ with $E_s(t)$. In addition, an automatic frequency control (AFC) loop is used to maintain the intermediate frequency (IF) fixed by tuning the LO laser frequency. Each of the two outputs of the optical 90° hybrid is sent to a photodetector and then through a DC block to a wideband lowpass filter. Then, using square-law detectors, each signal is multiplied with itself. The two output signals are combined at this point, and the phase noise terms are canceled due to the phase difference produced by the optical 90° hybrid. Finally, the combined signal passes through a DC block and a narrowband lowpass filter.

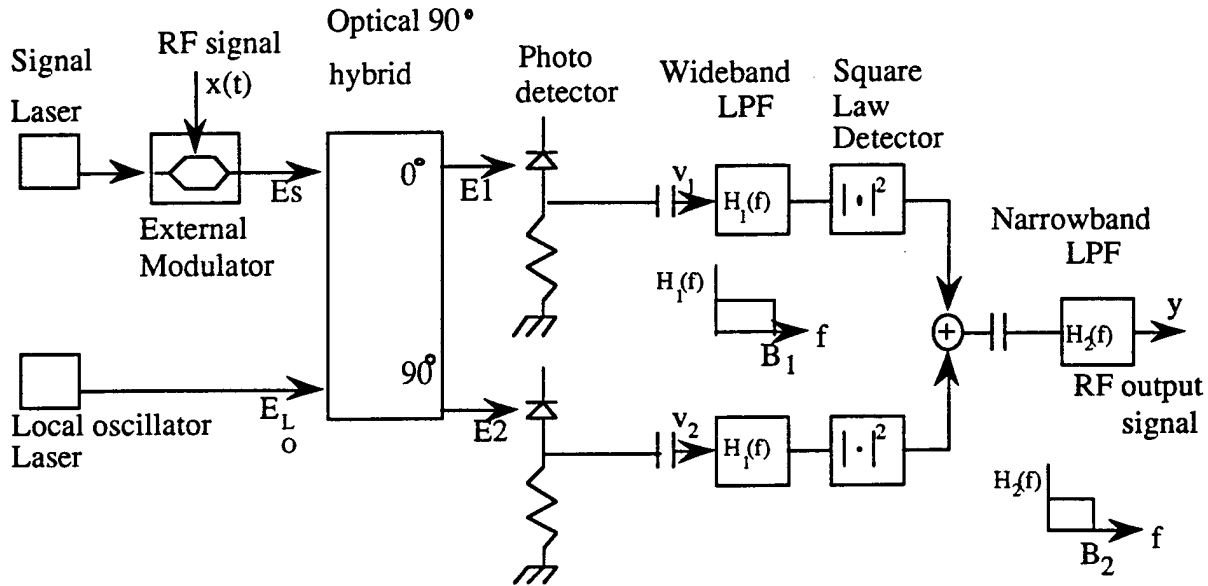


Figure 1-2. Block diagram of the homodyne AM-WIRNA link.

1.3.2 System Evaluation

Table 1-1 contains the definitions of the variables used in the analysis. The output current of the photodetectors are given by:

$$i_1(t) = A(P_s \sin x(t) + \sqrt{2P_s P_{LO}} \{ \cos[x(t) + \phi(t)] - \sin \phi(t) \}) + n_1(t) \quad (1.1)$$

$$i_2(t) = A(P_s \sin x(t) + \sqrt{2P_s P_{LO}} \{ \sin[x(t) + \phi(t)] + \cos \phi(t) \}) + n_2(t) \quad (1.2)$$

where $\phi(t)$ is combined phase noise of the signal laser and the local oscillator laser given by $\phi(t) = \phi_S(t) - \phi_{LO}(t)$, and $n_1(t)$ and $n_2(t)$ are two independent additive white Gaussian noise processes with power spectral densities of $\eta_1 = \eta_2 = \eta = \eta_{in} + 2qRL(P_S + P_{LO})$. To evaluate the SNR of the system in Fig. 1-2, we assume a normalized sinusoidal RF input signal $x(t) = \cos(2\pi f_m t + \theta)$, where f_m is the signal frequency and θ is the random initial phase uniformly distributed between 0 and 2π . The output of the link contains five terms:

- (a) recovered signal with the power P_S ;
- (b) direct detection squared term $P_{direct-direct}$;
- (c) direct detection - phase noise product with the power $P_{direct-phase}$;
- (d) white additive noise - phase noise product with the power $P_{white-phase}$;
- (e) white additive noise squared term with the power $P_{white-white}$.

Table 1-1: Definition of variables

E_S, E_{LO}	Phasor of the optical signal and local oscillator
E_1, E_2	Output phasor of the optical hybrid port 1 and port 2
ω_S, ω_{LO}	Optical signal and local oscillator frequency
φ_S, φ_{LO}	Phase noise of the optical signal and local oscillator
$\phi(t)$	Combined linewidth of the signal and the local oscillator lasers
m	Modulation index to the external modulator
$x(t)$	Normalized RF input signal to the modulator
P_S	Received optical power
P_{LO}	Local oscillator optical power
L	Total loss of the optical hybrid from an input port to an output port
A	=RL; coefficient of the signal amplitude
B_1	Bandwidth of the lowpass filter (first stage: wide bandwidth)
B_2	Bandwidth of the lowpass filter (last stage: narrow bandwidth)

We assume that the bandwidth of the wideband lowpass filters is sufficiently large such that the amplitude noise to phase noise conversion is negligible. This filter helps to reduce the impact of the white additive noise [7].

Evaluating the power of each component, the output signal-to-noise ratio (SNR) can be expressed as:

$$\begin{aligned}
SNR &= \frac{P_{signal}}{P_{direct-direct} + P_{direct-phase} + P_{white-phase} + P_{white-white}} \\
&= \frac{8A^4 P_s^2 P_{LO}^2 m^2}{\frac{1}{2} A^4 P_s^4 m^4 + 8A^4 P_s^3 P_{LO} m^2 (1 - \Gamma_1) + 16A^2 P_s P_{LO} B_2 \eta (1 - \Gamma_2) + 2\eta^2 B_2 (4B_1 - B_2)} \quad (1.3)
\end{aligned}$$

where Γ_1 and Γ_2 expresses a portion of the noise power outside the signal bandwidth given by

$$\Gamma_1 = \begin{cases} \frac{1}{\pi} \tan^{-1} \frac{4\Delta\nu B_2}{4B_2^2 - \Delta\nu^2} & , \quad \text{if } \Delta\nu < 2B_2 \\ 1 - \frac{1}{\pi} \tan^{-1} \frac{4\Delta\nu B_2}{\Delta\nu^2 - 4B_2^2} & , \quad \text{if } \Delta\nu > 2B_2 \end{cases} \quad (1.4)$$

$$\Gamma_2 = \frac{\Delta\nu}{2\pi B_2} \ln \left(\frac{B_1 + B_2}{B_1 - B_2} \right) \quad (1.5)$$

and $\Delta\nu$ is the total linewidth of the signal and local oscillator lasers, B_1 and B_2 are the wideband and narrowband filter bandwidth, respectively. From (1.3), the FLDR is obtained as:

$$FLDR = \frac{8A^4 P_s^2 P_{LO}^2}{\frac{1}{2} A^4 P_s^4 + 8A^4 P_s^3 P_{LO} (1 - \Gamma_1) + 16A^2 P_s P_{LO} B_2 \eta (1 - \Gamma_2) + 2\eta^2 B_2 (4B_1 - B_2)} \quad (1.6)$$

Fig. 1-3 shows the dependence of the FLDR on the received optical power. For this graph, values of the parameters are chosen as $B_1 = 1$ GHz, $B_2 = 6$ MHz, linewidth = 20MHz and $P_{LO} = 10$ dBm. Inspection of the graph reveals that at high received optical powers, the FLDR becomes worse. It is because of the noise term generated by the multiplication of the direct detection term and the phase noise term. From this graph, we conclude that the 2-port homodyne system cannot achieve high dynamic range.

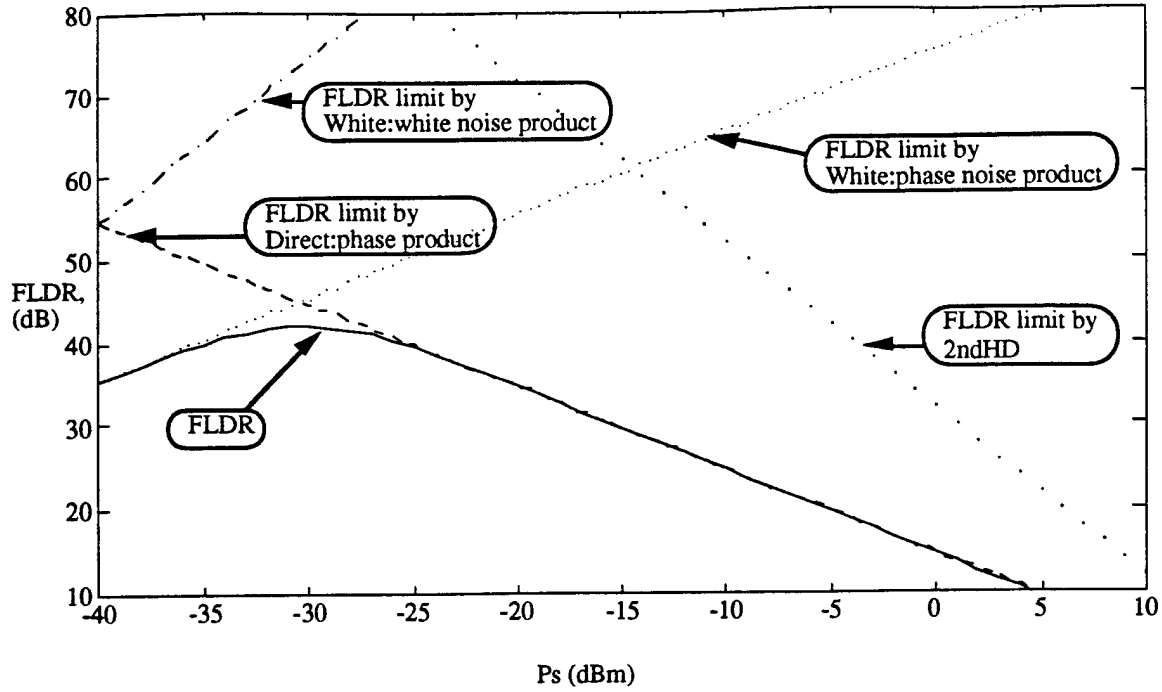


Figure 1-3. FLDR of the 2-port homodyne AM-WIRNA receiver vs. received optical power.

1.3.3 Multi-port Homodyne Link Description

To increase the dynamic range, a multi-port homodyne system can be used. In a multiport homodyne system, the $P_{direct-phase}$ noise term, which limits the performance in the 2-port homodyne system, is canceled because of the symmetry in the optical hybrid. The structure of this system is similar to the 2-port system, except that it uses an N-port optical hybrid and N sets of receivers. The resulting FLDR is

$$\begin{aligned}
 FLDR &= \frac{P_{signal}}{P_{direct-direct} + P_{white-phase} + P_{white-white}} \\
 &= \frac{2N^2 A^4 P_s^2 P_{LO}^2}{\frac{N^2}{8} A^4 P_s^4 + 8NA^2 P_s P_{LO} B_2 \eta (1 - \Gamma_2) + N\eta^2 B_2 (4B_1 - B_2)} \quad (1.7)
 \end{aligned}$$

Higher dynamic range is obtained by this structure than the 2-port system. However, as seen in Fig. 1-4, an FLDR limit still exists for high optical signal input. This limit stems from the noise term generated by the squaring operation of the direct detection term, i.e., second harmonic noise.

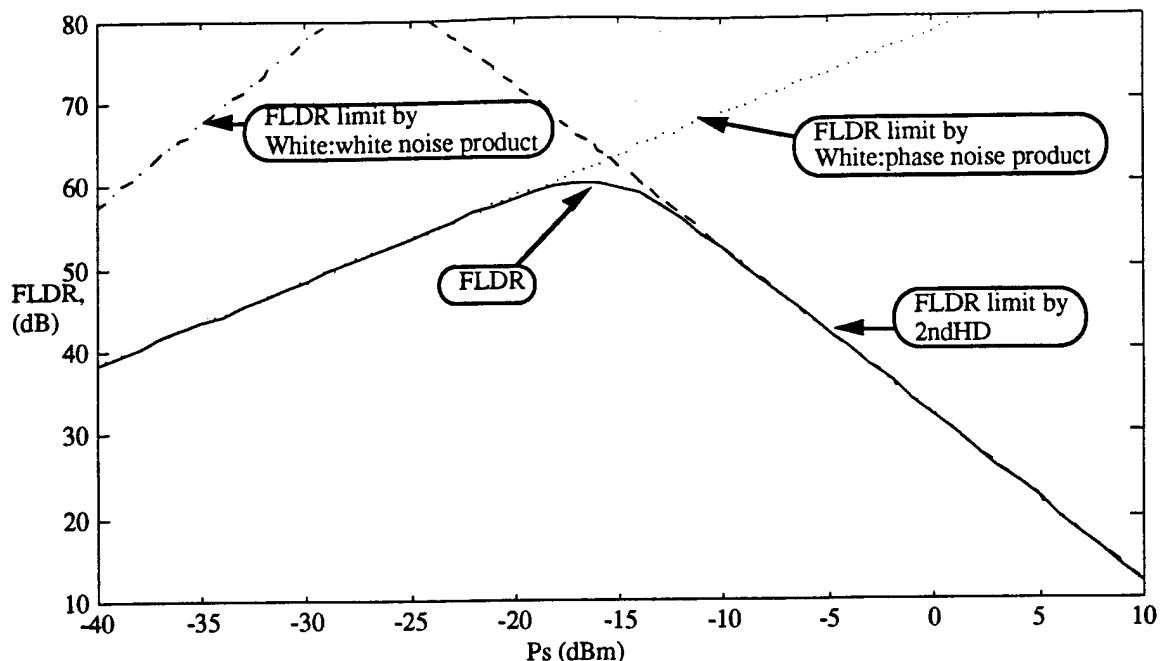


Figure 1-4 FLDR of the multi-port homodyne AM WIRNA receiver vs. received optical power.

1.3.4 2K-port Homodyne Link Description

For further improvement of the link, balanced receiver structure can be introduced. The block diagram of 2K-port homodyne link is shown in Fig. 1-5. In this receiver, balanced receiver structure is applied, as well as 2K-port optical hybrid. The optical signal and the local oscillator output are combined by a 2K-port optical hybrid (2K means the number of the output ports is even number, and not two). We choose n th and $(n+K)$ th outputs as a pair of outputs. Each of the paired outputs of the 2K-port optical hybrid is sent to a balanced receiver. Since balanced receivers reject the common mode signals, the direct detection term and the common mode noises, such as the LO RIN, are canceled at this point. Each output from balanced receivers is sent through a DC block and a wideband lowpass filter to a square-law detector. All the output signals are combined at this point, and the phase noise terms are canceled due to the phase difference produced by the multiport optical hybrid. Finally, the combined signal passes through a DC block and a narrowband lowpass filter. In this way, we make use of the WIRNA structure, balanced receivers and a phase diversity receiving method.

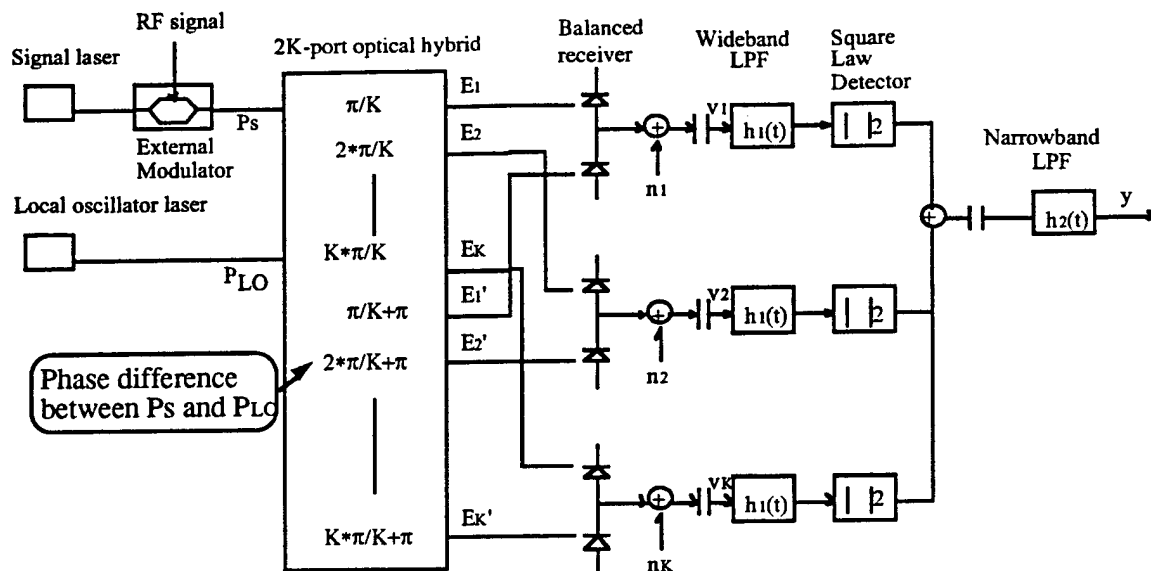


Figure 1-5. Block diagram of 2K-port homodyne receiver.

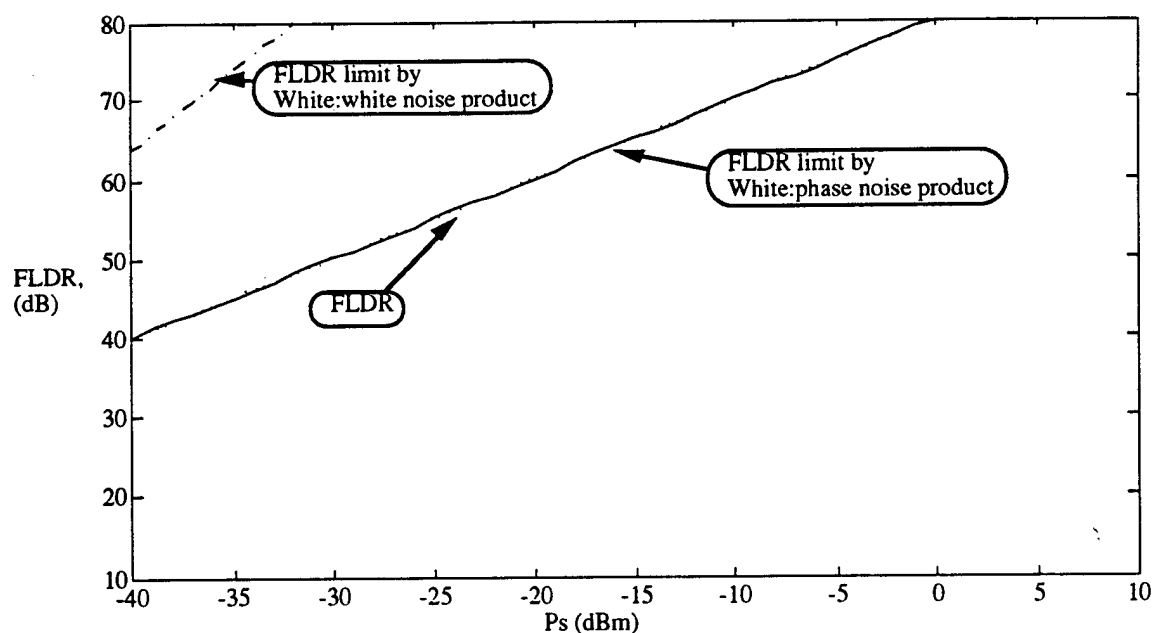


Figure 1-6. FLDR of the 2-port homodyne AM WIRNA receiver vs. received optical power.

By similar analysis, the FLDR of this system can be derived as:

$$\begin{aligned}
 FLDR &= \frac{P_{\text{signal}}}{P_{\text{white-phase}} + P_{\text{white-white}}} \\
 &= \frac{8(2K)^2 A^4 P_s^2 P_{LO}^2}{16(2K) A^2 P_s P_{LO} B_2 \eta_3 (1 - \Gamma_2) + \frac{2K}{2} \eta_3^2 B_2 (4B_1 - B_2)}
 \end{aligned} \tag{1.8}$$

where

$$\eta_3 = \eta_{th} + 4qRL(P_s + P_{LO}) \tag{1.9}$$

By this double canceling technique, noise terms with large P_s dependency are eliminated. Fig. 1-6 shows that there is no dependence of the FLDR on the optical received power. This system can achieve good performance.

1.4 Heterodyne WIRNA Link

1.4.1 Link Description

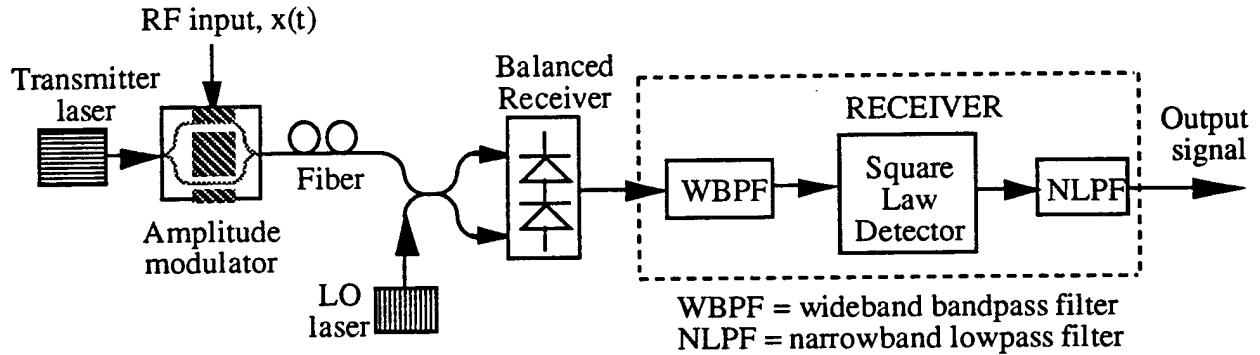


Figure 1-7. Block diagram of the heterodyne AM-WIRNA link.

The block diagram of an externally modulated coherent AM-WIRNA link is shown in Fig. 1-7. The link consists of an optical transmitter, fiber and a coherent optical receiver. The optical transmitter is the same as the one used in a conventional direct detection receiver. The RF input signal modulates the optical carrier using an external modulator. In the coherent detection, the received optical signal is mixed with the output of the local oscillator (LO) laser before it is incident on the photodetector. The polarization state of the receiver optical signal is tracked using a polarization controller and a feedback control technique is used to match the polarization state of $E_{LO}(t)$ with $E_s(t)$. In addition, an automatic frequency control (AFC) loop is used to maintain the

intermediate frequency (IF) fixed by tuning the LO laser frequency. In the receiver, the output current of the balanced receiver is an IF signal and the RF signal is recovered by a square-law detector (SLD) and a lowpass filter (LPF). A bandpass filter (BPF) is used to filter excess additive noise before squaring.

1.4.2 System Evaluation and Optimization

In this section, we analyze the coherent AM link shown in Fig. 1-7. The results of this section will serve as a basis for comparison of the coherent AM link with the direct detection link. The definitions of the variables used in this analysis are listed in Table 1.1.

The light from the transmitter laser is modulated by the external Mach-Zehnder modulator. To accomplish quasi-linear modulation, the modulator is biased at the half power point; the output optical power of the modulator can be expressed as:

$$E_s(t) = \sqrt{\frac{P_s}{2}[1 + r_s(t)]} \left\{ \exp[j(\omega_s t + \phi_s(t) + m \cdot x(t))] + \exp[j(\omega_s t + \phi_s(t) + \pi/2)] \right\} \quad (1.10)$$

The output of the LO laser has a complex amplitude $E_{LO}(t)$ given by:

$$E_{LO}(t) = \sqrt{P_{LO}[1 + r_{LO}(t)]} \cdot \exp\{j[\omega_{LO}t + \phi_{LO}(t)]\} \quad (1.11)$$

After the balanced receiver, the IF signal current is as follows:

$$i(t) = s(t) + n(t) \quad (1.12)$$

where $s(t)$ is the IF signal and $n(t)$ is the additive noise process at the output of the balanced receiver. The receiver performance is affected by noise in two ways: (a) phase noise and (b) additive noise. Description of the noise processes and their properties can be found in Appendix 1-A. The IF signal $s(t)$ in (1.3) can be expressed as:

$$\begin{aligned} s(t) &= A \left\{ \cos[\omega_{IF}t + \phi(t) + m \cdot x(t)] - \sin[\omega_{IF}t + \phi(t)] \right\} \\ &= \text{Real} \{ \hat{s}(t) \cdot e^{j\omega_{IF}t} \} \end{aligned} \quad (1.13)$$

where $\hat{s}(t) \equiv Ae^{j\phi(t)}[e^{jm \cdot x(t)} + e^{j\pi/2}]$ is the complex envelope of the IF signal. The IF signal is processed by the SLD whose output voltage is:

$$|\hat{s}(t)|^2 \equiv 2A^2\{1 + \sin[m \cdot x(t)]\} \quad (1.14)$$

Assuming that the modulation index is small ($m \ll 1$),

$$|\hat{s}(t)|^2 \approx 2A^2[1 + m \cdot x(t)] \quad (1.15)$$

Thus, ideally, in the absence of additive noise, the transmitted signal can be recovered upon the removal of the DC term in (1.6).

However, as a result of the spectral broadening due to the phase noise, the selection of the IF bandwidth is critical to the system performance. If the bandwidth of the BPF is too narrow, some of the signal power will be lost and the laser phase noise will be converted to intensity noise at the output of the SLD; if it is too wide, more additive noise will be collected [9].

A single test tone is used to study the degradation of the link performance due to the phase noise. Consider a sinusoidal RF input signal $x(t) = \cos(2\pi f_m t + \theta)$, where f_m is the signal frequency and θ is the random initial phase uniformly distributed between 0 and 2π . For $m \ll 1$, the output signal-to-noise ratio (SNR) can be expressed as:

$$SNR \approx \frac{2m^2 A^4}{2m^2 A^4(1 - \Gamma_\phi) + 8A^2 \eta B_2 \left(1 + \frac{m^2}{4}\right) \left[1 + \frac{2}{\pi} \tan^{-1}\left(\frac{2B_1}{\Delta\nu}\right)\right] + 4\eta^2 B_2(4B_1 - B_2)} \quad (1.16)$$

where the parameter

$$\Gamma_\phi \equiv \frac{4}{\pi} \tan^{-1}\left(\frac{2B_1}{\Delta\nu}\right) + \frac{2}{\pi} \tan^{-1}\left(\frac{B_1}{\Delta\nu}\right) - 2 \quad (1.17)$$

expresses the degradation of the link performance due to the laser phase noise. The first term in the denominator of (1.8) is due to the phase-to-intensity-noise conversion in the IF filter. The second term is due to the beat between the signal and the additive noise. The third term is due to the squared additive noise.

If the optical power is large (i.e., $A^2 \gg \eta B_2$), the optimum IF bandwidth which minimizes the noise can be expressed as:

$$B_{1,opt} \approx \sqrt{\frac{2\Delta v m^2 A^4}{\pi \eta^2 B_2} + (2B_2)^2} \quad (1.18)$$

(1.9) can be rewritten as [10]:

$$B_{1,opt} \approx \sqrt{B_\phi^2 + (2B_2)^2} \quad (1.19)$$

where B_ϕ represents the spectral broadening due to the laser phase noise. In analog systems, the required SNR is fairly high; for example, in AM CATV, it is equal to 56 dB (compared) to 22 dB for typical digital systems). As a result, B_ϕ may be orders of magnitude larger than B_2 due to large optical powers, and hence, a much wider B_1 is needed (in contrast to the digital case where $B_\phi = 12.7 \Delta v$ [10]).

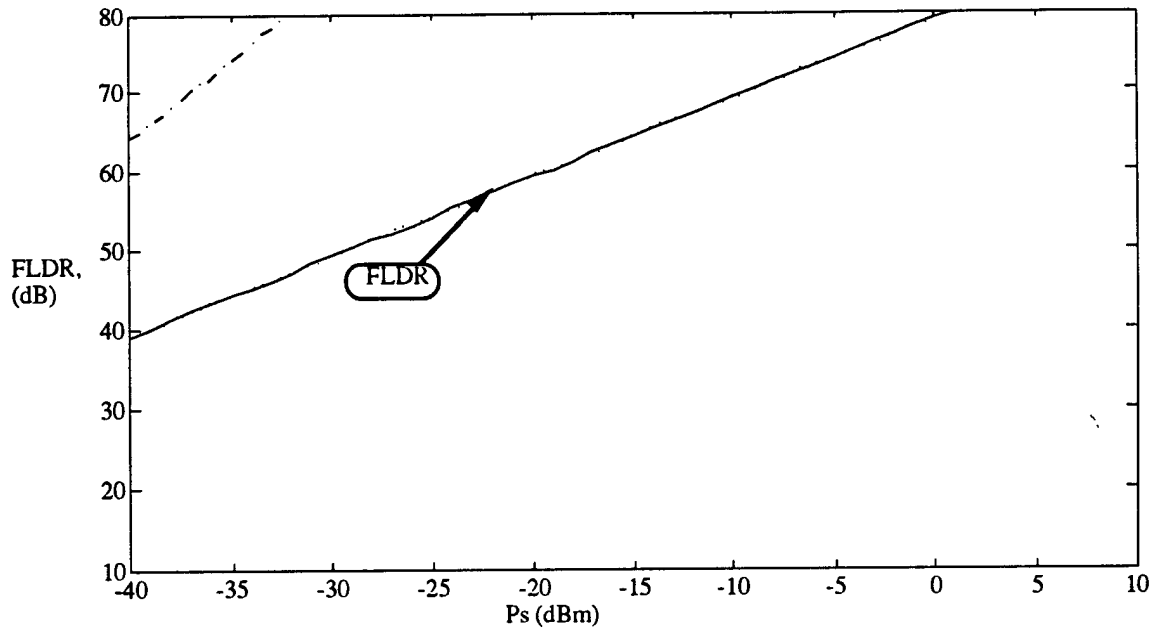


Figure 1-8. FLDR of the heterodyne AM WIRNA receiver vs. received optical power.

1.4.3 Link Dynamic Range

To evaluate the FLDR, we use a single-tone signal as the RF input. From (1.7), if the IF bandwidth B_1 , is optimized as per (1.9), the FLDR for a coherent AM link can be expressed as:

$$FLDR \approx \frac{2A^4}{16A^2\eta B_2 + 4\eta^2 B_2(4B_1 - B_2)} \quad (1.20)$$

The SFDR for a coherent AM link can be expressed as:

$$SFDR \approx 4 \left[\frac{4A^4}{16A^2\eta B_2 + 4\eta^2 B_2(4B_1 - B_2)} \right]^{2/3} \quad (1.21)$$

For the purpose of comparison, the SFDR for an AM direct detection link can be expressed as [1]:

$$SFDR_{dd} = 4 \left(\frac{R^2 P_s^2}{\eta_{dd} B} \right)^{2/3} \quad (1.22)$$

where

$$\eta_{dd} = \eta_{th} + 2qRP_s + R^2 P_s^2 10^{RIN/10} \quad (1.23)$$

1.5 Comparison between the techniques

To summarize, we explain the difference in the system performance intuitively in this section. Fig. 1-9 shows the comparison of the performance of each system for a typical values of the parameters, $B_1 = 1$ GHz, $B_2 = 6$ MHz, linewidth = 20 MHz, and $P_{LO} = 10$ dBm. In Fig. 1-10, the spectra before and after the square-law detector in the homodyne WIRNA systems are shown and compared with those in the heterodyne

WIRNA system. In the heterodyne system, the direct detection term is outside the passband of the IF bandpass filter. Thus, it is rejected, and there is no $P_{direct-phase}$ term at the receiver output; as the result, the SNR of heterodyne WIRNA systems is close to the $P_{white-phase}$ limited condition. Therefore, the larger the P_s , the larger the FLDR. In the 2-

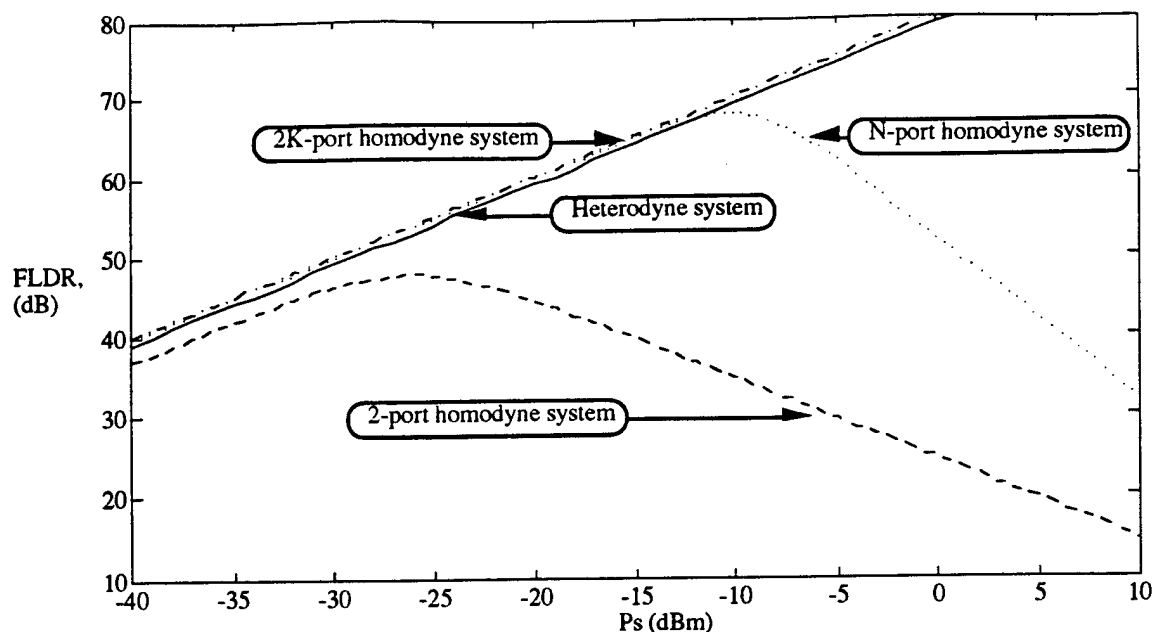


Figure 1-9. Comparison of the homodyne and heterodyne system .

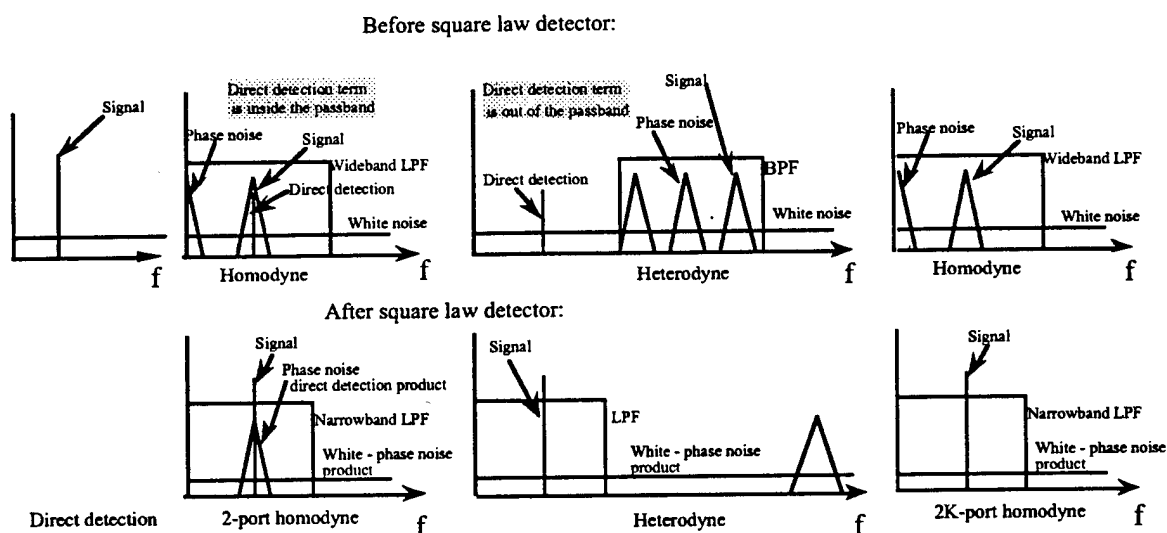


Figure 1-10. Comparison of the homodyne and heterodyne system .

port homodyne system, the main noise term is caused by the multiplication of the direct detection signal and the phase noise. Since a homodyne system uses the same frequency region for the signal processing as that of the RF signal, it is impossible to remove this noise term. This noise term increases proportionally to P_s^3 and degrades the FLDR at large P_s region. The achievable SNR is thus much smaller than that of the heterodyne system. To overcome this problem, in 2K-port homodyne system, the balanced receivers are utilized to reject direct detection terms with their common mode rejection effect. The

noise components contained in 2K-port homodyne system are effectively identical to those in heterodyne system. Thus the 2K-port homodyne system has very similar performance to the heterodyne system. Note that in heterodyne system the bandwidth of the IF filter should be twice as much as that in the homodyne system. This leads to larger noise power. But it affects only the white:white noise product and it is not usually the dominant noise term. Therefore, the heterodyne system can achieve similar performance with simpler structure despite the larger IF bandwidth required.

1.6 Experimental AM-WIRNA Link

1.6.1 Link Description

The block diagram of the AM-WIRNA heterodyne link we constructed and investigated is shown in Fig. 1-11. The transmitter laser is a 1.55 μm distributed feedback (DFB) laser which launches approximately 2 mW of optical power into the fiber and has a relative intensity noise (RIN) of -153 dB/Hz to -140 dB/Hz, depending on the drive current and temperature.

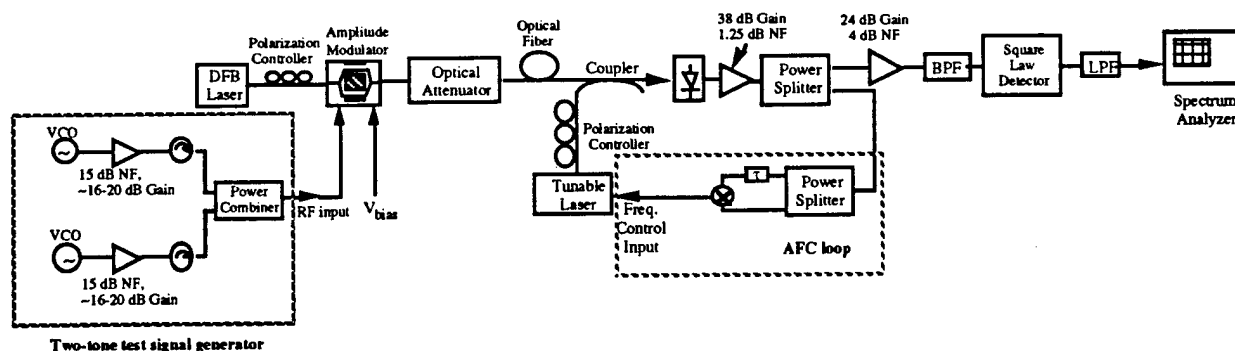


Fig. 1-11. Block diagram of the AM-WIRNA heterodyne link.

BPF = bandpass filter and LFP = lowpass filter.

The RF signal modulates the optical carrier via a Mach-Zehnder external amplitude modulator. The modulator is biased at its half-power point to eliminate even harmonics and even intermodulation products. It is important that the bias remain at this half power point; thus, we implemented an automatic bias control circuit in our set-up. We use the zeroing of the second-order distortion to implement a closed-loop control of the bias.

At the receiver, an external cavity tunable semiconductor laser (TSL) is used as the local oscillator (LO) laser. This laser has a built-in optical isolator and a temperature

controller. The TSL has an output power of 600 μ W, RIN of -148 dB/Hz, and linewidth of 20 kHz. A manual polarization controller is used to align the polarization of the LO laser to that of the incoming optical signal at the input of the coupler. The coupler is followed by a single-photodetector with a 3 dB bandwidth greater than 15 GHz, and a 38 dB gain, 1.5 dB noise figure preamplifier. After the preamplifier, the signal is split into the demodulation path and the automatic frequency control (AFC) loop. The AFC loop maintains the receiver intermediate frequency (IF) fixed at 10 GHz. The AFC loop consists of a frequency discriminator whose output is fed into the external frequency control connector of the LO laser. For demodulation, the signal passes through an amplifier, bandpass filter, square law detector, and lowpass filter. We refer to the combination of a bandpass filter (BPF), square law detector (SLD) and lowpass filter (LPF) in the receiver as the WIRNA (which stands for Wideband filter-Rectifier-Narrowband filter) structure [11, 12].

To measure link performance experimentally, we generated a two-tone input test signal using two voltage controlled oscillators (VCO) running at 0.9 GHz and 1.0 GHz. To control the amplitudes, and therefore, the modulation index of the test signals, each VCO is connected to a variable gain amplifier. The signals are then combined with a power combiner and applied to the RF input port of the EOM. The amplitudes of the fundamental, the third order IMDs and noise floor at the link output are then measured using a spectrum analyzer and from this information, the dynamic range is determined.

1.6.2 Linewidth and the IF Bandwidth

The SFDR measurements as a function of the laser linewidth using three different IF filter bandwidths are shown in Fig. 1-12. To vary the linewidth beyond 20 MHz, we directly modulated the DFB laser with a noise source so that the spectral linewidth was broadened by laser chirping [13].

From Fig. 1-12, it is observed that for IF bandwidths of 3 and 4 GHz, the SFDR is almost constant at $84 \text{ dB}\cdot\text{Hz}^{2/3}$ and $82 \text{ dB}\cdot\text{Hz}^{2/3}$, respectively, for linewidths from 10 to 300 MHz. For an IF bandwidth of 2 GHz, the SFDR is at least 3 dB less. As the linewidth is increased beyond 300 MHz, all three bandwidth cases show a considerable drop in the SFDR, with the 2 GHz case having the most rapid decrease, and the 4 GHz, the least.

The explanation of the foregoing experimental results is as follows. Laser phase noise (which is associated with wide laser linewidths) causes the received signal spectrum to widen. If the IF filter cuts off part of the signal spectrum, this results in phase noise-

to-amplitude noise conversion which causes a deterioration of the link performance. The signals used in this experiment are sinusoids at 0.9 and 1 GHz; therefore, it is clear why the link with an IF bandwidth of 2 GHz has the worst SFDR -- for any finite linewidth, a part of the signal spectrum will always be rejected by the IF filter. As the linewidth increases, a larger and larger part of the signal power will be rejected by the bandpass filter causing signal distortion and phase noise-to-amplitude noise conversion, resulting in a poorer SFDR.

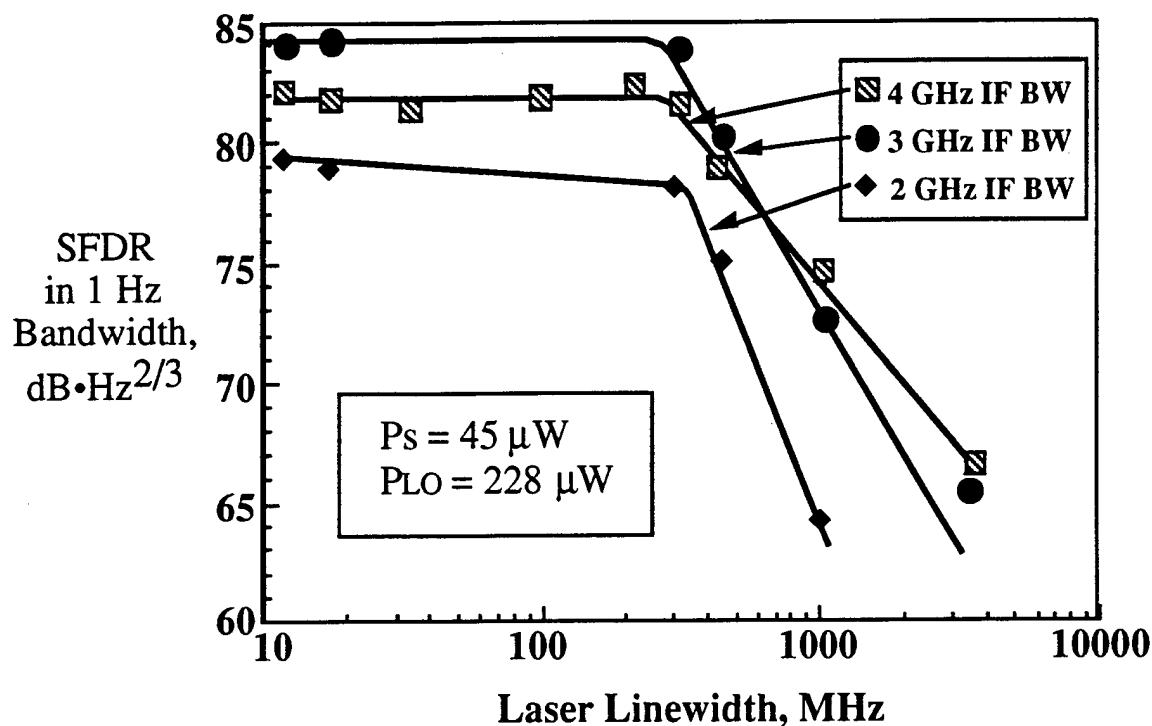


Fig. 1-12. Experimentally measured impact of the laser linewidth and the IF bandwidth on the spurious-free dynamic range of the coherent AM link.

For the 3 and 4 GHz bandwidth cases, when the linewidths are less than 300 MHz, the IF bandwidth is much wider than the signal spectral width, so that only a negligible part of the phase noise-widened signal spectrum is cut off. This causes the link to be linewidth-insensitive; i.e., the SFDR is virtually independent of the laser linewidth. However, similar to the 2 GHz case, when the linewidth is increased to the point when a considerable amount of the signal power is cut off, the SFDR deteriorates. For both the 3 and 4 GHz cases, this occurs for linewidths greater than 300 MHz.

The disadvantage of a wider IF bandwidth is that it collects more additive noise, which translates to a higher noise floor, and therefore, to a lower SFDR. This is supported by Fig. 1-12: the 4 GHz IF bandwidth link has a poorer SFDR than the link

with a 3 GHz IF bandwidth, for linewidths less than 300 MHz. The choice of IF bandwidth is therefore very important: A narrow IF filter increases the amount of phase noise-to-amplitude noise conversion while a wide IF filter collects more additive noise. For example, in Fig. 1-12, when the linewidth is 700 MHz or more, the link with a 4 GHz IF bandwidth outperforms the link with a 3 GHz IF bandwidth. This is because there is much more phase-to-amplitude noise degradation in the 3 GHz case than the 4 GHz case, and for this situation, the degradation due to phase noise-to-amplitude noise conversion is more significant than the degradation caused by additive noise.

An important conclusion of this section is that as long as the bandpass filter is designed to be wide enough to pass the phase noise-widened spectrum of the signal, the AM-WIRNA link is insensitive to laser linewidth and to any changes in the linewidth that may be brought about by temperature and drive current fluctuations. The SFDR can be maximized by having the smallest possible IF bandwidth that is wide enough to avoid cutting off a considerable amount of signal power while minimizing the additive noise collected.

1.6.3 Received Signal Power

The SFDR measurements of the AM-WIRNA heterodyne link as a function of the received optical signal power are shown in Fig. 1-13. The SFDR measurements for a similar externally-modulated direct detection link are also shown for comparison. The maximum received optical power (signal plus LO) at the photodetector is limited largely due to the optical modulator losses, and also by the optical output power of our DFB laser used as the transmitter and the tunable semiconductor laser as the LO laser. However, these modest powers are sufficient for a proof-of-concept experiment on the merits of this coherent AM link.

Fig. 1-13 also contains theoretical SFDR estimates obtained using Eqs. (1.21) and (1.22); the estimates take into account laser linewidth and are further modified to take into account the RIN of both lasers, the receiver amplifier noise, and the finite optical power of the LO laser.

Fig. 1-13 shows that the coherent AM link has a higher SFDR (by up to 10 dB) than the corresponding direct detection link when the received optical signal power is less than 85 μW . This is because the direct detection link is thermal noise-limited at these power levels while the coherent link is closer to being shot noise-limited. As the received optical signal power increases beyond 85 μW , both types of receivers approach the shot

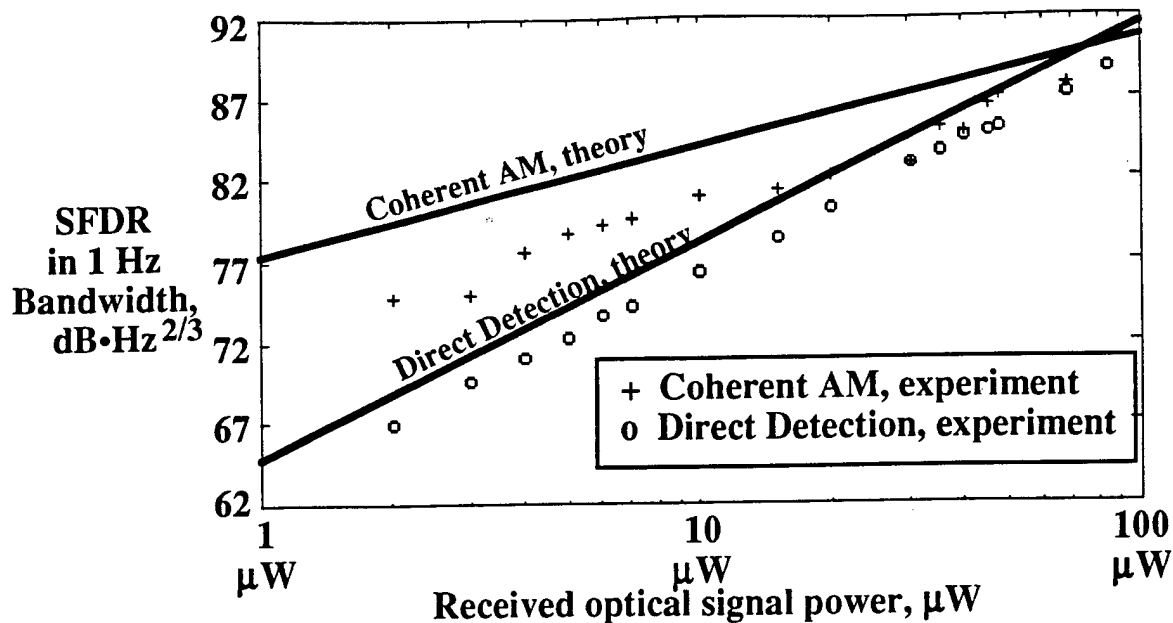


Fig. 1-13. Spurious-free dynamic range versus received optical signal power for the coherent and direct detection links.

(The transmitter laser for both coherent and direct detection links had a RIN = -153.8 dB/Hz and a linewidth = 7.9 MHz. The LO laser had a received power of 228 μ W, RIN = -148.7 dB/Hz and linewidth of 19.2 kHz.)

noise-limited regime. In this case, the direct detection link has a higher dynamic range than the coherent AM link [1]. This is shown by the theoretical curves in Fig. 1-13. This cross-over optical power point between the coherent AM and direct detection links can be increased using an LO laser with a higher output power (we are currently limited to an optical LO power at the photodetector of 228 μ W by our tunable laser).

Fig. 1-13 shows that the measurements agree very well with theory for the direct detection case, with a difference of only 1 dB. The experimental data for the coherent AM link differs from the theory by 2 to 4 dB. This is attributed partially to optical connector losses in the receiver (up to 1 dB) and fluctuations and instabilities in the output of the LO laser (a penalty of about 1 dB). The latter is due to polarization changes and tuning required to maintain the IF at 10 GHz. However, the main reason for the difference is the third order distortion introduced by the square law detector (SLD) at the link output. The SLD introduces third order distortion in the output signal resulting in a lower SFDR than that predicted by theory. By varying the input RF power into the SLD (so that only the nonlinearities produced by the SLD, as the RF input to it changes, can be studied), we verified that the additional distortion is caused mainly by the SLD. Since the RF input power to the SLD changes as the received optical signal power

changes, third order nonlinearities produced by the SLD affect the measured link SFDR. Table 1-2 below shows the additional SFDR penalty due to the SLD as a function of the received optical signal power that corresponds to the RF power we input to the SLD. Inspection of Table 1-2 reveals that the SFDR penalty due to the SLD corresponds to most of the discrepancy between the theoretical and experimental results.

Table 1-2. SFDR penalty due to the SLD imperfections.

Received Optical Signal Power, (μ W)	SFDR penalty due to SLD (dB)
50.0	0.5
27.5	1.1
17.6	1.5
10.0	2.3
6.2	3.0
3.9	3.8

1.7 Conclusions

In this chapter, we have investigated the fundamental limit of the dynamic range (FLDR) of homodyne and heterodyne coherent amplitude-modulated links using the WIRNA (WIdeband - Rectifier - NArrowband) demodulator structure. We have found that the FLDR of a 2-port homodyne link is degraded at high optical powers by the direct detection - phase noise product noise term, and thus that this system cannot achieve high dynamic range. We have found that FLDR performance is improved for a multi-port homodyne link because the direct detection - phase noise product is canceled due to symmetry in the optical hybrid. The FLDR of this link is limited at high powers by the noise term generated by the second harmonic noise generated by the squaring of the direct detection term. By introducing a balanced receiver and a 2K-port optical hybrid, we have designed a homodyne link with FLDR independent of optical power. This link can achieve high dynamic range.

We have optimized the FLDR of a heterodyne coherent WIRNA link by optimizing the intermediate frequency (IF) bandwidth to balance the degradation due to additive white noise and due to phase noise. We have verified our theoretical predictions by constructing an experimental WIRNA link. The experimental link exhibits linewidth-

insensitive performance for laser linewidths up to several hundred MHz and outperforms an experimental direct detection link for received optical signal powers less than 85 μW .

Appendix 1.A Noise in Analog Optical Links

1.A.1 The Additive Noise

Shot noise and thermal noise are the two fundamental noise mechanisms responsible for current fluctuations in all optical receivers even when the incident optical power P is constant. Of course, additional noise is generated if P is itself fluctuating because of relative intensity noise associated with the system. The photodiode current generated in response to a constant optical signal can be written as:

$$I(t) = I_p + i_t(t) + i_s(t) + i_r(t) \quad (1.A-1)$$

where $I_p = RP$ is the average current and $i_t(t)$, $i_s(t)$, $i_r(t)$ are current fluctuations related to thermal noise, shot noise and relative intensity noise, respectively.

1.A.1.1 Thermal noise

Random thermal motion of electrons in a resistor manifests as a fluctuating current even in the absence of an applied voltage. The load resistor in the front end of an optical receiver adds such fluctuations to the current generated by the photodiode. Mathematically, $i_t(t)$ is modeled as a stationary Gaussian random process with a spectral density that is frequency independent and is given by:

$$S_i(f) = \frac{4kT}{r}, \quad \text{for } 0 < f < \infty \quad (1.A-2)$$

where k is the Boltzmann constant, T is the absolute temperature, and r is the load resistor.

1.A.1.2 Shot noise

Shot noise is a manifestation of the fact that electric current consists of a stream of electrons that are generated at random times. Mathematically, the photocurrent

fluctuation is a stationary random process with Poisson statistics which in practice can be approximated by the Gaussian statistics with a spectral density given by:

$$S_s(f) = 2qI_p, \quad \text{for } 0 < f < \infty \quad (1.A-3)$$

where q is the charge of an electron.

1.A.1.3 Relative Intensity Noise

In practice, light emitted by any transmitter exhibits power fluctuations. Such fluctuations are called relative intensity noise. An exact analysis of $i_r(t)$ is complicated, as it involves the calculation of photocurrent statistics which in turn depends on the intensity-noise statistics at the receiver. A simple approach is to assume the spectral density to be:

$$S_r(f) = R^2 P^2 10^{\frac{RIN}{10}}, \quad \text{for } 0 < f < \infty \quad (1.A-4)$$

The parameter RIN , in dB/Hz, is a measure of the noise level of the incident optical signal.

1.A.2 The Phase Noise

The spectral shape for semiconductor lasers can be approximated by the Lorentzian lineshape, i.e., the phase noise is dominated by white frequency noise. The one-sided PSD of $\phi(t)$ is given by the following expression:

$$S_\phi(f) = \frac{\Delta\nu}{\pi f^2}, \quad \text{for } 0 < f < \infty \quad (1.A-5)$$

where $\Delta\nu$ is the FWHM linewidth.

1.8 References

- [1] T. K. Fong, D. J. M. Sabido IX, R. F. Kalman, M. Tabara, and L. G. Kazovsky, "Linewidth-insensitive coherent AM optical links: design, performance, and potential applications," *J. Lightwave Technol.*, vol. 12, no. 3, pp. 526-534, 1994.

- [2] R. F. Kalman, J. C. Fan, and L. G. Kazovsky, "Dynamic range of coherent analog fiber-optic links," *J. Lightwave Technol.*, vol. 12, no. 7, pp. 1263-1277, 1994.
- [3] T. E. Darcie and G. E. Bodeep, "Lightwave subcarrier CATV transmission systems," *IEEE Trans. Microwave Theory and Tech.*, vol. 38, no. 5, pp. 524-533, 1990.
- [4] W. I. Way, "Optical fiber-based microcellular systems: an overview," *IEICE Trans. Commun.*, vol. E76-B, no. 9, pp. 1091-1102, 1993.
- [5] C. H. Cox, G. E. Betts, and L. M. Johnson, "An analytic and experimental comparison of direct and external modulation in analog fiber-optic links," *IEEE Trans. Microwave Theory and Tech.*, vol. 38, no. 5, pp. 501-509, 1990.
- [6] R. T. Olshansky, V. A. Lanzisera, and P. M. Hill, "Subcarrier multiplexed lightwave systems for broadband distribution," *IEEE J. Lightwave Technol.*, vol. 7, no. 9, pp. 1329-1342, 1989.
- [7] L. G. Kazovsky, P. Meissner, and E. Patzak, "ASK multiport optical homodyne receivers," *J. Lightwave Technol.*, vol. LT-5, no. 3, pp. 770-791, June 1987.
- [8] L. G. Kazovsky, and O. K. Tonguz, "ASK and FSK coherent lightwave systems: A simplified approximate analysis," *J. Lightwave Technol.*, vol. LT-8, no. 3, pp. 338-352, Mar. 1990.
- [9] T. K. Fong, D. J. M. Sabido, R. F. Kalman and M. Tabara, and L. G. Kazovsky "Linewidth-Insensitive Coherent AM Optical Links: Design, Performance, and Potential Applications," *J. Lightwave Technol.*, vol. LT-12, no. 3, pp. 526-534, Mar. 1994.
- [10] L. G. Kazovsky, "Impact of laser phase noise on optical heterodyne communication systems," *J. Optical Communicat.*, vol. 7, no. 2, pp. 66-78, 1986.
- [11] L. G. Kazovsky, P. Meissner, and E. Patzak, "ASK multiport optical homodyne receivers," *J. Lightwave Technol.*, vol. LT-5, no. 2, pp. 770-791, June 1987.

- [12] L. G. Kazovsky, R. Welter, A. F. Elfeiaie, and W. Sessa, "Wide-linewidth phase diversity homodyne receivers," *J. Lightwave Technol.*, vol. LT-6, no. 10, pp. 1527-1536, October 1988.
- [13] K. Petermann, *Laser Diode Modulation and Noise*, Norwell, Massachusetts: Kluwer Academic Publishers, 1988, pp. 198-200.

Chapter 2

Angle-Modulated Links

2.1 Potential Dynamic Range Improvement Using Angle Modulation

Angle modulation is well-known to offer potential performance advantages over amplitude modulation in analog links. These advantages are exploited in commercial FM radio and video. There are a number of reasons to believe that angle modulation could be useful in optical systems. Wideband angle modulation provides improved signal-to-noise ratio at the expense of increased transmission bandwidth. Because optical fiber offers a very large potential transmission bandwidth, optical transmission systems are well-suited to handle expanded bandwidth signals. Optical phase modulators are essentially ideally linear, in contrast to the highly nonlinear characteristics of Mach Zehnder amplitude modulators. The linearity of optical phase modulators can be exploited to both PM and FM systems to achieve large spurious-free dynamic range (SFDR - see Section 1.2).

Coherent detection provides both amplitude and phase information about the detected optical field, and it is thus well-suited to the detection of angle modulated signals. However, because angle modulated links carry their information in the optical phase, they are intrinsically sensitive to the laser phase noise in coherent detection links. In Section 2.2, we present an analysis of the spurious-free dynamic range of PM and FM links, and compare their performance to that of AM coherent and AM direct detection links. In Section 2.3, we introduce the reference transport concept for phase noise cancellation (PNC) and describe our motivation for investigating it. In Section 2.4, we describe conventional approaches and why they do not work for coherent angle-modulated analog links. We then present our novel approach to deal with the PNC problem, which utilizes interferometric links. In Section 2.5, we describe our novel approach to optical frequency shifting through sideband generation using electro-optic external modulation and other possible approaches. In Section 2.6, we describe the heterodyne interferometric link using phase modulation (HIPM), which is based upon the novel approach of Section 2.5, and compare its SFDR to that of coherent PM and AM direct detection links. In Section 2.7, we describe and give results for a proof-of-concept HIPM link built in our laboratory. Section 2.8 presents the conclusions of this work. Appendix 2.A contains a derivation of output currents for the angle-modulated

links discussed in this chapter. Appendix 2.B derives noise properties for the noise terms defined in this chapter. Section 2.9 contains references.

2.2 Coherent PM and FM Links

2.2.1 Link Descriptions

A PM coherent link is shown in Fig. 2-1. The input signal is phase modulated on an optical carrier. At the receiver the signal is combined with the LO laser light using a 3 dB directional coupler and detected. It is then amplified at the IF, limited, put through a delay line filter, envelope detected, and integrated.

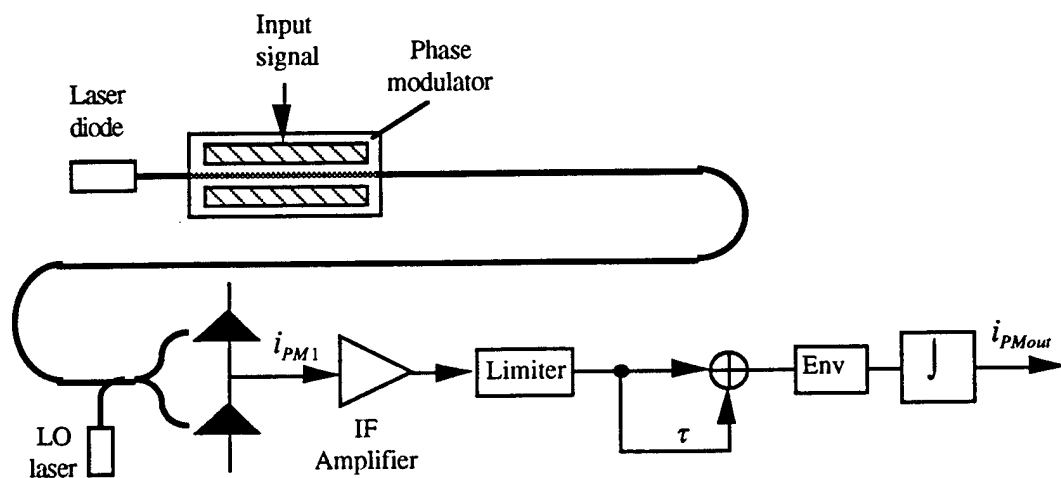


Figure 2-1. Coherent PM link

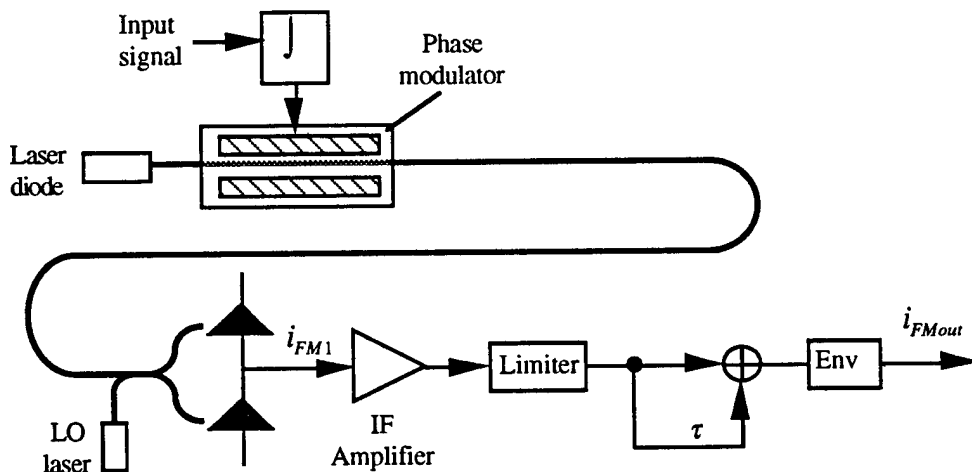


Figure 2-2. Coherent FM link

In the FM system, shown in Fig. 2-2, the input signal is integrated before being applied to a phase modulator. The FM receiver is identical to the PM receiver, except that there is no integrator before the output.

In both cases, there is filtering implied in the baseband and IF amplifiers. For the purposes of our analysis, we assume that the amplifier bandwidths are sufficiently broad to pass signals undistorted, including signals with bandwidths broadened by phase noise. In the coherent systems, balanced receivers are utilized to both increase the collected signal power and suppress part of the laser relative intensity noise (RIN) [1].

2.2.2 Impact of Laser Linewidth, RIN, and Receiver Noise

The received signal optical power P_R at a receiver can be expressed as $P_R = P_{laser} L_e L_{in}$, where P_{laser} is the output power of the transmitter laser, L_e is excess loss of the link, and L_{in} is the intrinsic loss of the external modulator. $L_{in} = 0.5$ for an external amplitude modulator biased to eliminate second-order distortion, and $L_{in} = 1.0$ for an external phase modulator. We define a normalized transmitted signal optical power $P_s = P_{laser} L_e$ and use this normalized power in the link comparisons in this chapter.

The incident optical signal field at each photodetector for the PM and FM links is given by

$$e_{PM}(t) = \sqrt{\frac{P_s}{2}} [1 + n_{RS}(t)] \exp i[\omega_s t + \varphi_\Delta x(t) + \varphi_{nS}(t)] \quad (2.1)$$

$$e_{FM}(t) = \sqrt{\frac{P_s}{2}} [1 + n_{RS}(t)] \exp i\left[\omega_s t + \omega_\Delta \int x(t) dt + \varphi_{nS}(t)\right] \quad (2.2)$$

where P_s is the total received signal optical power at each receiver, $n_{RS}(t)$ is the relative intensity noise (RIN) of the signal laser, ω_s and $\varphi_{nS}(t)$ are the optical frequency and phase noise of the signal laser, respectively, $x(t)$ is the normalized applied signal, φ_Δ is the phase deviation, and ω_Δ is the frequency deviation.

The local oscillator field at each photodetector for the coherent links is given by

$$e_{LO}(t) = \sqrt{\frac{P_{LO}}{2}} [1 + n_{RLO}(t)] \exp i[\omega_{LO} t + \varphi_{nLO}(t)] \quad (2.3)$$

where P_{LO} is the total received local oscillator power at the photodetector, $n_{RLO}(t)$ is the relative intensity noise (RIN) of the LO laser, and ω_{LO} and $\varphi_{nLO}(t)$ are the optical frequency and phase noise of the LO laser, respectively.

Neglecting DC terms, the detected currents (indicated by the subscript '1') in the PM and FM links are given by

$$\begin{aligned} i_{PM1}(t) = & [h_1(t) + h_2(t)] * \left\{ R \sqrt{P_S P_{LO} [1 + n_{RS}(t)] [1 + n_{RLO}(t)]} \right. \\ & \times \cos[\omega_{IF} t + \varphi_A x(t) + \varphi_{nS}(t) - \varphi_{nLO}(t)] + n_{sh}(t) \Big\} + n_{th}(t) \\ & + [h_1(t) - h_2(t)] * \frac{1}{2} R [P_S n_{RS}(t) + P_{LO} n_{RLO}(t)] \end{aligned} \quad (2.4)$$

$$\begin{aligned} i_{FM1}(t) = & [h_1(t) + h_2(t)] * \left\{ R \sqrt{P_S P_{LO} [1 + n_{RS}(t)] [1 + n_{RLO}(t)]} \right. \\ & \times \cos\left[\omega_{IF} t + \omega_A \int x(t) dt + \varphi_{nS}(t) - \varphi_{nLO}(t)\right] + n_{sh}(t) \Big\} + n_{th}(t) \\ & + [h_1(t) - h_2(t)] * \frac{1}{2} R [P_S n_{RS}(t) + P_{LO} n_{RLO}(t)] \end{aligned} \quad (2.5)$$

where R is the responsivity of the photodetectors, $h_1(t)$ and $h_2(t)$ are the impulse responses of the two photodetectors, and $n_{sh}(t)$ and $n_{th}(t)$ are due to shot and thermal noise, respectively. The shot noise is defined per photodetector in each system (see Appendix 2.B). Since the thermal noise is added after detection, it is not affected by the impulse responses of the detectors. Ideally, the impulse responses of the photodetectors in a balanced receiver are perfectly matched; in practice, they are somewhat different. We will assume that the transfer functions of the photodetectors are approximately flat over the received signal bandwidth, and that they differ by a small factor. Under this assumption, we can write $[h_1(t) + h_2(t)] * A(t) \equiv 2A(t)$ and $\Delta h(t) \equiv h_1(t) - h_2(t)$.

Now we derive expressions for the output currents of the links. We neglect high-order noise terms and products between the noise and the modulated signal (which does not include the IF carrier component) since analog links have high SNRs and small modulation depths. The PM signal is recovered by a chain consisting of a limiter, phase discriminator, and envelope detector. The derivation of the PM output signal is given in Appendix 2.A. The result is

$$i_{PM\ out}(t) \equiv K \left\{ 2R\sqrt{P_S P_{LO}} \left[\varphi_\Delta x(t) - \frac{\varphi_\Delta^3}{6} \left(\frac{1}{4f_{IF}} \right)^2 \int \dot{x}^3(t) dt \right] + 2R\sqrt{P_S P_{LO}} [\varphi_{nS}(t) - \varphi_{nLO}(t)] \right. \\ \left. + \frac{1}{2} \Delta h(t) * [RP_S n_{RS\ bp}(t) + RP_{LO} n_{RLO\ bp}(t)] + n_{D\ bp}(t) \right\} \quad (2.6)$$

The term proportional to φ_Δ^3 arises due to the imperfect linearity of the delay-line phase discriminator. It is obtained through a small-signal expansion of the discriminator transfer function, and results in intermodulation distortion.

The FM output current is recovered in a similar way to the PM output current, except that a frequency discriminator is used instead of a phase discriminator. The result, derived in Appendix 2.A, is

$$i_{FM\ out}(t) \equiv T \left\{ 2R\sqrt{P_S P_{LO}} \left[\omega_\Delta x(t) - \frac{\omega_\Delta^3}{6} \left(\frac{1}{4f_{IF}} \right)^2 x^3(t) \right] + 2R\sqrt{P_S P_{LO}} [\dot{\varphi}_{nS}(t) - \dot{\varphi}_{nLO}(t)] \right. \\ \left. + \frac{1}{2} \Delta h(t) * [RP_S \dot{n}_{RS\ bp}(t) + RP_{LO} \dot{n}_{RLO\ bp}(t)] + \dot{n}_{D\ bp}(t) \right\} \quad (2.7)$$

where T is a constant with the dimensions of time associated with the frequency discriminator. The term proportional to ω_Δ^3 arises due to the imperfect linearity of the delay-line frequency discriminator, and results in intermodulation distortion.

The corresponding signal-to-noise ratios (SNRs) for the PM and FM links are given by

$$SNR_{PM} = \varphi_\Delta^2 \frac{4R^2 P_S P_{LO} \langle x^2(t) \rangle}{4R^2 P_S P_{LO} \langle (\varphi_{nS} - \varphi_{nLO})^2 \rangle + \frac{1}{4} b(RP_S)^2 \langle n_{RS\ bp}^2 \rangle + \frac{1}{4} b(RP_{LO})^2 \langle n_{RLO\ bp}^2 \rangle + \langle n_{D\ bp}^2 \rangle} \\ = \varphi_\Delta^2 SNR_{PMo} \quad (2.8)$$

$$\begin{aligned}
SNR_{FM} &= \left(\frac{\omega_{\Delta}}{B} \right)^2 \frac{4B^2 R^2 P_S P_{LO} \langle x^2(t) \rangle}{4R^2 P_S P_{LO} \langle (\dot{\phi}_{ns} - \dot{\phi}_{nLO})^2 \rangle + \frac{1}{4} b (RP_S)^2 \langle \dot{n}_{RS bp}^2 \rangle + \frac{1}{4} b (RP_{LO})^2 \langle \dot{n}_{RLO bp}^2 \rangle + \langle \dot{n}_{D bp}^2 \rangle} \\
&= \left(\frac{\omega_{\Delta}}{B} \right)^2 SNR_{FMo}
\end{aligned} \tag{2.9}$$

where B is the bandwidth of the baseband signal $x(t)$ and b is the photodetector matching factor, which is defined in Appendix B. The normalized SNRs SNR_{PMo} , and SNR_{FMo} are the SNRs for each of the links for a unity modulation index; note that the modulation indices may exceed unity. The various noise expressions in Eqs. (2.8)-(2.9) are evaluated in Appendix 2.B.

Eqs. (2.8)-(2.9) indicate that the SNR increases monotonically with the modulation index. The maximum useful modulation index is limited by intermodulation distortion associated with nonlinear effects. In the next section, we derive expressions for the maximum useful modulation index and the associated spurious-free dynamic range.

2.2.3 Spurious-Free Dynamic Range (SFDR)

In this section, we derive the spurious-free dynamic range (SFDR) for a link with a single channel. The output current expressions of Eqs. (2.6)-(2.7) can be written in the form

$$i_{out}(t) = s \left\{ r x(t) + b_3 [r x(t)]^3 \right\} + n_{tot}(t) \tag{2.10}$$

where r is the modulation index, s is the signal amplitude, b_3 is the coefficient describing the third-order nonlinearity, and $n_{tot}(t)$ is the total noise. The nonlinearity for the PM link (Eq. (2.6)) is of a slightly different form and is discussed below. Table 2-1 gives r and b_3 for the two links. In Section 2.2.2, we showed that generic SNR expressions for the various links can be written as

$$SNR = r^2 \frac{s^2 \langle x^2(t) \rangle}{\langle n_{tot}^2(t) \rangle} = r^2 SNR_o \tag{2.11}$$

Table 2-1. Modulation index r and nonlinear coefficient b_3 for the various links.

	PM	FM
r	φ_Δ	ω_Δ/B
b_3	$-1/6(\pi f_{max}/2f_{IF})^2$	$-1/6(B/4f_{IF})^2$

The key performance measure of an analog link is the spurious-free dynamic range (SFDR), defined as the ratio of the maximum signal power to the minimum signal power the link can transport. At high modulation depths, the third order nonlinearity results in significant intermodulation products falling within the signal band. It can be shown that the SFDR is the SNR at which the intermodulation power is equal to the noise power [2]. We assume a normalized test signal of the form

$$x(t) = \alpha_1 \cos(\omega_1 t + \varphi_1) + \alpha_2 \cos(\omega_2 t + \varphi_2) \quad (2.12)$$

where $\alpha_1^2 + \alpha_2^2 = 1$, giving $\langle x^2(t) \rangle = 0.5$; and φ_1 and φ_2 are arbitrary constant phases. For less than one octave of bandwidth, the maximum intermodulation power falling within the band is

$$\langle i_{NL3}^2 \rangle = \frac{9}{128} s^2 b_3^2 r^6 \quad (2.13)$$

where the only important terms falling within the signal band are those at $2\omega_1 - \omega_2$ and $2\omega_2 - \omega_1$. This occurs for $\alpha_1 = \alpha_2 = 1/\sqrt{2}$. Setting the intermodulation power equal to the noise power, we find that the maximum useful modulation depth is given by

$$r^2 = \left(\frac{64}{9} \frac{1}{b_3^2 SNR_o} \right)^{1/3} \quad (2.14)$$

Because the SFDR is defined as the SNR at the maximum useful modulation depth, Eq. (2.14) is substituted into Eq. (2.11) to give the SFDR,

$$SFDR = \left[\frac{8SNR_o}{3|b_3|} \right]^{2/3} \quad (2.15)$$

For a PM link with the test signal of Eq. (2.12), the total intermodulation power is given by

$$\langle i_{NL3}^2 \rangle = \frac{K^2}{2} \left[\frac{\varphi_{\Delta}^3}{6} \frac{3}{4} \left(\frac{1}{4f_{IF}} \right)^2 \right]^2 \left[\left(\alpha_1^2 \alpha_2 \frac{\omega_1^2 \omega_2}{2\omega_1 - \omega_2} \right)^2 + \left(\alpha_2^2 \alpha_1 \frac{\omega_2^2 \omega_1}{2\omega_2 - \omega_1} \right)^2 \right] \quad (2.16)$$

It can be shown that the worst case (i.e., maximum $\langle i_{NL3}^2 \rangle$) occurs for $\alpha_1 = \alpha_2 = 1/\sqrt{2}$ and $\omega_1 = \omega_2 = 2\pi f_{max}$, where f_{max} is the maximum signal frequency; for a one octave signal bandwidth, $f_{max} = 2B$. The corresponding value of b_3 is given in Table 2.1. Using this value of b_3 , the SFDR is then given by Eq. (2.15).

2.2.4 Results and Discussion

We are now in a position to evaluate the SFDR of the PM and FM coherent links for a variety of parameter values, and to compare their performance to that of coherent AM and DD links. The main system parameters include signal power, LO power, RIN, laser linewidth, signal bandwidth, and receiver intermediate frequency. In the examples considered, the signal occupies a one octave of bandwidth from 1 - 2 GHz.

We consider only combinations of laser parameters corresponding to two lasers typically used in optical communication systems: a diode-pumped Nd:YAG laser and a distributed feedback (DFB) laser diode. Diode-pumped Nd:YAG lasers exhibit low relaxation oscillation frequencies and narrow linewidths, whereas DFB laser diodes exhibit high relaxation oscillation frequencies and wider linewidths. In the following calculations, we will assume the two sets of laser parameters shown in Table 2-2. We will also assume, for the coherent links, that the local oscillator exhibits the same RIN and linewidth characteristics as the signal laser for each case. The DFB laser parameters are typical of a number of commercial lasers (e.g., Toshiba model TOLD335S-AH1, Fujitsu model FLD150F2KP) as are the Nd:YAG parameters (Lightwave Electronics Series 122, Amoco Laser Company model ALC 1320-25EHS). The quantities in Table 2-2 are defined in Appendix 2.B.

Table 2-2. Laser parameters used in numerical calculations

	DFB Laser Diode	Nd:YAG Laser
Linewidth $\Delta\nu$	10 MHz	5 kHz
RIN PSD η_R	-155 dB/Hz	-110 dB/Hz
RIN roll-off freq. f_R	3 GHz	200 kHz

Throughout our analysis, we assume a receiver front-end thermal noise power of $3.31 \times 10^{-22} \text{ A}^2/\text{Hz}$, corresponding to a $50 \text{ } \Omega$ resistor at room temperature. In principle, receivers operating at lower frequencies can achieve lower thermal noise power spectral densities (PSDs) than those operating at high frequencies by incorporating higher input impedances [3], and we would thus expect that the DD link, which has a received current at baseband, might exhibit a lower thermal noise PSD than the coherent links, which operate at an IF received current. However, to utilize standard microwave amplifiers with input impedances of $50 \text{ } \Omega$, it is convenient to use photodiodes with an output impedance of $50 \text{ } \Omega$. There are a number of commercial photodiodes with 3 dB frequencies of $> 20 \text{ GHz}$ which provide a $50 \text{ } \Omega$ output impedance (e.g., BT&D model no. PDC4310). We assume that such a photodiode is utilized in the systems analyzed. We also assume that the two photodiodes in each balanced receiver are well-matched, so the photodetector matching factor b for each link is 0.01 (b is defined in Appendix 2.B).

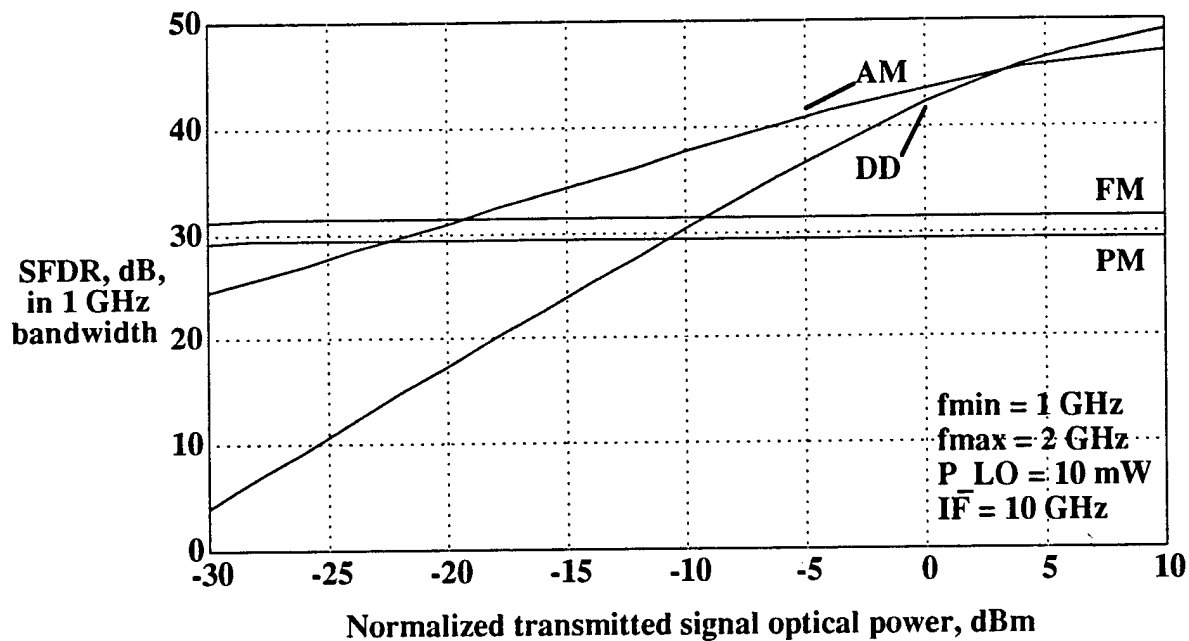


Figure 2-3. SFDRs of DD, AM, PM, and FM links plotted against received signal optical power for a DFB laser with parameters in Table 2-2.

Fig. 2-3 compares the SFDR of the various links vs. normalized transmitted signal optical power (P_s) for the DFB laser considered. At signal power levels less than 1 mW, the SFDR of the DD link is dominated by receiver thermal noise, and its curve has a slope of $4/3$. Above 1 mW, shot noise and RIN become significant. In the RIN-limited regime, the DD link SFDR is independent of signal power. At low signal levels, the coherent AM link SFDR is dominated by LO shot noise (slope of $2/3$), and shows a marked advantage

over the DD link. At higher power levels, the coherent AM link has an intrinsic disadvantage with respect to the DD link due to the extra baseband RIN and shot noise encountered in a heterodyne receiver. At very low signal power levels (< -30 dBm), the SFDR of the PM and FM links is dominated by LO shot noise. However, above -30 dBm, phase noise is dominant and the SFDR is essentially independent of signal power level for both the PM and FM links.

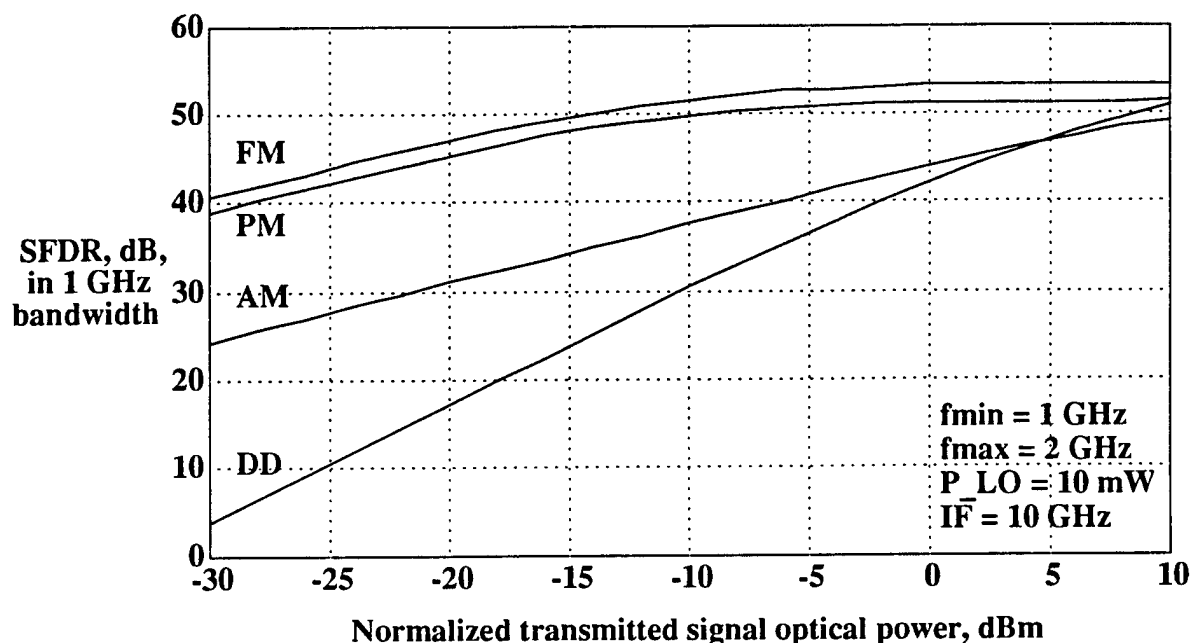


Figure 2-4. SFDRs of DD, AM, PM, and FM links plotted against received signal optical power for an Nd:YAG laser with parameters in Table 2-2.

In Fig. 2-4, SFDR is plotted vs. P_s for the Nd:YAG laser parameters in Table 2-2. At low signal power levels, the behavior of the DD and AM links is identical to that with the laser diode. However, at high power levels, the low RIN of the Nd:YAG laser results in a higher SFDR for both the AM and DD links. The PM and FM links exhibit substantial improvements in performance compared to the laser diode case, due almost entirely to the decreased phase noise of the Nd:YAG laser. The PM and FM links exhibit larger SFDRs than the DD link up to a signal power level of 10 dBm.

Fig. 2-5 shows a plot of SFDR vs. laser linewidth for the PM and FM links for P_s values of -30 dBm, -15 dBm, and 0 dBm. We have chosen the RIN level and the RIN roll-off frequency to be representative of the laser diode in Table 2-2. The signal and local oscillator lasers are both assumed to have linewidths equal to the linewidth value at each point on the plot. Due to the inherent immunity of PM and FM links to RIN, the curves

for the Nd:YAG RIN parameters will be nearly identical. At low received power levels, the linewidth has little impact, since the noise is dominated by thermal noise. At high received power levels, the impact of phase noise on the PM and FM links is severe, with the SFDR being reduced by 7 dB for every factor of 10 increase in the linewidth. At signal power levels of -30 dBm, -15 dBm, and 0 dBm, the phase noise becomes dominant over all other noises for linewidths of 5 MHz, 200 kHz, and 5 kHz, respectively.

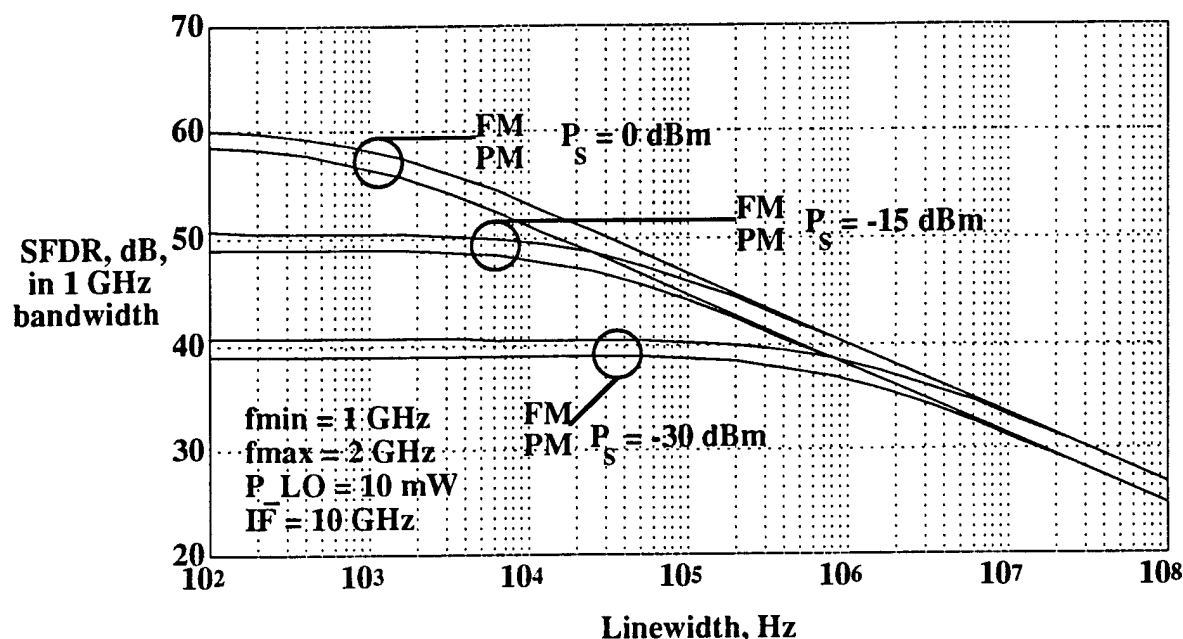


Figure 2-5. SFDRs of PM and FM links plotted versus linewidth for received signal power levels of 0 dBm, -15 dBm, and -30 dBm.

Fig. 2-6 shows the SFDR of the PM and FM links vs. the intermediate frequency (IF). The two sets of curves correspond to the two lasers considered (see Table 2-2). For a signal bandwidth of 1 GHz, increasing the IF from 5 GHz to 25 GHz increases the SFDR by approximately 10 dB for all four cases shown. The increase in SFDR is due to two causes: (1) the improved linearity of the frequency discriminator (which is utilized in both the PM and FM links), and (2) the reduced RIN at frequencies above the RIN roll-off frequency (see Appendix B). The reduction in RIN due to roll-off plays a much more significant role in links using single-photodetector receivers than in links using balanced receivers; for the cases shown, essentially all of the improvement in SFDR is due to the improved discriminator linearity. In these calculations, we have again assumed that the receiver thermal noise PSD is independent of the IF, as explained at the beginning of this section.

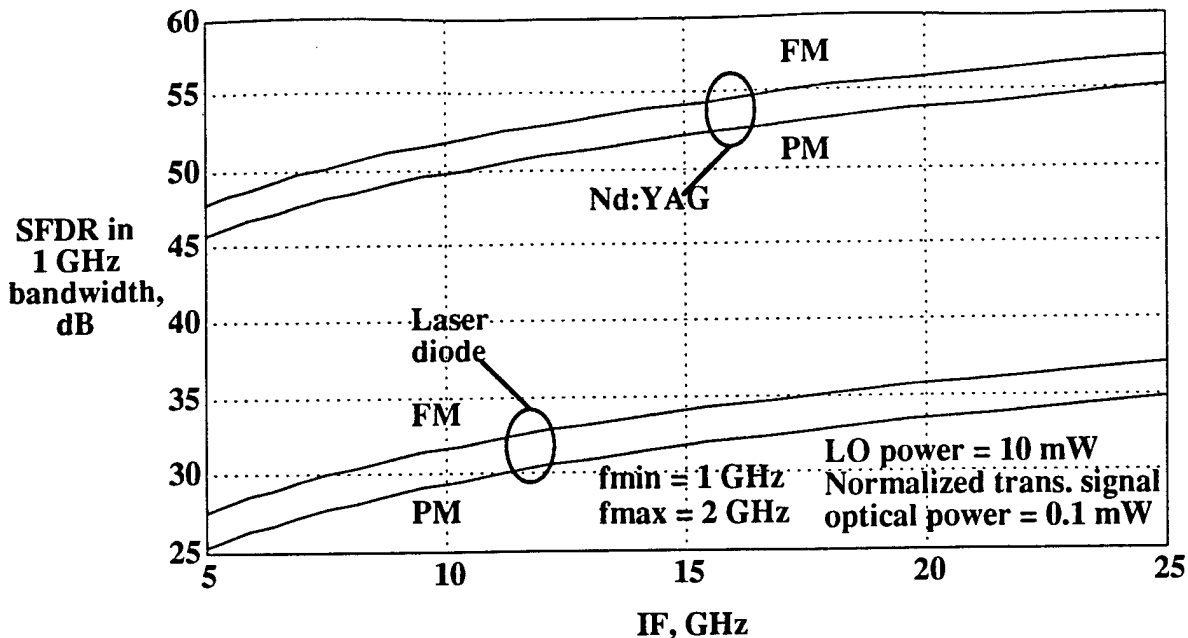


Figure 2-6. SFDRs of PM and FM links plotted versus IF for the two different sets of laser parameters. The received signal optical power is set at 0.1 mW.

At low received signal power levels ($P_s < 100$ mW), coherent links exhibit notable SFDR advantages over direct-detection links. This is expected because the local oscillator "pulls" the detected signal up to higher levels, and thus allows operation in the shot noise limit for LO power levels in the milliwatt range or higher.

For PM and FM links at low power levels, the shot and thermal noise dominate phase noise effects and the PM and FM links exhibit superior performance to AM and DD links. For laser linewidths of 10 MHz, the phase noise dominates link performance for $P_s > -30$ dBm. For laser linewidths of 5 kHz, the phase noise dominates link performance for $P_s > 0$ dBm. Figs. 2-3 to 2-5 show that, for the performance of the PM and FM links to exceed that of a DD link at a received power level of 0 dBm, the combined linewidth of the signal and LO lasers must be < 100 kHz. In the PM and FM links, a balanced receiver suppresses the self-homodyne RIN terms, as is the case in AM links. However, because there is no signal information in the envelope of PM and FM signals, these systems can use a limiter to suppress heterodyne RIN, and PM and FM links can thus be made completely insensitive to RIN.

2.3 Reference Transport Links

As seen in Section 2.2, laser phase noise is the primary factor limiting the SFDR of coherent angle-modulated analog links, particularly those using semiconductor lasers. Techniques to reduce or eliminate the impact of phase noise are, as a result, of great interest for these links. Reference transport techniques for phase noise cancellation (PNC) modulate only part of the source laser power while transporting the remainder to the receiver. That power is used as a reference to cancel the phase noise of the transmitter. Such systems can be realized in a variety of ways which may bear little resemblance to each other.

In basic reference transport systems, the power from the source laser is split before modulation. The light in one of these arms is modulated with the signal, while the light on the second arm is sent to the receiver through an auxiliary path and used as the local oscillator (Fig. 2-7). An auxiliary path can be realized in a variety of ways, including a separate fiber or an orthogonal polarization in a single fiber [4]. The optical portion of this system is essentially an interferometer. In order to obtain the desired performance, the phase of the optical carrier in the reference arm must be related to that in the signal arm. This means that the optical lengths of the two arms must be matched to within a fraction of the coherence length of the source laser; for laser diodes with linewidths on the order of 100 MHz, this requires matching path lengths to within less than 1 m. Note that this kind of approach cannot be used for coherent links, since the phase noise of the local oscillator (LO) laser cannot be canceled.

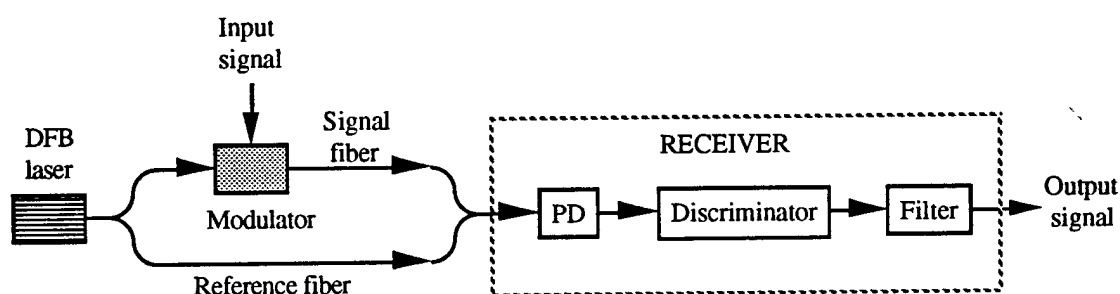


Figure 2-7. A basic reference transport system employing an additional fiber to deliver the local oscillator signal to the receiver.

A more sophisticated reference transport system [5] is shown in Fig. 2-8. It has no auxiliary path and a second laser can be used as the LO. The operation of this system depends on the presence of a strong unmodulated carrier term embedded in the received signal spectrum. In the receiver, the unmodulated carrier is separated from the modulated

signal spectrum and used as a reference, allowing cancellation of phase noise. This technique is applicable when there is appreciable power in the carrier and when the signal sidebands are well separated from the carrier.

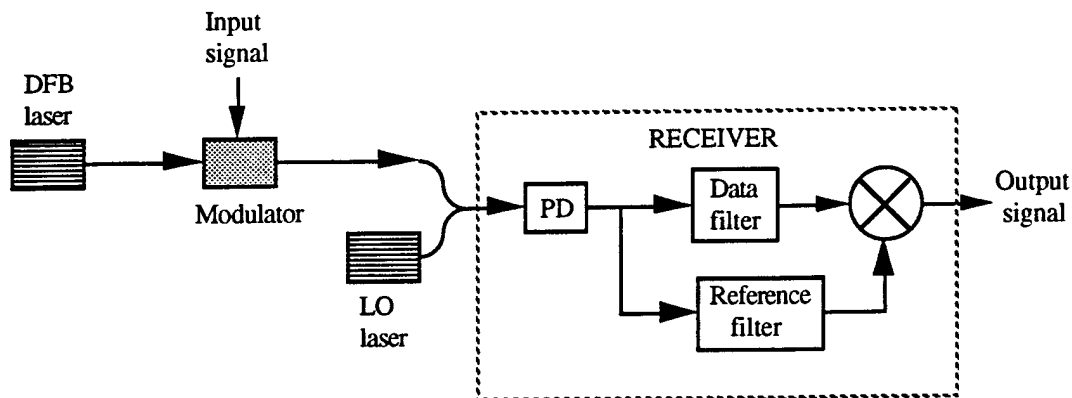


Figure 2-8. Reference transport system utilizing an unmodulated carrier as a reference.

Reference transport links like that of Fig. 2-8 have been used successfully in narrowband phase-modulated analog links [5]. This is because the small modulation index ($\ll 1$) of narrowband phase-modulated signals allows the signal to be expanded as so:

$$\begin{aligned} \cos(\omega t + \phi[x(t)]) &= \cos(\omega t)\cos(\phi[x(t)]) - \sin(\omega t)\sin(\phi[x(t)]) \\ &\approx \cos(\omega t) - \left(\phi[x(t)] - \frac{(\phi[x(t)])^3}{3!} + \dots \right) \sin(\omega t) \end{aligned} \quad (2.17)$$

Eq. (2.17) shows that the signal sideband $\phi[x(t)]\sin(\omega t)$, which is an AM signal, can be filtered out and demodulated just as in the heterodyne AM-WIRNA link. In this case, the signal will be distorted by third-order intermodulation distortion (IMD) products of exactly the same form as in AM-WIRNA. The SFDR performance and bandwidth requirements of narrowband angle-modulated links, as a result, are identical to those of AM-WIRNA.

It is well-known that a modulation index of at least 1 is required for angle-modulated links to show a significant SNR improvement over AM links. To detect the resulting wideband signal, a delay-line discriminator which mixes the signal and a delayed version of itself is required. This discriminator behaves differently from a heterodyne AM demodulator. During this project we have investigated the feasibility of reference transport for wideband angle-modulated links.

2.4 Reference Transport in Analog Links

2.4.1 Why Conventional Approaches Fail

Fig. 2-8 shows a possible receiver configuration for PNC in a coherent link using wideband angle modulation. Assuming that the modulation format is FM, the signal entering the discriminator, omitting white noise terms, is proportional to $\cos\left(\omega t + \omega_\Delta \int x(t') dt' + \Delta v(t)\right)$. This can be written in the form

$$\cos\left(\omega t + \int \left(\omega_\Delta x(t') + \frac{d}{dt'} \Delta v(t')\right) dt'\right) \quad (2.18)$$

The results of Appendix 2.B indicate that the derivative of the laser phase noise process is white noise. As a result, laser phase noise in links using direct FM is equivalent to white noise in the original applied RF signal; this noise is clearly not removable using electronic processing at the receiver.

The above statement is validated by the following brief discussion of the residual carrier approach of Fig. 2-8. Fig. 2-9 shows the frequency spectrum of an FM signal corrupted by phase noise.

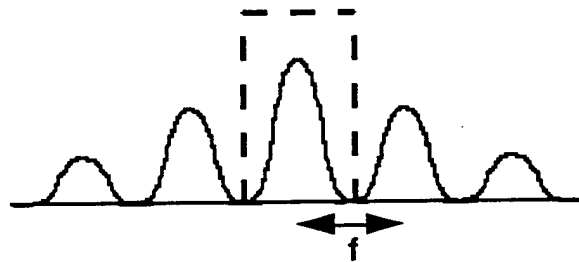


Figure 2-9. Frequency spectrum of an FM signal corrupted by phase noise.

The dashed lines show the frequency response of an idealized reference filter. After the filtered carrier component is mixed with the corrupted FM signal, an FM signal is recovered which is corrupted only by the tails of the phase noise which lay outside the reference filter bandwidth. After detection, the power spectrum of the detected signal is then corrupted by $S_\phi(\omega)S_{HPF}(\omega)S_D(\omega)$, where $S_\phi(\omega)$ and $S_D(\omega)$ are the power spectra of the phase noise and the discriminator, respectively. $S_{HPF}(\omega)$ is ideally equal to 0 from DC to a frequency equal to half the width of the reference filter and 1 for all other

frequencies. Since the derivative of the laser phase noise process is white noise, the detected signal is corrupted by white noise with a "hole" at DC. It is impossible for this hole to extend to the signal frequency band unless the reference filter is of width greater than twice the maximum signal frequency; the detected signal will then be severely distorted, since the reference filter will then pass frequency components other than the carrier.

The above argument can also be used to show that the residual carrier PNC receiver of Fig. 2-8 will not work for a coherent PM link. The FM photocurrent for these links is of an identical form to Eq. (2.18), and hence the residual carrier method of Section 2.3 will not work. The PM photocurrent is of the form $\cos(\omega t + \phi_{\Delta} x(t) + \Delta v(t))$. Though this looks slightly different from Eq. (2.18), the laser phase noise in links using external PM is equivalent to noise in the original applied RF signal with power spectral density given in Eq. 2.B-12 of Appendix 2.B. As a result, the arguments of section 2.4.1 again apply.

It is certainly possible to cancel phase noise in externally modulated links by using a two-fiber approach such as that in Fig. 2-7. The problem with this method is that since there is no LO laser, the detected photocurrent is at baseband. This is acceptable for digital systems using phase-shift-keying (PSK) [6]. Analog links using FM or PM, however, use discriminators which must operate at an IF frequency much larger than the maximum signal frequency. Any reference transport approach which will succeed for analog angle-modulated links, therefore, must generate an angle-modulated signal at an IF before demodulation without using an LO laser.

2.4.2 Our Novel Approach: Linewidth-Insensitive Interferometric Links

The name "interferometric links" refers to the novel class of reference transport links which (a) cancel phase noise by splitting power from the transmitter laser and transporting this reference with the optical signal to the receiver, in a single fiber or in separate fibers; and (b) generate an angle-modulated signal at an IF before demodulation without using an LO laser. A heterodyne interferometric link is shown in Fig. 2-10. In this link, references separated from the transmitter laser frequency by the desired IF are generated using optical single-sideband frequency shifting or sideband generation. The received photocurrent is then at the desired IF, and demodulation can take place immediately after IF amplification.

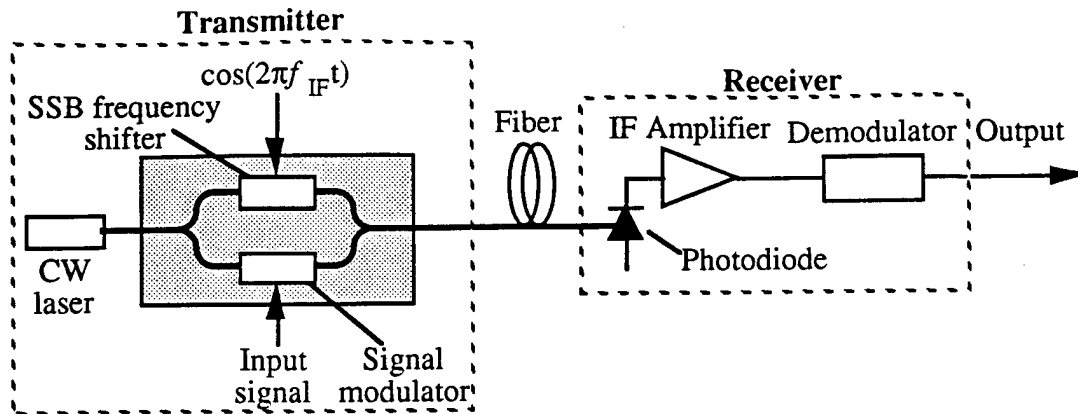


Figure 2-10. Heterodyne interferometric link using optical single-sideband frequency shifter.

2.5 Optical Frequency Shifting in Heterodyne Interferometric Links

The ideal optical frequency shifter for use in a heterodyne interferometric link is lossless and transfers the input optical power fully to an optical frequency separated from the original frequency by the desired IF without generation of spurious components. In section 2.5.1, we briefly describe the state-of-the-art in true single-sideband (SSB) optical frequency shifters. In section 2.5.2, we present a novel electro-optic sideband generator which can generate the desired reference with relatively low loss for desired IFs well above 10 GHz.

2.5.1 Single-Sideband Optical Frequency Shifters

SSB optical frequency shifting for interferometric links can be performed using acousto-optic or magneto-optic modulation of the reference. In both cases, acoustic or magnetic waves are propagated in a material which will generate the desired phase grating, which has maxima spaced by a distance corresponding to the desired IF frequency. After passing through the material, the input reference field is split into several diffraction orders, each separated from the input reference by some multiple of the IF. The nice feature of these approaches is that true single-sideband frequency shifting by the IF occurs for the first diffraction order. The problems, however, are numerous. There is tremendous loss of more than 20 dB due to the low conversion efficiency of the first diffracted order of the grating. It is very difficult to integrate such an optical frequency shifter into a rugged, compact form, and there will be significant additional loss due to coupling of the first diffracted order into a fiber. Though magneto-optic shifters have

been demonstrated which operate at above 10 GHz [7], acousto-optic shifters are limited to IFs of a few GHz by acoustic attenuation and transducer fabrication limitations [8].

2.5.2 A Novel Approach: Sideband Generation Using External Modulation

We present a novel electro-optic modulation technique which can be used in the reference leg to generate a phase-modulated signal which has significant components at the desired IF above and below the laser optical frequency. This method can generate an angle-modulated signal at an IF at the receiver with a small penalty relative to ideal SSB frequency shifting and is well-suited to monolithic integration with other electro-optic devices. We refer to it as quasi-SSB frequency shifting. The signal modulator could be any sort of external modulator, but it is only sensible to use external PM or FM.

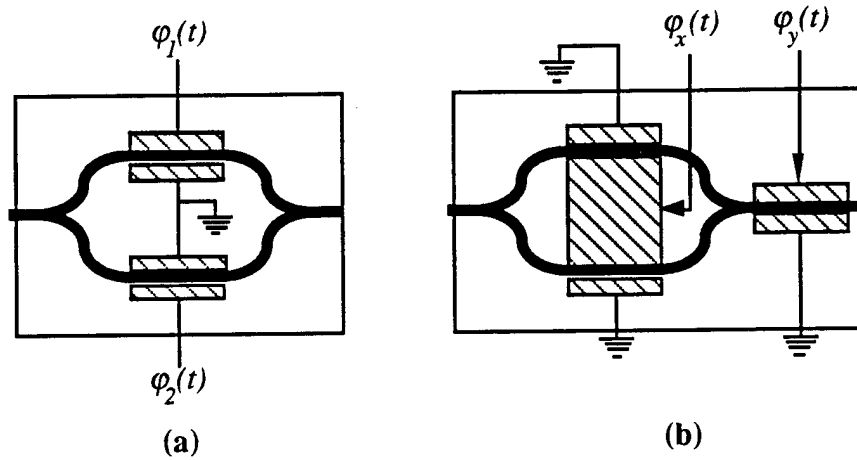


Fig. 2-11. Two implementations of an electro-optic quasi-SSB frequency shifter.

Fig. 2-11 shows two functionally identical implementations of the quasi-SSB frequency shifter. In Fig. 2-11(a), the modulator legs are phase modulated by quadrature CW RF signals at the desired shifting frequency. The DC optical phase bias between the legs must be $\pi/2$, which is the same bias required in a typical MZ amplitude modulator. In Fig. 2-11(b), the frequency shifter is implemented using a MZ amplitude modulator followed by a phase modulator (the order of the two sections is irrelevant). For $\phi_1(t) = \beta \cos(\omega_{IF}t) + \frac{\phi_b}{2}$ and $\phi_2(t) = \beta \sin(\omega_{IF}t) - \frac{\phi_b}{2}$, the output field phasor for a bias phase of $\pi/2$ is easily shown to be

$$E_{out}(t) = E_{in}(t)J_1(\beta)\exp(i\omega_{IF}t) + \frac{E_{in}(t)}{\sqrt{2}}[J_0(\beta) + J_2(\beta)\cos(2\omega_{IF}t) + \dots] \quad (2.19)$$

where $E_{in}(t)$ is the input optical field phasor. The first term is the desired SSB frequency-shifted optical field, while the other terms are the unshifted carrier and higher-order terms. If ω_{IF} is much larger than the modulating signal bandwidth (which must be the case in any angle-modulated analog system), the undesired cross terms between the signal and the output of the frequency shifter can be filtered out in the post-detection electronics. The implementation in Fig. 2-11(b), which is used in the experiment in Section 2.7, is equivalent to that in Fig. 2-11(a) for $\varphi_x(t) = \frac{1}{2}(\varphi_1(t) - \varphi_2(t))$ and $\varphi_y(t) = \frac{1}{2}(\varphi_1(t) + \varphi_2(t))$.

2.6 Heterodyne Interferometric Phase-Modulated Link: Theory

In this section, we present the heterodyne interferometric link using phase modulation (HIPM). We give its SNR and SFDR. We then briefly discuss implementation details for this type of link and compare its performance to AM direct detection and coherent angle-modulated links.

2.6.1 Link Description

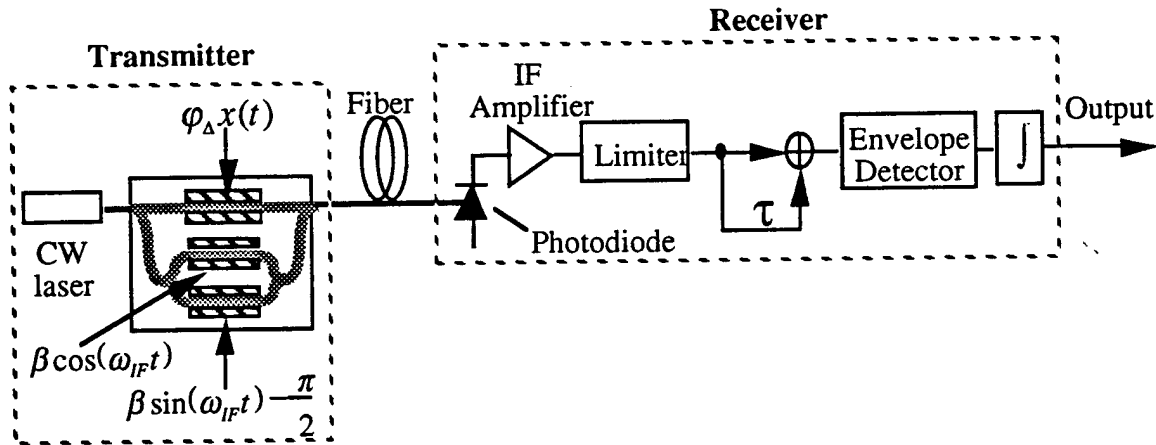


Fig. 2-12. Phase-modulated implementation of IAOL with novel electro-optic modulator.

The proposed link is shown in Fig. 2-12. The transmitter consists of a CW laser and a novel three-leg modulator. The modulator is an integrated version of the electro-optic sideband generator of section 2.5.2, with one leg driven by the signal and the other two legs driven by quadrature CW RF signals at a frequency ω_{IF} and optically phase

shifted by $p/2$ from each other. After traversing a fiber-optic link, the signal is detected at the receiver. The optical signals of the second and third legs of the modulator mix with the signal at the detector and result in a series of single-sideband signals at multiples of ω_{IF} . Following IF amplification and filtering, the signal is limited. It is then put through a delay-line filter, an envelope detector, and an integrator; these three components function in tandem as a phase demodulator. We refer to the entire system as an HIPM link. An HIFM link has only one difference, which is that the integrator precedes the signal leg of the phase modulator rather than following the envelope detector.

2.6.2 Spurious-free Dynamic Range (SFDR)

To derive the SFDR of the HIPM link, it is first necessary to derive expressions for the link SNRs and nonlinearity coefficients. Both of these are easily obtainable from the link output current. After that, the SFDR can be simply obtained from Eq. (2.15).

The optical fields contributed by the three arms of the modulator are given at the detector by

$$e_1(t) = \sqrt{\varepsilon_1 P [1 + n_R(t)]} \exp i [\omega_o t + \varphi[x(t)] + \varphi_p(t)] \quad (2.20)$$

$$e_2(t) = \sqrt{\varepsilon_2 P [1 + n_R(t)]} \exp i \left[\omega_o t + \beta_s \sin \omega_{IF} t - \frac{\pi}{2} + \varphi_p(t) \right] \quad (2.21)$$

$$e_3(t) = \sqrt{\varepsilon_3 P [1 + n_R(t)]} \exp i [\omega_o t + \beta_c \cos \omega_{IF} t + \varphi_p(t)] \quad (2.22)$$

where $x(t)$ is the normalized input signal, $\varphi[]$ refers to the type of modulation (could be either phase or frequency, in general), ω_{IF} is the angular intermediate frequency (IF), β_c and β_s are the phase deviations of the IF terms, ε_1 , ε_2 , and ε_3 are the splitting coefficients within the modulator, P is the laser optical power with link and modulator excess losses assumed compensated by amplification in the link, $n_R(t)$ is the laser RIN, and $\varphi_p(t)$ is the laser phase noise. The delays through the arms of the modulator are assumed to be matched.

The current generated at the photodiode, $i_1(t)$, is given by

$$\begin{aligned}
i_1(t) = & RP[1 + n_R(t)] \{ 4\sqrt{\varepsilon_1 \varepsilon_2} J_1(\beta_s) \sin[\omega_{IF}t + \varphi[x(t)]] \\
& + 4(\sqrt{\varepsilon_1 \varepsilon_3} J_1(\beta_c) - \sqrt{\varepsilon_1 \varepsilon_2} J_1(\beta_s)) \sin[\varphi[x(t)]] \cos \omega_{IF}t \\
& + 4\sqrt{\varepsilon_2 \varepsilon_3} \{ [-J_0(\beta_s)J_1(\beta_c) + J_2(\beta_s)J_3(\beta_c) - \dots] \cos \omega_{IF}t \\
& \quad + [J_0(\beta_c)J_1(\beta_s) + J_2(\beta_c)J_3(\beta_s) - \dots] \sin \omega_{IF}t \} \\
& + D.C. \text{ terms} + 2\omega_{IF}t \text{ terms} + 3\omega_{IF}t \text{ terms} + \dots \} + n_D(t) + An_R(t)
\end{aligned} \tag{2.23}$$

where R is the photodetector responsivity, $n_D(t)$ is the contribution from the receiver thermal noise and the shot noise, and A is the coefficient of the DC RIN. The phase noise is eliminated due to the equal optical path lengths through the three legs of the modulator. The first term is the desired phase-modulated term at the IF. The second term can be eliminated by choosing $\varepsilon_1 = \varepsilon_2 = \varepsilon_3 = 1/3$ and $\beta_s = \beta_c = \beta$. The third term can be eliminated by choosing $\beta = 1.8$. This creates only a 0.35 dB penalty from the maximum value of $J_1(\beta)$, which occurs at $\beta \approx 2.2$. If the maximum signal frequency is much smaller than the IF, the signal bands around ω_{IF} , $2\omega_{IF}$, $3\omega_{IF}$, ... are well separated and we can filter out all terms not around ω_{IF} . The current after the limiter is given by

$$i_2(t) = \frac{4}{9} RP J_1(\beta) \sin[2\pi f_{IF}t + \varphi[x(t)] + \varphi_n(t)] \tag{2.24}$$

where K is the amplitude of $i_2(t)$. The limiter suppresses all variations in the envelope of the signal, resulting in suppression of the RIN term in the signal amplitude. To avoid threshold effects in the limiter, the carrier-to-noise ratio (CNR) before the limiter must be at least 12 dB. The noise contribution to the phase is given by

$$\varphi_n(t) = \frac{9}{4RPJ_1(\beta)} \left[n_{Dq}(t) + \frac{RP}{3} \left(1 + \frac{2}{3} J_0(\beta) \right) n_{Rq}(t) \right] \tag{2.25}$$

where $n_{Dq}(t)$ and $n_{Rq}(t)$ are the quadrature components within the IF band of $n_D(t)$ and $n_R(t)$, respectively. Applying the identical discriminator analysis as in Appendix 2.B gives an output current for the HIPM link of the form

$$i_{HIPM \text{ out}}(t) = K \left\{ -\frac{1}{4f_{IF}} [\varphi_\Delta x(t) + \varphi_n(t)] + \frac{1}{6} \left(\frac{1}{4f_{IF}} \right)^3 \left[\varphi_\Delta \ddot{x}(t) - i \frac{3}{2} \varphi_\Delta^2 \dot{x}^2(t) - \varphi_\Delta^3 \int \dot{x}^3(t) dt \right] \right\} \tag{2.26}$$

The SNR can then be written in the simple form

$$SNR_{HIPM} = \varphi_{\Delta}^2 \left[\left(\frac{4RPJ_1(\beta)}{9} \right)^2 \frac{\langle x^2(t) \rangle}{\langle n_{shot\ bp}^2 \rangle + \langle n_{thermal\ bp}^2 \rangle + \left(\frac{RP}{3} \right)^2 \left(1 + \frac{2}{3} J_0(\beta) \right)^2 \langle n_{RIN\ bp}^2 \rangle} \right] \quad (2.27)$$

where the noise expressions are evaluated in Appendix 2.A. Then the SFDR of both links can be expressed by

$$SFDR = \left[\frac{8SNR_o}{3|b_3|} \right]^{2/3} \quad (2.28)$$

where SNR_o is defined as the term in square brackets in Eq. (2.27) and $|b_3|$, the third-order nonlinearity coefficient, is $\frac{1}{6} \left(\frac{\pi f_{max}}{2f_{IF}} \right)^2$ for the HIPM link. These terms are identical to those derived for the coherent PM and FM links in Section 2.2, where the details of that derivation are contained. The noise terms in the denominators are defined in Appendix 2.A.

2.6.3 Implementation Considerations

In this section, we briefly consider some implementation details of heterodyne interferometric links. For simplicity, details will be listed and addressed in order.

Maximum available external modulation depth and RF loss: For the low received powers ($< 100 \mu W$) at which coherent links are frequently operated, thermal noise is the dominant noise at the receiver. Since the thermal noise power is independent of the transmitted optical power while the IMD power is clearly dependent on optical power, the optimum modulation depth (corresponding to the SFDR) increases with decreasing optical power. Under these conditions, it is important to know the modulation depth limitations of devices which will be used to generate externally modulated PM and FM signals.

From our experience in our laboratory, phase modulators can normally be comfortably operated for voltages up to 1.5 times V_π . This means that the maximum available modulation depth is about 4.71 (or 1.5π) for an applied signal normalized to lie between 1 and -1. This modulation depth is not exceeded for any point in the plots of this chapter.

External frequency modulation requires an integrator followed by an external phase modulator. For an integrator which can be modeled by a single-pole lowpass filter, there will be a significant power loss since the rolloff of the lowpass filter will be inversely proportional to ω for $\omega R_{\text{int}} C_{\text{int}} \gg 1$. It is clear that the FM modulation index $\frac{\omega_\Delta}{\omega_{\text{max}}} = \frac{\pi V}{V_\pi \omega_{\text{max}} R_{\text{int}} C_{\text{int}}}$ from section xxx, and hence that to attain the maximum available modulation depth of 4.71, RF amplification must be applied after integration to compensate for the power loss. A sufficiently linear region in the integrator characteristic must be chosen such that link operation is satisfactory, but this may reduce the available modulation depth depending on the available RF amplification. With careful construction, an integrator can be built which will have a highly linear region which is not also high loss.

Choice of IF frequency: It is possible using commercially available components to build modulators and receivers which operate for frequencies in the 10 GHz to 20 GHz range. The benefits of a high IF are more linear discriminator operation and greater RIN suppression. The disadvantages of a high IF are larger discriminator loss, higher thermal noise, and greater receiver cost and complexity.

Modulator splitting coefficients: It is important that the spurious IF terms be eliminated through the appropriate choice of β , amplitude of the applied IF sinusoids. It is possible to determine a β for which the signal loss is insignificant provided that the loss in the two arms of the modulator corresponding to the IF sinusoids are nearly equal. This condition holds in regular Mach-Zehnder amplitude modulators and should not be difficult to achieve in a three-legged integrated device. Note that the splitting loss in the signal arm need not be the same as the loss in the two IF arms.

Bias phase: There can be an arbitrary bias phase between the signal arm and the IF arms in the modulator. This bias phase is slowly varying relative to the signal and will not impact discriminator operation.

Quadrature of IF sinusoids: If the RF sinusoids are off of quadrature by an angle θ , the ratio of signal to distortion due to this goes as $\cot^2 \theta$. For a θ of 1 degree, this gives a signal to distortion ratio of 35 dB. Given that the wavelength of a 10 GHz signal is 3 cm, it is easily possible using delay lines in integrated form to achieve a θ of far less than one degree, if necessary. Including these delay lines in the modulator will not significantly increase its complexity or its size.

2.6.4 SFDR Results for HIPM Link

In Fig. 2-13, the SFDR versus laser linewidth of the HIPM link, the coherent PM link, and the AM direct detection link are compared. For an IF of 10 GHz, the increased losses associated with the HIPM modulator are compensated for by the increased linearity of its discriminator, giving an SFDR equal to that of the AM direct detection link. For higher values of the IF, the HIPM link will begin to outperform the direct detection link for the 1 mW laser power chosen. The coherent PM link outperforms the HIPM and AM direct detection links for linewidths lower than about 200 kHz. This linewidth is much larger than that of solid-state lasers but is lower than those of presently available semiconductor lasers.

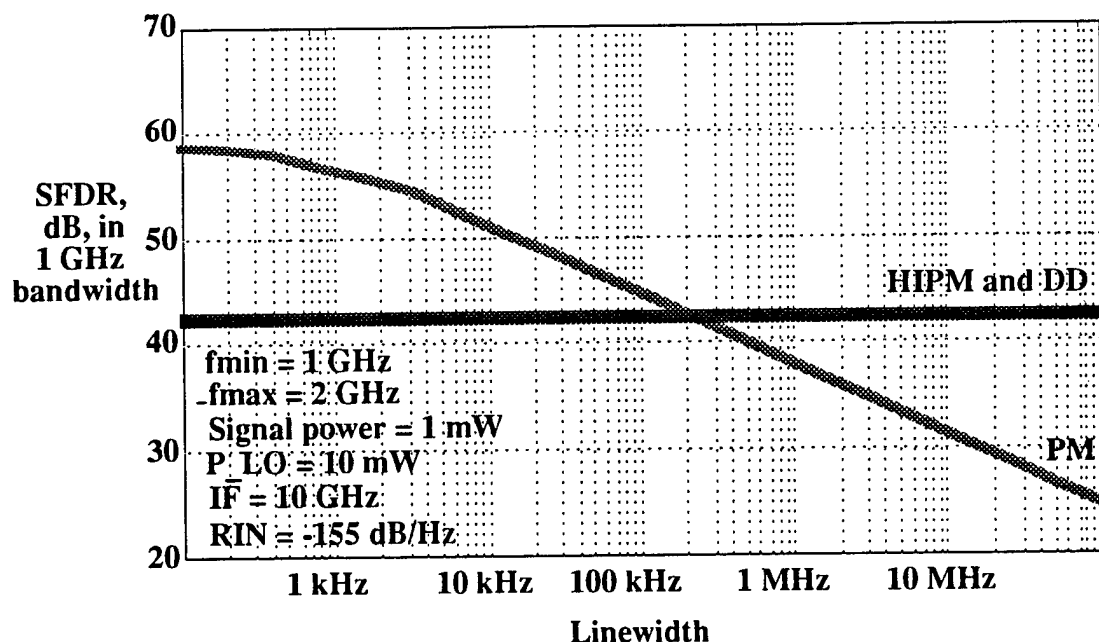


Figure 2-13. SFDRs of HIPM, coherent PM, and AM direct detection links plotted versus laser linewidth for a representative laser power of 1 mW.

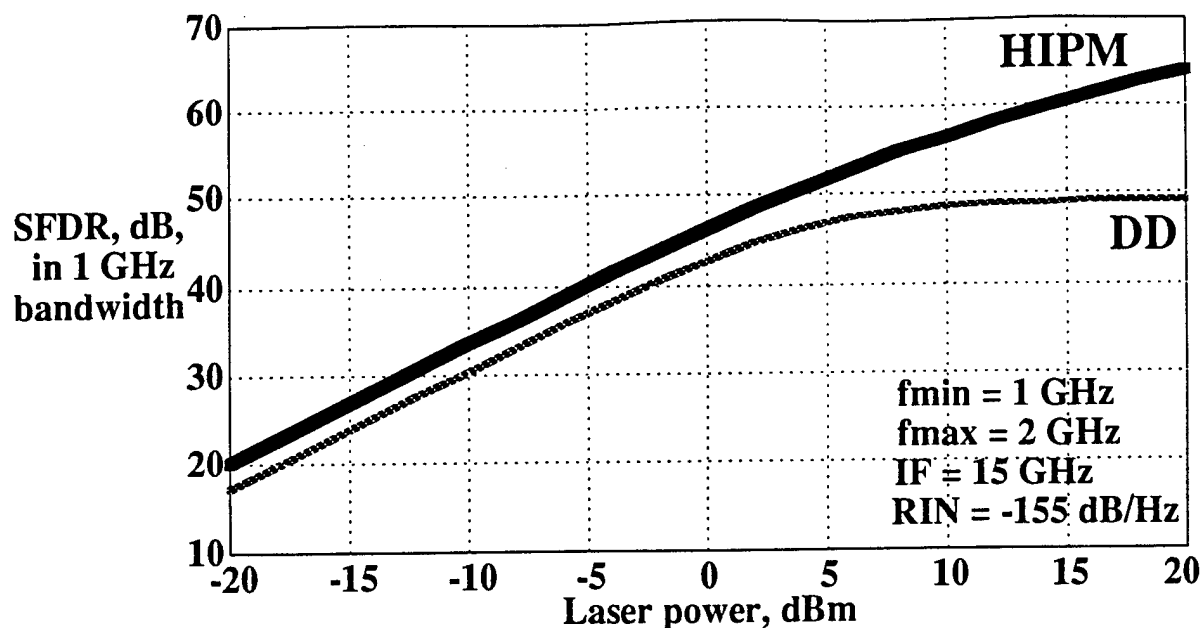


Figure 2-14. SFDRs of HIPM and AM direct detection links plotted versus laser power for an intermediate frequency of 15 GHz.

In Fig. 2-14, the SFDR versus laser power of the HIPM link is compared to that of the AM direct detection link. The HIPM link can potentially outperform the AM direct detection link over the entire range of laser powers shown. For low laser powers, the better linearity of the HIPM link gives it a 3 dB SFDR advantage. For high laser powers above 1 mW, the HIPM link begins to significantly outperform the AM direct detection link due to the suppression of laser RIN at high IFs. For a laser output power of 40 mW and assuming sufficient amplification in the link to balance the link loss, the SFDR improvement of the HIPM link over the AM direct detection link is 10 dB (though there may be a degradation of a few dB due to amplified spontaneous emission). This output power assumption is realistic and has been greatly exceeded in research devices [9, 10]. As a result, the HIPM link is potentially useful if future high-power semiconductor lasers are used.

2.7 Heterodyne Interferometric Phase-Modulated Link: Experiment

This section presents preliminary results from the proof-of-concept experimental HIPM link which we have constructed in our laboratory [11]. Fig. 2-15 shows a simplified block diagram of the experimental link. The optical source consists of a CW Nd:YAG laser followed by an optical attenuator. The three-leg HIPM modulator is implemented using combination amplitude/phase modulators with 1 GHz 3 dB

bandwidths which were available in our laboratory. The two sections of modulator 1 are driven with sinusoidal IF signals (at 650 MHz, in this implementation) in quadrature; modulator 2 is driven by the signal to be transmitted. The AM section of modulator 1 was biased where MZ modulators are typically biased, at $V\pi/2$ below the maximum transmission point. After detection, the electrical signal is amplified, bandpass filtered, and sent through a phase discriminator. The discriminator consists of an RF power splitter, two delay lines of different length, a mixer, and an integrator (single pole lowpass filter). The length difference between the two delay lines was set to one quarter of the IF RF wavelength.

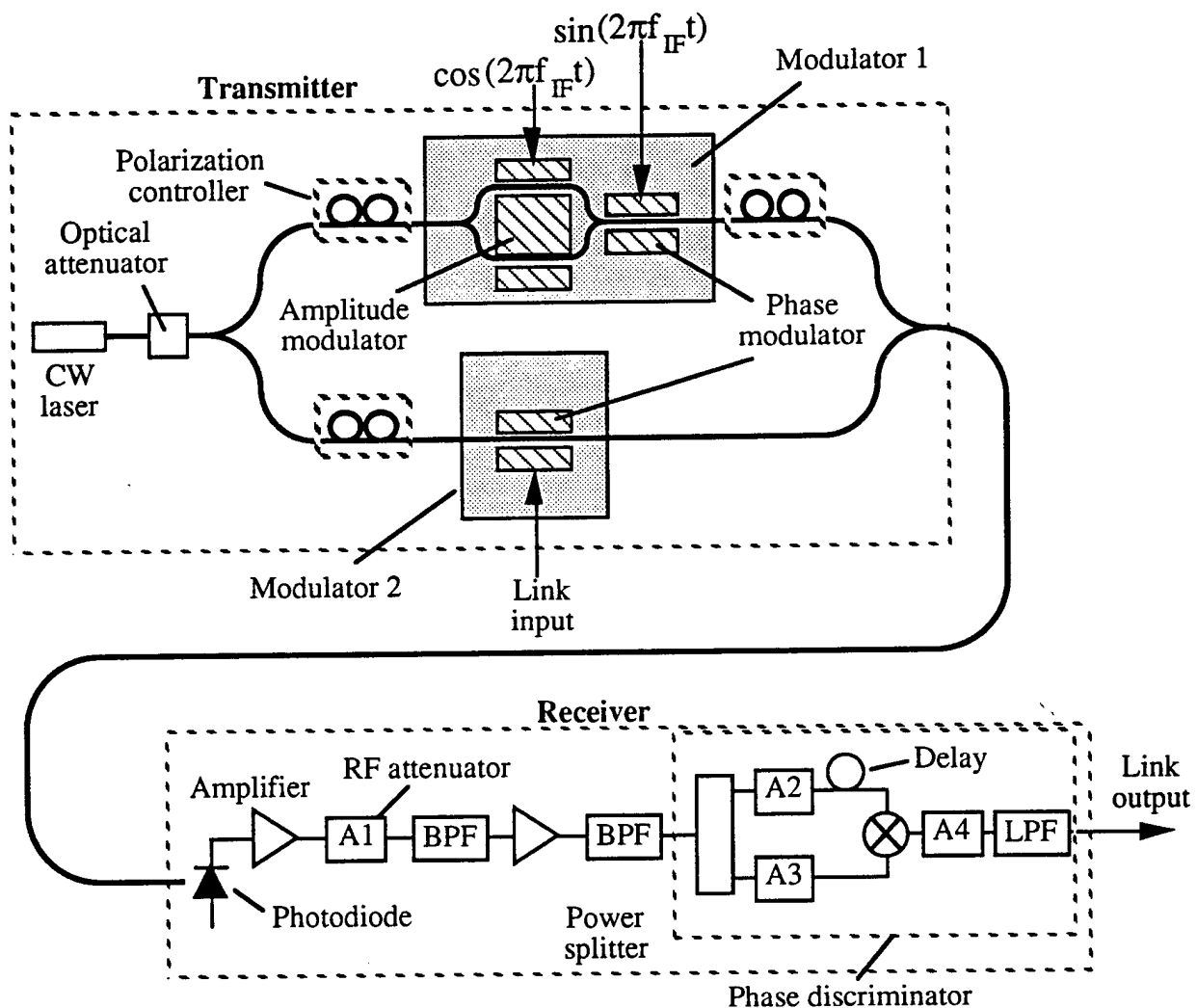


Fig. 2-15. Block diagram of experimental phase-modulated IAOL.

For an applied signal made up of sinusoids with frequencies f_{min} and f_{max} , we measured the two-tone third-order IMP levels at frequencies $2f_{min} - f_{max}$ and $2f_{max} - f_{min}$ at

the link output using an RF spectrum analyzer. The theoretical ratios of the IMP power levels, $\langle i_{IMP}^2 \rangle$, to the signal power levels, $\langle i_s^2 \rangle$, for the AM direct detection link and the HIPM link are given by

$$\left[\frac{\langle i_{IMP}^2 \rangle}{\langle i_s^2 \rangle} \right]_{AM} = \frac{\varphi_{\Delta}^4}{64} \quad (2.29)$$

$$\left[\frac{\langle i_{IMP}^2 \rangle}{\langle i_s^2 \rangle} \right]_{HIPM} = \left(\frac{2\pi f_{max}}{4f_{IF}} \right)^4 \frac{\varphi_{\Delta}^4}{64} \quad (2.30)$$

where φ_{Δ} is the modulation depth. These equations come directly from the results in Section 2.2.3. The AM direct detection link IMP measurements were made by removing modulator 1, modulating the AM port of modulator 2, and measuring the IMP levels after detection.

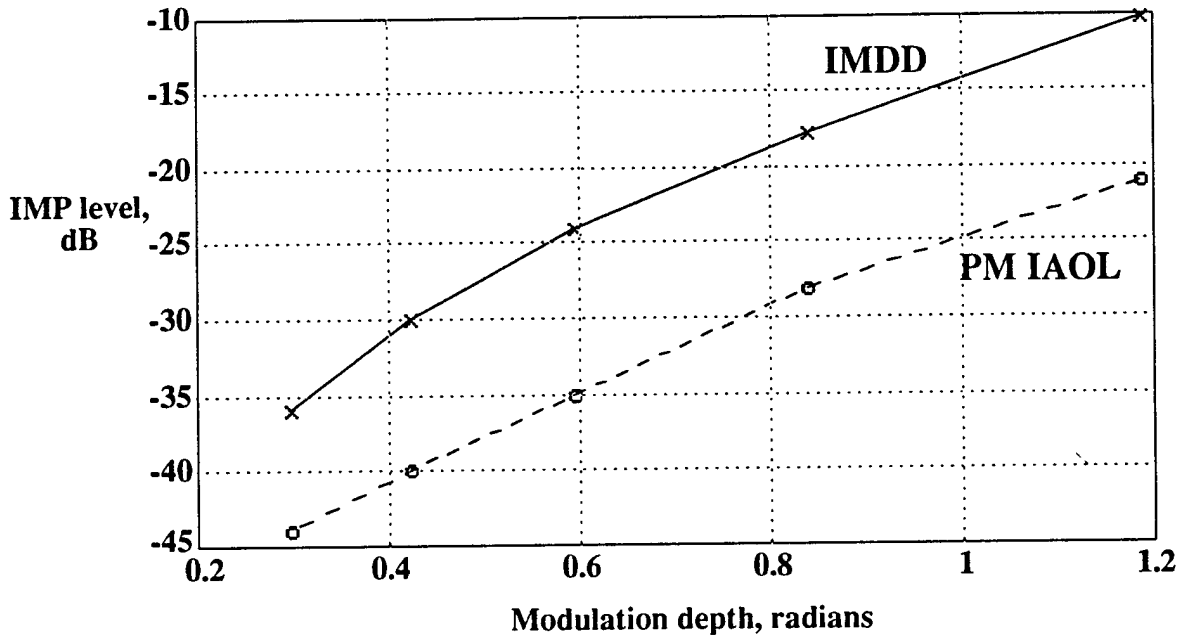


Fig. 2-16. Intermodulation product level vs. modulation depth for PM IAOL (o) and IMDD (x) links; $f_{min} = 95$ MHz and $f_{max} = 105$ MHz.

Fig. 2-16 compares the measured ratios of third-order IMP levels to signal levels vs. modulation depth of modulator 2 in radians of the HIPM and AM direct detection links. The two applied tones have frequencies $f_{min} = 95$ MHz and $f_{max} = 105$ MHz. Our HIPM link demonstrated IMP levels that are consistently lower than those of an

externally modulated AM direct detection link for the same modulation depths. The corresponding SFDR improvement in dB equals one-third of the IMP suppression in dB (see Eqs. (2.13)-(2.15)).

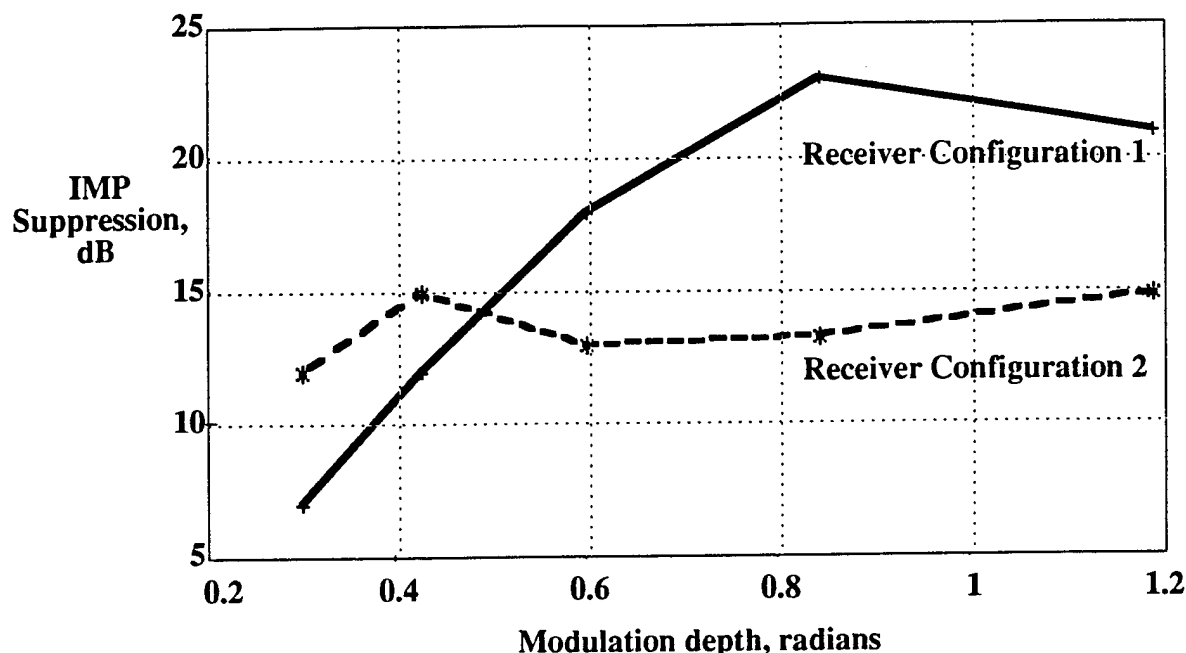


Fig. 2-17. Intermodulation distortion suppression of the PM IAOL link over an IMDD link for receiver configuration 1 ($A_1 = 6$ dB, $A_2 = 3$ dB, $A_3 = 6$ dB, $A_4 = 6$ dB) and receiver configuration 2 ($A_1 = 10$ dB, $A_2 = 0$ dB, $A_3 = 6$ dB, $A_4 = 6$ dB). $f_{min} = 47.5$ MHz and $f_{max} = 52.5$ MHz.

We investigated nonideal receiver component characteristics, such as amplifier, mixer, and discriminator nonlinearities, by altering the values of the RF attenuators in the receiver ($A_1 - A_4$), shown in Fig. 2-15. Fig. 2-17 shows the ratio of the HIPM link IMP levels to the AM direct detection link IMP levels vs. of modulation depth for two receiver configurations. For this case, $f_{min} = 47.5$ MHz and $f_{max} = 52.5$ MHz. Configuration 1 corresponds to $A_1 = 6$ dB, $A_2 = 3$ dB, $A_3 = 6$ dB, and $A_4 = 6$ dB. Configuration 2 corresponds to $A_1 = 10$ dB, $A_2 = 0$ dB, $A_3 = 6$ dB, and $A_4 = 6$ dB. The HIPM link demonstrates as much as 23 dB IMP suppression, which corresponds to 7.7 dB SFDR improvement. However, the HIPM link third-order nonlinear coefficient $(2\pi f_s / 4f_{IF})^4$ gives a theoretical two-tone third-order IMP suppression of 44 dB. Clearly, the link performance is limited by nonideal receiver component characteristics, and not by the intrinsic link nonlinearity predicted using Eq. (2.30). Fig. 2-17 shows that the IMP levels at various modulation depths can be varied over a large range by changing the position and value of RF attenuators in the receiver. This effect cannot be explained

by considering ideal receiver component characteristics, but can be caused by a number of nonideal factors including mixer nonlinearities, nonideal discriminator and filter characteristics, and amplifier nonlinearities.

Even though our receiver could be significantly improved through the use of better components, the best third-order IMP suppression that we demonstrated is comparable to that in optimized implementations of linearized IMDD links [12]. This result suggests that the HIPM link may be a promising alternative to conventional linearized AM direct detection links for achieving high SFDR.

2.8 Conclusions

We have analyzed the performance of coherent analog links employing phase modulation (PM) and frequency modulation (FM). We have also compared their spurious-free dynamic range (SFDR) to that of intensity modulated direct-detection (DD) links and coherent AM links. Coherent angle-modulated analog fiber-optic links can offer increased SFDR as compared to DD and coherent AM links, particularly at low signal levels, where coherent systems can operate in the shot noise-limited regime while DD links are thermal noise-limited.

Coherent angle modulated systems, comprising both phase and frequency-modulated links, are intrinsically sensitive to phase noise because their signal information is contained in the optical phase. For a combined transmitter and local oscillator laser linewidth of 20 MHz, phase noise is the dominant noise in PM and FM links for normalized transmitted signal power levels above -30 dBm, and limits the SFDR to 30 dB and 31 dB in a 1 GHz bandwidth for PM and FM links, respectively. For a combined linewidth of 10 kHz, phase noise dominates the noise characteristics for normalized transmitted signal power levels above -5 dBm, and limits the SFDR to 51 dB and 53 dB in a 1 GHz bandwidth for PM and FM links, respectively. Angle modulated systems can exhibit substantial RIN insensitivity through the use of a limiter in the receiver and by operating at an IF well above the RIN roll-off frequency. The linearity of angle modulated links tends to improve for high IFs due to the improved linearity of the phase or frequency discriminator in the receiver.

We have described conventional approaches to phase noise cancellation (PNC) using reference transport and have shown that they do not work for analog links. Instead, we have focused on interferometric links, which both cancel laser phase noise and generate a received signal at an intermediate frequency without the use of a separate local oscillator laser. We have shown theoretically that the heterodyne interferometric phase modulated

(HIPM) link provides a 3 dB spurious-free dynamic range (SFDR) improvement at laser powers of less than 1 mW for representative link parameters and that the SFDR improvement increases for higher powers due to the suppression of laser relative intensity noise (RIN). For a RIN of -155 dB/Hz, the SFDR in a 1 GHz bandwidth improves by 10 dB for a laser output power of 40 mW. We have constructed a proof-of-concept HIPM link and have demonstrated up to 23 dB suppression of third-order intermodulation products (IMPs) over an AM direct detection link, which translates into a 7.7 dB improvement in SFDR. As a result, the HIPM link appears to have potential for future applications using high-power semiconductor lasers, such as in cellular base station to antenna connection.

Appendix 2.A: Derivation of PM and FM Output Currents

After the limiter, the RIN terms multiplying the cosine term are eliminated and the quadrature components of the amplitude noise terms become part of the cosine argument,

$$i_{PM2}(t) = 2R\sqrt{P_S P_{LO}} \cos[\omega_{IF}t + \varphi_{\Delta}x(t) + \varphi_{n_{tot}}(t)] \quad (2.A-1)$$

where the total noise in the phase of the signal is given by

$$\varphi_{n_{tot}}(t) = \varphi_{n_S}(t) - \varphi_{n_{LO}}(t) + \frac{1}{2R\sqrt{P_S P_{LO}}} (RP_S n_{RSq}(t) + RP_{LO} n_{RLOq}(t) + n_{Dq}(t)) \quad (2.A-2)$$

The delay-line filter has a transfer function given by

$$H(f) = \cos\left(\frac{\pi f}{2 f_{IF}}\right) \quad (2.A-3)$$

where we have chosen the filter delay $t = 1/2f_{IF}$. For a signal centered at f_{IF} , we can expand the transfer function as

$$H(f) \cong -\frac{\pi}{2f_{IF}}(f - f_{IF}) + \frac{1}{6}\left[\frac{\pi}{2f_{IF}}(f - f_{IF})\right]^3 \quad (2.A-4)$$

Using the Fourier derivative theorem to relate the input current to the discriminator to the output current, we obtain [13]:

$$i_{PM3}(t) = KR\sqrt{P_S P_{LO}} \left\{ -\frac{1}{4f_{IF}} [\varphi_{\Delta} \dot{x}(t) + \dot{\varphi}_{n_{tot}}(t)] + \frac{1}{6} \left(\frac{1}{4f_{IF}} \right)^3 [\varphi_{\Delta} \ddot{x}(t) - i3\varphi_{\Delta}^2 \dot{x}(t) \ddot{x}(t) - \varphi_{\Delta}^3 \dot{x}^3(t)] \right\} \\ \times \cos[2\pi f_{IF} t + \varphi_{\Delta} x(t) + \varphi_{n_{tot}}(t) + \varphi_o] \quad (2.A-5)$$

In Eq. (2.A-5), we have neglected higher order noise and signal cross noise terms (which are small compared to the first-order signal and noise terms). After the envelope detector and the integrator, we have

$$i_{PM\ out}(t) = KR\sqrt{P_S P_{LO}} \left\{ -\frac{1}{4f_{IF}} [\varphi_{\Delta} x(t) + \varphi_{n_{tot}}(t)] + \frac{1}{6} \left(\frac{1}{4f_{IF}} \right)^3 \left[\varphi_{\Delta} \ddot{x}(t) - i\frac{3}{2} \varphi_{\Delta}^2 \dot{x}^2(t) - \varphi_{\Delta}^3 \int \dot{x}^3(t) dt \right] \right\} \quad (2.A-6)$$

It can be shown that, for a sub-octave signal band, the only significant intermodulation terms falling within the signal band are those coming from the term proportional to φ_{Δ}^3 , and we thus arrive at Eq. (2.A-6).

The only difference between the FM and PM receivers is the absence of an integrator after the envelope detector in the FM case. This results in

$$i_{FM\ out}(t) = TR\sqrt{P_S P_{LO}} \left\{ -\frac{1}{4f_{IF}} [\omega_{\Delta} \dot{x}(t) + \dot{\varphi}_{n_{tot}}(t)] + \frac{1}{6} \left(\frac{1}{4f_{IF}} \right)^3 [\omega_{\Delta} \ddot{x}(t) - i3\omega_{\Delta}^2 x(t) \dot{x}(t) - \omega_{\Delta}^3 x^3(t)] \right\} \quad (2.A-7)$$

It can be shown that, for a sub-octave signal band, the only significant intermodulation terms falling within the signal band are those coming from the term proportional to ω_{Δ}^3 , and we thus arrive at Eq. (2.A-7).

Appendix 2.B. Noise in Analog Optical Links

In this section, we evaluate the noise components used in Eqs. (2.8), (2.9), and (2.27). In the following expressions, we encounter both bandpass noise terms around the IF and baseband noise. We will use the subscript *bp* to indicate bandpass noise, which is related to the unfiltered noise by

$$n_{bp}(t) = h_{bp}(t) * n(t) \quad (2.B-1)$$

where $h_{bp}(t)$ is the impulse response of the IF amplifier. We will use the subscript bb to indicate baseband noise, which is related to the unfiltered noise by

$$n_{bb}(t) = h_{bb}(t) * n(t) \quad (2.B-2)$$

where $h_{bb}(t)$ is the impulse response of the baseband circuitry.

The shot noise $n_{sh}(t)$ is white with a single-sided power spectral density (PSD) after *each* photodiode given by (for coherent and direct detection, respectively)

$$G_{n_{sh}}(f) = \eta_{sh} = \begin{cases} eR(P_s + P_{Lo}) & \text{(CD)} \\ 2eRP_s & \text{(DD)} \end{cases} \quad (2.B-3)$$

The thermal noise $n_{th}(t)$ is also white with a single-sided PSD given by

$$G_{n_{th}}(f) = \eta_{th} = \frac{4kT}{R_r} \quad (2.B-4)$$

In the above expressions, e is the electron charge, k is Boltzmann's constant, T is the absolute temperature, and R_r is the effective receiver resistance. Assuming perfectly matched photodetectors, the sum of the shot and thermal noise, $n_D(t)$, has a PSD given by $\eta_D = 2\eta_{sh} + \eta_{th}$. The root mean squared (RMS) power in $n_D(t)$ is thus given by

$$\langle n_{D\ bb}^2 \rangle = \eta_D B \quad (2.B-5)$$

$$\langle n_{D\ bp}^2 \rangle = 2\eta_D B \quad (2.B-6)$$

where B is the bandwidth of the baseband signal $x(t)$. For the FM case, we must evaluate the PSD of $\dot{n}_D(t)$, which is given by

$$G_{\dot{n}_D}(f) = (2\pi f)^2 \eta_D \quad (2.B-7)$$

leading to

$$\langle \dot{n}_{D_{bp}}^2 \rangle = \frac{(2\pi)^2}{3} \eta_D (f_2^3 - f_1^3) \quad (2.B-8)$$

f_1 and f_2 are the lower and upper baseband signal frequency, respectively, and thus obey the relationship

$$B = f_2 - f_1 \quad (2.B-9)$$

The PSD of the frequency noise $\dot{\phi}_n(t)$ is given by [14]

$$G_{\dot{\phi}_n}(f) = 4\pi\Delta\nu \quad (2.B-10)$$

which leads to

$$\langle \dot{\phi}_n^2 \rangle = 4\pi\Delta\nu B \quad (2.B-11)$$

where $\Delta\nu$ is the combined linewidth of the transmitter and local oscillator lasers. The PSD of the phase noise $\phi_n(t)$ is given by

$$G_{\phi_n}(f) = \frac{\Delta\nu}{\pi f^2} \quad (2.B-12)$$

which leads to

$$\langle \phi_n^2 \rangle = \frac{\Delta\nu}{\pi} \left(\frac{1}{f_1} - \frac{1}{f_2} \right) \quad (2.B-13)$$

The PSD of the RIN is a complicated function of a number of laser parameters [15]. For the purpose of our analysis, we will describe the RIN PSD phenomenologically as

$$G_{n_R}(f) = \frac{\eta_R}{[1 + (f/f_R)^2]^2}, \quad (2.B-14)$$

where h_R is an "average" low frequency RIN PSD and f_R is RIN roll-off frequency, which is related to the relaxation oscillation frequency of the laser. Through an appropriate choice of h_R and f_R , we can adequately model the impact of RIN on the analog links analyzed. Eq. (2.B-14) leads to

$$\langle n_R^2 \rangle = g_1(f_2) - g_1(f_1) \quad (2.B-15)$$

where

$$g_1(f) = \frac{\eta_R f_R}{2} \left[\tan^{-1}(f/f_R) + \frac{(f/f_R)}{1 + (f/f_R)^2} \right] \quad (2.B-16)$$

For the bandpass RIN, we find

$$\langle n_{Rbp}^2 \rangle = g_1(f_{IF} + f_2) - g_1(f_{IF} + f_1) + g_1(f_{IF} - f_1) - g_1(f_{IF} - f_2) \quad (2.B-17)$$

In the FM SNR expression, we can evaluate $\langle \dot{n}_R^2 \rangle$ as

$$\langle \dot{n}_R^2 \rangle = g_2(f_{IF} + f_2) - g_2(f_{IF} + f_1) + g_2(f_{IF} - f_1) - g_2(f_{IF} - f_2) \quad (2.B-18)$$

where

$$g_2(f) = \frac{\eta_R f_R^3}{2} \left\{ \tan^{-1}(f/f_R) - \frac{(f/f_R)}{1 + (f/f_R)^2} \right\} \quad (2.B-19)$$

The photodetector matching factor b is defined in the PM system as

$$b = \frac{\langle [h_1(t) - h_2(t)] * n_R(t) \rangle^2}{\langle n_R^2(t) \rangle} \quad (2.B-20)$$

where $h_1(t)$ and $h_2(t)$ are the impulse responses of the two photodetectors in the balanced receiver. In the FM system,

$$b = \frac{\langle [h_1(t) - h_2(t)] * \dot{n}_R(t) \rangle^2}{\langle \dot{n}_R^2(t) \rangle} \quad (2.B-21)$$

b ranges from 0 for two perfectly matched photodetectors to 1 for a single photodetector.

2.9 References

- [1] G. L. Abbas, V. W. S. Chan, and T. K. Yee, "A dual-detector optical heterodyne receiver for local oscillator noise suppression," *IEEE J. Lightwave Technol.*, vol. LT-3, no. 5, pp. 1110 - 1122, 1987.
- [2] W. E. Stephens and T. R. Joseph, "System characteristics of direct modulated and externally modulated RF fiber-optic links," *IEEE J. Lightwave Technol.*, vol. LT-5, no. 3, pp. 380 - 387, 1987.
- [3] N. Takachio and K. Iwashita, "A novel resonance-type optical receiver for high-speed optical heterodyne transmission systems," *IEEE J. Lightwave Technol.*, vol. 7, no. 9, pp. 1371-1378, 1989.
- [4] S. Betti et al., "Phase noise and polarization state insensitive optical coherent systems," *IEEE J. Lightwave Technol.*, vol. 8, no. 5, pp. 756 - 767, 1990.
- [5] R. Gross, R. Olshansky, and M. Schmidt, "Coherent FM-SCM system using DFB lasers and a phase noise cancellation circuit," *IEEE Photon. Technol. Lett.*, vol. 2, no. 1, 1990.
- [6] K. Tamura et al., "Phase-noise canceled differential phase shift keying (PNC-DPSK) for coherent optical communication systems," *IEEE J. Lightwave Technol.*, vol. 8, no. 2, pp. 190 - 201, 1990.
- [7] Y. Pu and C. Tsai, "Wideband integrated magneto-optic frequency shifter and modulator at X-band," *Proc. of the IEEE 1992 Ultrasonics Symposium*, pp. 161 - 164, 1992 (Tuscon, AZ).

- [8] C. S. Tsai, "Integrated acoustooptic circuits and applications," *IEEE Trans. Ultrasonics, Ferroel., and Freq. Control*, vol. 39, no. 5, pp. 529 - 554, 1992.
- [9] Farries, M. C. et al., "High power semiconductor lasers for lidar and sensing applications," *Proc. of the SPIE*, vol. 2088, pp. 55 - 58, 1994.
- [10] T. Tanbun-ek et al., "High output power single longitudinal mode graded index separate confinement multiple quantum well InGaAs/InP distributed feedback (GRIN SCH MQW DFB) lasers," *IEEE Photon. Technol. Lett.*, vol. 2, no. 7, pp. 453 - 455, 1994.
- [11] R. F. Kalman and L. G. Kazovsky, "Demonstration of an analog heterodyne interferometric phase-modulated (HIPM) link," accepted for publication in *IEEE Photon. Technol. Lett.*
- [12] M. Nazarathy et al., "Progress in externally modulated AM CATV transmission systems," *IEEE J. Lightwave Technol.*, vol. 11, no. 1, pp. 82 - 105, 1993.
- [13] P. F. Panter, *Modulation, Noise, and Spectral Analysis*. New York: McGraw-Hill, 1965.
- [14] L. G. Kazovsky, "Performance analysis and laser linewidth requirements for optical PSK heterodyne systems," *J. Lightwave Technol.*, vol. LT-4, pp. 415-425, 1986.
- [15] S. L. Woodward, T. L. Koch, and U. Koren, "RIN in multisection MQW-DBR lasers," *IEEE Photon. Technol. Lett.*, vol. 2, no. 2, pp. 104-108, 1990.

PART 2:

DYNAMIC WAVELENGTH DIVISION MULTIPELXING OPTICAL NETWORKS

Chapter 3

STARNET Physical Layer: Combined ASK and PSK Modulation

3.1 Introduction

Wavelength-division multiplexing (WDM) is a promising technique for building future high-capacity optical communications systems. Advanced WDM systems have been experimentally investigated for point-to-point [1], distribution [2], and computer communication applications [3]. Since wavelength-division multiplexing segments the available fiber bandwidth into multiple lower bandwidth channels, it is particularly attractive for WDM computer communication networks. Networks for lossless transfer of digital medical images, super computer visualization, 3D computer-aided design, cartography, and newspaper and magazine production could benefit from the current research in WDM technology. In addition, the increased use of visualization and expected use of multimedia applications will require increased traffic capacities in backbone networks interconnecting more conventional LANs. WDM technology could prove to be more cost effective than either centralized or distributed electronic switching for some of these future high-capacity networks.

Several important WDM networking experiments have shown the potential of WDM technology and also highlighted some difficulties [3-4]. Two current problems with WDM networks are: accommodating packet-switched traffic in an intrinsically circuit-switched environment and control of the circuit switched channels before the circuit connections are established. To accommodate packet-switching, multihop networks [4-5] and fast wavelength-switching using tunable lasers [6] have been proposed. Methods for controlling circuit switched channels make use of polling the individual transmit wavelengths [3], a separate control wavelength [7], or subcarrier multiplexed control channels [8-9].

STARNET, a coherent wavelength-division multiplexed (WDM) computer communication network being developed at Stanford University [10-12], addresses both of these problems using unique properties of coherent detection. STARNET is designed to address the need of future computer networks to support a wide variety of applications

and traffic types, both circuit-switched and packet-switched. STARNET supports both circuit-switched applications and packet-switched applications by creating two logical sub-networks, a 2.488 Gb/s (SONET OC-48 rate) per node tunable circuit-switched sub-network and a 125 Mb/s FDDI-compatible, fixed-tuned, packet-switched, ring sub-network, on a single physical star topology. In addition to transmitting packet-switched data, the 125 Mb/s virtual-ring sub-network is used for network management of the circuit-switched sub-network. The two logical sub-networks are implemented with only one transmitter laser per node by multiplexing packet-switched data using amplitude shift-keyed (ASK) modulation and circuit-switched data using phase shift-keyed (PSK) modulation on the same optical carrier. Each node is equipped with two coherent heterodyne receivers to recover the ASK and PSK data separately. The use of coherent detection and a new carrier allocation strategy permits the implementation of each STARNET node with only two lasers.

In this chapter we report the theoretical and experimental investigation of a STARNET node transceiver. With our transceiver, we investigated the feasibility of transmitting and receiving ASK and PSK data using the same optical carrier. The transmitter of our transceiver operates at a wavelength of $1.32\text{ }\mu\text{m}$ and has an output power of -1 dBm. The receiver pair has a sensitivity of -27.6 dBm when a 2.488 Gb/s pseudo-random bit sequence (PRBS) is transmitted using phase modulation while a 125 Mb/s FDDI signal is transmitted using amplitude modulation. The resulting system power budget is 26.6 dB.

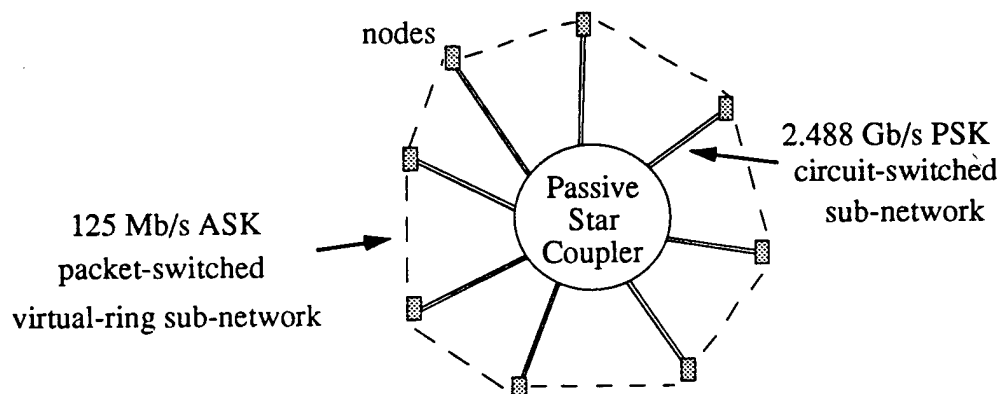


Figure 3-1. The STARNET architecture.

In Section 3.2, we give a detailed description of the STARNET physical layer. In Section 3.3, we describe the experimental transceiver which we have constructed. In Section 3.4, we present a simple theory to optimize the performance of a PSK receiver for

fast circuit-switched data and an ASK receiver for slower packet-switched data. In Section 3.5, we present experimental data for the performance penalty of each receiver in the presence of combined PSK and ASK modulation. In Section 3.6, we present experimental data for the optics of a fully operational STARNET node, with simultaneous reception of PSK and ASK data. Section 3.7 provides conclusions. Section 3.8 contains references.

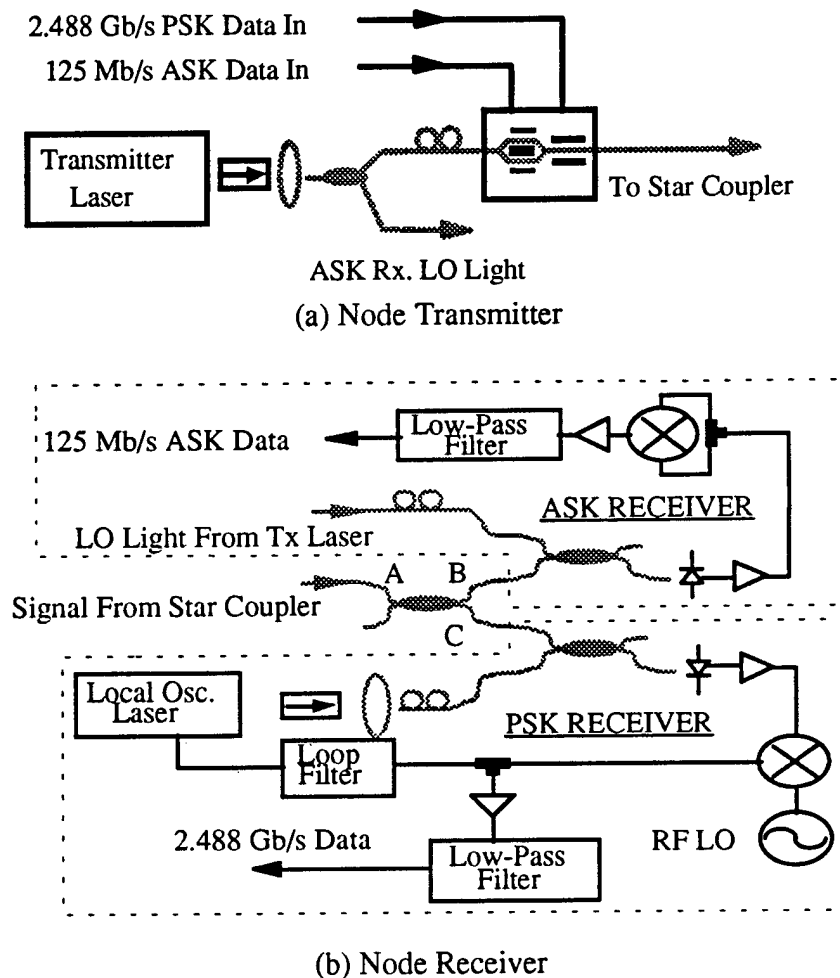


Figure 3-2. STARNET node transceiver.

3.2 STARNET Operation

Each STARNET node is optically connected to all the other nodes through a passive optical star coupler, as shown in Fig. 3-1. Each STARNET node (Fig. 3-2) is equipped with one laser transmitter. The transmitter laser is tunable, but tunability is used only for

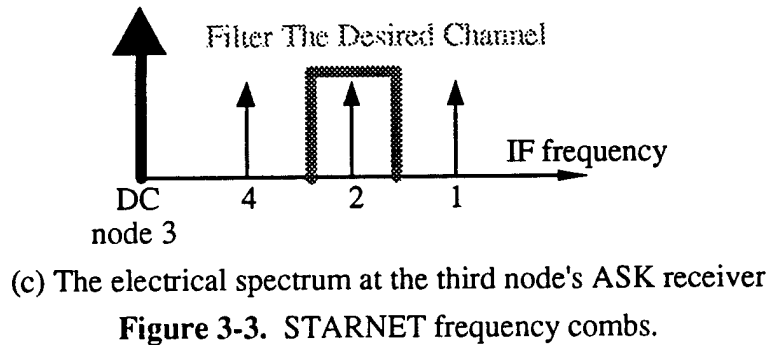
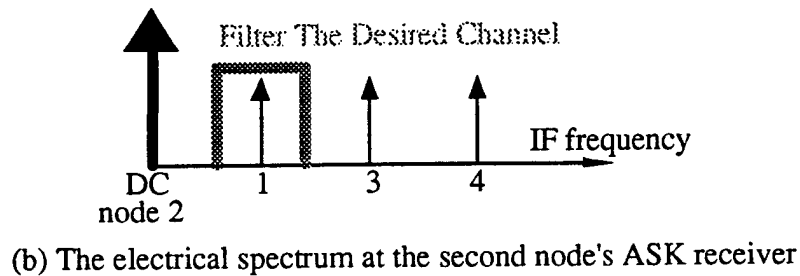
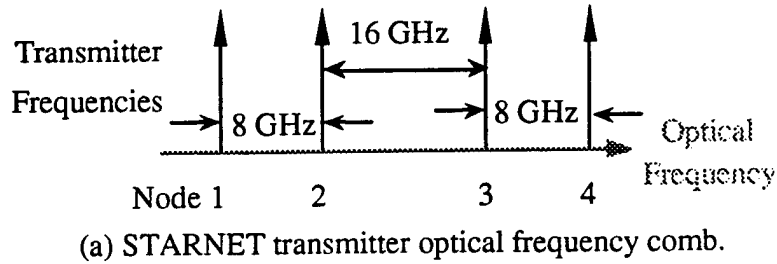
network setup and flexibility, rather than wavelength switching. In normal operation of the network, the transmitter laser source is tuned to a unique fixed wavelength so that a comb of light carriers is formed. Using a novel LiNbO_3 optical modulator with a phase modulator and an amplitude modulator integrated on the same chip, each node transmits a 125 Mb/s packet-switched ASK modulated data stream and a 2.488 Gb/s PSK modulated circuit-switched data stream.

Each node has a tunable coherent PSK heterodyne receiver that can be tuned to any transmitter in the network and decodes its PSK modulated data stream. In addition, each node also has an auxiliary fixed-tuned coherent ASK heterodyne receiver that is permanently tuned to the previous node in the network frequency comb and decodes its ASK modulated packet-switched data stream. Therefore, each node receives packet-switched data from the previous node and transmits packet-switched data to the next node. This way, a multihop virtual-ring packet-switched sub-network is created as shown in Fig. 3-1. To close this store-and-forward chain to form a ring, the first node of the chain (the one whose transmitter is first in the frequency comb) is equipped with a receiver that decodes the packet-switched data stream of the last node in the chain. This packet-switched sub-network can be used for transmission of moderate speed packet-switched data as well as transmission of network control and scheduling information for the circuit switched sub-network.

Using combined ASK and PSK modulation to multiplex two independent data streams onto the same carrier avoids the need for two transmitter lasers in each node transceiver. In addition, a new carrier allocation strategy [13] allows us to implement a complete node transceiver with only one tunable local oscillator laser per node, even though each STARNET node has two coherent heterodyne receivers. To accomplish this, part of the transmitter laser light is tapped out before it enters the optical modulator (Fig. 3-2(a)) and is used as the laser local oscillator (LO) field for the fixed-tuned ASK receiver (Fig. 3-2(b)) thus eliminating the need for an additional LO laser in the auxiliary ASK receiver. A tunable laser is still used as the LO for the tunable PSK receiver (Fig. 3-2(b)).

Fig. 3-3(a) shows the transmitter optical frequency comb for a 4-node STARNET. Carriers are grouped into pairs along the optical comb. The optical channel spacing between channels belonging to the same pair is set to 8 GHz while the separation between different pairs is set to 16 GHz. Fig. 3-3(b) shows the resulting electrical spectrum at the second node's intermediate frequency (IF) using a portion of the transmitter light for the laser LO. The desired channel (in this case, node 1) is then selected by electrical filtering. One unavoidable effect is that the desired IF signal alternates between 8 GHz and 16 GHz for every other node in the frequency comb. For example, Fig. 3-3(c) shows the resulting

electrical spectrum at node 3's IF. In this case, node 3 must tune to node 2 which is at 16 GHz rather than 8 GHz. In addition, this carrier allocation strategy still permits heterodyne reception of any of the channels by the PSK receivers without interference [13], and therefore does not impact the circuit-switched sub-network. The STARNET operation is described in more detail in [10-12].



3.3 Transceiver Description

Fig. 3-2 shows a block diagram of the STARNET transceiver. The 2.488 Gb/s PSK data and the 125 Mb/s ASK data are multiplexed in the transmitter using a custom LiNbO₃ external modulator. The modulator is a lumped electrode device with both a phase modulator and a Mach-Zehnder intensity modulator integrated on the same chip. The lasers are Lightwave Electronics 25 mW, single-frequency, 1320 nm, miniature diode-

pumped Nd:YAG lasers. The tuning range of these Nd:YAG lasers is approximately 35 GHz and limits the number of channels in our WDM network to four. The optical signals from the lasers are passed through optical isolators with isolation greater than 40 dB. The signals are then focused on bare optical fibers, angle polished to 7° to prevent reflections.

In the transmitter, the light signal is then split into two parts. Half of the light is used for data transmission and the other half is used as laser LO light for the fixed tuned ASK receiver as described in Section 3.2. After splitting the laser light, there is 9 dBm left for both the ASK receiver LO power and for input to the modulator. The amplifier for the 2.488 Gb/s PSK data has a bandwidth of 4 kHz to 3 GHz and 28 dBm of maximum output power. The phase modulation of the lightwave is limited to $\pm 52^\circ$ using this amplifier. The amplifier for the 125 Mb/s ASK data has a bandwidth of 4 kHz to 500 MHz and 28 dBm of maximum output power. The DC bias point of the intensity modulator is manually controlled using a variable voltage supply with the voltage set so that the modulated output light intensity is given by:

$$P_{out} = \begin{cases} P_{max} & \text{ASK data} = 1 \\ P_{max} \cdot (1 - m) & \text{ASK data} = 0 \end{cases} \quad (3.1)$$

where P_{max} is the maximum output light power from the modulator and m is the amplitude modulation depth. P_{max} for our transmitter was -1 dBm. The phase section of the modulator has a sharp cutoff at 2.3 GHz and the amplitude section has a sharp cutoff at 1 GHz.

The light coming to the node receiver (Fig. 3-2(b)) from the star coupler is split into two branches. One branch goes to a heterodyne PSK receiver and the other branch goes to a heterodyne ASK receiver. Manual polarization controllers are used for polarization alignment in our experiments. In a field deployable network, another solution will be required. Polarization diversity, automatic control, and other common techniques [14] are compatible with our transceiver. The 2.488 Gb/s PSK receiver performs synchronous heterodyne pilot-carrier reception [15]. The 125 Mb/s ASK heterodyne receiver performs nonsynchronous reception. Saturation of the photodiodes limited the local oscillator (LO) powers to around 8 dBm at the input to the ASK and PSK receivers. After splitting the transmitter laser light with a 3 dB coupler, there is 9 dBm for LO light for the ASK receiver. Both receivers have simple single-photodetector, low impedance front ends (100Ω) with 3 dB bandwidths greater than 15 GHz and intermediate frequencies of 8 GHz. Even with single-photodetector receivers (rather than balanced receivers), local oscillator intensity noise is not problem in our heterodyne receivers since

most of the Nd:YAG laser intensity-noise power is concentrated at frequencies less than 500 kHz [15]. This intensity noise is greatly reduced by the IF bandpass filter/amplifiers of the heterodyne receiver.

The PSK receiver's IF signal is sent to a low noise amplifier with 60 dB of gain and a 16 GHz bandwidth centered at 10 GHz. The amplifier output is fed to a double balanced mixer for synchronous demodulation. The second input port of the mixer is connected to the RF local oscillator. The double balanced mixer output is divided into two parts: one part is used for phase control and the second part is used for data recovery. At the data recovery branch, the signal passes through a baseband amplifier and fifth-order Bessel filter with a 3 dB cutoff frequency of 2 GHz. The phase control signal is fed to a variable gain amplifier, through a first order lead-lag passive loop filter, and then to the PZT port of the LO laser for optical phase locking. The PZT port has a tuning coefficient of 3.4 MHz/V. The time constants of the optical phase-locked loop (OPLL) filter's pole and zero are 12.3 ms and 6.8 ms respectively.

The ASK receiver's IF signal is sent to an amplifier with a 16 GHz bandwidth centered at 8 GHz and two output ports. One output is fed to the LO port of a double balanced mixer and the other output is fed to the RF port of the same mixer for square law detection. The baseband signal is amplified and then filtered using a single-pole RC filter.

3.4 Combined ASK and PSK Modulation: Theory

In the experimental STARNET transceiver, data stream multiplexing of the circuit-switched data and the packet-switched data is achieved using a combined phase and amplitude modulation format. Using a custom LiNbO₃ optical modulator, the circuit switched stream is PSK modulated on the transmitter lightwave at 2.488 Gb/s (SONET OC-48 rate) while the packet-switched data is low-level ASK modulated on the same lightwave at 125 Mb/s (provided by commercial FDDI hardware in a workstation). To investigate simultaneous transmission and reception of ASK and PSK data on the same optical carrier, we analyzed the impact of the ASK modulation depth on the sensitivity of both the ASK and PSK receivers. The receiver sensitivity is defined as the peak received signal power required for a BER of 10⁻⁹. A simple analytical estimate of BER can be obtained using the Gaussian approximation [16-17]:

$$BER = Q(\gamma) = \frac{1}{2} \operatorname{erfc}\left(\frac{\gamma}{\sqrt{2}}\right) \quad (3.2)$$

where erfc and Q are the complementary error function and the Gaussian Q-function defined in [18], and γ is the digital signal-to-noise ratio at the input of the decision gate.

For the PSK receiver, we assume that the BER is determined by the received signal power when an ASK '0' is transmitted. Following the analysis in [16], γ_{PSK} for a single-detector, shot-noise limited, synchronous PSK heterodyne receiver can be found to be:

$$\gamma_{PSK} = \sqrt{\frac{(1-m) \cdot R \cdot P_s}{q \cdot r_{PSK}}} \quad (3.3)$$

where

$$R \equiv \frac{\eta \cdot q \cdot \lambda}{h \cdot c}, \quad (3.4)$$

is the photodiode responsivity (Amperes per Watt), m is the amplitude modulation depth, P_s is the peak received signal power, q is the electron charge, r_{PSK} is the bit rate of the PSK modulation, η is the photodiode quantum efficiency, λ is the optical wavelength, h is Planck's constant, and c is the speed of light. The factor of $(1-m)$ in the numerator of Eq. (3.3) accounts for the reduced received signal power when an ASK '0' is transmitted.

Following the analysis in [17], γ_{ASK} for a single-detector, shot-noise limited, asynchronous ASK heterodyne receiver can be found to be:

$$\gamma_{ASK} = \frac{0.5 \cdot m \cdot R \cdot P_s}{\sqrt{R \cdot P_s \cdot q \cdot r_{ASK} + K \cdot (q \cdot r_{ASK})^2} + \sqrt{(1-m) \cdot R \cdot P_s \cdot q \cdot r_{ASK} + K \cdot (q \cdot r_{ASK})^2}} \quad (3.5)$$

where $K \equiv B_{IF}/r_{ASK}$, B_{IF} is the intermediate frequency (IF) filter noise bandwidth, and r_{ASK} is the bit rate of the ASK modulation. We assume that the IF filter bandwidth is large enough to accept the full bandwidth of the PSK/ASK modulated signal and does not cause conversion of the PSK modulation into amplitude noise in the ASK receiver. With no PSK modulation the IF filter bandwidth, B_{IF} , would be set to the bit rate of the ASK data, r_{ASK} (i.e. an ideal matched filter).

In our analysis we have investigated two cases. For case A, the high-speed data are transferred via PSK modulation; the low-speed data are transferred via ASK modulation; and the ASK receiver IF bandwidth is increased to 16 GHz (as in our

experiments) to accept the PSK modulated signal. For case B, the low-speed data are transferred via PSK modulation; the high-speed data are transferred via ASK modulation; and the ASK receiver IF bandwidth is set to 2.488 GHz to accept the ASK modulated signal.

Fig. 3-4 shows the results of our analysis. Fig. 3-4(a) shows the results for case A. The sensitivity of the ASK receiver improves as the modulation depth is increased while the sensitivity of the PSK receiver deteriorates due to the reduced signal power at the PSK receiver when an ASK '0' is transmitted. For an amplitude modulation depth of 0.54, the ASK and PSK receivers operate with equal sensitivities of -45.3 dBm. Fig. 3-4(b) shows the results for case B. The ASK and PSK receivers operate with an equal sensitivity of -41.6 dBm for an amplitude modulation depth of 0.99.

Comparison of Fig. 3-4(a) with Fig. 3-4(b) shows that case A is a better choice due to the higher sensitivity of the receiver pair. Although the sensitivity difference between the two cases is only 3.7 dB, our experimental results have shown that the PSK receiver does not function properly when the ASK modulation depth is close to one. This precludes using case B at its optimum point. Therefore, the proper combination is case A, PSK modulation for the high-speed circuit-switched data and ASK modulation for the low-speed packet-switched data. A summary of our results is given in Table 3-1.

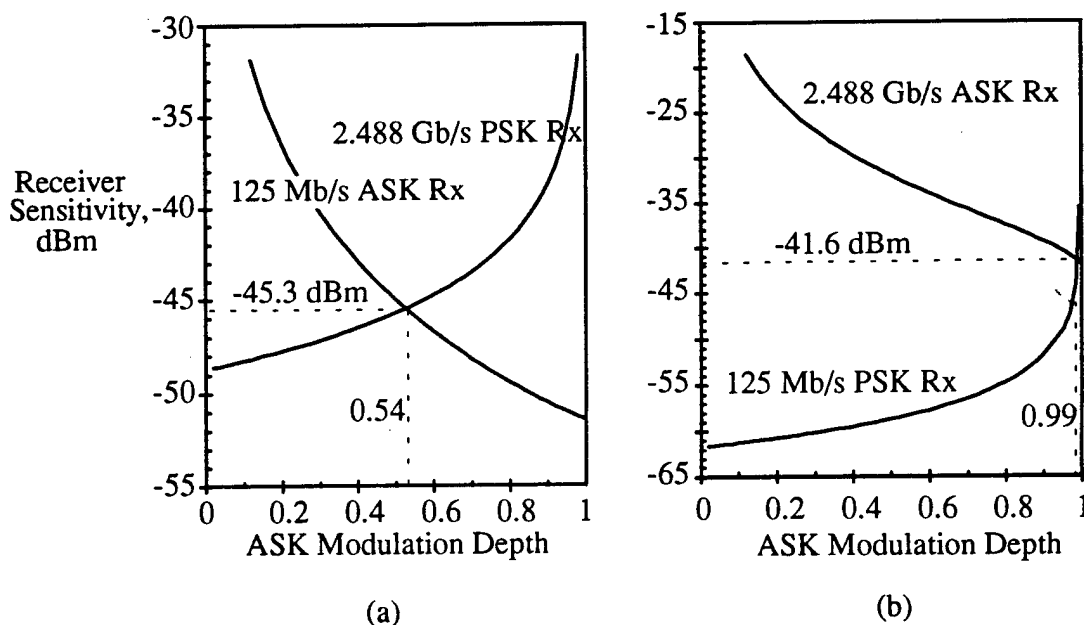


Figure 3-4. Theoretical receiver sensitivities versus amplitude modulation depth; (a) 2.488 Gb/s PSK and 125 Mb/s ASK receivers, and (b) 125 Mb/s PSK and 2.488 Gb/s ASK receivers.

Table 3-1. Systems Parameters

	Case A	Case B
Figure	7a	7b
r_{ASK}	125 Mb/s	2.488 Gb/s
B_{IF}	16 GHz	2.488 GHz
r_{PSK}	2.488 Gb/s	125 Mb/s
λ	1319 nm	1319 nm
η	1	1
P_{sens}	-45.3 dBm	-41.6 dBm
m_{opt}	0.54	0.99

3.5 Combined ASK and PSK Modulation Format: Experiment

3.5.1 Impact of the ASK modulation on the PSK receiver

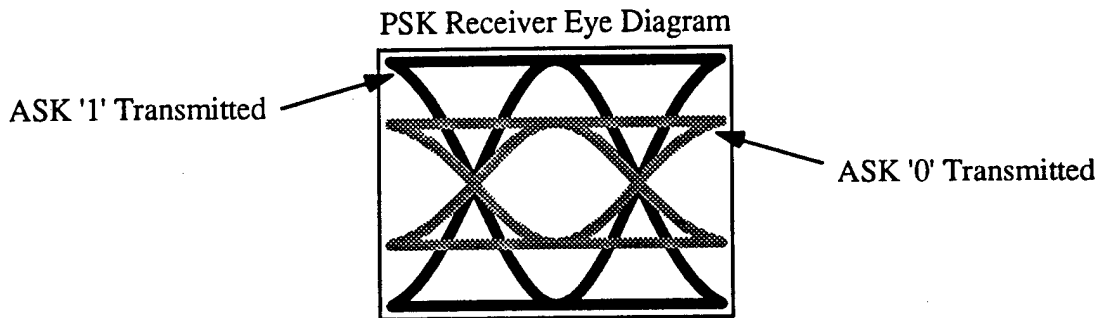


Figure 3-5. PSK receiver eye diagram illustrating the impact of ASK modulation on the received PSK bit stream.

Fig. 3-5 illustrates the impact of ASK modulation on the PSK receiver. When an ASK '0' is transmitted, the received optical signal power at the PSK receiver is reduced by a factor of $(1-m)$, and the received electrical signal is reduced by a factor of $\sqrt{1-m}$. For example, an amplitude modulation depth of 1 will cause all of the PSK data to be lost when an ASK '0' is transmitted. Fig. 3-6 shows a theoretical plot and experimental measurements of the sensitivity penalty to the PSK receiver versus the ASK modulation depth, m . The theoretical sensitivity penalty for a quantum-limited receiver is calculated using expressions (3.2), (3.3), and (3.4). The sensitivity penalty is defined as the difference between the receiver sensitivity for a given m and the receiver sensitivity without any ASK modulation ($m=0$):

$$penalty_{PSK}(m) = P_{PSK}(m) - P_{PSK}(m=0) \quad (3.6)$$

where $P_{PSK}(m)$ is the peak received signal power required for a BER of 10^{-9} .

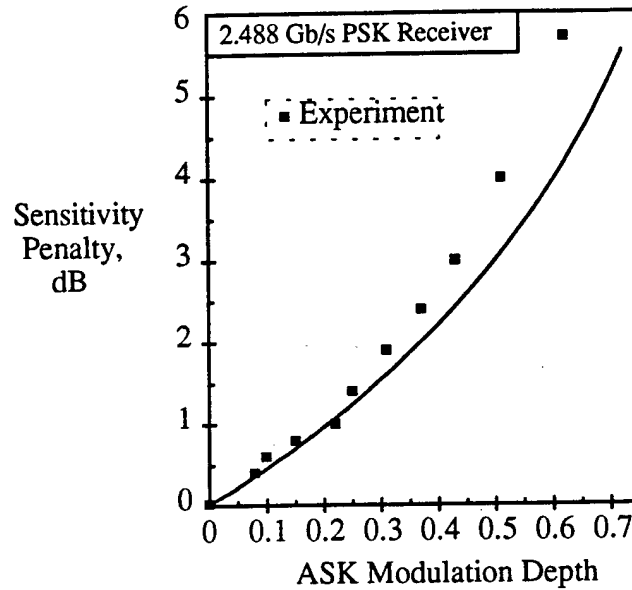


Figure 3-6. PSK receiver sensitivity penalty versus the ASK modulation depth.

The experimental values of the sensitivity penalty are measured by varying the ASK modulation depth and measuring the resulting degradation in the PSK receiver sensitivity. Fig. 3-6 shows that for low ASK modulation depths ($m < 0.3$) the experimental results agree with the theoretical predictions. As m increases, the measured penalty tends to increase more rapidly than the theoretical penalty. This is probably due to an interaction of ASK induced power fluctuations with the PSK receiver optical phase-locked loop (OPLL). As we increased m in our experiments, the larger signal fluctuations made it increasingly difficult to lock the OPLL. For m greater than about 0.6, we were unable to lock the OPLL in the PSK receiver. Although the OPLL parameters (loop bandwidth, damping factor, etc.) are a function of the received signal power [16], automatic gain control circuitry and further optimization of the OPLL parameters could alleviate some of the degradation due to ASK modulation / OPLL crosstalk.

3.5.2 Impact of the PSK modulation on the ASK receiver

To measure the impact of the phase modulation on the ASK receiver, we first determined the performance of the ASK-FDDI ring without phase modulation of the lightwave. For $m = 1$, the ASK-FDDI ring sensitivity is -42.2 dBm, measured at point B in Fig. 3-2(b). This is 1.5 dB greater than the received signal power required for a BER of 10^{-9} when the BER test set is used for measurements. This 1.5 dB penalty is due to the reduced performance of the FDDI interfaces compared to the BER test set.

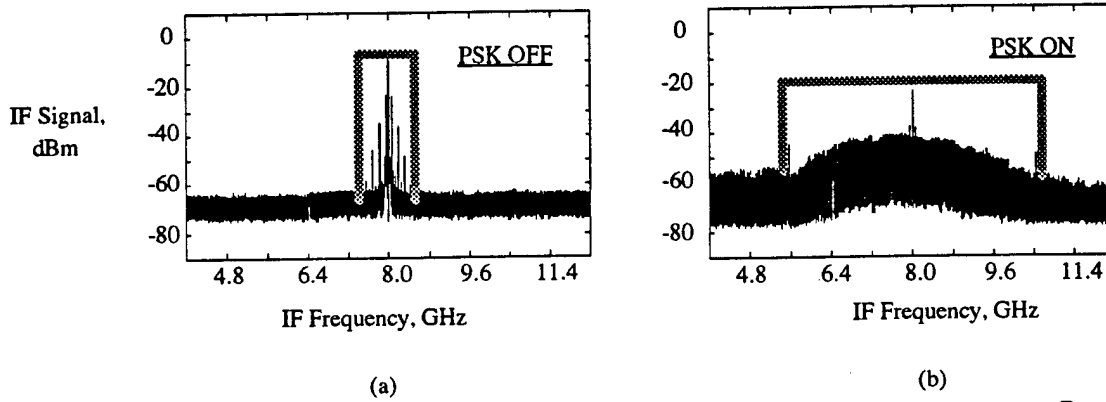


Figure 3-7. ASK receiver IF signal, (a) without PSK modulation, and (b) with 2^7-1 PRBS PSK modulation.

Fig. 3-7 illustrates the impact of the PSK modulation on the electrical IF signal in the ASK receiver. Fig. 3-7(a) shows the electrical IF spectrum with only ASK modulation. The addition of a 2.488 Gb/s 2^7-1 PRBS spreads the spectrum of the ASK signal as shown in Fig. 3-7(b). With no PSK modulation the IF filter bandwidth, B_{IF} , could be set to the bit rate of the ASK data, r_{ASK} . To minimize the degradation of the ASK receiver sensitivity due to the PSK modulation, the IF bandwidth of the ASK receiver must be broadened to accommodate the broadened IF spectrum. If the IF filter is wide enough, the phase modulation will be canceled by the squaring circuit in the ASK receiver (Fig. 3-2(b)) and the ASK receiver sensitivity will be the same with or without phase modulation. Using expressions (3.2), (3.4), and (3.5), we can estimate the penalty to the ASK receiver due to the broadening of the IF filter bandwidth:

$$penalty_{ASK} = P_{ASK}(B_{IF} = 16 \text{ GHz}) - P_{ASK}(B_{IF} = 125 \text{ MHz}) = 4 \text{ dB}. \quad (3.7)$$

Fig. 3-8 shows a theoretical plot and experimental measurements of the sensitivity penalty to the ASK receiver versus the ASK modulation depth. During these measurements, the phase of the lightwave is also modulated by a 2.488 Gb/s 2^7-1 PRBS. The theoretical sensitivity penalty of the ASK receiver as a function of the ASK modulation depth is calculated using expressions (3.2), (3.4), and (3.5) with the IF filter bandwidth set to 16 GHz. The sensitivity penalty is defined as the difference between the receiver sensitivity for a given m and the receiver sensitivity with 100% ASK modulation ($m=1$):

$$\text{penalty}_{\text{ASK}}(m) = P_{\text{ASK}}(m) - P_{\text{ASK}}(m=1). \quad (3.8)$$

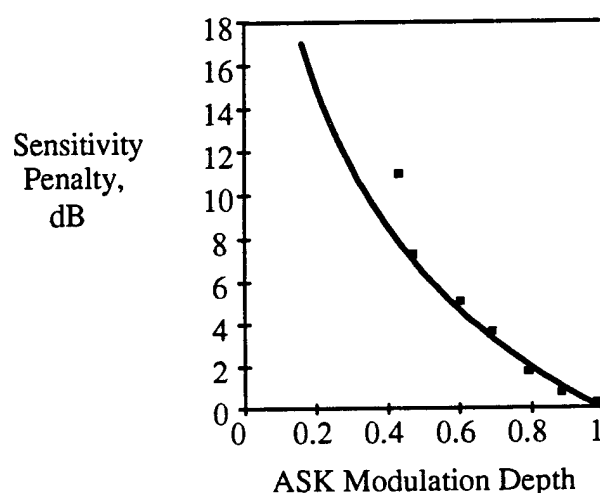


Figure 3-8. ASK receiver sensitivity penalty versus the ASK modulation depth.

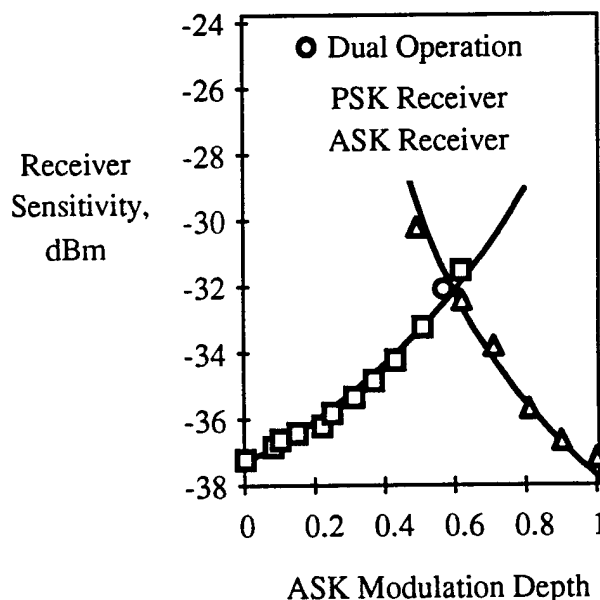


Figure 3-9: PSK and ASK receiver sensitivity versus ASK modulation depth.

The experimental values of the sensitivity penalty are measured by varying the ASK modulation depth and measuring the resulting sensitivity degradation. For large values of m ($m > 0.5$), the experimental data agree with the theoretical predictions. As m decreases, the measured penalty tends to increase more rapidly than the theoretical penalty. This is probably due to a BER floor caused by the PSK modulation being converted to amplitude noise in the ASK receiver IF filter and squaring circuit. For very small values of m ($m < 0.4$), the ASK-FDDI receiver BER could not be reduced below 10^{-7} .

3.6 Optimum Amplitude Modulation Depth Experiment

The sensitivity of the ASK-FDDI receiver is -37.4 dBm when $m=1$, and the PSK receiver sensitivity is -37.2 dBm when $m=0$. Fig. 3-4(a) shows that the ASK and PSK receivers should operate with equal sensitivities for $m=0.54$. For the highest combined sensitivity, the transceiver should operate at the ASK modulation depth yielding equal ASK and PSK receiver sensitivities. Fig. 9 shows the measured experimental ASK and PSK receiver sensitivities versus the ASK modulation depth. The dashed lines drawn through the experimental points predict an intersection for $0.5 < m < 0.6$. We adjusted m to a level where the ASK-FDDI receiver *and* the PSK receiver operate with BER's of 10^{-9} simultaneously. This occurs for $m = 0.57$ as shown by the solid black circle in Fig. 3-9. The resulting optimum receiver sensitivities are -32.1 dBm, measured at points B and C in Fig. 3-2(a).

3.7 Conclusions

We investigated a PSK/ASK transceiver for STARNET, a wavelength-division multiplexed computer communication network, to demonstrate the feasibility of simultaneously transmitting and receiving 125 Mb/s FDDI-compatible, packet-switched, ASK data and 2.488 Gb/s circuit-switched PSK data on the same optical carrier. The transmitter uses an integrated phase and amplitude modulator and has an output power of -1 dBm at 1.32 μ m. The simultaneous use of ASK and PSK modulation on a single lightwave creates sensitivity penalties in both the ASK and PSK subsystems. Nevertheless, both subsystems function properly with error rates less than 10^{-9} and a sensitivity of -32.1 dBm. Including the additional input power splitter and multi-channel interference reduces the combined receiver sensitivity to -27.6 dBm. The resulting transceiver power budget is 26.6 dB using our lasers. While the sensitivity of our experimental transceiver is a modest -27.6 dBm, the power budget we achieved is still

large enough for a 100 node passive star network with a diameter of 5 km and a power margin of 3 dB. The results of our work demonstrate the feasibility of using coherent technology to transmit 125 Mb/s ASK and 2.488 Gb/s PSK data on the same lightwave. Our transceiver has only two lasers but can still be used in a network that supports the use of both 2.488 Gb/s circuit-switched data simultaneously with 100 Mb/s packet-switched data and network control information by all users.

3.8 References

- [1] H. Taga, N. Edagawa, S. Yamamoto, Y. Yoshida, Y. Horiuchi, T. Kawazawa, and H. Wakabayashi, "Over 4,500 km IM-DD 2-channel WDM transmission experiments at 5 Gbit/s using 138 in-line Er-doped fiber amplifiers," OFC/IOOC '93 Post Deadline Papers, PD4, Feb. 1993.
- [2] H. Toba, K. Oda, N. Nakanishi, K. Nosu, K. Kato, and Y. Hibino, "128-channel OFDM information-distribution system with interactive video channels based on DA-OFDMA," OFC/IOOC '93 Technical Digest, pp. 66-68, Feb. 1993.
- [3] N. R. Dono, P. E. Green, K. Liu, R. Ramaswami, and F. F. Tong, "A wavelength division multiple access network for computer communication," *IEEE Journal on Selected Areas in Communications*, vol. 8, no. 6, pp. 983-993, August 1990.
- [4] R. Gidron, "TeraNet: a multi-gigabits per second ATM network," *Computer Communications*, vol. 15, no. 3, pp. 143-152, April 1992.
- [5] B. Mukherjee, "WDM-based local lightwave networks-part II: multihop systems," *IEEE Network*, vol. 6, no. 4, pp. 20-32, July 1992.
- [6] B. Glance, U. Koren, R. W. Wilson, D. Chen, and A. Jourdan, "Fast optical packet switching based on WDM," *IEEE Photonics Tech. Letters*, vol. 4, no. 10, pp. 1186-1188, Oct. 1992.
- [7] M. W. Maeda, A. E. Willner, J. R. Wullert II, J. Patel, and M. Allersma, "Wavelength-division multiple access network based on centralized common-wavelength control," *IEEE Photonics Tech. Letters*, vol. 5, no. 1, pp. 83-85, Jan. 1993.

- [8] S. F. Su and R. Olshansky, "Performance of WDMA networks with baseband data packets and subcarrier multiplexed control channels," *IEEE Photonics Tech. Letters*, vol. 5, no. 2, pp. 236-239, Feb. 1993.
- [9] W. I. Way, D. A. Smith, J. J. Johnson, and H. Izadpanah, "A self-routing WDM high-capacity SONET ring network," *IEEE Photonics Tech. Letters*, vol. 4, no. 4, pp. 402-405, April 1992.
- [10] P. Poggiolini and L. G. Kazovsky, "STARNET: an integrated services broadband optical network with physical star topology," in *Proc. SPIE 1579, Advanced Fiber Communications Technologies*, pp. 14-29, Boston, MA, Sept. 1991.
- [11] C. Barry, M. Hickey, C. Noronha, P. Poggiolini, and L. Kazovsky, "An experimental multi-Gb/s WDM broadband network," ICC '93, Geneva, Switzerland, May 1993.
- [12] L. G. Kazovsky and P. Poggiolini, "STARNET: a multi-Gbit/s optical LAN utilizing a passive WDM star," *IEEE/OSA Journal of Lightwave Technology*, May 1993, accepted for publication.
- [13] V. A. O'Byrne, "A method for reducing the channel spacing in a coherent optical heterodyne system," *IEEE Photonics Tech. Letters*, vol. 2, no. 7, pp. 513-515, July 1990.
- [14] R. Noé, H. J. Rodler, A. Ebberg, G. Gaukel, B. Noll, J. Wittmann, and F. Auracher, "Comparison of polarization handling methods in coherent optical systems," *IEEE/OSA Journal of Lightwave Technology*, vol. 9, no. 10, pp. 1353-1366, Oct. 1991.
- [15] D. A. Atlas and L. G. Kazovsky, "Optical PSK synchronous heterodyne experiments at 560 Mbit/s through 4 Gbit/s," *Journal of Optical Communications*, vol. 12, no. 4, pp. 130-137, Dec. 1991.
- [16] L. G. Kazovsky, "Performance analysis and laser linewidth requirements for optical PSK heterodyne communications systems," *IEEE/OSA Journal of Lightwave Technology*, vol. 4, no. 4, pp. 415-425, April 1986.

- [17] L. G. Kazovsky and O. K. Tonguz, "ASK and FSK coherent lightwave systems: A simplified approximate analysis," *IEEE/OSA Journal of Lightwave Technology*, vol. 8, no. 3, pp. 338-352, March 1990.
- [18] C. B. Rorabaugh, *Communications Formulas and Algorithms for Systems Analysis and Design*, McGraw Hill, 1990, pp. 24-26.

Chapter 4

Modeling of Combined Modulation Using Semiconductor Lasers

4.1 Introduction

STARNET is a computer communications network which utilizes wavelength-division multiplexing (WDM), coherent detection, and a novel combined modulation format for simultaneous transmission of high-speed circuit-switched data and lower-speed packet-switched control data. The original STARNET configuration used a combined modulation format consisting of 2.488 Gb/s phase shift keying (PSK) for fast circuit-switched data and 125 Mb/s amplitude shift keying (ASK) for slower packet-switched data at each node. The advantage of combined modulation in STARNET is the potential for accomodation of both types of traffic on a single physical star topology through the creation of multiple logical sub-networks.

However, the original STARNET configuration depends on phase-locking in the synchronous PSK receiver, and thus requires the use of extremely low-linewidth lasers (such as Nd:YAGs) as transmitters and local oscillators. To make conventional semiconductor lasers an option, we have investigated a combined modulation format which is more resistant to linewidth-induced degradation. This format consists of differential PSK (DPSK) for circuit-switched data and ASK for packet-switched data. We present theoretical results for this combined modulation format in Section 4.2. We have also constructed an experiment which demonstrates simultaneous transmission of DPSK and ASK data. We describe this experiment in Section 4.3.

In the remainder of this chapter, we present extensions of the rigorous model of Jacobsen and Garrett and of the Gaussian approximation of Tonguz and Kazovsky for the performance of optically amplified direct detection (OADD) ASK receivers. All prior optimizations of OADD system performance have assumed complete ASK modulation or complete extinction (modulation depth = 1). However, real systems under modulation may have extinction ratios as low as 10-15 dB. To minimize the chirp of semiconductor lasers under direct modulation, it is necessary to maintain the dc bias current above threshold, which reduces the extinction ratio [1]. The extinction ratio of external intensity

modulators is limited by the inequality of the splitting ratios to the modulator legs and by bias point drift with temperature. In addition, it is desirable to determine an optimum modulation depth in optical networks such as STARNET which utilize combined intensity and phase modulation. The optimum ASK modulation depth, as described in Sections 3.4 and 3.6, is often between 0.5 and 0.6 for such a network.

Our analysis, as described in Section 4.4, is directly applicable to coherent ASK receivers. These new models take into account incomplete ASK modulation, nonzero laser linewidth, and spontaneous emission noise from the optical amplifier in both polarization control (PC) and polarization diversity (PD) receiver configurations. In Section 4.5, we describe the numerical evaluation procedure for the bit error rate (BER). In Section 4.6, we give our principal numerical results. The penalty associated with the polarization diversity configuration is shown to be consistently under 1 dB for a wide range of ASK modulation depths. The penalty due to the noise in the orthogonal polarization decreases with ASK modulation depth. We find optimum optical filter bandwidths and linewidth-induced performance penalties as a function of ASK modulation depth and linewidth. We provide detailed tables of optimum filter bandwidths for both PC and PD receivers using both the rigorous method and the Gaussian approximation; the Gaussian approximation frequently underestimates the optimum bandwidth values.

The chapter concludes with conclusions in Section 4.7 and references in Section 4.8.

4.2 Combined ASK and DPSK Modulation: Theory

System diagrams for both types of modulation are shown in Fig. 4-1, parts (a) and (b). The DPSK coherent receiver utilizes delay and multiply detection with a delay equal to exactly one bit period and does not require a phase-locked loop. The ASK receiver is unchanged from the present STARNET setup.

The theoretical modeling of the DPSK and ASK systems is based on [2] and [3]. The models take into account laser phase noise, receiver noise (shot and thermal), and nonideal IF and lowpass filtering. The filters are modeled as finite integrators, and the impact of such filters on the phase and receiver noises is taken into account. Numerical results are presented in Fig. 4-2. A photodiode responsivity of unity and infinite local oscillator power (no thermal noise impact) are assumed for all plots. Realistic IF filter bandwidths of 7.5 GHz and 6.25 GHz are assumed in the DPSK and ASK receivers, respectively. The graphs show plots of DPSK and ASK receiver sensitivities versus the

ASK modulation depth based on power. The available power for DPSK transmission as a function of ASK modulation depth is assumed to be worst-case; for example, it is assumed that no power is available for DPSK when the ASK modulation depth is unity.

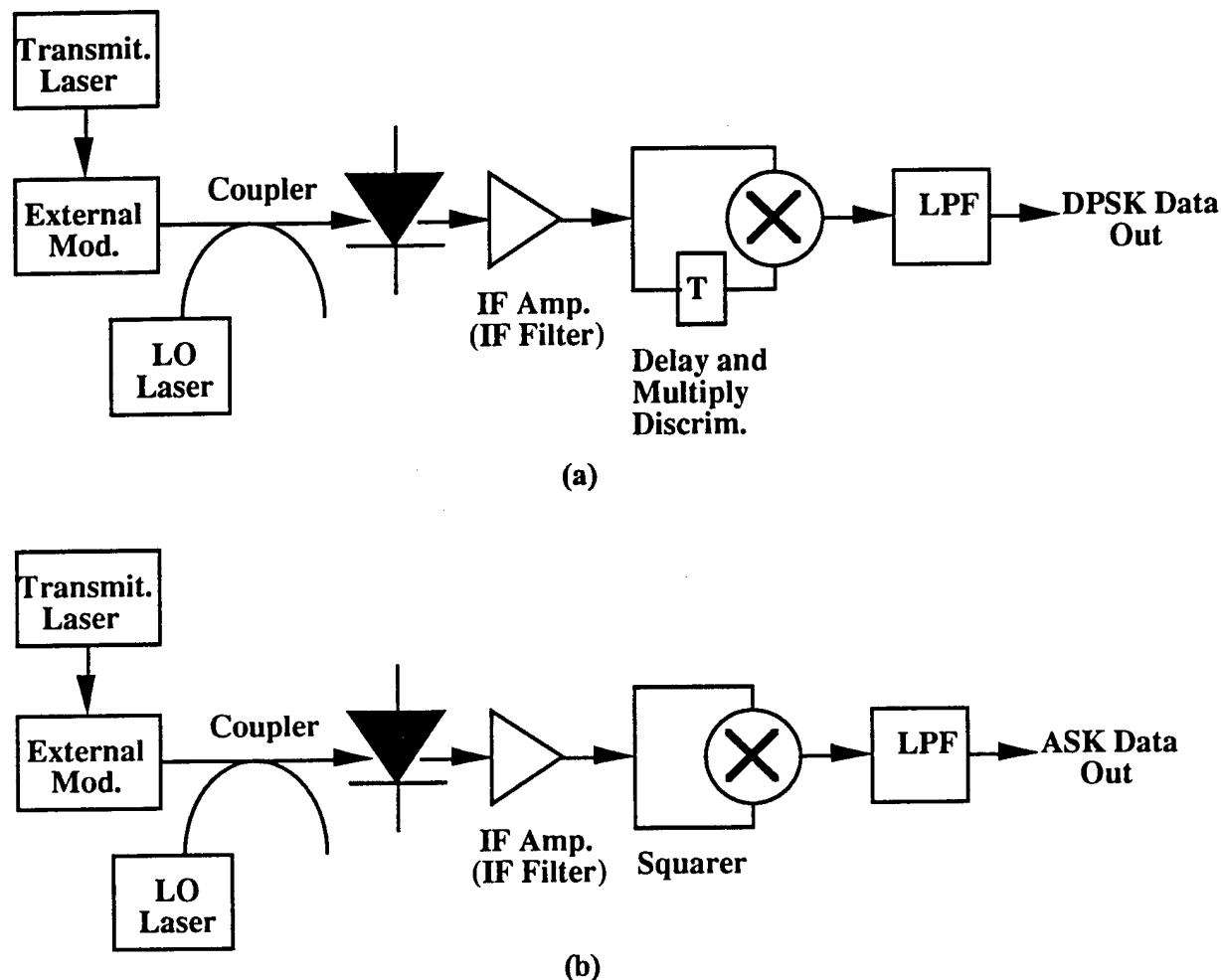


Figure 4-1. Block diagrams of (a) DPSK heterodyne system with delay and multiply detection and (b) ASK heterodyne system using envelope detection.

Graph (a) assumes an ideal available phase modulation depth of ± 90 degrees. For this case, a combined linewidth of 1% of the DPSK bit rate (25 MHz) causes a performance degradation of approximately 3 dB. The optimum ASK modulation depth shifts from about 0.48 for zero linewidth to about 0.39 for a 25 MHz combined linewidth, since more available power for DPSK is needed to compensate for the increase in linewidth. The only plot shown for ASK is for no linewidth because the wide IF filter in the ASK receiver renders negligible the effect of a linewidth equal to 20% of the ASK bit rate (25 MHz).

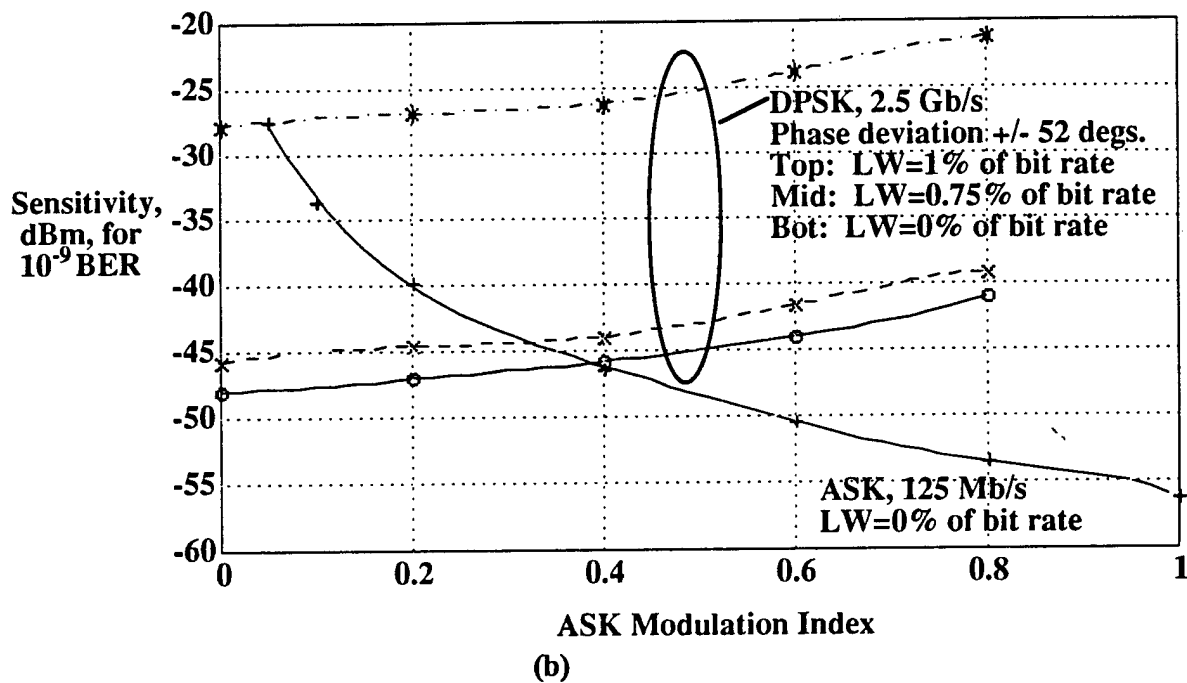
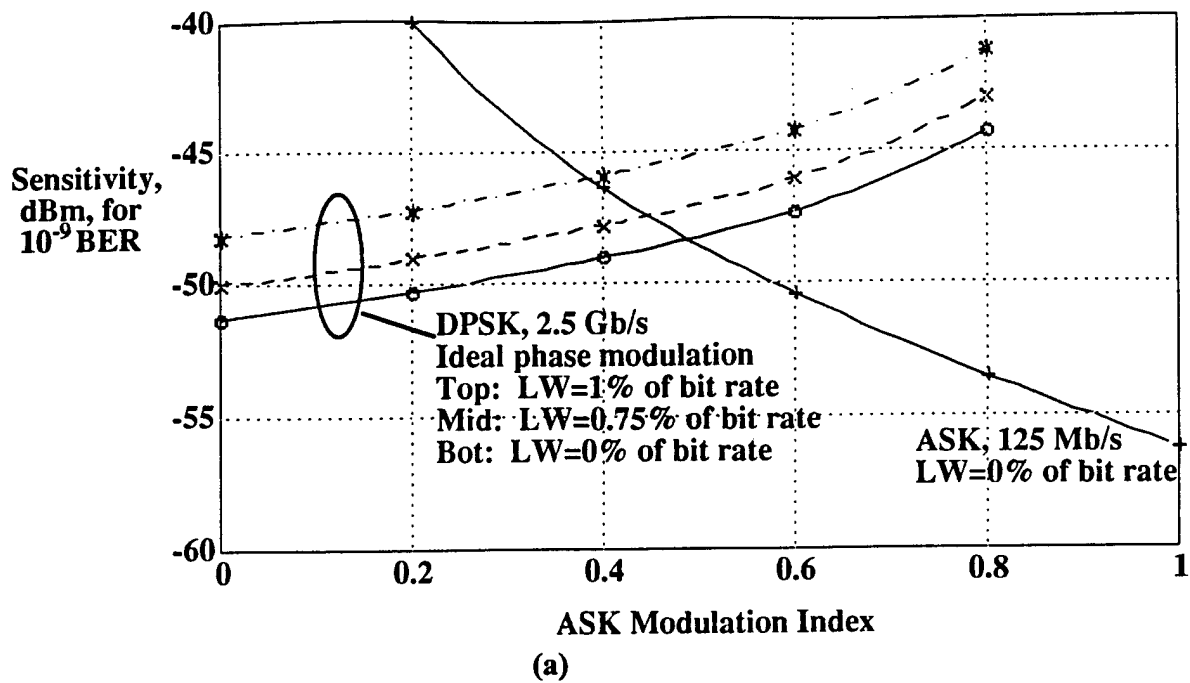


Figure 4-2. Plots of DPSK and ASK receiver sensitivities versus ASK modulation depth (power basis) for different values of laser linewidth. The marked points are the results of theoretical modeling. Plot (a) is for ideal phase modulation; plot (b) is for a modulator phase deviation of +/- 52 degrees.

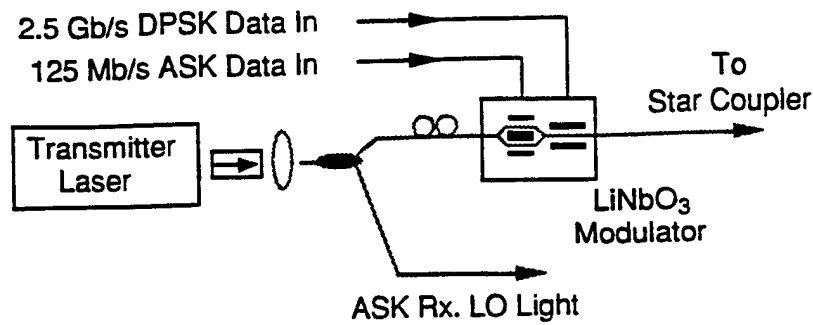
Graph (b) assumes a limited available phase modulation depth of ± 52 degrees. This results in a penalty, for zero linewidth, of about 3 dB for DPSK. For this case, a combined linewidth of 1 % of the DPSK bit rate causes a performance degradation of about 20 dB, which indicates that the bit error rate (BER) floor occurs at about 10^{-9} . Under these circumstances, the optimum ASK modulation depth is near zero, which corresponds to nearly full power availability for DPSK.

These results indicate that the use of semiconductor lasers in future STARNET implementations is potentially feasible, provided that the transmitter and local oscillator have sufficiently low linewidths to give acceptable receiver sensitivities. Since the linewidth-induced degradation of DPSK is dependent on bit rate, each transmitter/local oscillator pair should be used with a DPSK bit rate at least 125 times the combined linewidth of the lasers. Also, the lasers should satisfy the power and tunability requirements dictated by the overall network configuration.

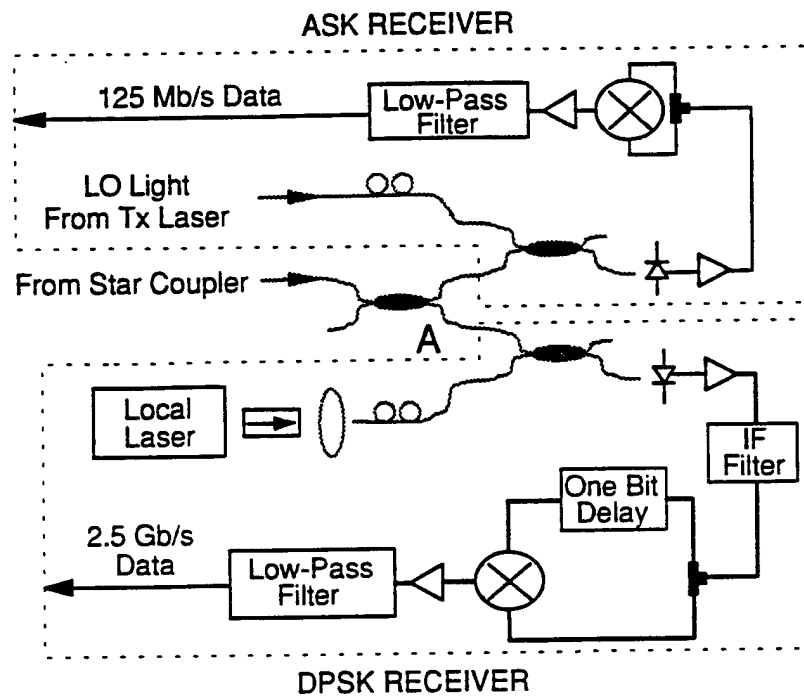
4.3 Combined ASK and DPSK Modulation: Demonstration

We have constructed a proof-of-concept experimental demonstration of simultaneous transmission and reception of fast DPSK circuit-switched data and slower ASK packet-switched data. Fig. 4-3 shows a block diagram of the experimental transceiver. The 2.5 Gb/s phase modulation and the 125 Mb/s amplitude modulation are multiplexed in the transmitter using a single LiNbO_3 modulator with both phase and amplitude modulation sections. The lasers are single frequency, 25 mW, 1320 nm, miniature diode-pumped Nd:YAG lasers.

Fig. 4-4 shows the BER curves and eye diagram for the 2.5 Gb/s DPSK receiver. The eye diagram is for a $2^{10} - 1$ pseudo-random bit sequence (PRBS) with a BER $< 10^{-10}$. The DPSK receiver sensitivity in the absence of ASK modulation is -37.3 dBm (measured in front of the 3 dB coupler at point A in Fig. 1), for a $2^{23} - 1$ PRBS. This sensitivity is 10.9 dB from the quantum limit for a single-detector DPSK heterodyne receiver. Of this penalty, 2.4 dB are due to non-ideal photodetection, 2.8 dB are due to thermal noise, and 5.7 dB are due to the electrical impedance mismatch in the modulator, crosstalk between the two modulator electrodes, and non-ideal IF and low-pass filtering. No appreciable pattern-dependent penalty is observed.



(a)



(b)

Figure 4-3. Block diagram of the experimental transceiver showing (a) the DPSK/ASK transmitter and (b) the 2.5 Gb/s DPSK receiver and the 125 Mb/s ASK receiver.

Fig. 4-5 shows the DPSK receiver sensitivity penalty versus ASK modulation depth. The theoretical curve is calculated for a simple model assuming that the power penalty is due to the reduced received signal power when an ASK zero is transmitted. The measured experimental points agree well with the theoretical predictions. Because DPSK and PSK modulation are the same on the transmitter side (except for differential

encoding), the performance of the ASK receiver under DPSK/ASK modulation is similar to [4].

This experiment shows that data can be transmitted simultaneously to two different receivers using DPSK and ASK modulation formats with good sensitivity. Though our demonstration used solid-state lasers for convenience, the performance of combined DPSK and ASK using semiconductor lasers can be expected to be very similar, with a slight penalty due to the linewidth of the lasers. From Fig. 4-2(a), a DPSK sensitivity penalty of 3 dB is observed assuming a combined linewidth of transmitter and local oscillator of 25 MHz. This combined linewidth is easily attainable using commercially available distributed feedback (DFB) lasers and can be exceeded with multi-quantum well DFB research devices.

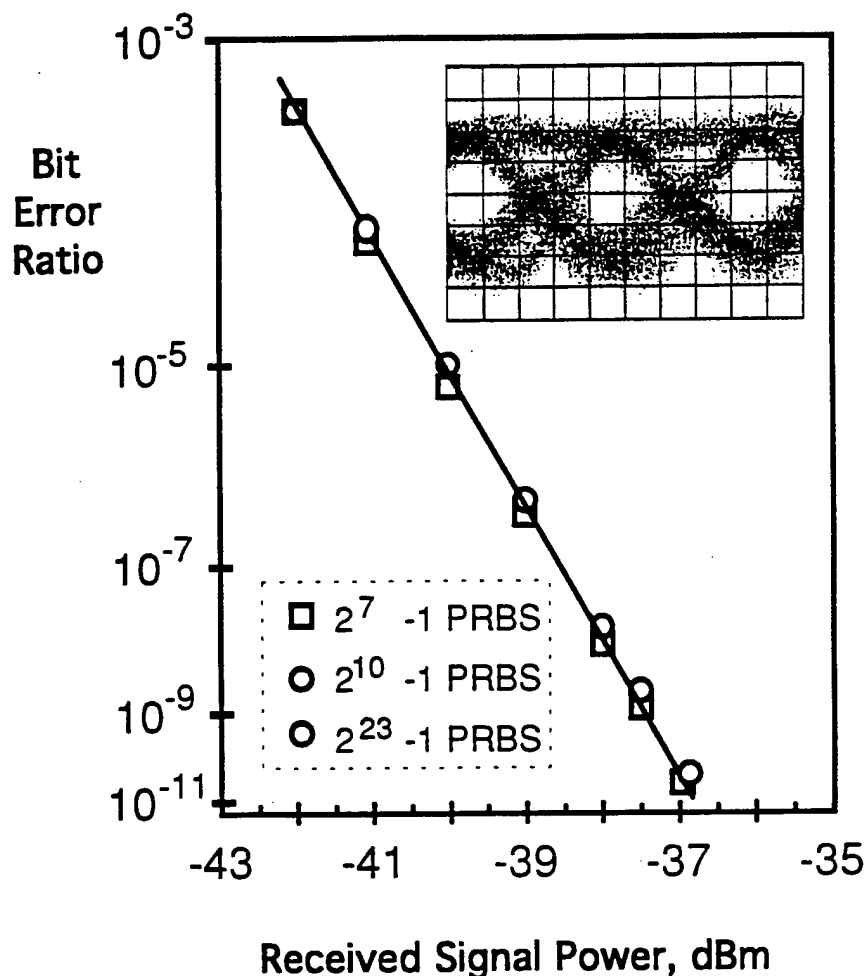


Figure 4-4. Bit error rate versus received signal power and eye diagram (2¹⁰-1 PRBS, BER < 10⁻¹⁰) for the 2.5 Gb/s DPSK receiver.

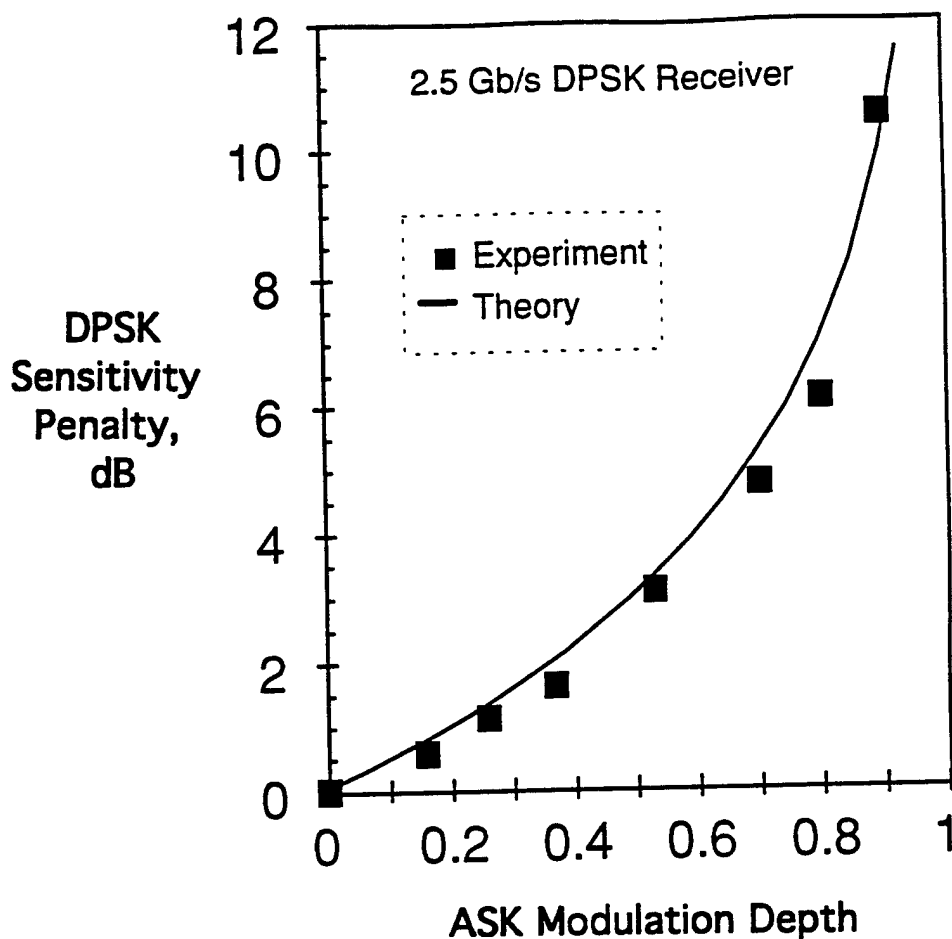


Figure 4-5. 2.5 Gb/s DPSK receiver sensitivity penalty versus ASK modulation index.

4.4 Incomplete ASK Modulation: Theory

4.4.1 Optically Amplified Direct Detection Versus Heterodyne ASK

The polarization control (PC) version of the OADD receiver is shown in Fig. 4-6. The optical amplifier (OA) is assumed to have a flat gain G over the bandwidth of interest. The PC receiver contains a polarization controller to maximize signal transmission and a polarization filter to filter out amplified spontaneous emission (ASE) noise in the orthogonal polarization. The simplest version of this receiver does not contain polarization control or filtering and hence is a polarization diversity (PD) configuration provided that ASE noise dominates receiver shot and thermal noise (since the amplifier is in general not polarization independent). The optical filter filters out

excess ASE noise and is followed by a direct detection receiver. As in [3], we model the optical filter with the normalized lowpass-equivalent impulse response of a bandpass integrator over duration τ . The lowpass filter sums M consecutive output samples, where M is the ratio between the bit duration T and the IF filter impulse response duration τ .

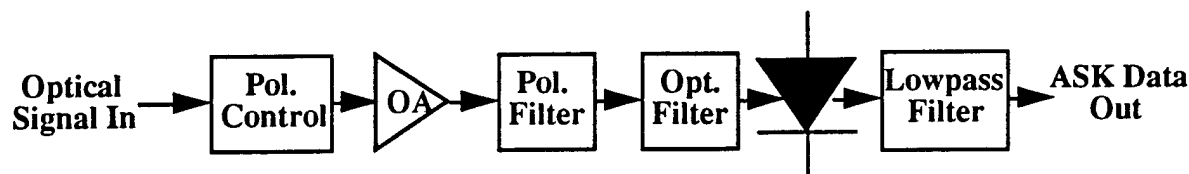


Figure 4-6. An optically amplified direct detection (OADD) receiver utilizing polarization control.

The analysis presented in this section is directly applicable not only to the OADD system, but also to the heterodyne coherent system shown in Fig. 4-7. The polarization control used during heterodyning corresponds to the polarization control in Fig. 4-6; the gain obtained through mixing with the local oscillator (LO) laser combined with the additive noise of the photodetector correspond to the optical amplifier; and the nonsynchronous receiver corresponds to the optical filter followed by the direct detection receiver. The responsivity of the photodiode in Fig. 4-7 corresponds to the spontaneous emission factor of the optical amplifier in Fig. 4-6; the LO shot noise corresponds to the ASE noise; and the conversion loss of the microwave squarer corresponds to the responsivity of the photodiode in Fig. 4-6. The duality of the results for these two systems is maintained so long as the ASE noise is dominant in the OADD system and the LO shot noise is dominant in the ASK heterodyne system. Hence, the analysis in this section is also applicable to the degradation of ASK performance in optical networks utilizing combined modulation, such as STARNET.

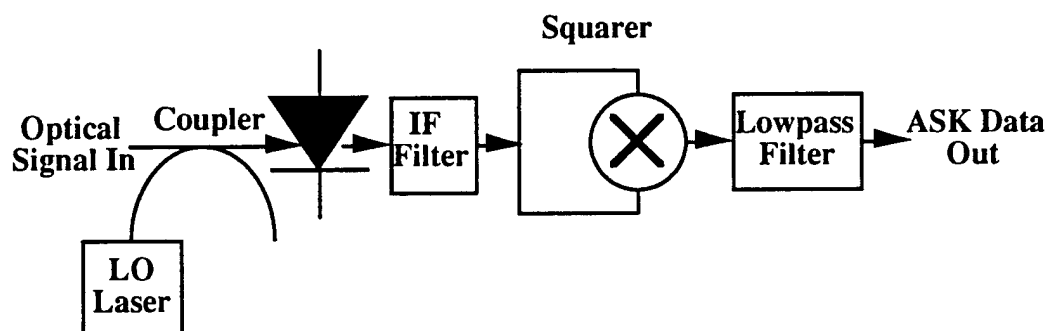


Figure 4-7. A heterodyne coherent ASK receiver utilizing nonsynchronous detection.

4.4.2 Analysis of OADD Systems with Incomplete ASK Modulation

4.4.2.1 Rigorous Method

For either ones or zeroes, the optical signal field prior to the optical filter in Fig. 4-6 is given by

$$E_A(t) = \sqrt{2GP_i} \exp(j\phi(t)) + n_{1s}(t) + Kn_{2s}(t) \quad (4.1)$$

where P_i corresponds to an input power P_{on} for a one (or "on" symbol) and to P_{off} for a zero (or "off" symbol). The influence of the optical amplifier on the phase noise process $\phi(t)$ is assumed to be negligible [5]. $n_{1s}(t)$ and $n_{2s}(t)$ represent the ASE white noise components in the signal polarization and orthogonal to the signal polarization, respectively. K is 0 for a PC receiver and 1 for a PD receiver. The single-sided power spectral density of each ASE component is [6]

$$N_{ss} = Ghfn_{sp} \quad (4.2)$$

where hf represents the average energy of the spontaneously emitted photons and n_{sp} is the amplifier spontaneous emission factor [7]. Since the optical filter has a rectangular impulse response over duration τ , the incident field on the photodiode at an output sampling instant is given by

$$E_B(t) = \sqrt{2GP_i} \left(\frac{1}{\tau} \int_0^\tau \exp(j\phi(t)) dt \right) + n_{1s} + Kn_{2s} \quad (4.3)$$

n_{1s} and n_{2s} are random noise samples with variances proportional to the noise-equivalent bandwidth of the optical filter. The current after photodetection is

$$i_d(\tau) = \frac{R}{2} E_B(\tau) E_B^*(\tau) + n_{rec}(t) \quad (4.4)$$

Since ASE noise is assumed to be dominant, the receiver shot and thermal noise ($n_{rec}(t)$) can be neglected. In this case, the detected photocurrent can be written as

$$i_d(\tau) = \frac{R}{2} \left[\sqrt{2GP_i} \left(\frac{1}{\tau} \int_0^\tau \exp(j\phi(t)) dt \right) + n_{1s} + Kn_{2s} \right] [c. c. terms] \quad (4.5)$$

After Taylor-expanding the phase noise terms and normalizing the peak photocurrent to $\sqrt{P_i}$, the photocurrent becomes

$$i(\tau) = \left[\left(\sqrt{P_i} \left\{ 1 + j\sqrt{D\tau} \int_0^1 \psi(x) dx - \frac{D\tau}{2} \int_0^1 \psi^2(x) dx + \dots \right\} \right) + n'_{1s} + Kn'_{2s} \right] [c. c. terms] \quad (4.6)$$

where $\psi(x) = \frac{1}{\sqrt{D\tau}} \phi(t)$ as in [8]. D represents the phase diffusion constant. After dropping higher-order cross-terms, the photocurrent can be written as

$$i(\tau) = \left| \sqrt{P_i} + n'_{1s} \right|^2 + \left| Kn'_{2s} \right|^2 + P_i D \tau \left[\left(\int_0^1 \psi(x) dx \right)^2 - \int_0^1 \psi^2(x) dx \right] \quad (4.7)$$

The first term, hereafter denoted as term 1, represents the signal and the ASE noise in the same polarization. Term 2 represents the ASE noise in the orthogonal polarization; due to the orthogonality, no cross terms are generated between this noise and the signal. Term 3 represents the cross-terms between the phase noise and the signal.

As in [3], the probability density functions (PDFs) of ones and zeroes at the output can be determined by inverse Laplace transforming the product of the moment generating functions (MGFs) of term 1 through term 3 for $P_i = P_{on}$ and $P_i = P_{off}$, respectively. The PDF of term 1 is given by a Rayleigh-Ritz distribution for both ones and zeroes. The MGF of term 1 can be expressed as [3], [8]

$$M_1(s) = \frac{\exp\left(\frac{-sm^2}{1+2s\sigma^2}\right)}{1+2s\sigma^2} \quad (4.8)$$

where $m^2 = P_i$ [9] and $\sigma^2 \approx \frac{Mn_{sp}}{2n_p}$ [3]. n_p is the number of photons entering the optical amplifier during a bit time T , and n_{sp} is the amplifier spontaneous emission factor [7].

The PDF of term 2 is given by a central chi-squared distribution with two degrees of freedom [6]. The MGF of term 2 is equal to $M_1(s)$ at $m = 0$, or

$$M_2(s) = \frac{1}{1 + 2s\sigma^2} \quad (4.9)$$

The MGF of term 3 is given by [10]

$$M_3(s) = \text{sinhc}^{\frac{1}{2}}(\sqrt{-2sD\tau}) \quad (4.10)$$

The overall MGF of the photocurrent is $M(s) = M_1(s)M_2(s)M_3(s)$. To obtain the output current, a baseband lowpass filter (which acts as a discrete-time integrator) sums M samples of the photocurrent. The MGF of the output current is then $[M(s)]^M$.

Unlike the case of complete ASK modulation, the zeroes PDF cannot be expressed by a chi-squared distribution with two degrees of freedom. Rather, the zeroes PDF is Rayleigh-Ritz, like the ones PDF, and has mean $\sqrt{P_{off}}$ and variance inversely proportional to $\sqrt{P_{off}}$. In the PD receiver, the PDFs of both ones and zeroes are convolved with the chi-squared PDF of the ASE noise of the orthogonal polarization. The impact of phase noise on the ones and zeroes is particularly interesting. Since term 3 is less than or equal to 0, the PDFs of both ones and zeroes will be shifted toward zero by an amount proportional to the linewidth and to the bit power level. As a result, the detection of zeroes is enhanced as phase noise increases, but the detection of ones is more degraded. As the difference between P_{on} and P_{off} becomes small, it is intuitive that the degradation in system performance due to linewidth should progressively decrease. This will be confirmed in the Section 4.6.

4.4.2.2 Gaussian Approximation

From Eq. (4.5) it clearly follows that the detected photocurrent is composed of signal-cross-signal, signal-cross-noise, and noise-cross-noise terms. These terms are of the form

$$\text{sig.} \times \text{sig.} = RGP_i \left| \frac{1}{\tau} \int_0^\tau \exp(j\phi(t)) dt \right|^2 \quad (4.11)$$

$$\text{sig.} \times \text{noise} = R\sqrt{2GP_i} \operatorname{Re} \left\{ \left(\frac{1}{\tau} \int_0^\tau \exp(j\phi(t)) dt \right)^* n_{1s}(t) \right\} \quad (4.12)$$

$$\text{noise} \times \text{noise} = \frac{R}{2} (n_{1s}^2(t) + Kn_{2s}^2(t)) \quad (4.13)$$

These terms then pass through a lowpass integrator before reaching the decision gate. Unlike previous papers in which the Gaussian approximation has been presented ([11-13]), all three cross-terms will in general be nonzero for both ones and zeroes. In addition, for the PD version of the OADD system, $K = 1$, which means that there is an additional noise-cross-noise component from the polarization orthogonal to the signal polarization.

The Gaussian approximation assumes that the PDFs for both ones and zeroes are Gaussian, and hence the bit error rate (BER) can be estimated as [11-13]

$$\text{BER} = Q(\gamma) = \frac{1}{\sqrt{2\pi}} \int_{\gamma}^{\infty} \exp\left(-\frac{x^2}{2}\right) dx \quad (4.14)$$

where γ is the SNR at the input to the decision gate and is defined as

$$\gamma \equiv \frac{m(\text{for "one" bit}) - m(\text{for "zero" bit})}{\sigma(\text{for "one" bit}) + \sigma(\text{for "zero" bit})} \quad (4.15)$$

with m being the first and σ being the second conditional moment at the receiver output, respectively. Using the method presented in [13], the expression for γ taking into account incomplete ASK modulation and a polarization diversity system configuration is

$$\gamma = \frac{\left(1 - \frac{P_{\text{off}}}{P_{\text{on}}}\right) E_{pn} \sqrt{2BT} (a + b - 1)}{\left\{ c E_{pn}^2 + (1 + K) \frac{(BT)^2 a^4}{2} + 2(BT) E_{pn} a^2 (a + b - 1) \right\}^{0.5} + \left\{ c \left(\frac{P_{\text{off}}}{P_{\text{on}}}\right)^2 E_{pn}^2 + (1 + K) \frac{(BT)^2 a^4}{2} + 2\left(\frac{P_{\text{off}}}{P_{\text{on}}}\right) (BT) E_{pn} a^2 (a + b - 1) \right\}^{0.5}} \quad (4.16)$$

where

$$a = \frac{\pi \Delta \nu}{B} \quad (4.17)$$

$$b = \exp(-a) \quad (4.18)$$

$$c = 2 \left[a^2 - \frac{11}{2}a - \frac{16}{3}ab + \frac{80}{9}(1-b) + (1-b^2) - \frac{1}{72}(1-b^4) \right] \quad (4.19)$$

E_{pn} is the peak normalized signal energy in photons/bit. As defined previously, $K = 0$ for a PC system and $K = 1$ for a PD system.

4.5 Incomplete ASK Modulation: Numerical Evaluation

In our implementations of the rigorous method and the Gaussian approximation, we assume that the spontaneous emission of the optical amplifier is the dominant additive noise to clarify the tradeoff between amplified spontaneous emission (ASE) and phase noise inherent to the choice of optical filter bandwidth.

4.5.1 Evaluation Procedure for Rigorous Method

The evaluation of the PDFs for zeroes and ones at the decision gate was performed with the help of a numerical discrete Fourier transform (DFT) routine. We found the PDFs by finding $M_3'(s)$ corresponding to the truncated phase noise PDF and then inverse-transforming the product $[M(s)]^M$ described after Eq. (4.10). We use this truncation to avoid the non-physical prediction of a negative decision voltage for a signal influenced, for instance, by phase noise alone [14, 15]. After summing the PDFs for zeroes and ones to give the cumulative distribution functions (CDFs), we assumed that the transmissions of zeros and ones were equally probable. The overall CDF was then found using the relation

$$cdf(v) = \frac{1}{2}cdf_1(v) + \frac{1}{2}cdf_0(v) \quad (4.20)$$

The optimum threshold voltage v_{opt} was then found by incremental search in the region of the dip in $cdf(v)$. $cdf(v_{opt})$ corresponds to the output bit error rate (BER).

The above procedure was carried out for both the PC and PD receivers for several different ASK modulation depths and laser linewidths. In each case, we incremented the optical filter bandwidth by integer multiples of the bit rate to find the optimum bandwidth which would balance the degradations due to ASE noise and due to laser linewidth, respectively. As the optical filter bandwidth is increased, more ASE noise is received along with the signal; as the optical filter bandwidth is reduced, the severity of phase-to-amplitude noise conversion increases. For each bandwidth, we incremented the received photons per bit in steps of 1 dB and interpolated linearly in dB of BER to find the number of photons per bit required for an output BER of 10^{-9} . The accuracy of this interpolation is shown for a variety of PC cases in Table 4-1 to be consistently within 0.03 dB of highly accurate results obtained from incrementing photons per bit with steps of 0.001 dB. The accuracy for PD cases is identical. As will be seen in Section 4.6, an interpolation error this small is not significant for the purposes of this paper. We have attempted to keep our results independent of the actual value of the bit rate by normalizing quantities such as the optical filter bandwidth, the laser linewidth, and the received optical power by the bit rate or bit duration. Our numerical results are in bit-rate-independent quantities.

Table 4-1. Comparison of photons/bit in dB
using different step sizes

Optical Filter Bandwidth (multiple of bit rate)	Linewidth (fraction of bit rate)	ASK Modulation Depth	Photons/bit in dB for BER = 10^{-9} using steps of 0.001 dB	Photons/bit in dB for BER = 10^{-9} using steps of 1 dB
1	0	0	18.843	18.825
50	0	0	21.772	21.746
1	0	0.6	27.268	27.246
50	0	0.6	27.547	27.519
1	0	0.2	38.102	38.092
50	0	0.2	38.120	38.108
10	0.5	0	20.557	20.549
25	0.5	0.6	27.604	27.577
15	1.0	0	21.062	21.055
45	1.0	0.6	27.724	27.701
91	1.0	0.2	38.203	38.180

We found that due to restrictions on the maximum number of points in the DFT and on the precision of our numerical computation, the accuracy and resolution of the

computed PDFs was limited by the significant extent of the phase noise MGF (given by Eq. (4.10)) for small $D\tau$. $D\tau$ represents the product of the phase diffusion constant and the optical filter time constant and is proportional to the optical power level on zeroes and ones, respectively. $D\tau$ is smaller for zeroes than for ones and decreases as the optical filter bandwidth increases. In our numerical computation, we restricted $D\tau$ to values larger than 0.05, a conservative threshold which guarantees numerical convergence of the DFT. As a result, some of our optimum bandwidths (see Tables 4-2 and 4-3 in Section 4.6) are lower bounds for the actual value of the optimum bandwidth. The error incurred, however, is not significant, since the optical filter bandwidth is always large enough for small $D\tau$ to severely limit the impact of phase noise on system performance.

4.5.2 Evaluation Procedure for Gaussian Approximation

We solved analytically for E_{pn} in Eq. (4.16) as a function of γ , the SNR at the decision gate, by using the basic quadratic formula. To choose between the two generated roots, we noted that E_{pn} increases monotonically with γ , which means that there is always exactly one positive root for any positive value of γ . We optimized the optical filter bandwidth for different ASK modulation depths and laser linewidths for both the PC and PD receiver implementations; as above, we minimized the received photons per bit required for an output BER of 10^{-9} . No interpolation is necessary in this computation.

4.6 Incomplete ASK Modulation: Numerical Results and Discussion

Our numerical results are divided into two sections. In Section 4.6.1, we consider the penalties in received photons per bit due to different ASK modulation depths and due to the PD receiver configuration relative to the PC receiver configuration for different optical filter bandwidths. In Section 4.6.2, we consider the impact of laser linewidth on receiver performance and present optimum optical filter bandwidths for different laser linewidth values.

4.6.1 Results for Zero Linewidth

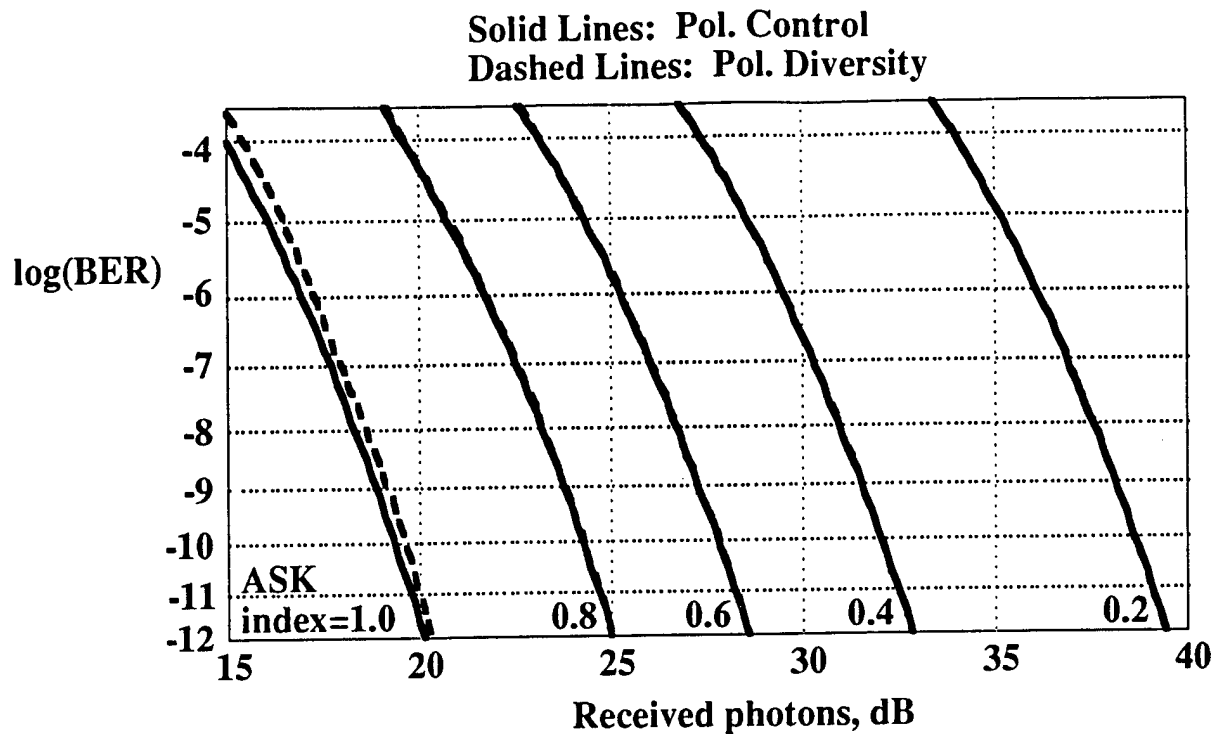


Figure 4-8. Output BER as a function of dBs of received photons. This plot is for the optical filter bandwidth equal to the bit rate and zero linewidth.

Fig. 4-8 shows the BER at the output decision gate as a function of dBs of received photons per bit. BER plots are given for both the PC and PD receiver configurations for ASK modulation depths ranging between 0.2 and 1.0 (complete modulation). Since zero linewidth is assumed for this plot, the optimum IF bandwidth is equal to the bit rate for all cases. For an ASK modulation depth of 1.0, there is a slight but noticeable degradation in the performance of the PD receiver due to the noise in the orthogonal polarization. For both the PC and PD systems, the performance degradation at small optical filter bandwidths as the ASK modulation depth is reduced from 1.0 to 0.8 is pronounced since an "off" symbol-ASE noise cross term is generated for incomplete ASK modulation depths. The introduction of this term has the greatest impact for narrow optical filter bandwidths because under such circumstances the "on" symbol-ASE noise cross term is less dominant for large ASK modulation depths. As the ASK modulation depth is further reduced by intervals of 0.2, the decreasing separation between the received powers of the "on" and "off" symbols also significantly affects system performance. At an output BER of 10^{-9} , this degradation is 0.27 dB, which corresponds to about 81.2 photons per bit for the PD case as compared to 76.3 photons per bit for the

PC case. This agrees with previously presented results by Henry and Jacobsen [3], [6]. For ASK modulation depths less than 1.0, the degradation in PD performance is barely discernible on the plot. The penalty at an output BER of 10^{-9} and an ASK modulation depth of 0.8 is 0.02 dB and is even less for more incomplete ASK modulation. Since the power of the noise in the orthogonally polarization is independent of the optical signal power, it has a less significant impact as the number of received photons increases for each ASK modulation depth. As the ASK modulation becomes more incomplete, the increasing optical signal power used for the transmission of zeroes results in a marked decrease in the impact of the noise in the orthogonal polarization.

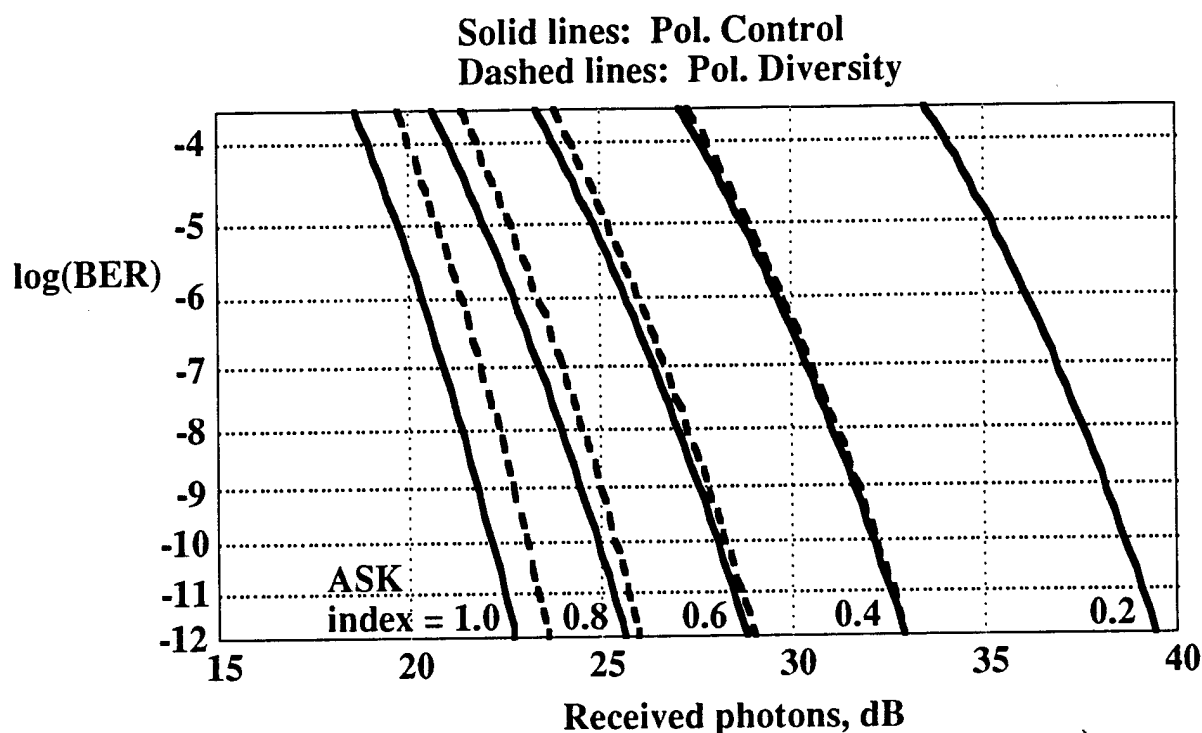


Figure 4-9. Output BER as a function of dBs of received photons. This plot is for the optical filter bandwidth equal to 50 times the bit rate and zero linewidth.

Fig. 4-9 is identical to Fig. 4-8 except that the optical filter bandwidth assumed for this plot is 50 times the bit rate. Since more ASE noise passes through the optical filter, there is clearly a power penalty relative to the case plotted in Fig. 3 (minimum IF filterbandwidth). The most obvious performance degradation is in the case of complete ASK modulation, which occurs due to the sharply increased impact of the "on" symbol-ASE noise cross term. There is also a greater penalty due to the impact of orthogonally polarized noise in the PD receiver. For complete ASK modulation, the penalty due to the increase in IF bandwidth for the PC receiver is 2.92 dB for an output BER of 10^{-9} . The

PD performance penalty for the larger IF bandwidth is 0.92 dB. For an ASK modulation depth of 0.8, the penalty due to the increase in IF bandwidth for the PC receiver is 0.71 dB and the PD performance penalty is 0.52 dB. It is clear from these two figures that the penalty due to the polarization diversity approach is consistently less than 1 dB even for an optical filter bandwidth of 50 times the bit rate.

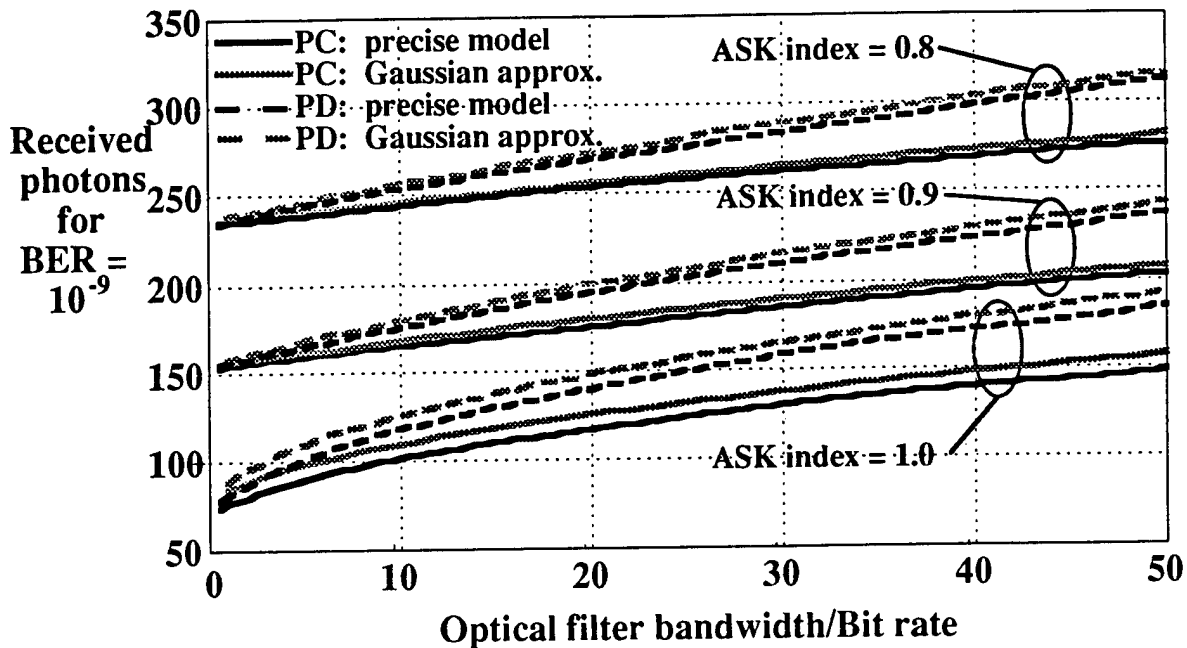


Figure 4-10. Received photons per bit as a function of the optical filter bandwidth.

Fig. 4-10 shows received photons per bit for an output BER of 10^{-9} as a function of optical filter bandwidth. Results for both the rigorous method and the Gaussian approximation are shown. The Gaussian approximation consistently overestimates the received photons per bit compared to the rigorous method for both the PC and PD receivers. This is consistent with the comparison made in [3] for the PC receiver and complete ASK modulation. It is clear that the Gaussian approximation is still very accurate for incomplete modulation and zero linewidth; it actually becomes more accurate as the ASK modulation becomes more incomplete due to the reduction in the impact of noise in the orthogonal polarization. For complete ASK modulation, the Gaussian approximation gives estimates of 84 photons per bit for an optical filter bandwidth equal to the bit rate and 157 photons per bit for an optical filter bandwidth equal to 50 times the bit rate. These estimates are 0.42 dB and 0.21 dB above the predictions of the rigorous method, respectively, which verifies the results of [12]. Also, both the rigorous

model and the Gaussian approximation predict that for optical filter bandwidths greater than about 5 times the bit rate, the PD performance degradation in received photons remains nearly constant for different ASK modulation depths due to the signal-independent noise in the orthogonal polarization. For both the PC and PD receivers, the required photons per bit increase linearly with optical filter bandwidth due to the signal-ASE noise cross term.

4.6.2 Results for Nonzero Linewidth

Tables 4-2 and 4-3 show the optimum optical filter bandwidths as a function of ASK modulation depth and linewidth as a percentage of the bit rate for the PC and PD receiver configurations. Tables 4-4 and 4-5 show the optimum optical filter bandwidths found using the Gaussian approximation. As described in Section 4.5, close lower bounds on the optimum optical filter bandwidth were found in some cases using the rigorous method due to the difficulties in the computation of the zeroes PDF for very small amounts of phase noise. The tables show that the optimum bandwidths are consistently smaller for the PD receiver than for the PC receiver. This is because the increase in ASE noise power passed through the optical filter in the PD receiver must be balanced by a reduction in the optimum optical filter bandwidth. Also, the optimum bandwidths found using the Gaussian approximation are smaller than those found using the rigorous method in all cases where an exact optimum is found. When the optimum is lower bounded using the rigorous method, then in most cases the bandwidths found using the Gaussian approximation are larger.

Fig. 4-11 shows the penalty due to linewidth in dB as a function of linewidth as a fraction of the bit rate. The penalty for a given ASK modulation depth and a given linewidth is determined relative to polarization control system performance for that modulation depth and a linewidth of zero. The optimum optical filter bandwidth for every case is used to provide a fair evaluation of the penalty. It is clear from the plot that the penalty is consistently underestimated by the Gaussian approximation. For the laser linewidth equal to the bit rate and a PD receiver, the Gaussian penalty estimate is over 1 dB below that of the rigorous method. The primary reason for this is its relatively large inaccuracy at zero linewidth, as described previously. Outside of this linewidth-independent error, the Gaussian approximation slightly underestimates the penalty due to linewidth, which is consistent with the smaller optimum filter bandwidths given in Tables 4-4 and 4-5. This shows that the assumption of Gaussian PDFs becomes less accurate when the noise in the orthogonal polarization is included. The Gaussian approximation

Table 4-2. Optimum optical filter bandwidths for the PC receiver using the rigorous method

		Linewidth (% of bit rate)				
		0	25	50	75	100
ASK Modulation Depth	Pol. Ctr. Case	1.0	0.9	0.8	0.6	0.4
	1.0	1	6	10	13	15
	0.9	1	11	15	19	23
	0.8	1	14	>12	>18	>25
	0.6	1	>12	>24	>37	45
	0.4	1	>18	>37	45	60
	0.2	1	>14	>29	>74	>91

Table 4-3. Optimum optical filter bandwidths for the PD receiver using the rigorous method

		Linewidth (% of bit rate)				
		0	25	50	75	100
ASK Modulation Depth	Pol. Div. Case	1.0	0.9	0.8	0.6	0.4
	1.0	1	6	9	12	14
	0.9	1	9	13	16	19
	0.8	1	11	>12	>18	23
	0.6	1	>12	>24	29	35
	0.4	1	>18	>37	45	51
	0.2	1	>14	>29	>74	>86

Table 4-4. Optimum optical filter bandwidths for the PC receiver using the Gaussian approximation

		Linewidth (% of bit rate)				
		0	25	50	75	100
ASK Modulation Depth	1.0	1	4	7	9	10
	0.9	1	7	11	13	15
	0.8	1	10	14	18	20
	0.6	1	17	24	29	34
	0.4	1	29	41	51	59
	0.2	1	65	94	115	133

Table 4-5. Optimum optical filter bandwidths for the PD receiver using the Gaussian approximation

		Linewidth (% of bit rate)				
		0	25	50	75	100
ASK Modulation Depth	1.0	1	4	6	8	9
	0.9	1	6	9	11	13
	0.8	1	8	11	14	17
	0.6	1	13	19	23	27
	0.4	1	23	32	40	46
	0.2	1	51	73	89	103

becomes more accurate as the ASK modulation depth decreases because the significance of the orthogonal noise is reduced. The plot also indicates that the penalty due to linewidth decreases with decreasing ASK modulation depth.

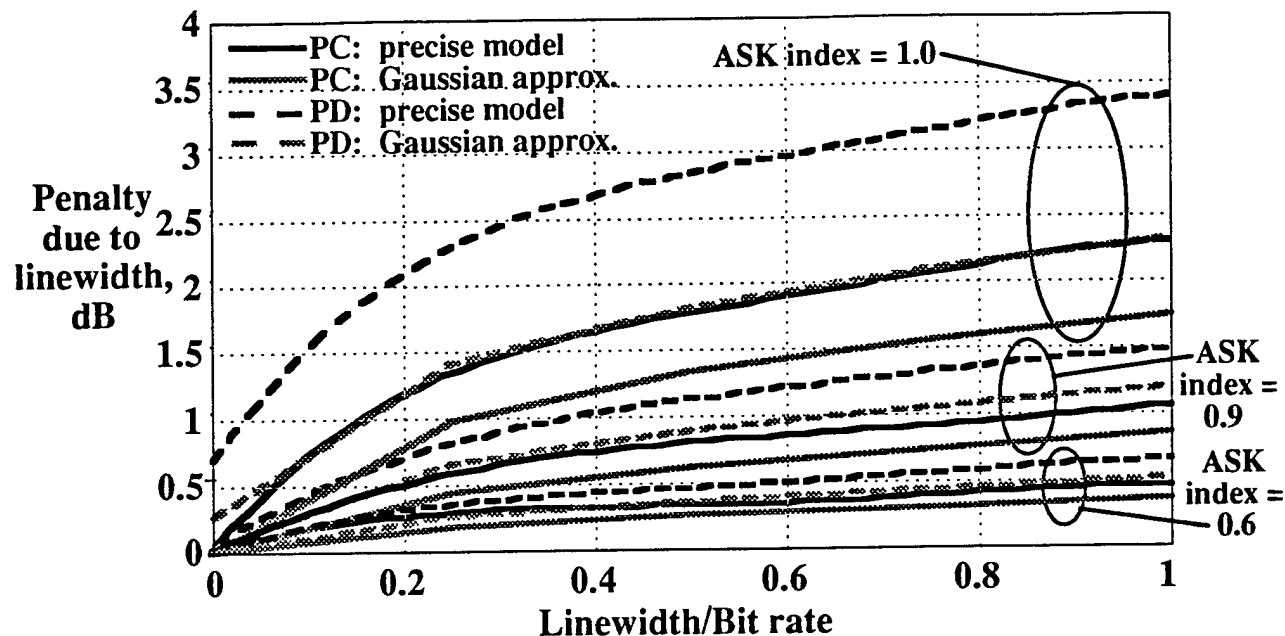


Figure 4-11. Penalty due to linewidth in dB as a function of linewidth as a fraction of the bit rate.

Fig. 4-12 shows the penalty due to linewidth as a function of ASK modulation index for different values of laser linewidth and an optical filter bandwidth of 10 times the bit rate. The penalty at each point is computed relative to system performance at that modulation depth for zero linewidth and an optical filter bandwidth equal to the bit rate. Fig. 4-12(a) shows the noise penalty due to the wider than optimal optical filter assuming zero linewidth for purposes of comparison. Fig. 4-12(b) shows a linewidth-induced floor in the usable ASK modulation depth. It was explained in the Theoretical Analysis section that the detection of zeroes is enhanced by linewidth. However, this is only true if the optical filter bandwidth is maintained at its *optimal* value. For a fixed optical filter bandwidth, there will be a minimum usable ASK modulation depth which is dependent on the laser linewidth. This floor is adequately predicted by the Gaussian approximation in Fig. 4-12(b), but for a laser linewidth equal to the bit rate in Fig. 4-12(c), the floor is not predicted accurately.

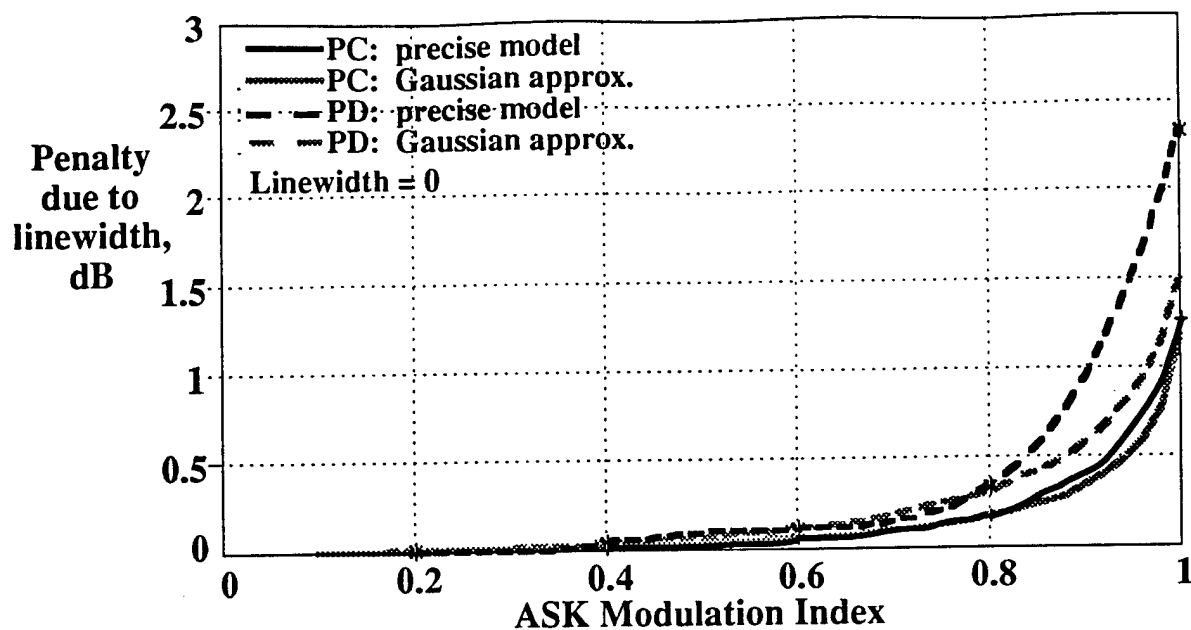


Figure 4-12(a). Penalty due to linewidth in dB as a function of ASK modulation depth for zero linewidth and an optical filter bandwidth of 10 times the bit rate.

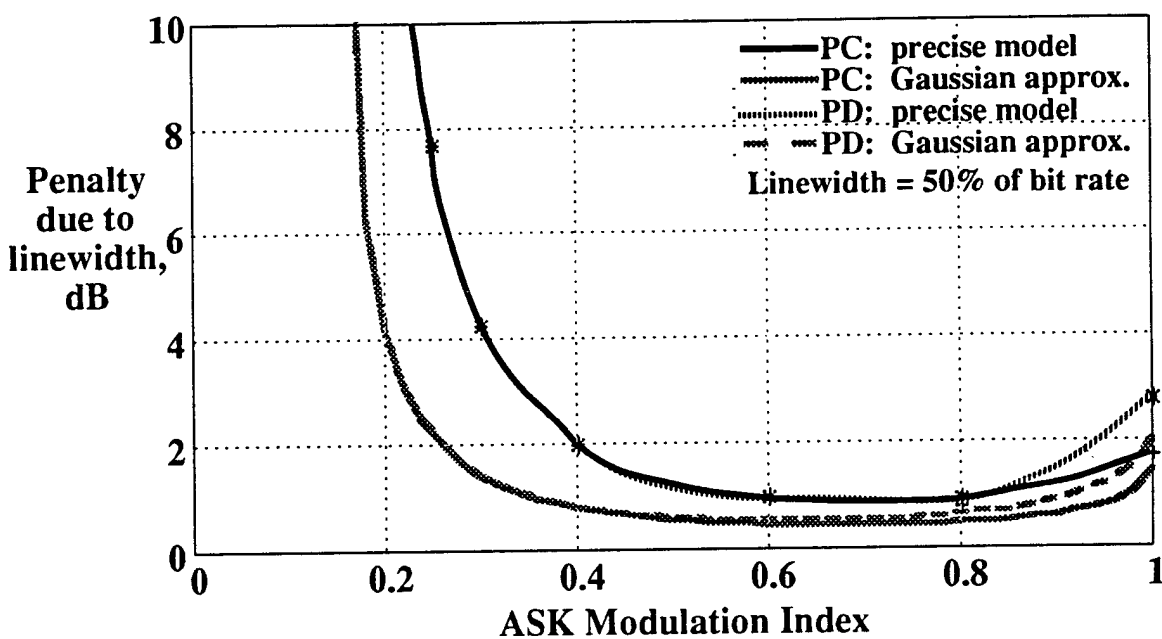


Figure 4-12(b). Penalty due to linewidth in dB as a function of ASK modulation depth for a linewidth of half the bit rate and an optical filter bandwidth of 10 times the bit rate.

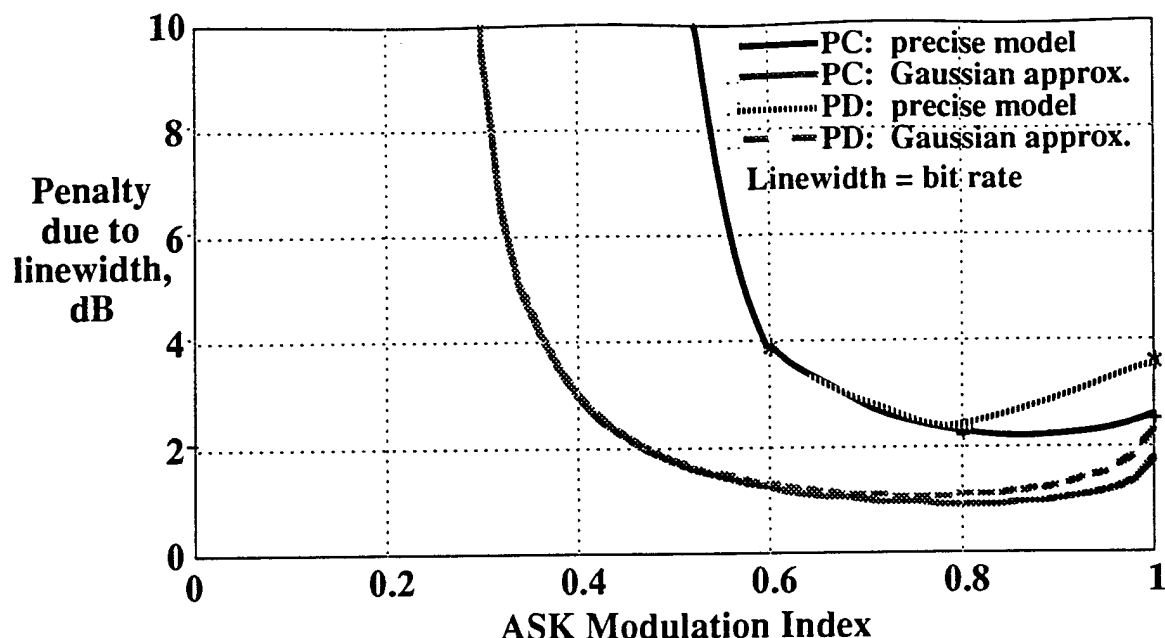


Figure 4-12(c). Penalty due to linewidth in dB as a function of ASK modulation depth for a linewidth equal to the bit rate and an optical filter bandwidth of 10 times the bit rate.

The situation described in Fig. 4-12 is an example of a practical situation which could occur in the design of a coherent optical network such as STARNET or in a network utilizing optical filters for channel selection and direct detection receivers. It may not be desirable for purposes of channel selection to restrict the choice of IF filter or optical filter bandwidth to the optimum value or even a value near the optimum. Therefore, for combined intensity and phase modulation to be used in such a network, it is of great importance to have accurate estimates of the minimum usable ASK modulation depth for linewidths equal to a significant fraction of the bit rate. For moderate-speed packet-switched applications and semiconductor laser transmitters, this will often be the case. It is clear from Fig. 4-12 that the Gaussian approximation consistently underestimates the minimum usable ASK modulation depth and that the rigorous method may be necessary to obtain accurate estimates.

4.7 Conclusions

The theoretical results for combined DPSK and ASK indicate that an excellent sensitivity may be simultaneously maintained by both receivers, even for linewidths up to one percent of the bit rate for DPSK. As a result, this combined modulation format is attractive for WDM networks using semiconductor lasers, since a phase-locked loop is

not required for the DPSK receiver (unlike the PSK receiver). Our experimental demonstration of simultaneous DPSK and ASK link operation indicates that this format for sending network data and control information is not difficult to implement.

We have extended the previously developed rigorous model of Jacobsen and Garrett and Gaussian approximation of Kazovsky and Tonguz for optically amplified direct detection (OADD) ASK systems. The new models account for incomplete ASK modulation, which is encountered in typical systems using either direct or external intensity modulation. The new models also include the impact of nonzero laser linewidth and spontaneous emission noise of the optical amplifier. As a result, the new models can be used to optimize the optical filter bandwidth in OADD systems for a wide range of ASK modulation depths and laser linewidths. The new models also explicitly take into account the spontaneous emission noise in the orthogonal polarization in polarization diversity (PD) OADD systems.

We provide comprehensive sets of results for both zero linewidth and nonzero linewidth cases. Plots of BER as a function of dBs of received photons and plots of received photons as a function of optical filter bandwidth for different ASK modulation depths are shown for zero linewidth. The penalty incurred by the use of a PD configuration is always less than 1 dB for the wide variety of cases considered. The Gaussian approximation is very accurate for both the polarization control (PC, with polarization filter) and PD configurations. For nonzero linewidth, tables of optimum optical filter bandwidths in the PC and PD configurations are provided for different ASK modulation depths and laser linewidths. The Gaussian approximation frequently underestimates the optimum filter bandwidths. Plots of the penalty due to linewidth as a function of laser linewidth and ASK modulation depth are also shown for both optimum and nonoptimum optical filter bandwidths. The maximum predicted penalty for laser linewidth equal to the bit rate for the optimum optical filter bandwidth is 3.5 dB (for complete ASK modulation and a PD configuration). For nonoptimum filter bandwidths, the maximum penalty occurs not for complete ASK modulation; instead, a floor exists for the minimum usable ASK modulation depth due to the severe phase-to-amplitude noise conversion. This floor is not accurately predicted using the Gaussian approximation. As a result, the rigorous method is applicable in real network design in cases where the available IF filters do not have bandwidths which correspond to the optimal value for the transmitted signal bandwidth and linewidths of the transmitter and local oscillator lasers.

4.8 References

- [1] S. J. Wang et al., "A 1.7 Gb/s ASK and a 622 Mb/s Incoherent FSK transmission experiment using a 1.55- μ m multiquantum well distributed feedback laser," *IEEE Photon. Technol. Lett.*, vol. 2, no. 12, pp. 920-922, 1990.
- [2] G. Jacobsen and I. Garrett, "The Effect of Crosstalk and Phase Noise in Multichannel Coherent Optical DPSK Systems with Tight IF Filtering," *IEEE J. of Lightwave Tech.*, vol. 9, no. 11, pp. 1609-1617, 1991.
- [3] G. Jacobsen, "Multichannel System Design Using Optical Preamplifiers and Accounting for the Effects of Phase Noise, Amplifier Noise, and Receiver Noise," *IEEE J. of Lightwave Tech.*, vol. 10, no. 3, pp. 367-377, 1992.
- [4] M. Hickey, C. Barry, C. Noronha, and L. Kazovsky, "Experimental PSK/ASK transceiver for the STARNET computer communication network," *IEEE Photon. Technol. Lett.*, vol. 5, no. 5, pp. 568 - 571, 1993.
- [5] G. J. Cowle et al., "Spectral broadening due to fibre amplifier phase noise," *Electron. Lett.*, vol. 26, pp. 424-425, 1990.
- [6] P. S. Henry, "Error-rate performance of optical amplifiers," in *Tech. Dig. OFC '89*, Feb. 1989 (Houston, TX), paper THK3.
- [7] C. H. Henry, "Theory of spontaneous emission noise in open resonators and its application to lasers and optical amplifiers," *J. Lightwave Technol.*, vol. LT-4, pp. 288-297, 1986.
- [8] G. J. Foschini and G. Vannucci, "Characterizing filtered lightwaves corrupted by phase noise," *IEEE Trans. Inf. Theory*, vol. IT-34, pp. 1437-1448, 1988.
- [9] C. W. Helstrom, *Probability and Stochastic Processes for Engineers*. New York: Macmillan, 1984, ch.3.

- [10] G. Jacobsen and I. Garrett, "The effect of crosstalk and phase noise in multichannel coherent optical ASK systems," *J. Lightwave Technol.*, vol. LT-9, pp. 1006-1018, 1991.
- [11] L. G. Kazovsky and O. K. Tonguz, "ASK and FSK coherent lightwave systems: a simplified approximate analysis," *J. Lightwave Technol.*, vol. LT-8, no.3, pp. 338-352, 1990.
- [12] O. K. Tonguz and L. G. Kazovsky, "Theory of direct-detection lightwave receivers using optical amplifiers," *J. Lightwave Technol.*, vol. 9, no. 2, pp. 174-181, 1991.
- [13] L. G. Kazovsky, P. Meissner, and E. Patzak, "ASK multiport optical homodyne receivers," *J. Lightwave Technol.*, vol. LT-5, pp. 770-791, 1987.
- [14] I. Garrett and G. Jacobsen, "Phase noise in weakly coherent systems," *IEE Proc.*, Pt. J, vol. 136, pp. 159-165, 1989.
- [15] G. Jacobsen and I. Garrett, "Impact of phase noise on coherent systems - a Fokker-Planck approach," in *Proc. of the 1989 Int. Tirrenia Workshop on Dig. Comm.*, Sept. 1989 (Tirrenia, Italy), pp. 133-148.

Chapter 5

STARNET Interface

5.1 Introduction

The widespread proliferation of workstations and personal computers in the workplace, school and home has led to an exponential increase in network users [5]. Since it is desirable that computer networks merge broadcast and interactive services with the existing services we are likely to see an exponential increase in demand per user as well. The expected user applications range from electronic mail which is low bandwidth and not guaranteed, to image retrieval which requires high bandwidth, low loss and bounded delay, to video retrieval which requires guaranteed high bandwidth, bounded delay, and finally, to live video conferencing which could require handling high bandwidth multicast streams with very low delay. Fig. 5-1 quantifies delay, jitter and error loss requirements for voice, video and conferencing. In addition to providing all of these services, it is desirable that the network also be economical, scaleable, modular, reliable, fault-tolerant and interoperable (i.e. it must support heterogeneous architectures, protocols and data formats).

Requirements for Different Traffic					
Traffic	Maximum Delay	Maximum Jitter	Acceptable BER	Acceptable PER	Average Bandwidth
Voice	250 ms	10 ms	0.1	0.1	0.064 Mbps
TV Video	250 ms	10 ms	0.01	0.001	100 Mbps
Compressed Video	250 ms	1 ms	1e-6	1e-9	2-10 Mbps
Video Conference	50-100 ms	1 ms	1e-6	1e-9	0.064-2 Mbps
Image	1s	---	1e-4	1e-9	2-10 Mbps
Data Transfer	1s	---	0	0	2-100 Mbps

Figure 5-1. Real-time requirements for some broadcast and interactive services.

We report on the design of a distributed, small, fast packet switch workstation to network interface that provides electronic buffering and switching for the data channel in reconfigurable multi-Gbps WDM optical networks. The high-speed interface has been constructed and tested in one such WDM network, STARNET, which is based on a physical passive star topology and is intended for backbone applications in Campus

Networks. A two node experimental STARNET is being implemented at the Optical Communications Research Laboratory at Stanford University. The interface prototype was completed in September, 1993; the printed circuit board version of the interface has been operational without modification since January, 1994. We have since developed software from the driver level to the applications layer (e.g. from read/write memory page transfer to high-speed image/file transfer and real-time video-conferencing).

In Section 5.2, we briefly describe the STARNET optical architecture. In Section 5.3, we present an overview of our design of the electronic interface architecture for the high-speed and low-speed subnetworks of STARNET. In Section 5.4, we give a detailed description of the design of the high-speed interface. In Section 5.5, we give average latency results for STARNET obtained through simulation. Section 5.6 provides conclusions. Section 5.7 contains references.

5.2 STARNET Optical Architecture

STARNET [1, 2] is a broadband optical network designed with the intent to provide backbone services for Campus Networks (network diameter less than 10 km, several thousand users). In this context, STARNET will provide users with a means for bridging of lower speed networks such as Ethernet, FDDI, and ATM, in addition to supporting real-time interactive multimedia services. Since we limit the geographic extent to less than 10 km, we can expect our fiber optic links to operate reliably with extremely low bit error rates ($BER < 10^{-9}$) for a very modest transmitted optical power.

STARNET uses WDM over a single physical passive star topology network, and offers all users both a moderate-speed (125 Mbps) packet-switched subnetwork and a reconfigurable high-speed (up to 2.5 Gbps) circuit-switched subnetwork (see Fig. 5-2). The moderate-speed subnetwork supports standard services such as e-mail, remote logins and low volume file transfer. In addition, the communication required to configure the high-speed subnetwork and set up virtual circuits is done over the moderate-speed subnetwork. The high-speed subnetwork supports the needs of high-bandwidth, time critical, retrieval, broadcast and interactive services.

Each STARNET node has a single fixed-wavelength transmitter, which uses novel combined modulation techniques to simultaneously send moderate-speed subnetwork traffic as well as high-speed subnetwork traffic on the same transmitter carrier wavelength [3]. Each node is also equipped with a fixed-wavelength receiver, for the packet-switched subnetwork, and a wavelength-tunable receiver, for the circuit-switched subnetwork.

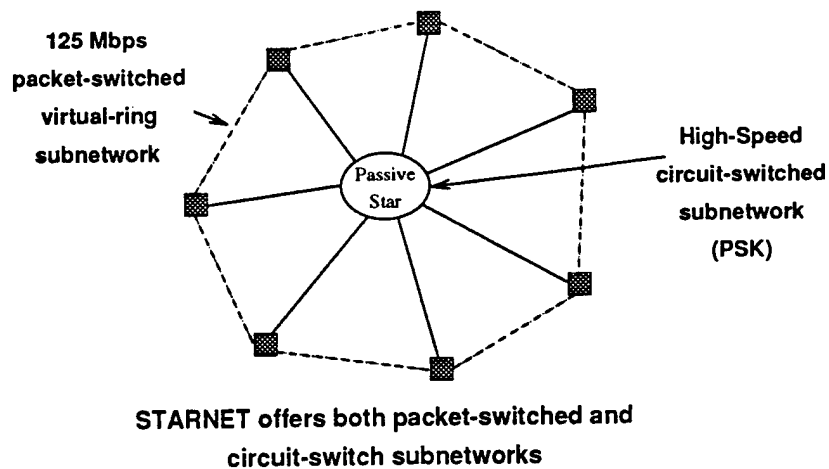


Figure 5-2. STARNET provides both a 125 Mbps packet-switched and a high speed (up to 2.5 Gbps) circuit-switched subnetworks over a single physical passive star topology. Each node is connected to the passive star by one transmit fiber and one receive fiber.

Fig. 5-3 shows how STARNET permits the two simultaneous and independent logical subnetworks over a single physical passive star. The moderate-speed subnetwork is configured by tuning each node's fixed receiver to the previous node's transmitter wavelength. This forms a fixed logical ring topology which includes all the nodes on the network. The tunable receivers that form the high-speed subnetwork are not required to be fast tuning because the intent is to form semi-permanent point-to-point or ring subgroups called "virtual LANs" for relatively long duration. Multiple virtual LANs exist simultaneously and independently, without interference. Virtual LANs can come or go or change size as deemed necessary by the network traffic under control of dynamic configuration software or under control of the system administrator using Simple Network Management Protocol (SNMP) software. In addition, the architecture can support heterogeneous communication and modulation formats (even analog) on the high-speed links, although the interface we present is specifically designed for packet-switching over virtual circuits.

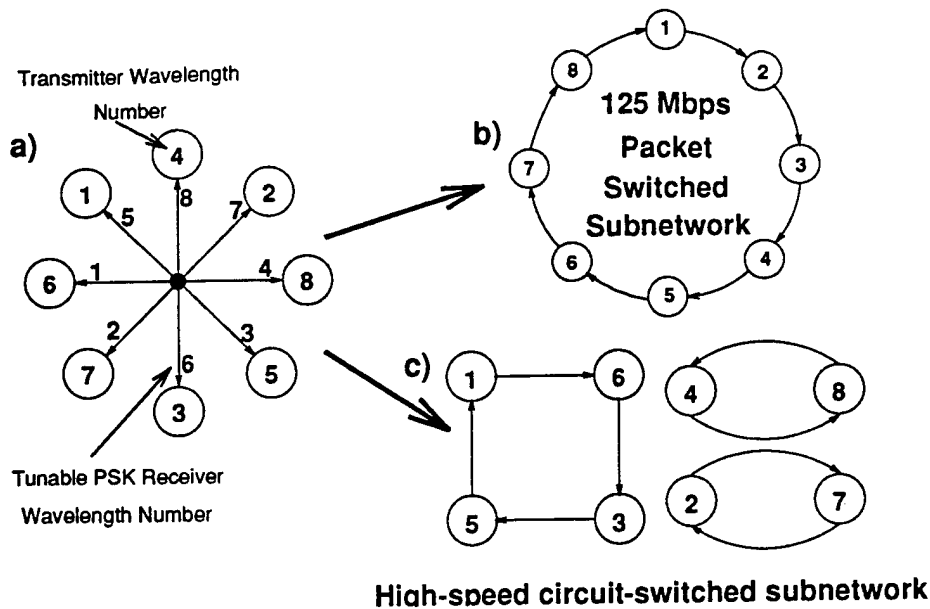


Figure 5-3. Through the use of WDM, STARNET maps (a) a physical star topology into both: (b) a logical ring topology in the moderate-speed subnetwork and (c) reconfigurable, variable size virtual-LAN rings in the high speed subnetwork.

5.3 STARNET Electronic Interface Architecture

A schematic of our experimental STARNET which interconnects two DECstation™ 5000/240 workstations is shown in Fig. 5-4. Each workstation is equipped with built-in Ethernet and SCSI ports. Off-the-shelf TURBOchannel™ bus interface cards provide real-time video and real-time audio, or access to ATM networks. Access to a CD-ROM is provided over the SCSI port. We are therefore capable of running an assortment of multimedia applications over STARNET.

5.3.1 Moderate-Speed Subnetwork

Since the intended applications of the 125 Mbps subnetwork are services such as control message passing, low-priority file transfer, e-mail, etc. and the moderate-speed network virtual topology is that of a ring, we decided to be FDDI compatible because FDDI provides excellent performance for the intended applications. We have successfully formed the moderate-speed subnetwork by interfacing commercially available FDDI-on copper interface cards to the moderate-speed section of the STARNET transceiver. The FDDI ring thus formed required no modifications to either the hardware or the software of the FDDI interface even though the connection is made through the passive star using the

STARNET transceiver. Over this subnetwork we have developed a control application using standard UNIX sockets calls and TCP/IP and UDP transport protocols to setup, configure and relay the status of the high-speed subnetwork. Since the moderate-speed subnetwork is strictly conventional, we already have access to all the normal network functions such as file-transfer, remote login, e-mail, etc.

Having now seen that the STARNET architecture naturally and easily provides for the customary data network services by way of the moderate-speed subnetwork, we turn our attention in the next section to the custom high-speed interface which provides the high bandwidth and interactive services.

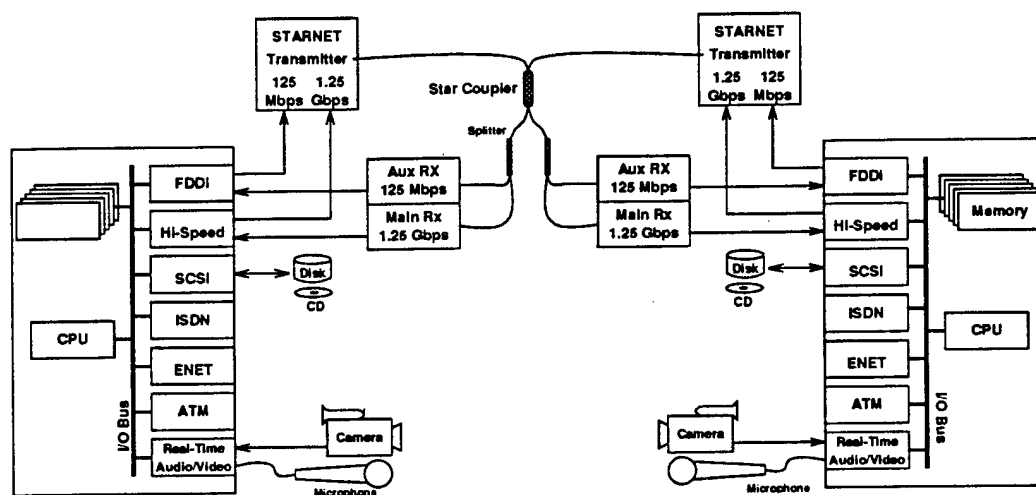


Figure 5-4. Two-node experiment.

5.3.2 High-Speed Subnetwork

The intended applications of the high-speed subnetwork have high-bandwidth and real-time requirements and are of relatively long duration. Therefore, we set it as our goal to design an interface which provides a large throughput while off-loading from the host processor as much as possible of the transport and lower layer protocols. These goals, and others are listed below:

- minimize host loading by the network interface;
- high-bandwidth to the network and to the host;
- low latency switching;
- support many simultaneous streams;
- fair bandwidth allocation among competing streams;

- provide an efficient data-link layer;
- optimize for block memory transfers;
- eliminate packet reassembly and reordering;
- provide for multi-cast and broadcast connections;
- minimal error checking;
- minimal buffer sizes;
- minimize dropped packets;
- modularity/upgradability;
- economical;
- fast debug turnaround.

Note that some of the goals are conflicting (e.g. dropped packets can be limited by increasing the buffer size which can increase latency, also large packet size improves high bandwidth data transfer at the cost of low-latency switching). With these goals and tradeoffs in mind, we now examine the interface architecture that we have designed, constructed and tested.

Our primary assumption is that the underlying STARNET high-speed optical link will provide a virtually reliable link ($BER \ll 1e-9$). This assumption allows us to minimize error checking and limits the need for retransmission. In fact, because the BER is so low, we are more concerned with packets that are due to lack of buffer space at the node than those lost due to bit errors.

5.4 High-Speed Interface Architecture

A block diagram of the high-speed subnetwork interface is shown in Fig. 5-5. Our approach was to first design the datapaths. The key goal here was simplicity because simple datapaths greatly simplify control design. To this end, we made our three key datapaths 32-bits wide; no byte operations are allowed. The first datapath is bidirectional and connects the interface to the host I/O bus. The second datapath accepts data words from the deserializer. The third supplies words to be transmitted by the serializer. Elements which provide connectivity between the host, network to the datapaths are the three FIFO queues (one each, for transmit, receive, and pass-through traffic).

Once the datapath had been designed, the control logic was easily partitioned into three distinct areas and implemented in separate FPGAs. These functions are performed by two bandwidth arbiters, and a routing switch. The first arbiter is responsible for managing which of two competing streams has access to the I/O bus (transmit vs.

receive), and the second manages access to the high-speed output link (transmit vs. pass). The routing switch determines if the packet header is valid, and whether the packet should be received, passed-through, or multi-cast.

In the current implementation, (de)serialization of the 32-bit data words is done by a separate board obtained from Vitesse, as well as 8B/10B encoding of the data (1.25 Gbps line rate/1.0 Gbps data rate). We intentionally partitioned our design to be quite flexible to the choice of (de)serializer hardware and format so as to be upgradable to higher data rates and other formats (e.g. 2.488 Gbps, SONET).

We now describe in detail the processes for transmitting and receiving of packets, routing of packets including multicasting, static and dynamic allocation of bandwidth, and segregation of different priority traffic.

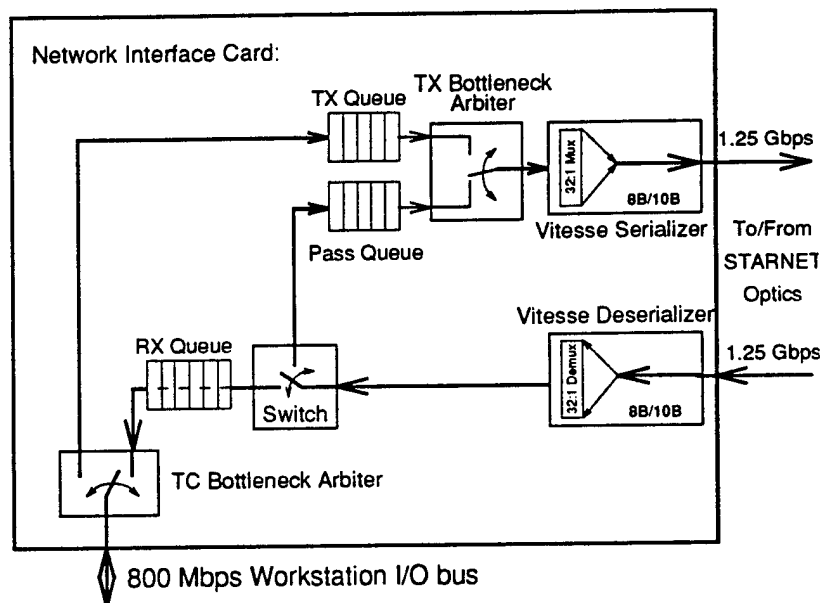


Figure 5-5. Block diagram of the high-speed subnetwork interface board.

5.4.1 Packet Transmission and Reception

The high-speed interface provides transmission and reception of packets over STARNET. The packets used in STARNET are organized as 16, 32-bit words (Fig. 5-6). The first word of the packet is a packet header which contains virtual circuit, packet sequence numbering, service class and synchronization information. The remaining 15 words are available for user data.

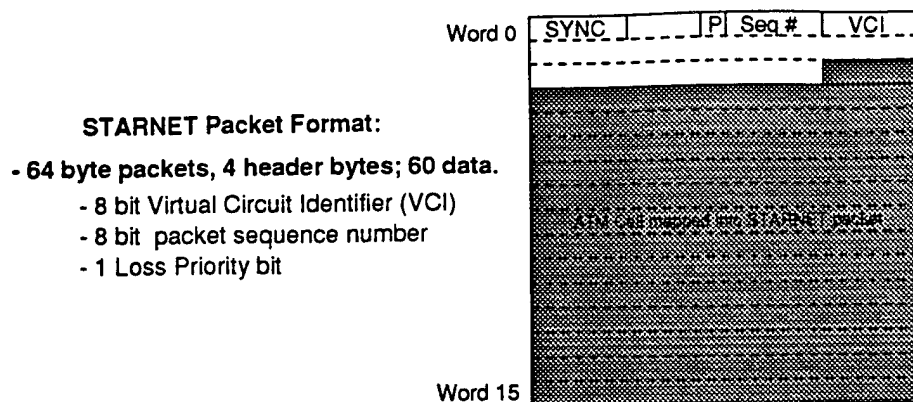


Figure 5-6. The STARNET high-speed subnetwork uses 64 byte fixed length packets.

Packets are organized contiguously in host memory in transmit buffers of up to 8KB (128 packets). Buffers are intentionally aligned on 8KB boundaries to ease DMA access and to reduce the number of bits required to specify an address.

The interface keeps a list of up to 64 separate transmit buffers¹. The interface board first loads a transmit buffer pointer from host memory using dynamic memory access (DMA). The pointer includes the physical base address in host memory of the buffer as well as additional bits which are used to determine the length of the buffer and its relative share of bandwidth. The interface then proceeds, using DMA, to copy packets from the host buffer into the transmit FIFO. Packets are taken from the buffer up to its share of bandwidth. Each transmit buffer is similarly serviced in round robin fashion, a small portion at a time, the portion being determined by its relative share of the bandwidth. This technique provides for fair access to the network bandwidth. Moreover, the technique serves to reduce overall burstiness in the network; since the buffers are read out piecemeal, it is more likely to limit the number of consecutive packets with identical destinations. Transmission of packets and buffers is shown in Figs. 5-7 and 5-8.

Note that the packet size and buffer size and alignment were intentionally chosen to speed the transfer of a page of host memory using DMA---After the initial connection has been made, the host need only compute the buffer pointer and write it to the transmit buffer pointer queue in order to transfer an entire 8KB page of memory. Subsequent transfers require only occasional polling to see if the buffer has been sent followed by a computing and writing a pointer to the next 8KB page.

¹ The various size limitations mentioned in the implementation are arbitrarily limited by the FPGA technology and not the architecture itself. A custom or semi-custom VLSI implementation would be able to support more virtual circuits, longer buffers, etc.

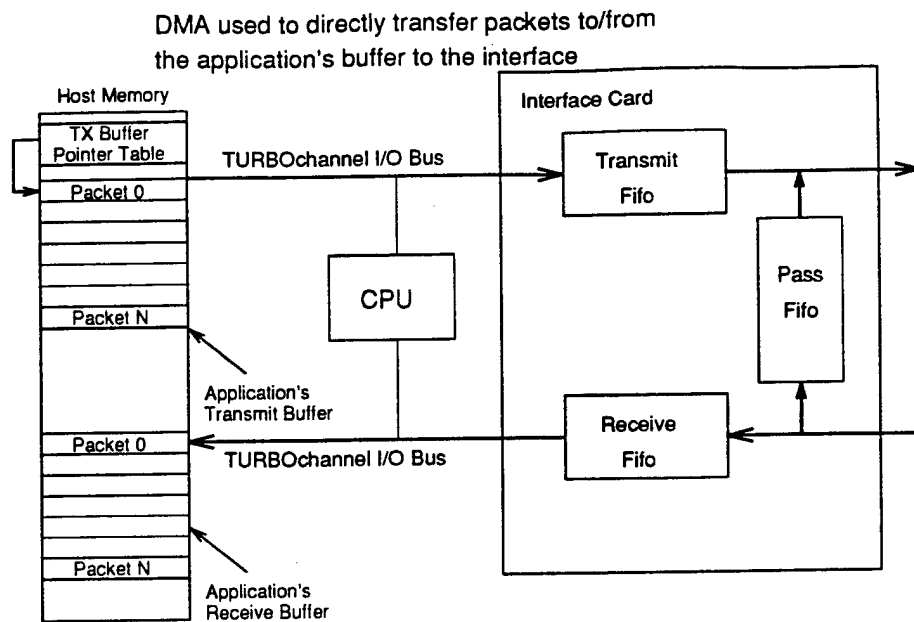
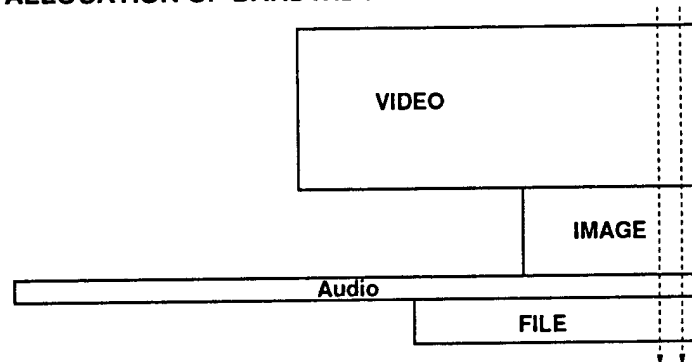


Figure 5-7. Packets for transmission over the network are read directly from the application's transmit buffer in host memory using DMA; received packets from the network are read directly from the receive FIFO and placed into the application's receive buffer in host memory using DMA.

ALLOCATION OF BANDWIDTH BETWEEN APPLICATIONS



Each stream is allocated a relative share of the bandwidth (vertical height)
Each stream is serviced in round robin fashion, a section at a time:
-Application receives fair share of bandwidth, in a timely manner

Figure 5-8. Transmit buffers are serviced in round-robin fashion with each receiving its allocated limit of slots per round.

Reception of packets from the network is shown in Fig. 5-7. Packets received from the network are first placed into the receive FIFO. The header word of the packet,

along with the packet number is used to generate a host memory DMA address. DMA is used to put the packet into host memory. Since the interface generates the DMA address directly, it is possible to transfer packets *directly* into an application's memory space without host intervention; this provides an extremely lightweight, low-latency connection².

It is essential to note here that although the node will receive packets from one connection interspersed with packets from another connection, all packets on a particular virtual circuit are *received in order*. This means that no reassembly or reordering of packets is necessary. This greatly reduces the overhead normally associated with network interfaces.

5.4.2 Network Bottlenecks and Bandwidth Allocation

A "bottleneck" exists whenever there are two or more streams simultaneously competing for a given network resource. There are two such bottlenecks associated with the high-speed network interface: the first is at the TURBOchannel I/O bus; the second is at the 1.0 Gbps serial output link. The bottlenecks exist because the TURBOchannel bandwidth must be shared between the node's transmit and receive streams, as well as with the host processor and other TURBOchannel devices; the serial output link must be shared between the node's transmit stream and the pass-through traffic. The allocation of bandwidth at each bottleneck is done in hardware by two arbiters, as shown in Fig. 5-9. The arbiters operate as follows: a two-slot cycle is formed, and each of the time slots is allocated to one of the competing streams. By adjusting the number of time slots per stream, it is possible to control the average bandwidth allocated to each stream. The process is illustrated in Fig. 5-10.

The granularity in the time slot sizes (T_1 and T_2 in Fig. 5-10) is one packet. If one stream becomes idle during its cycle, then its remaining slots are available to the other stream up to a maximum slot allocation. The average number of slots available to each stream is modified by software as necessary when connections are accepted to, or removed from, the network. The interface also allows dynamic readjustment of the bandwidth allocation. In times of low network utilization the bandwidth allocation will be adjusted according to the instantaneous load which is given by the number of packets

² Note that this means that the application buffer must be considered volatile, or non-cacheable, by the host processor and certain precautions must be taken to ensure that receive buffers are not re-allocated or swapped out while the receive path virtual circuits are active otherwise this will result in incoming packets overwriting the memory space of another application or the system itself resulting in data integrity problems and system crashes which we nevertheless occasioned upon during debug.

queued by each of the competing streams. For example, if the transmit packet stream experiences a momentary burst of traffic and the pass-through FIFO is relatively empty (i.e. there is little danger of dropping pass-through packets), then the number of slots allocated for transmitting packets is increased. This policy is only maintained until the FIFOs of both competing streams are relatively full. At this point, the arbiter will enforce the average bandwidth allocation. Since we implemented this bandwidth allocation policy, we have found that a somewhat similar policy was proposed in a paper on fair bandwidth allocation [6]. Our policy is generally fair in that it prevents one stream from starving another, and each stream can receive its allocated bandwidth. Another criterion for fair allocation is that the stream which is using less than its requested bandwidth is rewarded with less latency. While this is generally true with our policy, we forego the fairness in times of lopsided loads to facilitate unloading of the congested stream at the short-term expense of the other.

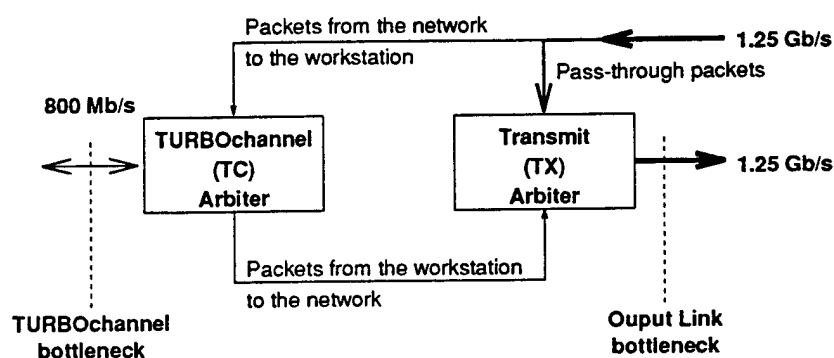
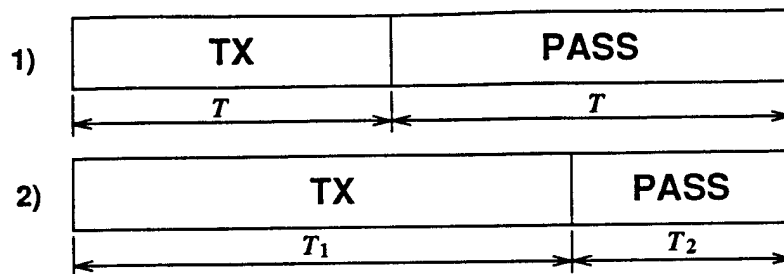


Figure 5-9. Bottlenecks in the high-speed network interface.

5.4.3 Virtual Circuit Routing

On-the-fly virtual circuit routing is performed by way of a lookup table in RAM (Fig. 5-11). The least significant byte of the packet header is used to address a location in RAM. The data at this location includes bits which tell the interface whether to receive or retransmit a packet (or both, in the multicast case). The RAM data also includes an outgoing virtual circuit number in the retransmit case or a pointer directly to host memory in the receive case. On-the-fly routing is essential to the off-loading of network duties from the host and provides for extremely low switching latencies.



Transmit Bandwidth, TX, set point negotiated over control subnetwork
Interface responds dynamically to burstiness by (de)creasing the
short term bandwidth when the network is uncongested.
Interface remains fair when the network is congested by enforcing the
long term bandwidth allocation (neither Pass nor Tx streams starve).

Figure 5-10. Dynamic bandwidth allocation in the high-speed network interface.

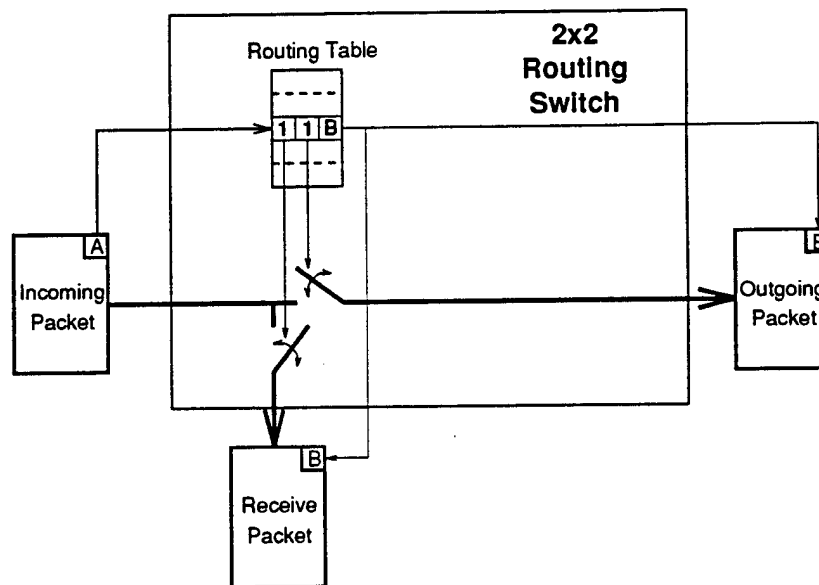


Figure 5-11. On-the-fly virtual circuit routing is performed by way of a lookup table in RAM. The incoming header is used as an offset into RAM. The value in the lookup table includes the outgoing header and two bits which are used to set the switch to receive and/or retransmit the packet.

5.4.4 Service Segregation

The high-speed interface accommodates different priority traffic by establishing separate packet loss rates for the two types of priority. File transfer applications would use the high-priority service; hierarchical video could send some packets as high priority and others as low priority. This mechanism is shown in Fig. 5-12. Whenever the number of

packets in the FIFO exceeds a programmable low priority threshold, the low priority packets are simply dropped. This leaves the remainder of the FIFO exclusively for high priority traffic. This policy is 'protective' of the high priority traffic. Analysis of this policy may be found in [4].

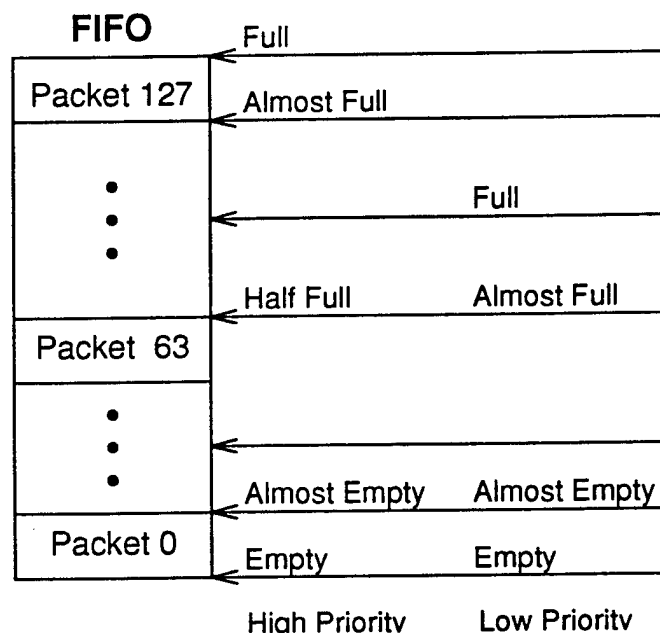


Figure 5-12. Segregation of traffic is provided by the interface. High-priority packets see a larger FIFO buffer than do low-priority packets.

5.4.5 Summary and Status

In summary, our entire scheme for transmitting and receiving packets is optimized for speed and efficiency while offloading from the host as much of the network tasks as possible. DMA is used to directly transfer packets to and from host memory. The interface can transfer 8KB pages at a time without host intervention. Virtual circuit operation on the high-speed subrings obviates the need for reassembly or reordering of packets. Furthermore, we have presented a round-robin scheduler which fairly distributes bandwidth among several host connections onto the interface. We have further presented a scheme which fairly allocates bandwidth between streams coming from, or destined to the network. Finally, we have presented a simple segregation scheme which is protective of high-priority traffic.

We have implemented all of the above techniques on a modest 6"x9" printed circuit board (PCB). The completed high-speed interface design relies heavily on commercial

FPGAs for (fast debug turnaround) and on FIFOs. The completed board, PCB included, was extremely economical at just \$1500 per node³. The cost in production run quantities would be substantially less.

We have conducted experiments to measure the maximum transmission and reception performance of the high-speed interface, which is a measure of the efficiency of our design. In the case of transmitting packets we first filled a 8KB user buffer in host memory with packets. We then started a measurement timer and initiated the data transfer. After all the packets had been sent the timer was stopped and the transmission time noted. The header word in each packet was counted as overhead and was not included as data throughput. Although the sustainable throughput is variable, depending upon CPU-host memory loading, we obtained an average of 685 Mbps throughput out of the 800 Mbps theoretical maximum (TURBOchannel I/O bus limit). In order to measure the maximum receive throughput, we first filled the receive FIFO and then allowed DMA to begin. We measured the total transaction time with an on board counter. On average, we saw an average throughput of 571 Mbps⁴. These high throughput measurements show that the design is very efficient in moving data to and from the host node.

With this design now in hand, we now present simulations of STARNET and provide experimental measurements to determine the performance and how effective the above policies are in actually providing the intended multimedia services.

5.5 STARNET Performance

Applications such as those listed in Fig. 5-1, i.e. voice, TV video, and especially video conferencing, put strict limits on acceptable latency and jitter. From the figure we see that tolerable delay for video-conferencing is 100 ms; jitter, 1-10 ms. We have performed simulations and experiments to investigate how STARNET will perform for such applications. We show that these constraints are met for a reasonable number of hops between STARNET nodes, by measuring the average latency of that packets experience passing through each node, for various traffic conditions. In the following, we describe our network model and present analytical and simulation results and experimental measurements.

³ A cheap Ethernet interface board runs \$50, or \$5/Mbps; our high-speed interface is just \$1.50/Mbps!

⁴ Since packets from several connections and nodes will be mixed in the received stream, the packets must be placed into host memory on a packet-by-packet basis, whereas transmit buffers can be emptied up to eight consecutive packets at a time (host DMA limit). Therefore the maximum receive throughput will not be as high as that for transmission of packets.

Returning to Fig. 5-5, we seek to develop a simulation model for the interface. The main elements are the routing switch, the three FIFO queues and the mechanisms for arbitrating access to the host and to the network. The three queues are the transmit queue which buffers transmit traffic from local host before it is transmitted to the network, the receive queue which buffers traffic from network before it is received at the local host's memory and the pass queue which buffers the traffic from the network which is only hopping through the node. There are two arbiters, one at each bottleneck. The first is the TX Arbiter at the network where transmit and pass traffic compete; the second is the TC Arbiter where transmit and receive traffic compete.

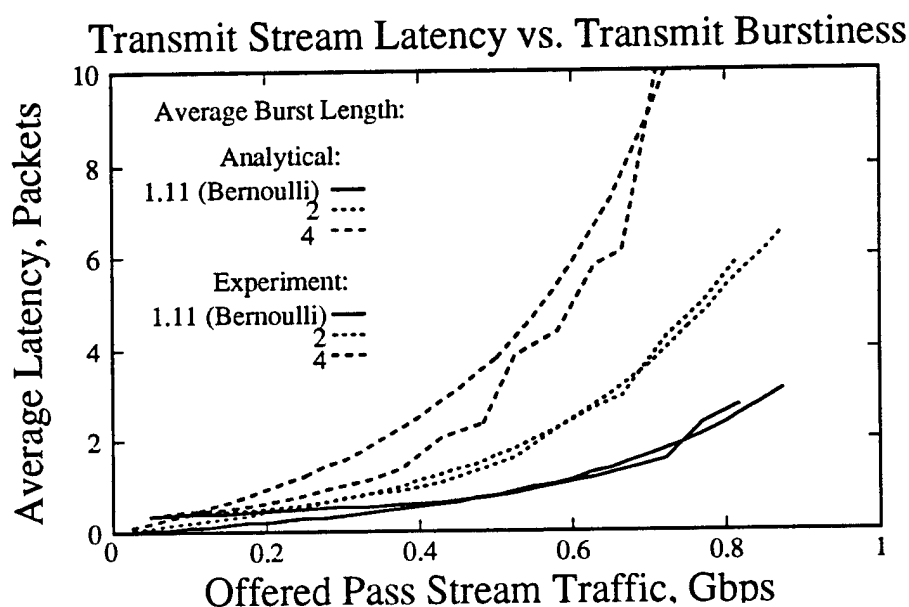


Figure 5-13. Analytical and experimentally measured latency behavior of the STARNET bandwidth arbitration scheme. The offered transmit traffic averages 100 Mbps, and assumes a two-state Markov model to generate correlated (bursty) traffic. The plot shows transmit latency vs. offered pass through traffic for various average burst lengths (Bernoulli traffic does not have correlated bursts).

Fig. 5-13 compares analytical predictions and experimental measurements of the average latency seen by a particular node which is offering bursty, 100 Mbps transmit traffic vs. the bandwidth of the pass through traffic for three values of transmit traffic burstiness. Burstiness is defined by the average number of consecutive packets that the host generates during a busy period. We used a simple two-state Markov model as a source of bursty transmit traffic. The analytical curves show that transmit latency increases both with increasing offered pass traffic, and with the burstiness of the data. This effect is

expected because the stream is exceeding its allocated share of bandwidth during the burst periods and this shows that the interface imposes a latency penalty on bursty transmit traffic. Also plotted are experimentally obtained curves which show fairly good correspondence with the analytical results. The measurements are obtained by having the first node send data through the second while the second offers bursty transmit traffic. Packet latency is measured by starting an on-board event timer when a specially tagged packet is placed in the transmit queues and stopping when the packet exits the transmit queue. Discrepancies between the analytical results and the experimental measurements are mostly due to the inherently difficult nature of getting a multi-tasking UNIX system to run just one task for the duration of the measurement.

Having now shown good correspondence between our experimental results and our analytical model, we now wish to consider the interface's operation in an 8-node network. Our results were obtained by using a simulation model that we developed in Mil-3's OPNET™ simulation tool to investigate the latency performance of STARNET.

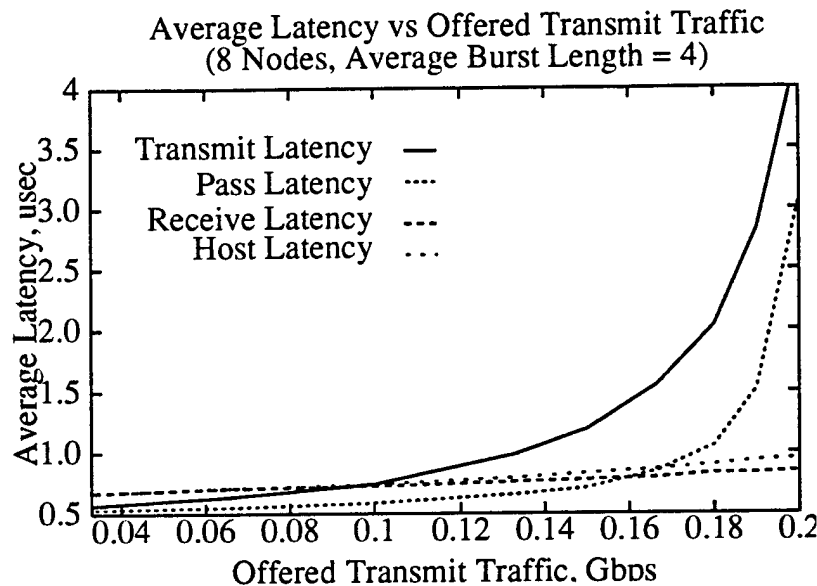


Figure 5-14. Latency behavior of traffic passing through the host, transmit, pass and receive queues of the high-speed interface versus the offered transmit traffic. Results were obtained for a 8-node subnetwork using OPNET.

Fig. 5-14 shows the latency of packets in each of the system queues vs. offered transmit traffic per node for an 8-node subnetwork. Latency increases in each of the system queues as the offered transmit traffic per node increases (total output link throughput approaches 1 Gbps). Assuming uniform destination distribution, the total

offered throughput at each node's output link is given by, $T_x(N+1)/2$, where T_x is the offered transmit bandwidth per node, and N is the number of nodes in the subnetwork. For 200 Mbps transmit traffic per node, this gives 900 Mbps total offered traffic at each of the output links and 1.6 Gbps total traffic on the 8-node subnetwork. In this example, the transmit latency is always higher than the pass through latency because, first, the transmit traffic has been allocated only one fourth of the link bandwidth (250 Mbps) and second, the pass-through traffic coming from the subnetwork is less bursty than the transmit traffic due to the smoothing effect of our bandwidth arbitration scheme. Packets from the host and packets for the host (receive queue) generally experience little latency because the total traffic across the bus is never more than half of the bus capacity.

We now show how the above behavior relates to providing multimedia service requirements. A typical high-quality (MPEG-1) video-conference requires about 2 Mbps of guaranteed, low-latency bandwidth. Calculation of the average latency that the stream will incur on its path from the host to the destination requires summing the latency in each queue that it passes through. If we consider the 2 Mbps traffic in an eight-node network, the switching latency is the sum of the time spent in the host queue, the transmit queue, a maximum of six hops through pass queues and lastly, in the receive queue. If we also assume that our 2 Mbps traffic is part of a 100 Mbps total transmit traffic (e.g. 50 simultaneous conversations), we can obtain these latencies from figure xxx.14. The latencies are, respectively, Host, $0.8\mu\text{s}$; Transmit, $1.0\mu\text{s}$; Pass, $0.7\mu\text{s}$; Receive, $0.8\mu\text{s}$. This yields a total switching latency of $(0.8 + 1.0 + 6 \cdot 0.7 + 0.8)\mu\text{s} = 6.8\mu\text{s}$. If we further assume 10km ($50\mu\text{s}$) spacing between nodes, the total latency through the network is still only about $357\mu\text{s}$ ⁵. Therefore, a moderate sized STARNET can *easily* support the audio and video delay requirements for video-conferencing, even for 50 simultaneous conversations per node, 400 per 8-node high-speed subnetwork virtual LAN, and 3,200 per 64-node STARNET consisting of 8, 8-node subnetworks. Thus we have shown that STARNET is suitable for interactive applications in LAN and MAN environments.

5.6 Conclusions

We have presented a detailed look at a network interface which provides buffering and distributed multi-hop virtual circuit routing of packets over a ring network topology. In general, the interface can be used in reconfigurable WDM networks. One such

⁵ Note that the inherent delay in the fiber is in fact greater than the delay in the switch which further validates using electronic buffering and switching.

network, STARNET, has served as a testbed for the design, development and verification of the interface.

The interface board acts as a 2x2 switch between the network and the TURBOchannel bus in the workstation. Packet routing is done on-the-fly by the interface. DMA operations are used to transfer packets to and from the network and the workstation thus leaving the CPU free for computational and other tasks. Moreover, the interface provides for programmable and dynamic bandwidth allocation as well as for segregation of high and low priority traffic on the basis of the acceptable packet loss.

Simulations and experimental results show that the interface enables STARNET to support a large number of distributed multimedia applications such as video-conferencing. The completed interface has been operational since January 1994 running large file transfer and multimedia applications in a two-node environment. Ongoing research on STARNET will determine its scalability, optimum call acceptance and congestion control strategies, and will provide future enhancements to the design.

5.7 References

- [1] P. Poggiolini, L. Kazovsky, "STARNET: an integrated services broadband optical network with physical star topology," SPIE meeting, Conference 1579 'Advanced Fiber Communication Technologies', *Proc. SPIE 1579*, pp. 14-29, Boston, September 1991.
- [2] P. Poggiolini, L. Kazovsky, "STARNET: A Multi-Gbit/s Optical LAN Utilizing A Passive WDM Star," *IEEE/OSA J. of Lightwave Tech.*, May 1993.
- [3] M. Hickey, C. Barry, C. Noronha, L. Kazovsky, "Experimental PSK/ASK transceiver for the STARNET WDM computer communication network," *IEEE Photonics Tech. Letters*, May 1993.
- [4] R. Guerin, I. Cidon, "On Protective Buffer Policies," *LEOS Summer Topical Meeting*, Paper T3.4, Santa Barbara, July 1993.
- [5] Peter S. Ford, Yakov Rekhter, Hans Werner Braun: "Improving the Routing and Addressing of IP," *IEEE Network*, pp. 10-15.
- [6] A. Demers, S. Keshav, S. Shenker, "Analysis and Simulation of a Fair Queuing Algorithm," *Internetworking: Research and Experience*, Vol. 1, pp. 3-26, 1990.

PART 3:

**NONLINEAR
EFFECTS IN
FIBER**

Chapter 6

Impact of Fiber Nonlinearities on Optical Communication Systems

6.1 Introduction

Optical fiber nonlinearities involve power-dependent fiber characteristics. These effects, which become important at high optical power levels or for many wavelength division multiplexed (WDM) channels, manifest themselves in changes in the index of refraction of the fiber. Optical fiber nonlinearities are now of particular concern due to the availability of high power lasers (> 100 mW output power) and optical amplifiers.

In this chapter, we consider several different types of fiber nonlinearities. In Section 6.2, we discuss the impact of four-wave mixing (FWM) on ASK optical WDM systems. In Section 6.3, we present our novel results on the statistical distribution of FWM interference in ASK optical WDM systems. In Section 6.4, we discuss the impact of FWM on FSK optical WDM systems. Our results in these three sections are all obtained through simulation. In Section 6.5, we present a precise theoretical model of the impact of cross-phase modulation (XPM) in dispersive fibers and give corroborating experimental results. In Section 6.6, we give experimental results on the impact of stimulated Brillouin scattering (SBS) in systems using high-power solid-state lasers. In Section 6.7, we present our novel theoretical and experimental results on the impact of fiber-induced parasitic phase modulation on ultra-long distance DPSK transmission.

6.2 Impact of Four-Wave Mixing on Optical WDM Systems

We evaluated the performance of optical WDM systems in the presence of four-wave mixing (FWM) by both theoretical model and simulations. The nonlinear FWM process limits the maximum optical power that can be launched into fibers, and the shot noise limits the minimum required power at the receiver. We have evaluated the power budget, defined as the ratio of the maximum transmitter power to the minimum optical power at the receiver, and derived the maximum transmission distance.

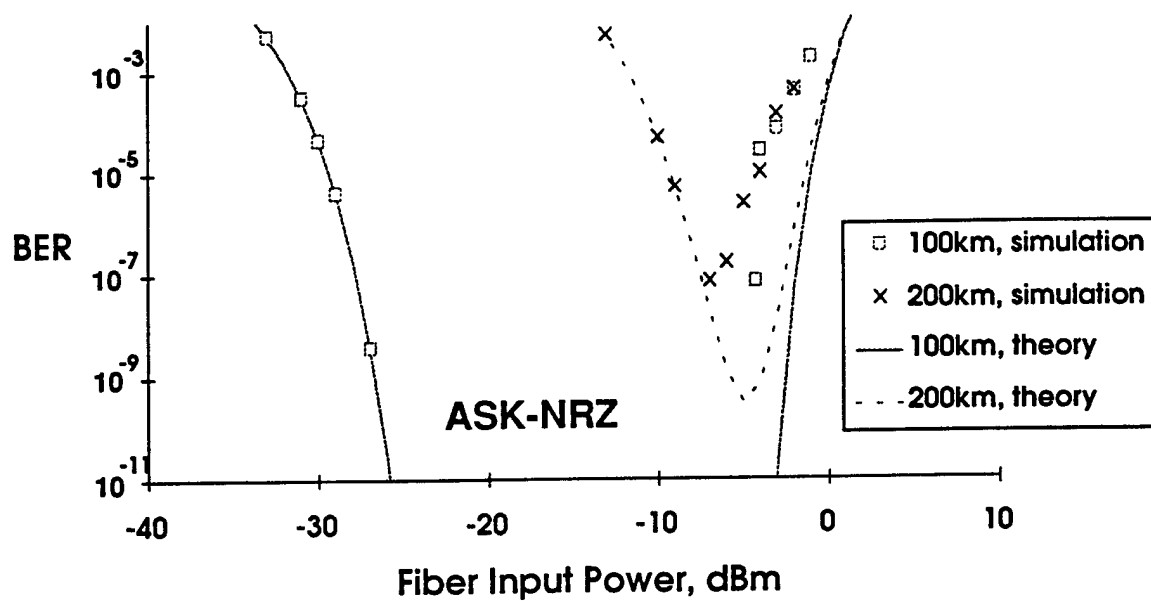
We have also proposed and investigated a FWM noise reduction method using Manchester coding. The performance of NRZ (non-return-to-zero) and Manchester coding in both ASK (amplitude-shift keying) and DPSK (differential phase-shift keying) modulated systems was evaluated. The effect of fiber dispersion on FWM noise was also investigated. Our analysis shows that Manchester coding improves both ASK and DPSK systems, and that systems utilizing dispersion-shifted fiber are more seriously impaired by FWM noise than those utilizing nondispersion-shifted fibers.

We also simulated 16-channel WDM ASK systems. The 16 independent optical channels were computer-generated with random laser phase noise, uncorrelated random data streams, and independent clocks with random jitter. The simulation was carried out for both NRZ and Manchester-coded cases. Using 16 optical channels, the IF signal was generated by the simulation program. Next, the program evaluated the pdf of FWM-impaired signals at the envelope detector output. Finally, the receiver BER was evaluated for NRZ and Manchester codes using the simulated pdf's of FWM-impaired signals.

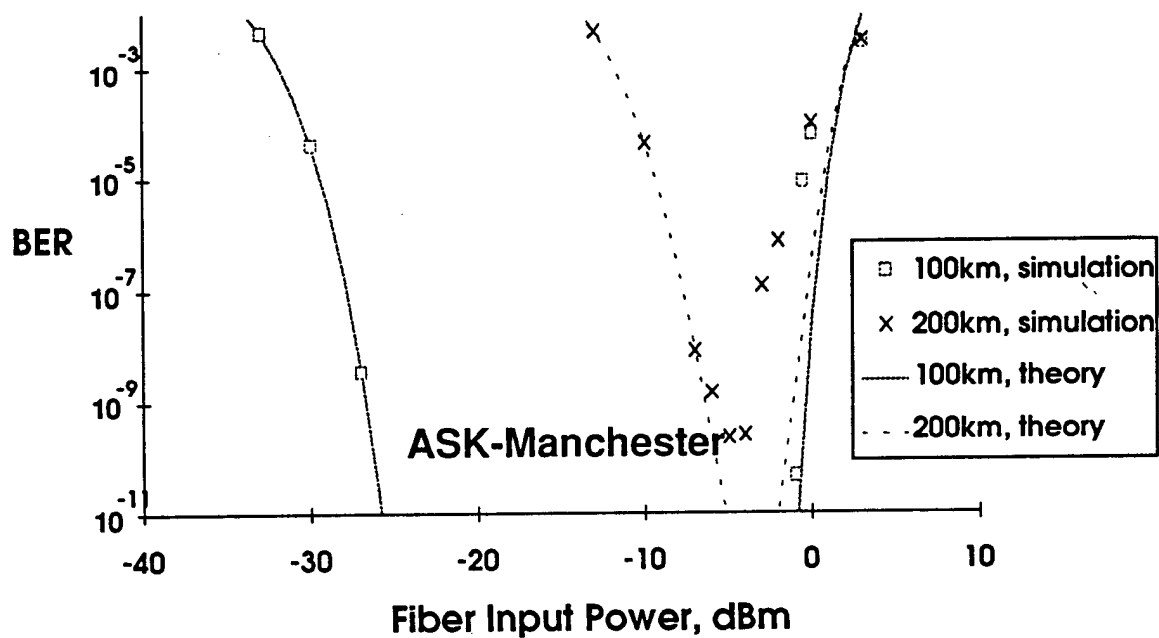
The simulation and theoretical BER results are shown in Figs. 6-1(a) and 6-1(b) for NRZ and Manchester coding, respectively. The BER curves in Fig. 6-1 are shown for the 8th channel (the worst case) of the 16-channel WDM system using a dispersion shifted (DS) fiber versus optical input power to the fibers with 100 km and 200 km lengths. The rest of system parameters are as follows: $n = 1.47$, $\lambda = 1.55 \mu\text{m}$, $\alpha = 0.2 \text{ dB/Km}$, channel spacing = 10 GHz, bit rate = 1 Gbit/s, laser linewidth = 10 MHz, $A_{\text{eff}} = 55 \mu\text{m}^2$, $\chi_{1111} = 6 \times 10^{-15} \text{ cm}^3/\text{erg}$, $R = 0.6 \text{ amp/watt}$ and group velocity dispersion = 15 ps/km-nm for non-DS (NDS) and 0.5 ps/km-nm for DS fibers.

It is evident from Fig. 6-1 that in the low power region the BER is limited by shot noise, while in the high power region the BER is determined by FWM. There is an optimum input power level yielding the minimum BER. This minimum value of BER increases with increase in fiber length. The maximum transmission distance for a BER $\leq 10^{-9}$ is 211 km for a Manchester coded system using the DS fiber; this distance is about 9 km longer than that for the NRZ system.

Further, inspection of Fig. 6-1 reveals that the theoretical results are similar to the simulation results but overestimate the receiver sensitivity especially near the threshold input power levels where the FWM interference becomes dominant over shot noise. The discrepancy is caused by the assumed Gaussian model of the FWM interference.



(a) ASK system with NRZ coding



(b) ASK system with Manchester coding

Figure 6-1. Bit error rate of 16-channel ASK systems impaired by FWM.

The maximum and minimum input powers for the 8th channel of a 16 channel WDM system needed to maintain BER below 10^{-9} are shown in Figure 6-2. The ratio of the maximum power to the minimum power is defined as the dynamic range. Manchester coded ASK systems have about 2 dB larger dynamic range than the corresponding NRZ coded ASK systems. The system power budget is defined as the ratio of the maximum input power to the minimum receiver power needed to keep BER below 10^{-9} . Figure 6-2 shows that the power budget decreases at long fiber lengths due to the drop of the maximum allowable input power caused by FWM. Manchester coded systems show about 2 dB improvement with respect to NRZ systems; the power budget of the systems using NDS fiber is 3 dB larger than that of the systems using DS fiber.

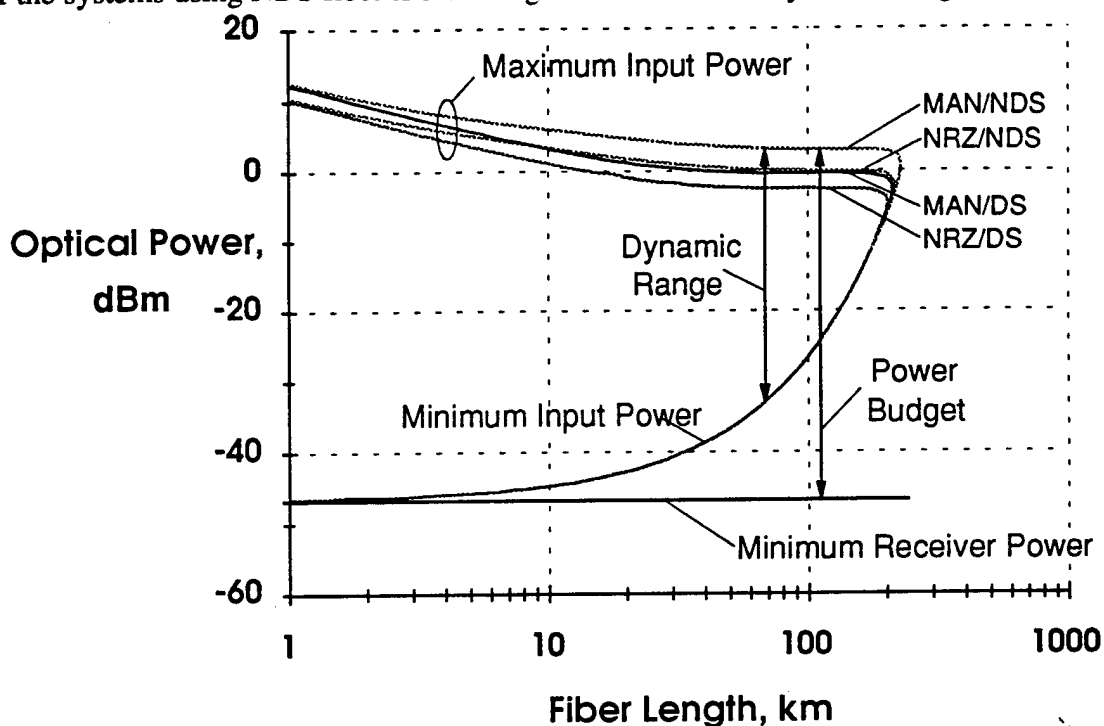


Figure 6-2. Maximum transmission distance of NRZ and Manchester coded ASK systems impaired by FWM.

6.3 Statistical Distribution of FWM in ASK Optical WDM Systems

The four-wave mixing (FWM) effect in optical fiber is caused by the third order nonlinear susceptibility of the fiber. If the frequency of the newly generated wave lies within the desired signal band, the resulting interference leads to crosstalk between channels and degrades system performance. In a wavelength-division-multiplexed (WDM) optical system, the number of interference terms increases rapidly with the number of channels. The power of each FWM interference term is proportional to the cube of the

power of the incident waves, and increases with transmission distance. The combined effect of a large number of FWM interference terms is treated as a Gaussian random process in some publications. However, the phase relationship between the interference terms makes the interference deviate from a Gaussian process. We performed computer simulations to investigate the statistical properties of the FWM interference. The simulation results are compared with the Gaussian approximation results.

Our simulation program simulates a coherent ASK (amplitude-shifted-keying) optical WDM system. In the program, several independent optical channels are computer-generated with random laser phase noise, uncorrelated random data streams, and independent clocks with random jitter. The program also generates all FWM interference terms that fall within the frequency band of the received channel. Each FWM term is calculated analytically. Next, the program evaluates the pdf of the sum of these FWM terms both at IF and at the envelope detector output.

The following numerical results are shown for the 8th channel (the worst case) of a 16-channel WDM system with a link of 100 km dispersion shifted fiber when all the channels except the 8th are transmitting '1'. The rest of system parameters are as follows: incident optical power = 0.1 mW/channel, wavelength = 1.55 μm , attenuation = 0.2 dB/km, channel spacing = 10 GHz, bit rate = 1 Gbit/s, laser linewidth = 10 MHz, $A_{\text{eff}} = 55 \mu\text{m}^2$, nonlinear susceptibility $\chi_{1111} = 6 \times 10^{-15} \text{ cm}^3/\text{erg}$, responsivity = 0.6 amp/watt, and group velocity dispersion = 0.5 ps/km·nm.

Fig. 6-3 shows the simulated pdf's of the sum of the FWM interference terms at IF when the received channel is transmitting '0'. The in-phase component represents the component of the FWM interference that is in-phase with the desired signal at IF, and the quadrature-phase component represents the one that is 90 degrees out-of-phase with the IF. The main lobe of the simulated pdf is seen to match very well with the Student's t-distribution for both in-phase and quadrature-phase components. The corresponding Gaussian pdf is also shown in Fig. 6-3 for comparison. In expanded scale, we find that the tails of the simulated pdf's drop off slower than the Gaussian pdf, and tend to decay exponentially.

Fig. 6-4 shows the simulated pdf of the voltage at the envelope detector output for '0' transmission. A Gamma distribution is seen to match the simulated pdf very well. If the interference had a Gaussian-like behavior at the IF, the voltage at the envelope detector output should have a Rayleigh distribution. The corresponding Rayleigh distribution is also shown in Fig. 6-4 for comparison. It can be found by expanding the scale in Fig. 6-4 that the simulation results have larger tails than the Rayleigh distribution corresponding to the Gaussian approximation.

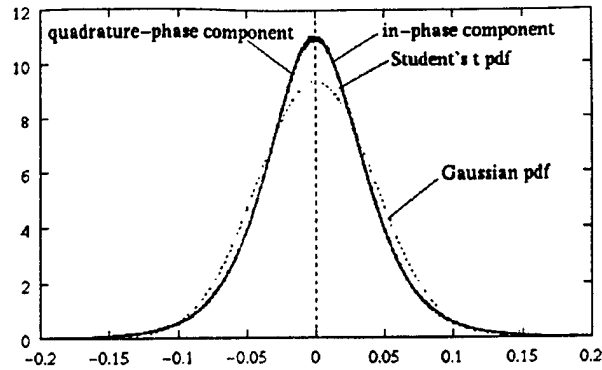


Figure 6-3. The pdf of FWM interference at IF; '0' transmission.

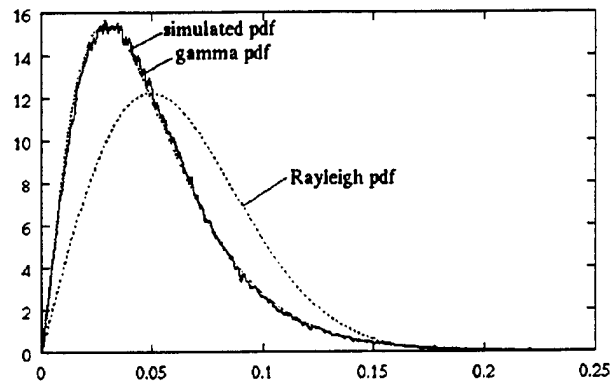


Figure 6-4. The pdf of FWM interference at the envelope detector output; '0' transmission.

Fig. 6-5 shows the simulated pdf's of the sum of the FWM interference terms at IF when the received channel is transmitting '1'. Similar to the '0' transmission case, the main lobe of the in-phase component is seen to match very well with the Student's t -distribution. The quadrature-phase component is shifted from the origin and distorted from the t -distribution shape due to cross-phase modulation. The corresponding Gaussian pdf is also shown in Fig. 6-5 for comparison. The tails of the simulated pdf's still drop off more slowly than the Gaussian pdf.

Fig. 6-6 shows the simulated pdf of the voltage at the envelope detector output for '1' transmission. The main lobe of the simulated pdf is seen to match the t -distribution in this low power case. If the interference had a Gaussian-like behavior at IF, the voltage at the envelope detector output should have a Rician distribution. The corresponding Rician distribution is also shown in Fig. 6-6 for comparison. It can be also found by expanding the scale in Fig. 6-6 that the simulation results have larger tails than the Rician distribution

corresponding to the Gaussian approximation. Therefore, the resulting BER is higher in simulation than in Gaussian approximated systems .

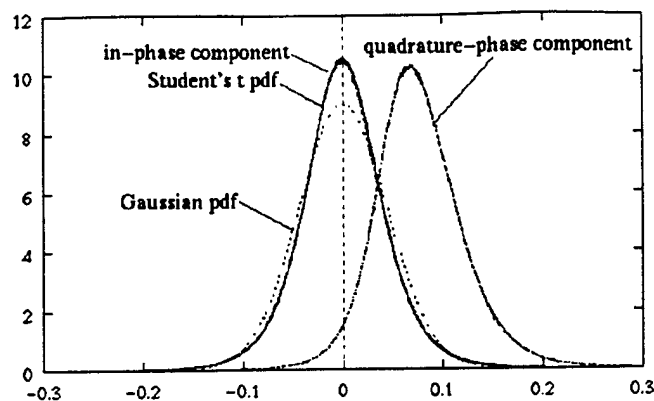


Figure 6-5. The pdf of FWM interference at IF; '1' transmission.

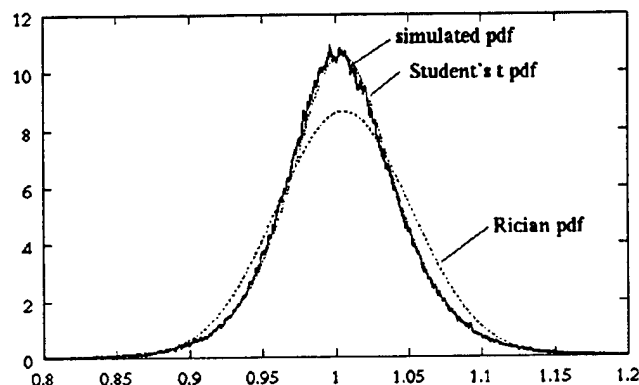


Figure 6-6. The pdf of FWM interference at the envelope detector output; '1' transmission.

In summary, the statistical behavior of FWM interference was investigated by computer simulations. The pdf of the FWM interference was found to be non-Gaussian. The distribution at the IF is well approximated by the Student's t-distribution. The resulting pdf at the envelope detector output is well approximated by the gamma distribution and Student's t-distribution for '0' and '1' transmission respectively. The simulated pdf has slower dropping tails than Gaussian pdf.

6.4 Impact of Four-Wave Mixing on FSK Optical WDM Systems

We theoretically analyze the impact of FWM in a 16 channel optical FSK (frequency-shift-keying) WDM system employing SFED (single-filter-envelope-

detection). The analysis takes into account the effects of bandpass filter (BPF) at intermediate frequency (IF) on the FWM interference process. The photodetected IF signal is demodulated by using a BPF at the IF corresponding to the 'mark' transmission followed by an envelope detector and a decision circuit. The BPF input for a receiver tuned to the j -th wavelength can be expressed as

$$i(t) = I_j \cos(\omega_{jM}t + \phi_j) + \sum_{m=k+l-j} Z_{klm} g_{klm}(t) \cos(\omega_{jM}t + \phi_{klm}) + n(t) \quad (6.1)$$

where, I_j and ϕ_j are the amplitude and phase of the signal component, ω_{jM} is the IF frequency for the mark transmission in the j -th channel, $Z_{klm}(t)$ and ϕ_{klm} represent the amplitude and phase of the FWM interference term produced by k -, l - and m -th channel signals, $g_{klm}(t)$ is a unit amplitude random rectangular pulse train representing the normalized envelope of the same FWM term and, $n(t)$ is the shot noise prior to IF filtering. We consider that the BPF is a bandpass matched filter at ω_{jM} . Since the lowpass equivalent of the BPF is an integrate-and-dump filter, at the end of each bit interval (T) in the desired channel, $g_{klm}(t)$ will result a filtered envelope which can be modelled as a random variable uniformly distributed in $[0, T]$.

Using Eq. (6.1), we first develop a statistical model for the filtered IF envelope resulting from the interference between the desired signal and the FWM components. At the end of a given interval (consider the 0-th interval in $[0, T]$), the mark and space envelopes at the BPF output ($a_M(T)$ and $a_S(T)$ respectively) due to the signal-FWM interference can be expressed as

$$a_{M,S}^2(T) = [A_{M,S} + \sum_{klm} B_{klm} \cos(\phi_{klm} - \phi_j)]^2 + [\sum_{klm} B_{klm} \sin(\phi_{klm} - \phi_j)]^2 \quad (6.2)$$

where, A_M and A_S are the filtered signal amplitudes for mark and space ($A_S = 0$) and, B_{klm} 's represent the filtered FWM amplitudes at $t = T$. It is interesting to note that $a_{M,S}(T)$ resemble the carrier envelopes encountered in radio communication channels with multipath fading. Following the similar steps and considering the contribution of filtered $g_{klm}(t)$ in A_M and B_{klm} , the statistics of $a_S(T)$ and $a_M(T)$ are found to follow Rayleigh and Rician distributions respectively. Next we find out the receiver bit error rate (BER) in presence of shot noise with the BER being conditioned on FWM impaired IF envelope following the above statistics. The overall BER is evaluated by averaging the conditional BER over the IF envelope statistics.

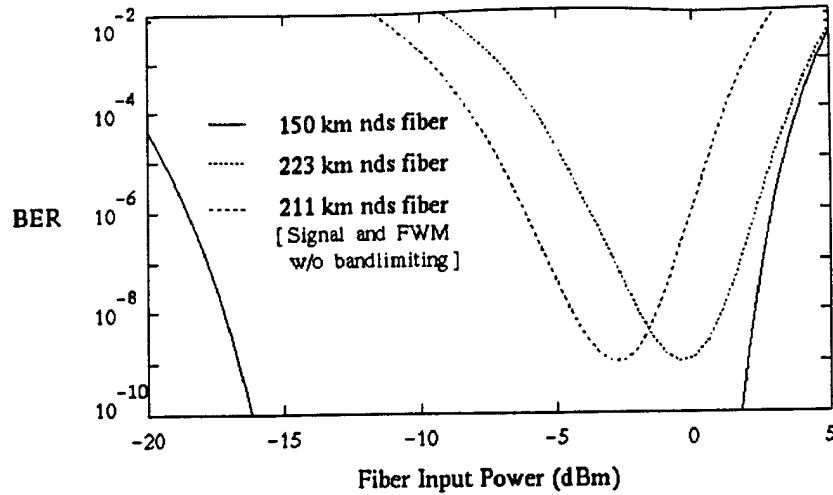


Figure 6-7. BER versus fiber input power for SFED receivers in 16-channel FSK WDM systems using NDS (non-dispersion-shifted) fibers.

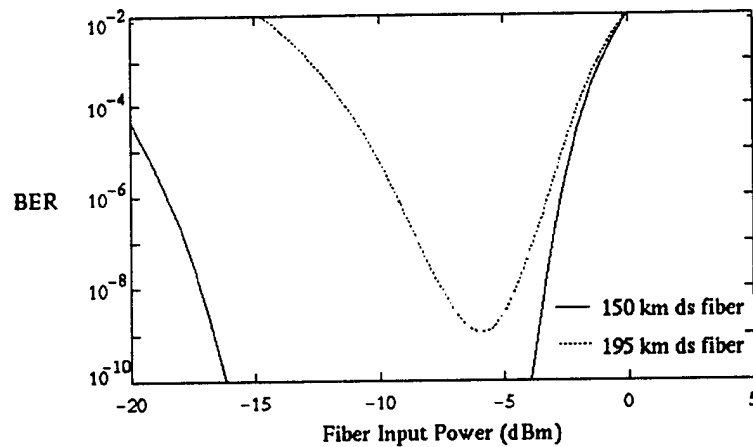


Figure 6-8. BER versus fiber input power for SFED receivers in 16-channel FSK WDM systems using DS (dispersion-shifted) fibers.

The receiver performance is evaluated from the plots of BER in the 8th channel (worst case) versus input optical power in the fiber for different lengths of fibers (effective core area = $55\mu\text{m}^2$, nonlinear susceptibility = $6 \times 10^{-15}\text{cm}^3/\text{erg}$) with 10 GHz channel spacing and 1Gbps bit rate/channel. Each BER curve exhibits a minimum at a certain power level. This minimum value of BER increases with increase in fiber length and should remain below 10^{-9} . Figs. 6-7 and 6-8 show the BER of SFED receivers in 16-

channel FSK WDM systems using NDS (non-dispersion-shifted) and DS (dispersion-shifted) fibers, respectively. The dispersion coefficients are 17 ps/nm·km and 0.5 ps/nm·km for NDS and DS fibers, respectively. The maximum transmission distances are 223 km and 195 km for systems using NDS and DS fibers, respectively.

6.5 Theoretical Analysis of XPM in Dispersive Fibers

We investigated theoretically the impact of modulation frequency on cross-phase modulation (XPM) in dispersive fibers. XPM is the modulation of the phase of one optical wave by the power fluctuations of another optical wave copropagating in the same fiber. XPM is particularly important in phase-sensitive lightwave systems. The impact of XPM on angle-modulated wavelength-division multiplexing (WDM) systems has been studied before for the case of near-zero group velocity dispersion (GVD). Conventional single-mode fiber is highly dispersive at 1.55 μm with the dispersion coefficient $D \approx 15$ ps/nm·km. In dispersive fibers, the group velocity mismatch among different wavelength channels can significantly influence the strength of XPM, depending on modulation frequency and wavelength separation. We found the XPM index to depend on fiber length, fiber chromatic dispersion, wavelength separation between the signal and the pump, and the intensity modulation frequency. At high modulation frequencies, the XPM index is inversely proportional to the product of the modulation frequency and wavelength separation.

XPM in a two-channel system with sinusoidal intensity modulation has been analyzed. We will show the influence of modulation frequency and wavelength separation on the XPM index.

Consider two optical waves with the same polarization copropagating in a single-mode optical fiber. Let $A_j(z, t)$ be the slowly-varying complex field envelope of each wave normalized to make $|A_j|^2$ equal to the instantaneous optical power. If channel 1 (probe) is CW and the intensity of channel 2 (pump) is sinusoidally modulated with angular frequency Ω_m , the expressions for optical powers at $z=0$ are

$$P_1(0, t) = |A_1(0, t)|^2 = P_{10} , \quad (6.3)$$

$$P_2(0, t) = |A_2(0, t)|^2 = P_{20} + P_{2m} \cos(\Omega_m t) . \quad (6.4)$$

The phase of channel 1 (probe) light is modulated by the sinusoidal power fluctuation in channel 2 (pump). The expression of the complex envelope of channel 1 at distance L can be expressed as

$$A_1(L, t) = A_1(0, t - \frac{L}{v_{g1}}) \exp(-\alpha L/2) \exp(i\phi_1(L, t)) , \quad (6.5)$$

where

$$\phi_1(L, t) = \gamma_1(P_{10} + 2P_{20})L_{eff} + \Delta\phi \cos(\Omega_m(t - L/v_{g2}) + \phi) , \quad (6.6)$$

is the phase shift caused by SPM and XPM, and $\Delta\phi$ is the XPM index given by

$$\Delta\phi = 2\gamma_1 P_{2m} \sqrt{\eta_{XPM}} L_{eff} ; \quad (6.7)$$

L is the fiber length; $L_{eff} \equiv \frac{1 - e^{-\alpha L}}{\alpha}$ is the effective fiber length; η_{XPM} is the XPM efficiency given by

$$\eta_{XPM} \equiv \frac{\alpha^2}{\Omega_m^2 d_{12}^2 + \alpha^2} \left[1 + \frac{4 \sin^2(\Omega_m d_{12} L/2) e^{-\alpha L}}{(1 - e^{-\alpha L})^2} \right] ; \quad (6.8)$$

and $d_{12} \equiv \frac{1}{v_{g1}} - \frac{1}{v_{g2}}$ is the walk-off parameter. In a non-zero dispersion region, $d_{12} \approx D\Delta\lambda_{12}$, where D is the dispersion coefficient and $\Delta\lambda_{12}$ is the wavelength separation between the two channels. $\Delta\phi$ can be approximated by

$$\Delta\phi \approx 2\gamma_1 P_{2m} \alpha L_{eff} / \Omega_m D \Delta\lambda_{12} \quad (6.9)$$

when $|\Omega_m d_{12}| \gg \alpha$ and $\alpha L \gg 1$.

Eqs. (6.6)-(6.9) show that the phase of the probe light is modulated at Ω_m . The strength of this phase modulation depends on γ_1 , P_{2m} , L_{eff} , and η_{XPM} . In turn, η_{XPM} given by Eq. (6.8) depends on D , $\Delta\lambda$, and Ω_m . Numerical values of $\Delta\phi$ for our experiments are presented in Fig. 6-9. In general, at low modulation frequencies, the walk-off time $T_w \equiv |L/v_{g1} - L/v_{g2}|$ is much less than the period $T_0 \equiv 2\pi/\Omega_m$ of pump modulation so that the portion of probe light that propagates along the higher pump intensity experiences a

larger refractive index throughout its propagation. Consequently, the resulting phase shift is larger than the phase shift on the probe light that propagates along the lower pump intensity. At higher modulation frequency, $T_w \geq T_0$, so that each portion of the probe light experiences several cycles of pump intensity fluctuation. Therefore, the phase variation among different time segments of the probe light is small. At high frequencies, $\Delta\phi$ is approximately proportional to $(\Omega_m \Delta\lambda)^{-1}$.

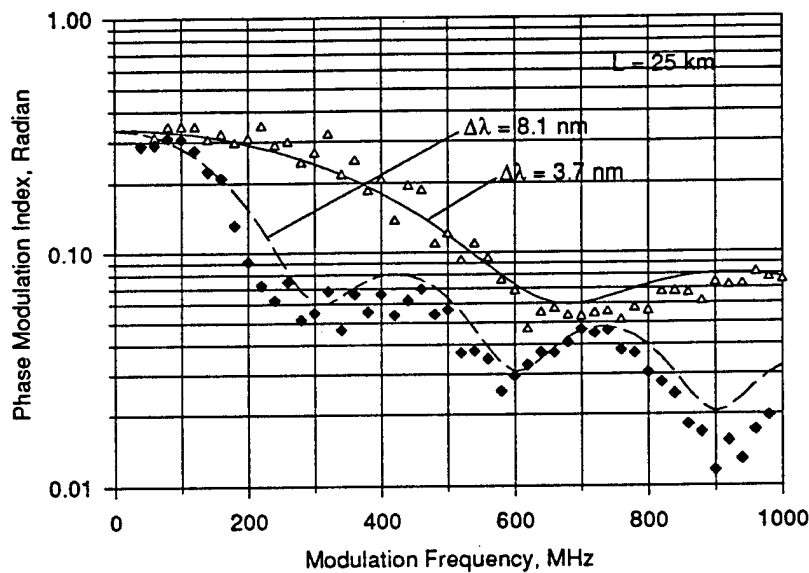


Figure 6-9. XPM index versus the modulation frequency of pump laser. Fiber length $L = 25$ km. The dots are experimental data, and the lines show the theoretical prediction.

We have shown theoretically that the cross-phase modulation (XPM) index depends on fiber length, fiber chromatic dispersion, wavelength separation, and the frequency of power fluctuation. A simple expression Eq. (6.7) for the XPM index has been derived and shown to agree well with experimental measurements. The results show that at high modulation frequencies, the XPM index is approximately inversely proportional to the product of the modulation frequency and wavelength separation. These results indicate that the XPM is expected to be smaller in communication systems operating at higher data rates and larger wavelength separations.

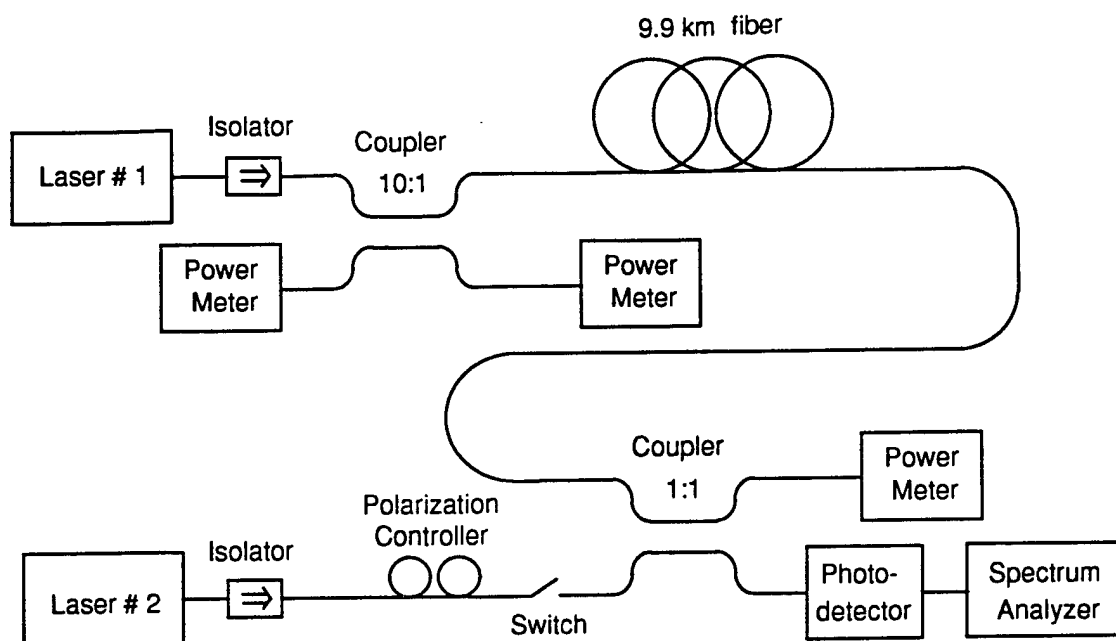


Figure 6-10. Experimental setup used to characterize signal under Brillouin scattering.

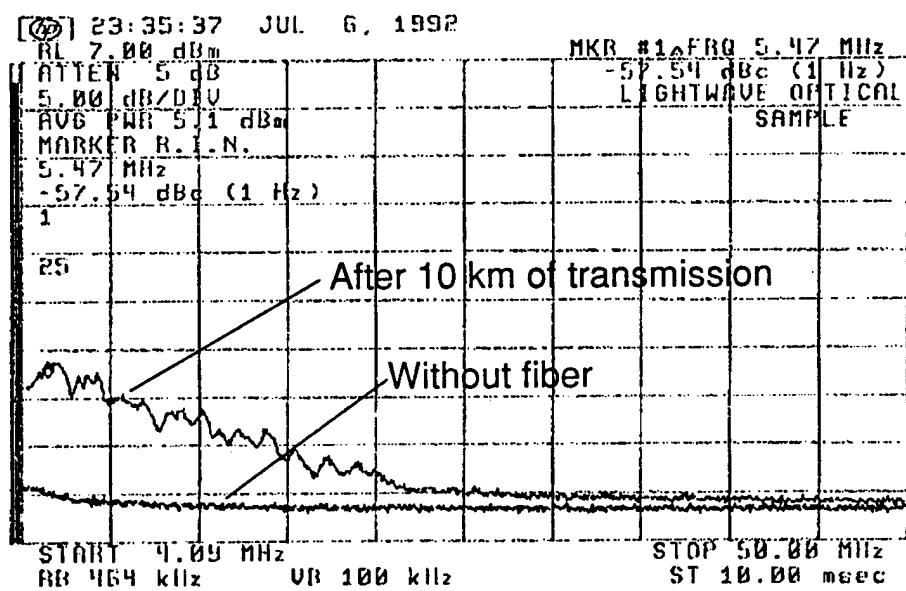


Figure 6-11. Spectrum of the transmitted light intensity.

6.6 Stimulated Brillouin Scattering

Another potentially limiting nonlinear effect is stimulated Brillouin scattering (SBS). The SBS process tends to reflect back the launched optical power exceeding a certain threshold, and also induces excess noise in the transmitted signals. Fig. 6-10 shows the experimental setup we used to measure the characteristics of transmitted signal under Brillouin scattering.

Two Nd:YAG lasers with very narrow linewidth are used in this experiment. By heterodyning the transmitted or back-scattered signal with the second laser, we can characterize the extra noise induced by Brillouin scattering effect.

The transmitted light has been found to be impaired by relaxation oscillation of stimulated Brillouin scattering once the launched power exceeded Brillouin threshold. As shown in Fig. 6-11, this effect causes low frequency intensity fluctuation of the transmitted signal.

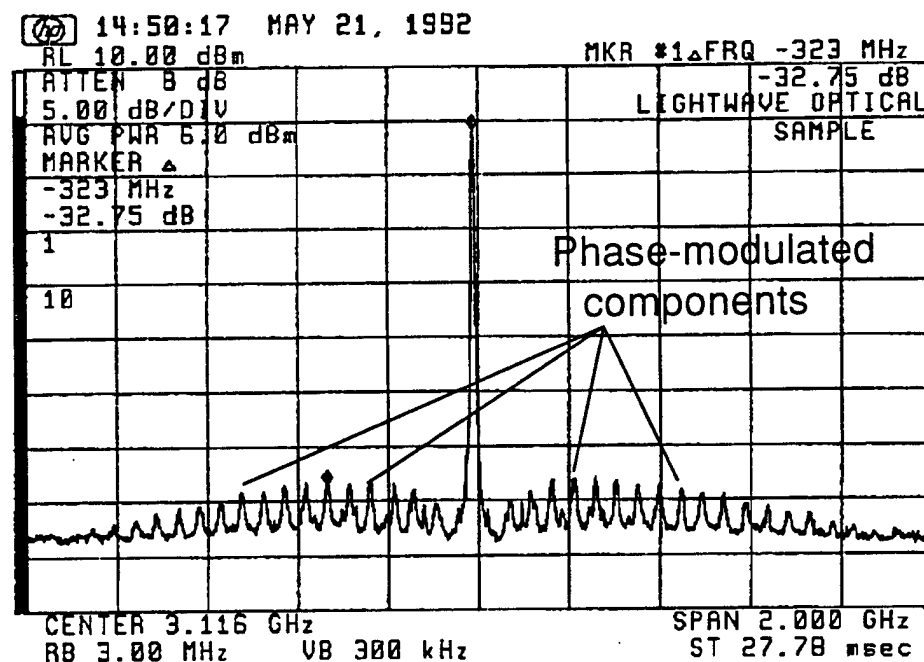


Figure 6-12. Heterodyned spectrum of the transmitted light modulated by thermal acoustic waves.

6.7 Fiber-Induced Parasitic Phase Modulation

We experimentally observed a phase modulation caused by thermal acoustic vibrations in the fiber. The acoustic wave excited by thermal vibrations modulates the phase of the light propagating along the fiber. The acoustic wave in the fiber has several discrete modes with different resonant frequency associated with each mode. More than 30 spectral lines have been observed in the phase modulated spectrum, as shown in Fig. 6-12. Spectral lines caused by the phase modulation are about 30 dB lower than the main spectral component, corresponding to a phase modulation index of 10^{-3} for 10 km of propagation. The strength of the effect grows proportionally to the square root of propagation distance.

Based on these experimental observations, we performed a theoretical analysis of the impact of parasitic fiber-induced phase modulation on ultra-long distance DPSK optical communication systems.

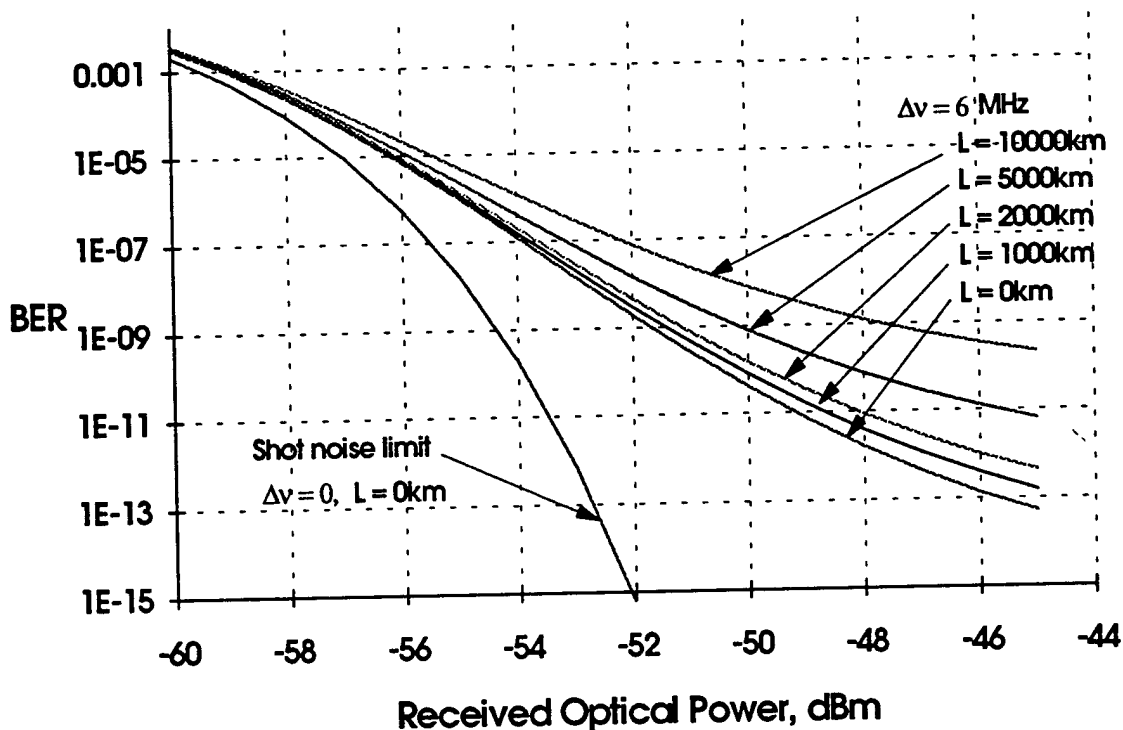


Figure 6-13. Calculated bit error rate of 1 Gb/s DPSK heterodyne systems. Shot noise, laser phase noise and fiber-induced parasitic phase noise are included in this analysis.

Our results show that the performance of ultra-long distance optical DPSK system can be impaired by thermal acoustic modulation. Fig. 6-13 shows the calculated bit error rate of 1 Gb/s DPSK systems versus received optical power for different fiber lengths in the presence of fiber-induced phase noise, laser phase noise, and shot noise. The total laser linewidth shown in Fig. 6-13 is 6 MHz. Inspection of Fig. 6-13 reveals that the power penalty at the BER of 10^{-9} is 2.7 dB for finite laser linewidth. The power penalties for the fiber induced phase noise are 0.2 dB, 0.5 dB, 1.5 dB, and 3.9 dB for transmission distances of 1,000 km, 2,000 km, 5,000 km, and 10,000 km, respectively.

Fig. 6-14 shows the calculated BER floor of 1 Gb/s DPSK systems versus laser linewidth for different fiber lengths in the presence of thermal acoustic phase noise. Shot noise is ignored to show the BER floor which is the minimum BER that can be achieved at high received power. Inspection of Fig. 6-14 reveals that the BER floor increases as the transmission distance increases. At transmission distance greater than 2,000 km, the fiber induced phase noise deteriorates system performance significantly. On the other hand, when transmission distance is less than 1,000 km, the BER floor is less than two times the BER floor of back-to-back system. Therefore, the fiber induced phase noise is negligible in DPSK systems with transmission distances less than 1,000 km.

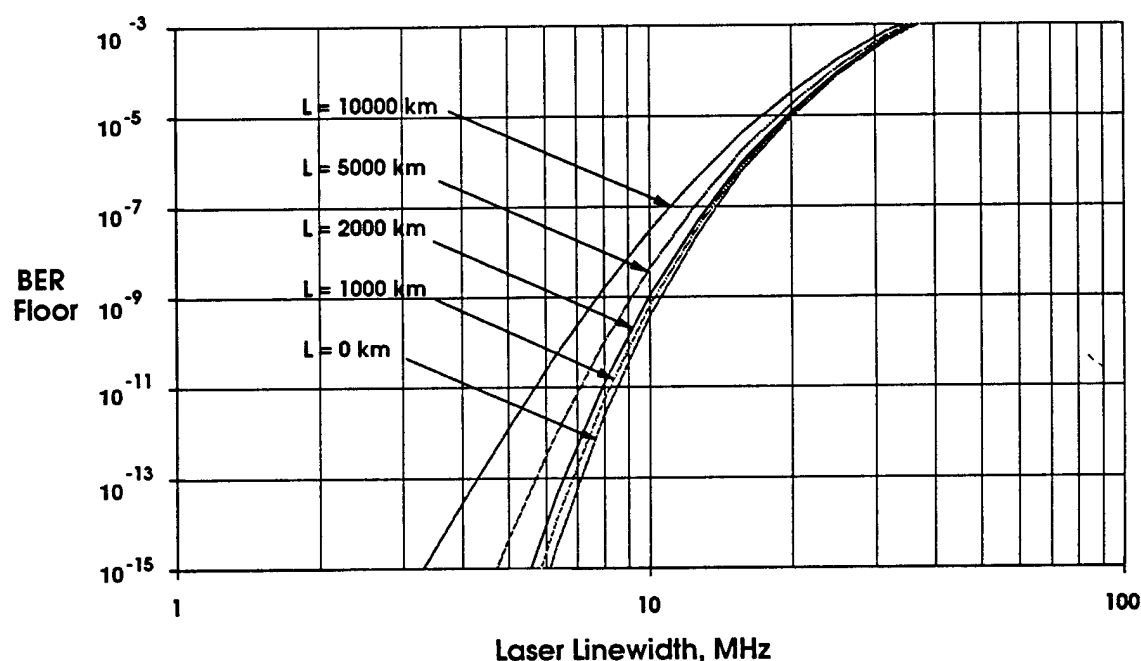


Figure 6-14. Calculated BER floor of 1 Gb/s DPSK heterodyne systems. Both laser phase noise and fiber-induced parasitic phase noise are included in this analysis.

6.8 Conclusions

In this chapter, we have analyzed and simulated the impact of four-wave mixing (FWM) on ASK, DPSK, and FSK wavelength division multiplexed (WDM) systems. We have found that Manchester coding improves ASK and DPSK systems, and that systems utilizing nondispersion-shifted fiber are less seriously impaired by FWM than those using dispersion-shifted fiber. We have tested the Gaussian theoretical model of FWM interference through simulation, and have found that the Gaussian assumption results in slight overestimates of the receiver sensitivity. Using simulation results, we have found that the Student's t distribution fits the probability density function of FWM interference after detection.

We have investigated the impact of modulation frequency on cross-phase modulation (XPM) in dispersive fibers. We have derived an expression for the XPM index as a function of frequency and have corroborated it using experimental results. The results show that at high modulation frequencies, the XPM index is approximately inversely proportional to the product of the modulation frequency and wavelength separation. This indicates that XPM is expected to be smaller in communication systems operating at higher data rates and larger wavelength separations.

We have experimentally investigated both stimulated Brillouin scattering (SBS) and fiber-induced parasitic phase modulation. Based upon the experimental results, we performed a theoretical analysis of parasitic phase modulation on ultra-long distance DPSK transmission. The sensitivity penalties for fiber-induced phase noise on a 1 Gb/s DPSK system are 0.2 dB, 0.5 dB, 1.5 dB, and 3.9 dB for transmission distances of 1,000 km, 2,000 km, 5,000 km, and 10,000 km, respectively.

CONCLUSIONS

During this project, our research has focused on three major aspects of advanced optical fiber communication systems: high dynamic range optical analog links, dynamic wavelength division multiplexing (WDM) optical networks, and fiber nonlinearities.

We have investigated the fundamental limit of the dynamic range (FLDR) of homodyne and heterodyne coherent amplitude-modulated links using the WIRNA (WIdeband - Rectifier - NArrowband) demodulator structure. We have found that a balanced receiver and 2K-port optical hybrid are essential for the FLDR of a homodyne WIRNA link to be comparable to that of a heterodyne WIRNA link. We have optimized the FLDR of a heterodyne WIRNA link by optimizing the receiver intermediate frequency (IF) bandwidth. By constructing an experimental heterodyne WIRNA link, we have verified that the link is linewidth-insensitive for laser linewidths up to several hundred MHz and that it outperforms an experimental direct detection link for received optical signal powers less than 85 μ W. We conclude that the heterodyne WIRNA link is potentially useful in real systems where there is a high link loss (such as in distribution systems) due to the reduced impact of receiver thermal noise in coherent links.

We have analyzed the performance of coherent analog links employing phase modulation (PM) and frequency modulation (FM). Coherent angle-modulated analog fiber-optic links can offer increased SFDR as compared to AM direct detection (DD) and coherent AM links, particularly at low signal levels, where coherent systems can operate in the shot noise-limited regime while DD links are thermal noise-limited. Coherent angle-modulated links using low-linewidth lasers such as solid-state Nd:YAGs or multi-quantum-well distributed feedback (DFB) semiconductor lasers have the potential to substantially outperform DD and coherent AM links, especially for low optical powers. For laser linewidths greater than about 200 kHz for 1 mW received optical power, coherent angle-modulated links will not outperform coherent AM links. Angle modulated systems can exhibit substantial RIN insensitivity through the use of a limiter in the receiver and by operating at an IF well above the RIN roll-off frequency. The linearity of angle modulated links tends to improve for high IFs due to the improved linearity of the phase or frequency discriminator in the receiver. We conclude that coherent angle-modulated links are, like the WIRNA link, potentially useful in real systems where there is a high link loss.

We have described conventional approaches to phase noise cancellation (PNC) using reference transport and have shown that they do not work for analog links. Instead, we have focused on interferometric links, which both cancel laser phase noise and generate a received signal at an intermediate frequency without the use of a separate local oscillator laser. We have shown theoretically that the heterodyne interferometric phase modulated (HIPM) link provides a 3 dB spurious-free dynamic range (SFDR) improvement at laser powers of less than 1 mW for representative link parameters and that the SFDR improvement increases for higher powers due to the suppression of laser relative intensity noise (RIN). For a RIN of -155 dB/Hz, the SFDR in a 1 GHz bandwidth improves by 10 dB for a laser output power of 40 mW. We have constructed a proof-of-concept HIPM link and have demonstrated up to 23 dB suppression of third-order intermodulation products (IMPs) over an AM direct detection link, which translates into a 7.7 dB improvement in SFDR. We conclude that the HIPM link appears to have potential for future applications using high-power semiconductor lasers, such as in cellular base station to antenna connection.

We have constructed a PSK/ASK transceiver for STARNET, a WDM computer communication network, to demonstrate the feasibility of simultaneously transmitting and receiving 125 Mb/s FDDI-compatible, packet-switched, ASK data and 2.488 Gb/s circuit-switched PSK data on the same optical carrier. Both subsystems function properly with error rates less than 10^{-9} and a combined sensitivity of -27.6 dBm. The power budget which we achieved is large enough for a 100 node passive star network with a diameter of 5 km in a power margin of 3 dB. In addition, the impact of the ASK modulation on the PSK receiver and vice versa have been quantified theoretically and agree with experimental data. We conclude that the use of coherent technology to transmit fast PSK data and slower ASK data on the same lightwave is feasible.

The theoretical results for the combined DPSK and ASK modulation format indicate that an excellent sensitivity may be simultaneously maintained by both receivers, even for linewidths up to one percent of the bit rate for DPSK. As a result, this combined modulation format is attractive for WDM networks using semiconductor lasers, since a phase-locked loop is not required for the DPSK receiver (unlike the PSK receiver). Our experimental demonstration of simultaneous DPSK and ASK link operation indicates that this format for sending network data and control information is not difficult to implement. We conclude that combined DPSK and ASK is a feasible combined modulation format for WDM networks using commercially available semiconductor lasers.

We have extended the previously developed rigorous model of Jacobsen and Garrett and Gaussian approximation of Kazovsky and Tonguz for optically amplified direct detection (OADD) ASK systems. The new models account for incomplete ASK modulation, which is encountered in typical systems using either direct or external intensity modulation. The new models also include the impact of nonzero laser linewidth and spontaneous emission noise of the optical amplifier. As a result, the new models can be used to optimize the optical filter bandwidth in OADD systems for a wide range of ASK modulation depths and laser linewidths. For nonoptimum filter bandwidths, the maximum penalty occurs not for complete ASK modulation; instead, a floor exists for the minimum usable ASK modulation depth due to the severe phase-to-amplitude noise conversion. This floor is not accurately predicted using the Gaussian approximation. As a result, the rigorous method is applicable in real network design in cases where the available IF filters do not have bandwidths which correspond to the optimal value for the transmitted signal bandwidth and linewidths of the transmitter and local oscillator lasers.

We have designed and constructed a network interface which provides buffering and distributed multi-hop virtual circuit routing of packets over a ring network topology. STARNET has served as a testbed for the design, development, and verification of the interface. The interface does packet routing on the fly, uses DMA operations to transfer packets to and from the network and the workstation (leaving the CPU free for other tasks), and provides for programmable and dynamic bandwidth allocation. Simulations and experimental results show that the interface enables STARNET to support a large number of distributed multimedia applications such as video-conferencing. The completed interface has been operational since January 1994 running large file transfer and multimedia applications in a two-node environment. We conclude that in general, the interface is potentially useful in reconfigurable WDM networks.

We have analyzed and simulated the impact of four-wave mixing (FWM) on ASK, DPSK, and FSK WDM systems. We have found that Manchester coding improves ASK and DPSK systems, and that systems utilizing nondispersion-shifted fiber are less seriously impaired by FWM than those using dispersion-shifted fiber. We have tested the Gaussian theoretical model of FWM interference through simulation, and have found that the Gaussian assumption results in slight overestimates of the receiver sensitivity. Using simulation results, we have found that the Student's *t* distribution fits the probability density function of FWM interference after detection.

We have investigated the impact of modulation frequency on cross-phase modulation (XPM) in dispersive fibers. We have derived an expression for the XPM index as a function of frequency and have corroborated it using experimental results. The

results show that at high modulation frequencies, the XPM index is approximately inversely proportional to the product of the modulation frequency and wavelength separation. This indicates that XPM is expected to be smaller in communication systems operating at higher data rates and larger wavelength separations.

We have experimentally investigated fiber-induced parasitic phase modulation. We have determined theoretically that this effect can degrade long-distance DPSK transmission, giving 1.5 dB and 3.9 dB penalties for transmission distances of 5,000 km and 10,000 km, respectively.

LIST OF PUBLICATIONS DURING THE PROJECT

I. Papers in Refereed Journals

1. J. C. Fan, R. F. Kalman, L. G. Kazovsky, "Interferometric Analog Optical Links," *IEEE/OSA J. of Lightwave Technology*, to be submitted for publication.
2. O. K. Tonguz, M. O. Tanrikulu, L. G. Kazovsky, "Performance of Coherent ASK Lightwave Systems with Finite IF Frequency," *IEEE/OSA J. of Lightwave Technology*, submitted for publication.
3. C. Barry, C. Noronha, N. Taranenko, S. K. Agrawal, L. G. Kazovsky, "Network Interface Design for Multi-Gbit/s WDM Optical Networks," *Journal of High Speed Networks*, accepted for publication.
4. L. G. Kazovsky, T. K. Fong, R. T. Hofmeister, "Optical Local Area Network Technologies," *IEEE Commun. Magazine*, accepted for publication in the Special Issue on Optically Multiplexed Networks, invited paper.
5. J. Fan, G. Jacobsen, L. G. Kazovsky, "Preamplifier ASK System Performance with Incomplete ASK Modulation: Influence of ASE and Laser Phase Noise," *IEEE J. of Lightwave Technology*, accepted for publication.
6. D. J. M. Sabido, M. Tabara, T. K. Fong, R. F. Kalman, L. G. Kazovsky, "Experimental Linewidth-Insensitive Analog Optical Links," *IEEE/OSA J. of Lightwave Technology*, accepted for publication.
7. R. F. Kalman, L. G. Kazovsky, "Demonstration of an Analog Heterodyne Interferometric Phase-Modulated (HIPM) Link," *IEEE Photonics Technology Letters*, accepted for publication.
8. R. F. Kalman, J. C. Fan, L. G. Kazovsky, "Dynamic Range of Coherent Analog Fiber-Optic Links," *IEEE/OSA J. of Lightwave Technology*, Vol. 12, No. 7, July 1994, pp. 1263-1277.
9. N. L. Taranenko, L. G. Kazovsky, Y. N. Taranenko, "Three-Wave Envelope Solitons: Possibility of Controlling the Speed of Light in the Fiber," *IEEE/OSA J. of Lightwave Technology*, Vol. 12, No. 7, July 1994, pp. 1101-1111.
10. M. Hickey, L. G. Kazovsky, "The STARNET Coherent WDM Computer Communications Network: Experimental Transceiver Employing a Novel Modulation Format," *IEEE/OSA J. of Lightwave Technology*, Vol. 12, No. 6, June 1994, pp. 876-884.

11. T. K. Chiang, N. Kagi, T. K. Fong, M. E. Marhic, L. G. Kazovsky, "Cross-Phase Modulation in Dispersive Fibers: Theoretical and Experimental Investigation of the Impact of Modulation Frequency," *IEEE Photonics Technology Letters*, Vol. 6, No. 6, June 1994, pp. 733-736.
12. T. K. Fong, D. J. M. Sabido IX, R. F. Kalman, M. Tabara, L. G. Kazovsky, "Linewidth-insensitive Coherent AM Optical Links: Design, Performance and Potential Applications," *IEEE/OSA J. of Lightwave Technology*, Vol. 12, No. 3, March 1994, pp. 526-534.
13. T. K. Fong, M. Tabara, D. J. M. Sabido IX, L. G. Kazovsky, "Dynamic Range of Externally Modulated Analog Optical Links: Optical Amplification Versus Coherent Detection," *IEEE Photonics Technology Letters*, Vol. 6, No. 2, February 1994, pp. 270-272.
14. T. K. Fong, D. J. M. Sabido IX, M. Tabara, L. G. Kazovsky, "Spurious-free Dynamic Range of Linewidth-Insensitive Coherent AM Analogue Optical Links," *IEE Electronics Letters*, Vol. 29, No. 23, November 11, 1993, pp. 2060-2061.
15. G. Fikshan, R. Gross, J. C. Fan, L. G. Kazovsky, "Performance Optimization of Directly Modulated FM-SCM Systems with Optical Discriminators," *IEEE Photonics Technology Letters*, Vol. 4, No. 7, July 1993, pp. 845-848.
16. R. F. Kalman, J. C. Fan, L. G. Kazovsky, "A Novel Analog Optical Link with High Dynamic Range," *IEEE Photonics Technology Letters*, Vol. 5, No. 6, June 1993, pp. 725-728.
17. M. Hickey, C. Barry, C. Noronha, L. G. Kazovsky, "Experimental PSK/ASK Transceiver for the STARNET WDM Computer Communication Network," *IEEE Photonics Technology Letters*, Vol. 5, No. 5, May 1993, pp. 568-571.
18. L. G. Kazovsky and P. T. Poggiolini, "STARNET: a Multi-Gbit/s Optical LAN Utilizing a Passive WDM Star," *IEEE/OSA J. of Lightwave Technology*, Special Issue on Broadband Optical Networks, Vol. 11, No. 5, May 1993, pp. 1009-1027.
19. T. K. Fong, J. Sabido, L. G. Kazovsky, "Linewidth-Insensitive Coherent Analog Optical Link Using Semiconductor Lasers," *IEEE Photonics Technology Letters*, Vol. 4, April 1993, pp. 469-471.
20. O. K. Tonguz, M. O. Tanrikulu, L. G. Kazovsky, "Impact of Finite Frequency Deviation on the Performance of Dual-Filter Heterodyne FSK Lightwave Systems," *IEEE/OSA J. of Lightwave Technology*, Vol. 11, No. 2, February 1993, pp. 316-330.

21. R. F. Kalman, L. G. Kazovsky, J. W. Goodman, "Space Division Switches Based on Semiconductor Optical Amplifiers," *IEEE Photonics Technology Letters*, Vol. 4, No. 10, October 1992, pp. 1048-1051.
22. J. C. Fan and L. G. Kazovsky, "Noise Analysis of Subcarrier-Multiplexed Coherent Optical Video Transmission Systems Using Direct Frequency Modulation of Semiconductor Lasers," *IEEE Photonics Technology Letters*, Vol. 4, No. 7, July 1992, pp. 777-780.
23. L. G. Kazovsky, C. Barry, M. Hickey, C. Noronha, P. T. Poggiolini, "Wavelength Division Multiplexed Local Area Networks," *IEEE Lightwave Telecommunications Systems*, Vol. 3, No. 2, May 1992, pp. 8-15.
24. Y. N. Taranenko and L. G. Kazovsky, "Three-Wave Envelope Solitons: Can the Speed of Light in the Fiber be Controlled?" *IEEE Photonics Technology Letters*, Vol. 4, No. 5, May 1992, pp. 494-497.

II. Conference Papers

25. M. Hickey, F. J. Westphal, J. Fan, G. Jacobsen, L. G. Kazovsky, "Combined ASK/FSK Modulation for the STARNET WDM Computer Network," *IEEE/LEOS Summer Topical Meeting on Optical Networks*, Lake Tahoe, Nevada, July 1994, Digest on Optical Networks and Their Enabling Technologies, pp. 38-39.
26. F. J. Westphal, M. Hickey, L. G. Kazovsky, "An Experimental DPSK/ASK Transceiver for the STARNET Coherent WDM Network," *CLEO '94*, Anaheim, CA, May 1994, pp. 337-338.
27. L. G. Kazovsky, "WDM Local Area Networks," *OFC '94*, Workshop on Multigigabit Communication, San Jose, CA, February 20-25, 1994, **invited talk**.
28. C. Barry, C. Noronha, N. Taranenko, S. K. Agrawal, L. G. Kazovsky, "Gigabit/s Optical Interface for WDM STARNET Network," *OFC '94*, San Jose, CA, February 1994, pp. 68-70.
29. D. J. M. Sabido, M. Tabara, T. K. Fong, L. G. Kazovsky, "Experimental Investigation of the Impact of Erbium-Doped Fiber Amplifiers on Coherent AM Optical Links," *OFC '94*, San Jose, CA, February 1994, pp. 264-266.
30. J. C. Fan, R. F. Kalman, L. G. Kazovsky, "A Comparison of Three Analog Optical Links for High Dynamic Range Applications," *IEEE Globecom '93*, Houston, TX, December 1993, pp. 1877-1881.

31. T. K. Fong, D. J. M. Sabido IX, M. Tabara, L. G. Kazovsky, "Coherent Analog Optical Links: Design, Performance and Potential Applications," **IEEE Globecom '93**, Houston, TX, December 1993, pp. 1886-1890.
32. L. G. Kazovsky, M. J. Hickey, "Towards Implementation of Multi-Gb/s Optical Networks," **IEEE LEOS Annual Meeting**, San Jose, CA, November 1993, **invited talk**, pp. 410-411.
33. M. Tabara, D. J. M. Sabido IX, T. K. Fong, C. Lu, L. G. Kazovsky, "A Linewidth-Insensitive Coherent AM Analog Optical Links: A Comparison of Direct and External Modulation Formats," **Sixth Annual Meeting, IEEE LEOS '93**, San Jose, CA, November 1993, pp. 368-369.
34. N. L. Taranenko, L. G. Kazovsky, Y. N. Taranenko, "Three-Wave Envelope Solitons: Possibility of Controlling the Speed of Light in the Fiber," **URSI General Assembly**, Kyoto, Japan, August 1993.
35. T. K. Chiang, D. Datta, L. G. Kazovsky, "Statistical Distribution of Four-Wave Mixing Interference in ASK Optical WDM Systems," **LEOS Summer Topical Meeting**, Santa Barbara, CA, July 26-27, 1993; Digest on Impact of Fiber Nonlinearities on Lightwave Systems, pp. 25-26.
36. D. Datta, T. K. Chiang, L. G. Kazovsky, "Impact of Four Wave Mixing on Optical FSK WDM Communication Systems," **LEOS Summer Topical Meeting**, Santa Barbara, CA, July 26-27, 1993; Digest on Impact of Fiber Nonlinearities on Lightwave Systems, pp. 27-28.
37. M. Hickey, C. Barry, C. Noronha, L. G. Kazovsky, "The STARNET Coherent Optical WDM Network: Modulation Format and Computer-to-Optics Interface," **LEOS Summer Topical Meeting**, Santa Barbara, CA, July 28-30, 1993; Digest on Gigabit Networks, pp. 58-59.
38. M. Tabara, D. J. M. Sabido IX, T. K. Fong, C. Lu, L. G. Kazovsky, "Experimental Investigation of a Linewidth-insensitive Coherent AM Optical Link," **LEOS Summer Topical Meeting**, Santa Barbara, CA, July 19-21, 1993; Digest on Optical Microwave Interactions, pp. 13-14.
39. R. F. Kalman, J. C. Fan, L. G. Kazovsky, "A Novel Phase-Modulated Analog Optical Link," **SPIE's International Symposium OE/Fiber's 93**, San Diego, CA, July 13-14, 1993; Conference Proceedings, pp. 20-29.
40. J. Sabido, M. Tabara, T. K. Fong, C. L. Lu, L. G. Kazovsky, "Theoretical and Experimental Investigations of the Dynamic Range of High Frequency Coherent AM Optical Links Using Semiconductor Lasers," **SPIE's International Symposium OE/Fiber's 93**, San Diego, CA, July 13-14, 1993; Conference Proceedings, pp. 11-19.

41. C. F. Barry, M. J. Hickey, C. A. Noronha, P. T. Poggiolini, L. G. Kazovsky, "A Experimental Multi-Gb/s WDM Local Area Network," **ICC '93**, Geneva, Switzerland, March 1993.
42. L. G. Kazovsky, C. Barry, M. Hickey, C. Noronha, P. T. Poggiolini, "A Multi-Gbit/s Optical LAN Utilizing a Passive WDM Star: Towards an Experimental Prototype," **IEEE INFOCOM**, San Francisco, CA, March 1993; Conference Proceedings, pp. 48-56.
43. T. K. Chiang and L. G. Kazovsky, "Scattering from Guided Acoustic Waves in Optical Fiber and It's Influence on DPSK Optical Communication Systems," **OFC '93**, San Jose, CA, February 1993; Conference Digest, pp. 208-209.
44. G. Fikshan, R. Gross, J. C. Fan, L. G. Kazovsky, "Optimization of Directly Modulated FM-SCM Systems Using an Optical Frequency Discriminator," **OFC '93**, San Jose, CA, February 1993; Conference Digest, pp. 228-229.
45. M. Hickey, C. Barry, C. Noronha, L. G. Kazovsky, "An Experimental PSK/ASK Transceiver for a Multigigabit WDM Local Area Network," **OFC '93**, San Jose, CA, February 1993; Conference Digest, pp. 233- 234.
46. H. Lee and L. G. Kazovsky, "Supression of Four-Wave Mixing Crosstalk in WDM Systems Using Manchester Coding and DPSK Modulation," **OFC '93**, San Jose, CA, February 1993; Conference Digest, pp. 135-136.
47. S. Benedetto, L. G. Kazovsky, P. T. Poggiolini, C. A. Barry, A. Djupsjobacka, B. Lagerstrom, S. Chandrasekhar, U. Koren, "Binary and Multilevel Polarization Modulation: Experimental System Design," **SPIE's International Symposium OE/Fibers '92, Multigigabit Fiber Communications**, Boston, MA, September 1992; Conference Proceedings, Vol. 1787, pp. 248-258.
48. M. Hickey, C. F. Barry, L. G. Kazovsky, "Combined ASK/PSK Modulation Format for the STARNET Wavelength Division Multiplexed Local Area Network," **SPIE's International Symposium OE/Fibers '92, Multigigabit Fiber Communications**, Boston, MA, September 1992; Conference Proceedings, Vol. 1787, pp. 326-335.
49. L. G. Kazovsky, "Coherent Optical Communications," **SPIE's International Symposium OE/Fibers '92, Multigigabit Fiber Communications**, Boston, MA, September 1992; short course.
50. L. G. Kazovsky, C. F. Barry, C. A. Noronha, P. T. Poggiolini, "STARNET-E: A Broadband Wavelength Division Multiplexed Optical Local Area Network," **SPIE's International Symposium OE/Fibers '92, Multigigabit Fiber**

Communications, Boston MA, September 1992; Conference Proceedings, Vol. 1787, pp. 20-31.

51. L. G. Kazovsky, K. Liu, C. A. Noronha, "Multigigabit Optical Networking," **Tutorial Overview, SPIE's International Symposium OE/Fibers '92, Multigigabit Fiber Communications**, Boston, MA, September 1992; Conference Proceedings, Vol. 1787, pp. 67-77.
52. H. Lee and L. G. Kazovsky, "Impact of Four Wave Mixing on Manchester Coded Optical WDM Communication Systems," **SPIE's International Symposium OE/Fibers '92, Multigigabit Fiber Communications**, Boston, MA, September 1992; Conference Proceedings, Vol. 1787, pp. 267-280.
53. L. G. Kazovsky, "Future Optical Fiber Communication Systems and Lasers for Their Implementation", **BILCON '92**, Ankara, Turkey, July 1992; **invited paper**; Conference Proceedings, pp. 1-14.
54. O. K. Tonguz, M. O. Tanrikulu and L. G. Kazovsky, "Impact of Finite Frequency Deviation on the Performance of Dual-Filter Heterodyne FSK Lightwave Systems", **BILCON '92**, Ankara, Turkey, July 1992; Conference Proceedings, pp. 63-69.
55. D. J. M. Sabido IX, T. K. Fong, R. K. Kalman, L. G. Kazovsky, "Linewidth-insensitive Coherent Optical Analog Links," **Optoelectronic Signal Processing for Phase Array Antennas III**, SPIE, Conference Proceedings, Vol. 1703, April 1992, pp. 504-522.
56. L. G. Kazovsky and P. Poggiolini, "STARNET: A Multi-Gbit/s Optical Local Area Network with Both Packet and Circuit Switching," **OFC '92**, San Jose, CA, February 1992, Conference Proceedings, pp. 297-298.
57. Y. Taranenko and L. G. Kazovsky, "Can the Speed of Light in the Fiber Be Controlled?" **OFC '92**, San Jose, CA, February 1992, Conference Proceedings, pp. 2-3.
58. L. G. Kazovsky and J. C. Fan, "Coherent Analog FM-SCM Video Transmission Using Direct Frequency Modulation of Semiconductor Lasers," **OFC '92**, San Jose, CA, February 1992, Conference Proceedings, pp. 24-25.
59. R. F. Kalman, L. G. Kazovsky, J. W. Goodman, "Space-Division Optical Switches Based on Semiconductor Optical Amplifiers," **OFC '92**, San Jose, CA, February 1992, Conference Proceedings, p. 131.
60. L. G. Kazovsky and P. Poggiolini, "STARNET: A Multi-Gbit/s Optical Local Area Network with Both Packet and Circuit Switching," **Sixth Annual IEEE**

Workshop on Computer Communications, Monterey, CA, October 21-24, 1991.

61. O. K. Tonguz and L. G. Kazovsky, "The Sensitivity of Direct-Detection Lightwave Receivers Using Optical Preamplifiers", **SPIE '91 Conference OE/Fibers**, Boston, MA, September 1991, Conference Proceedings, pp. 179-183.
62. P. Poggiolini and L. G. Kazovsky, "STARNET: An Integrated Services Broadband Optical Network with Physical Star Topology," **SPIE '91 Conference OE/Fibers**, Boston, MA, September 1991, Conference Proceedings, pp. 14-29.
63. S. Benedetto, L. G. Kazovsky, P. Poggiolini, "Minimum Polarization Modulation: A Highly Bandwidth Efficient Coherent Optical Modulation Scheme," **SPIE '91**, Boston, MA, September 1991, Conference Proceedings, pp. 112-121.